

---

# The bar of the Andromeda galaxy revealed by integral field spectroscopy

Michael Opitsch

---



München 2016



---

# **The bar of the Andromeda galaxy revealed by integral field spectroscopy**

**Michael Opitsch**

---

Dissertation  
an der Fakultät für Physik  
der Ludwig–Maximilians–Universität  
München

vorgelegt von  
Michael Opitsch  
aus Weissenburg i. Bay.

München, den 30. September 2016

Erstgutachter: PD Dr. Roberto Saglia

Zweitgutachter: Prof. Dr. Andreas Burkert

Tag der mündlichen Prüfung: 11. November 2016

# Zusammenfassung

Die Andromedagalaxie M31 ist die unser eigenen Milchstraße am nächsten gelegene große Spiralgalaxie und gibt uns daher die einzigartige Gelegenheit, eine Galaxie dieses Typs im Detail zu studieren. Eine lange offene Frage bezüglich M31 ist, ob sie einen Balken enthält oder nicht. Die Galaxie ist gegenüber dem Blickwinkel stark geneigt, sodass man den Balken in der Photometrie nicht direkt erkennen kann, jedoch ist sie nicht stark genug geneigt, um den Balken als kasten- bzw. erdnussförmigen Umriss oberhalb und unterhalb der Scheibenebene hervorzuragen zu sehen.

In dieser Arbeit werden Ergebnisse einer Beobachtungskampagne der Zentralregion von M31 mit dem Integralfeldspektrographen VIRUS-W vorgestellt. In VIRUS-W sind 267 Fasern rechteckig angeordnet, jede Aufnahme hat ein Gesichtsfeld von  $105'' \times 55''$ , was bei einer Entfernung von M31 von  $D = 780 \text{ kpc} = 397 \text{ pc} \times 208 \text{ pc}$  entspricht. Insgesamt wurden 198 Felder beobachtet, die den Bulge komplett abdecken und die Scheibe entlang von sechs verschiedenen Richtungen stichprobenartig bis zu einer Entfernung von einer Scheibenskalenlänge entlang der großen Halbachse untersuchen. Als Ergebnis erhalten wir ca. 50.000 Spektren, die zu 7563 Bins zusammengefasst werden, um den Signal-zu-Rausch-Wert soweit zu erhöhen, dass stellare Geschwindigkeitsverteilungen entlang der Sichtlinie abgeleitet und die Stärke der Absorptionslinien sowie die Flüsse und die Kinematik der Emissionslinien gemessen werden können. Der Wellenlängenbereich der Spektren ist  $4802 \text{ \AA} - 5500 \text{ \AA}$ , stellare Absorptionslinien sind dort  $H\beta$  bei  $4861 \text{ \AA}$ , das Mgb-Triplett bei  $5167 \text{ \AA}$ ,  $5173 \text{ \AA}$  und  $5187 \text{ \AA}$  sowie Eisen-Absorptionsfeatures bei  $5015 \text{ \AA}$ ,  $5270 \text{ \AA}$ ,  $5335 \text{ \AA}$  und  $5406 \text{ \AA}$ . Wir beobachten auch Emissionslinien des ionisierten Gases, und zwar ebenfalls  $H\beta$  und die Doublets  $[OIII]\lambda\lambda 4959, 5007$  sowie  $[NI]\lambda\lambda 5198, 5200$ . Die Kinematik der Sterne und des Gases werden gleichzeitig gefittet, die stellare Kinematik anhand der Absorptionslinien und die Gaskinematik anhand der Emissionslinien.

Die Geschwindigkeitsverteilung entlang der Sichtlinie wird als Gauss-Hermite-Reihe mit den Momenten  $v$ ,  $\sigma$ ,  $h3$  und  $h4$  beschrieben. Die stellare Kinematik weist mehrere Merkmale auf, die in Balkengalaxien beobachtet werden, wie einen "Doppelbuckel" im Geschwindigkeitsprofil und bei denselben Radien Plateaus im Profil der Geschwindigkeitsdispersion. Das Gauss-Hermite-Moment  $h3$  ist mit der Geschwindigkeit über den Großteil der Bulgeregion korreliert, was wieder mit der Präsenz eines Balkens erklärt werden kann. Wir vergleichen unsere Messungen mit einem N-Körper-Modell von M31 mit Balken und finden eine gute Überein-

stimmung.

Die Gaskinematik, die an der [OIII] $\lambda$ 5007-Linie gemessen wird, ist komplizierter. Bei etwa der Hälfte der gebinteten Spektren hat die Linie zwei in Geschwindigkeit getrennte Maxima, was auf zwei getrennte Komponenten hinweist. Beide Komponenten zeigen ein S-förmiges Muster in den Geschwindigkeitskarten, was man auch in anderen Balkengalaxien beobachtet. Die Positions-Geschwindigkeits-Diagramme ähneln ebenfalls denen von Balkengalaxien. Die Morphologie des ionisierten Gases hat eine Spiralstruktur, die auch Gemeinsamkeiten mit der erwarteten Morphologie des Gases in Balkengalaxien aufweist.

Außerdem untersuchen wir die Eigenschaften der stellaren Populationen, indem wir Absorptionslinienstärken messen und sie mit einfachen Stellarpopulationsmodellen vergleichen. Die Sterne sind alt (11 Milliarden Jahre) in der Bulgeregion, in den äußersten Scheibepointings fällt das Alter auf einige wenige Milliarden Jahre. Die Metallizitätsverteilung ist nicht axisymmetrisch, sondern entlang einer Richtung langgestreckt, was wieder auf den Balken hinweist. Die Gradienten der Metallizität entlang der großen und kleinen Halbachse des vermuteten Balkens sind ähnlich zu denen in anderen Balkengalaxien. Die  $\alpha$ /Fe-Überhäufigkeit ist homogen über den gesamten Bulgebereich, mit leicht höheren Werten als für die Sonne.

Wir untersuchen, ob ein einfaches Galaxienmodell aus einem Bulge und einer Scheibe die Morphologie der stellaren Populationen erklären kann, vor allem das homogene Alter. Um dieses Modell zu erzeugen, führen wir eine kinematische Dekomposition an der gemessenen stellaren Kinematik durch. Dabei fitten wir die Geschwindigkeitsverteilung entlang der Sichtlinie mit zwei Gausskurven, jeweils eine für den "Bulge" und die "Scheibe". Die kinematische Dekomposition resultiert in zwei entarteten Lösungen, von denen eine der Kombination eines langsam rotierenden Bulges mit einer schnell rotierenden Scheibe gleicht. Wir konvolvieren mit dieser Lösung ein Modellspektrum für den Bulge und eines für die Scheibe und addieren die beiden entsprechend dem Bulge-zu-Scheibenverhältnis an der jeweiligen Position in der Galaxie. Auf diese Weise erzeugen wir einen Modell-Datenkubus, an dem die Lick-Indizes und die stellaren Populationen auf die gleiche Art gemessen werden wie für unsere beobachteten Daten. In den resultierenden Karten erkennt man einen klaren Gradienten im Alter, der viel stärker ist als der, den wir für die Beobachtungen erhalten. Die Metallizität ist homogen, aber runder als in den beobachteten Karten. Diese Übung macht deutlich, dass die stellaren Populationen in M31 nicht durch eine einfache Überlagerung der Populationen eines Bulges und einer Scheibe erklärt werden können, ohne dass ein Balken vorhanden ist. Zusammenfassend lässt sich also sagen, dass sich die Kinematik der Sterne und die des Gases am besten mit der Anwesenheit eines Balkens erklären lässt. Die Morphologie des Gases weist auch darauf hin. Zusätzlich sind die Karten der Metallizität in der Richtung langgestreckt, wo man diesen Balken vermutet. Unsere Beobachtungen stützen also Modelle, in denen die Scheibe in den zentralen Bereichen der Galaxie einen Balken geformt hat, der dann auch zu einem kasten- bzw. erdnussförmigen Bulge geworden ist.

# Abstract

The Andromeda galaxy M31 is the nearest large spiral galaxy to our own Milky Way and therefore gives us the unique opportunity to study this galaxy type in great detail.

A longstanding question regarding M31 has been if it harbors a bar. The orientation of the galaxy is too far from face-on to clearly recognize the bar in photometry, but also not sufficiently edge-on to see the boxy/peanut-shape clearly above and below the disk plane.

In this thesis, we present results from an observation campaign of the central region of M31 with the Integral Field Unit Spectrograph VIRUS-W. In VIRUS-W, 267 fibers are arranged in a rectangular pattern, each pointing has a field-of-view of  $150'' \times 55''$ , which, assuming a distance to M31 of  $D = 780$  kpc, corresponds to  $397$  pc  $\times$   $208$  pc. We observed 198 pointings in total, completely covering the bulge and sampling the disk along six different directions, reaching approximately one disk scalelength along the major axis. The resulting 50,000 spectra are rebinned to 7563 bins in order to increase the signal-to-noise sufficiently to derive stellar line-of-sight velocity distributions and measure absorption line strengths, as well as emission line fluxes and kinematics. The wavelength range of the spectra is  $4802 \text{ \AA} - 5500 \text{ \AA}$ , stellar absorption lines covered are the  $H\beta$  line at  $4861 \text{ \AA}$ , the Mg b triplet at  $5167 \text{ \AA}$ ,  $5173 \text{ \AA}$  and  $5187 \text{ \AA}$ , as well as several Fe absorption features at  $5015 \text{ \AA}$ ,  $5270 \text{ \AA}$ ,  $5335 \text{ \AA}$  and  $5406 \text{ \AA}$ .  $H\beta$  is also seen in an emission line of ionized gas, other gas lines are the doublets at  $[\text{OIII}]\lambda\lambda 4959, 5007$  and  $[\text{NI}]\lambda\lambda 5198, 5200$ . The stellar and gas kinematics are fitted simultaneously, the stellar kinematics using the absorption lines and the gas kinematics using the emission lines.

The line-of-sight velocity distribution of the stellar kinematics is approximated as a Gauss-Hermite series with the moments  $v$ ,  $\sigma$ ,  $h3$  and  $h4$ . The stellar kinematics exhibit several features that are regularly seen in bars, like a “double-hump” in the velocity profile and plateaus of the velocity dispersion at the same positions as the “humps”. The Gauss-Hermite moment  $h3$  is correlated with the velocity over much of the bulge region, which can again be explained by the presence of a bar. We compare our measurements to results from a barred N-body model of M31 and find good agreement.

The gas kinematics, measured on the  $[\text{OIII}]\lambda 5007$  line, is more complicated. For about half the binned spectra, the line has two peaks separated in velocity, pointing to two distinct components. The components corresponding to these peaks show an S-shape in the velocity maps, which has also been found in other barred

galaxies, additionally, the position-velocity diagrams are similar to what is expected from simulations of gas in barred galaxies. The morphology of the gas exhibits a spiral pattern, which also shows similarities to gas morphology in a barred potential.

Furthermore, we investigate the stellar population properties by measuring absorption line strengths and comparing them to simple stellar population models. The stars are predominantly old (11 Gyr) over much of the bulge, with a drop in the outermost disk pointings, where the values go down to a few Gyr. The distribution of the metallicity is not axisymmetric, but rather elongated along the direction where the bar is expected. The gradients of the metallicity along the estimated bar major and minor axes are similar to what is found in other barred galaxies. The  $\alpha/Fe$ -overabundance is homogeneous over the whole bulge region, having slightly supersolar values.

We investigate if a simple galaxy model consisting of a bulge and a disk can reproduce the morphology of the stellar populations, especially the homogeneous age distribution. In order to construct this model, we perform a kinematic decomposition on our measured stellar kinematics, fitting the line-of-sight velocity distributions with two Gaussians, one each for “bulge” and “disk”. The kinematic decomposition results in two degenerate solutions, one of which resembles the combination of a slowly rotating bulge and a fast rotating disk. This solution is used to convolve a model bulge spectrum and a model disk spectrum and to combine them according to the bulge-to-disk ratio at the corresponding position in the galaxy. This results in a model galaxy datacube, on which the Lick indices and the stellar populations are measured in the same way as for our observed data. In the resulting maps we see a clear gradient in age, which is much stronger than the one we see in the measured data. The metallicity is homogeneous, but rounder than in the measured maps. This exercise makes it clear that the stellar populations cannot be explained by a simple superposition of bulge and disk populations without the presence of a bar.

We conclude that the stellar and gaseous kinematics of M31 are best explained by the presence of a bar. The gas morphology also points in that direction. Further, the metallicity maps show an elongation along the axis where this bar is expected. Our observations thus strengthen models which claim that the disk in the central regions has formed a bar, which has then buckled into a boxy/peanut-shaped bulge.

# Contents

<b>Zusammenfassung</b>	<b>v</b>
<b>Abstract</b>	<b>vii</b>
<b>1 The Andromeda galaxy M31</b>	<b>1</b>
1.1 Historical observations . . . . .	1
1.2 Spectroscopy of M31 . . . . .	3
1.3 General properties of M31 . . . . .	5
1.4 The bar in M31 . . . . .	6
1.5 Outline of the thesis . . . . .	9
<b>2 Observations and data reduction</b>	<b>11</b>
2.1 Observations . . . . .	11
2.1.1 The IFU spectrograph VIRUS-W . . . . .	11
2.1.2 Description of the observations . . . . .	13
2.1.3 Data reduction . . . . .	14
2.2 Obtaining the kinematics . . . . .	21
2.2.1 Fitting the stellar kinematics with pPXF . . . . .	21
2.2.2 Fitting the emission lines with GANDALF . . . . .	22
2.2.3 Fitting double lines with GANDALF . . . . .	24
2.2.4 Error calculation . . . . .	25
2.3 Photometric model image . . . . .	33
2.4 Flux calibration . . . . .	36
<b>3 Bar signatures in the stellar kinematics</b>	<b>45</b>
3.1 Description of the measured stellar kinematics . . . . .	45
3.2 Bar signatures in the kinematics . . . . .	56
<b>4 Bar signatures in the kinematics and morphology of the gas</b>	<b>63</b>
4.1 Gas velocities . . . . .	63
4.1.1 Description . . . . .	63
4.1.2 Discussion . . . . .	65
4.2 Velocity dispersion . . . . .	77
4.3 Gas fluxes . . . . .	77
4.4 Ionization mechanisms of the gas . . . . .	84

4.5	Conclusion . . . . .	86
<b>5</b>	<b>Stellar populations</b>	<b>87</b>
5.1	Lick indices . . . . .	87
5.2	Stellar population analysis . . . . .	98
5.2.1	Measurements . . . . .	98
5.2.2	Discussion . . . . .	100
<b>6</b>	<b>Kinematic Decomposition</b>	<b>111</b>
6.1	Fit of the LOSVD with two Gaussians . . . . .	111
6.2	Test on N-body model . . . . .	121
6.3	Simple bulge and disk model . . . . .	125
6.3.1	Lick indices . . . . .	125
6.3.2	Population properties . . . . .	127
<b>7</b>	<b>Summary and Outlook</b>	<b>133</b>
7.1	Summary . . . . .	133
7.2	Outlook . . . . .	136
	<b>Appendices</b>	<b>137</b>
<b>A</b>	<b>Observed objects and lines for wavelength calibration</b>	<b>139</b>
	<b>Acknowledgements</b>	<b>157</b>

# List of Figures

1.1	Optical image of M31 . . . . .	5
1.2	Bar model by <a href="#">B16</a> . . . . .	9
2.1	VIRUS-W IFU spectrograph . . . . .	12
2.2	Observed pointings . . . . .	13
2.3	Flatfielding . . . . .	16
2.4	Image after data reduction . . . . .	17
2.5	Relative position of guider camera field-of-view and spectrograph field-of-view for M37 . . . . .	18
2.6	Collapsed data cube for M37 . . . . .	18
2.7	Finder chart for the guider camera for M37 . . . . .	19
2.8	Signal map . . . . .	20
2.9	Map of the bins . . . . .	20
2.10	Map of number of fibers per bin . . . . .	20
2.11	Map of binned signal-to-noise ratio . . . . .	20
2.12	Different Gauss-Hermite functions . . . . .	22
2.13	Example spectrum with GANDALF bestfit . . . . .	26
2.14	Example spectrum with GANDALF bestfit with two lines . . . . .	27
2.15	Example spectrum with GANDALF bestfit with two lines, one higher than the other . . . . .	28
2.16	Example spectrum with GANDALF bestfit with two lines that are almost blended . . . . .	29
2.17	Example spectrum with GANDALF bestfit with skewed emission line that can be fitted with two Gaussians . . . . .	30
2.18	Schematic view of the cross correlation . . . . .	31
2.19	Fit to cross correlation with one and two Gaussians . . . . .	31
2.20	Spectra with random noise for bin 7232 . . . . .	32
2.21	Decomposition by <a href="#">Kormendy &amp; Bender (1999)</a> . . . . .	34
2.22	PA and $\epsilon$ profiles of ellipse fit to K-band image . . . . .	34
2.23	Model image . . . . .	35
2.24	Bulge-to-total ratio . . . . .	35
2.25	V - $3.6\mu\text{m}$ color image . . . . .	35
2.26	Calculation of the throughput for the photometric standard star Feige 110 . . . . .	39

2.27	Model image converted to flux. . . . .	42
2.28	Integrated flux map . . . . .	42
2.29	Map of the correction factors . . . . .	42
2.30	Map of the integrated corrected fluxes . . . . .	42
2.31	Model image fluxes divided by integrated corrected fluxes . . . . .	42
2.32	Position of the PMAS pointing . . . . .	43
2.33	Comparison of PMAS spectrum to VIRUS-W spectrum . . . . .	43
3.1	Stellar velocity . . . . .	46
3.2	Schematic view of M31 . . . . .	47
3.3	Stellar velocity, plotted logarithmically . . . . .	48
3.4	Velocity map with slits from S10 . . . . .	48
3.5	Comparison of our velocities with the ones from S10 . . . . .	49
3.6	Stellar velocity dispersion . . . . .	50
3.7	Comparison of our velocity dispersions to the ones from S10 . . . . .	51
3.8	$h3$ moment . . . . .	52
3.9	Correlation between $v$ and $h3$ . . . . .	52
3.10	Comparison of our $h3$ measurements to the ones from S10 . . . . .	53
3.11	$h4$ moment . . . . .	54
3.12	Comparison of our $h4$ measurements to the ones from S10 . . . . .	55
3.13	Stellar kinematics of intermediate bar model by Bureau & Athanassoula (2005) . . . . .	56
3.14	Cuts along the disk major axis for the stellar velocity . . . . .	56
3.15	Cuts through velocity map along disk and bar major axis . . . . .	57
3.16	Comparison between photometric and kinematic position angle . . . . .	58
3.17	Kinematic misalignment of M31 compared to the CALIFA survey . . . . .	59
3.18	Cuts through velocity dispersion map along disk and bar major axis . . . . .	60
3.19	Cuts through $h3$ map along disk and bar major axis . . . . .	60
3.20	Cuts through $h4$ map along disk and bar major axis . . . . .	61
4.1	Velocity map of first gas component . . . . .	64
4.2	Velocity map of second gas component . . . . .	65
4.3	Comparison of cuts with data from Saglia et al., 2010 . . . . .	69
4.4	Velocity map of first gas component with contours from $250\mu m$ observations . . . . .	70
4.5	Comparison between photometric and kinematic position angle for the gas . . . . .	70
4.6	Kinematic misalignment of the M31 gas compared to the CALIFA survey . . . . .	71
4.7	First gas component with axes for the position-velocity diagram . . . . .	71
4.8	Position-velocity diagram of first and second component . . . . .	72
4.9	Position-velocity diagram of first component . . . . .	72
4.10	Position-velocity diagram of second component . . . . .	72
4.11	Comparison of full position-velocity diagram to position-velocity diagram by Athanassoula & Beaton (2006) . . . . .	73

4.12	Major axis cut through the velocity maps . . . . .	73
4.13	Position-velocity diagrams of HI and [OIII] . . . . .	74
4.14	NGC 2683 . . . . .	74
4.15	Comparison of velocity components with CO . . . . .	75
4.16	Ring model by Melchior & Combes (2011) . . . . .	75
4.17	Comparison of the velocities of the ring model with [OIII] velocities. . . . .	76
4.18	Comparison of the profiles of the ring model with [OIII] velocities. . . . .	76
4.19	Velocity dispersion of first gas component . . . . .	77
4.20	Velocity dispersion of second gas component . . . . .	77
4.21	Flux of first $H\beta$ component . . . . .	78
4.22	Flux of second $H\beta$ component . . . . .	78
4.23	Flux of both $H\beta$ components combined . . . . .	79
4.24	Flux of first [OIII] component . . . . .	80
4.25	Flux of the second [OIII] component . . . . .	80
4.26	Flux of both [OIII] components combined . . . . .	80
4.27	Flux of the first [NI] component . . . . .	81
4.28	Flux of the second [NI] component . . . . .	81
4.29	Flux of both [NI] components combined . . . . .	81
4.30	Comparison of combined [OIII] flux and $H\alpha$ +NII flux . . . . .	82
4.31	Comparison of combined [OIII] flux with predictions from bar model . . . . .	82
4.32	Comparison of combined [OIII] flux with predicted flux from collision of M31 with M32 . . . . .	83
4.33	[NI]/ $H\beta$ vs. [OIII]/ $H\beta$ diagnostic diagrams . . . . .	85
5.1	Lick Index Mg b . . . . .	88
5.2	Map of Lick index $H\beta$ . . . . .	91
5.3	Map of Lick index Mg b . . . . .	91
5.4	Map of Lick index Fe5015 . . . . .	91
5.5	Map of Lick index Fe5270 . . . . .	91
5.6	Map of Lick index Fe5335 . . . . .	91
5.7	Map of Lick index Fe5406 . . . . .	91
5.8	Comparison of $H\beta$ with S10 . . . . .	92
5.9	Comparison of Mg b with S10 . . . . .	93
5.10	Comparison of Fe5015 with S10 . . . . .	94
5.11	Comparison of Fe5270 with S10 . . . . .	95
5.12	Comparison of Fe5335 with S10 . . . . .	96
5.13	Comparison of Fe5406 with S10 . . . . .	97
5.14	Map of SSP Lick index $H\beta$ . . . . .	102
5.15	Map of SSP Lick index Mg b . . . . .	102
5.16	Map of SSP Lick index Fe5270 . . . . .	102
5.17	Map of SSP Lick index Fe5335 . . . . .	102
5.18	Map of SSP Lick index Fe5406 . . . . .	102
5.19	Age map . . . . .	103
5.20	Metallicity map . . . . .	103

5.21	$\alpha/Fe$ -overabundance map . . . . .	103
5.22	Comparison of age with S10 . . . . .	104
5.23	Comparison of metallicity with S10 . . . . .	105
5.24	Comparison of $\alpha/Fe$ with S10 . . . . .	106
5.25	Metallicity profile along major and minor axis of the bar . . . . .	107
5.26	Fitted gradients to bar major and minor axis profiles . . . . .	107
5.27	Comparison of the metallicity gradient with other galaxies . . . . .	108
5.28	Comparison of stellar population values with other galaxies . . . . .	109
6.1	Example LOSVD . . . . .	112
6.2	Sampled parameter space for one bin . . . . .	113
6.3	Number of solutions for the fitting routine . . . . .	113
6.4	Two symmetric solutions . . . . .	114
6.5	Two asymmetric solutions . . . . .	115
6.6	Velocity for the two solutions . . . . .	116
6.7	Velocity dispersion maps for the two solutions . . . . .	117
6.8	Cuts through the velocity maps of the different solutions . . . . .	117
6.9	Velocity maps for the two sorted solutions . . . . .	118
6.10	Velocity dispersion for the two sorted solutions . . . . .	119
6.11	Cuts through the velocity maps of the different sorted solutions . . . . .	119
6.12	Cuts through the velocity dispersion maps of the different sorted solutions . . . . .	120
6.13	Profiles of $v_{bulge}$ and $v_{disk}$ for sorted solution 1 and sorted solution 2 . . . . .	120
6.14	Profiles of $\sigma_{bulge}$ and $\sigma_{disk}$ for sorted solution 1 and sorted solution 2 . . . . .	120
6.15	Number of solutions for the N-body model . . . . .	121
6.16	Sorted velocity maps for the N-body model . . . . .	122
6.17	Sorted velocity dispersion maps for the N-body model . . . . .	123
6.18	Cuts through the velocity maps of the different solutions of the N-body model . . . . .	123
6.19	Cuts through the velocity dispersion maps of the different solutions of the N-body model . . . . .	124
6.20	Bulge and disk spectra . . . . .	126
6.21	Model bulge and disk spectra . . . . .	126
6.22	Model spectra for bin with $\frac{B}{T} = 0.45$ and $\frac{D}{T} = 0.55$ . . . . .	127
6.23	Lick index $H\beta$ for the bulge and disk model . . . . .	128
6.24	Lick index Mg b for the bulge and disk model . . . . .	128
6.25	Lick index Fe5015 for the bulge and disk model . . . . .	128
6.26	Lick index Fe5270 for the bulge and disk model . . . . .	128
6.27	Lick index Fe5335 for the bulge and disk model . . . . .	128
6.28	Lick index Fe5406 for the bulge and disk model . . . . .	128
6.29	Profiles of the Lick index $H\beta$ . . . . .	129
6.30	Profiles of the Lick index Mg b . . . . .	129
6.31	Profiles of the Lick index Fe5015 . . . . .	129
6.32	Profiles of the Lick index Fe5270 . . . . .	129

---

6.33	Profiles of the index Fe5335 . . . . .	129
6.34	Profiles of the index Fe5406 . . . . .	129
6.35	Age of the bulge and disk model . . . . .	130
6.36	Comparison of ages between the measurement and the model . . . .	131
6.37	Metallicity of the bulge and disk model . . . . .	131
6.38	Comparison of metallicities between the measurement and the model	132



# List of Tables

1.1	Properties of M31 . . . . .	6
2.1	VIRUS-W characteristics . . . . .	12
2.2	Quantities and errors measured with GANDALF and the Monte-Carlo simulation . . . . .	25
2.3	Parameters of the bulge-disk decomposition . . . . .	34
2.4	Constants used for the flux calibration . . . . .	36
5.1	Definition of Lick indices . . . . .	88
5.2	Major and minor axis gradients in metallicity . . . . .	100
A.1	Photometric standard stars . . . . .	139
A.2	Open clusters . . . . .	139
A.3	Kinematic standard stars . . . . .	140
A.4	M31 pointings . . . . .	141
A.5	Lines used for wavelength calibration . . . . .	144



# Chapter 1

## The Andromeda galaxy M31

### 1.1 Historical observations

Astronomy as the oldest natural science has a long history of watching the heavens. Studying an object as well known as the Andromeda galaxy therefore builds on a vast wealth of previous observations. M31 was mentioned for the first time by the Persian astronomer Abd al-Raman al-Sufi in his *Book of the fixed stars* (Abd al-Rahman al-Sufi, c. 964). He mentions it in passing as a “nebulous smear”, while describing the constellation of Andromeda<sup>1</sup>:

The Arabs mentioned two lines of stars surrounding an image resembling a large fish below the throat of the Camel. Some of these stars belong to this constellation (Andromeda) and others belong to the constellation Pisces which Ptolemy mentioned as the twelfth constellation of the Zodiac. These two lines of stars begin from the *al-Laṭkhā al-Saḥābiya* (nebulous smear) located close to the fourteenth star which is found at the right side of the three (stars) which are above the girdle.

It seems that the object was already well known (Hafez, 2010), therefore it is not described as anything special.

Several centuries later, the German astronomer Simon Marius was the first one to observe M31 with a telescope and he realized that it was a peculiar object. In his book *Mundus Iovialis* (Marius, 1614) about his observations of the four moons of Jupiter, he mentions it in a brief summary of several other observations he conducted with his telescope. He writes:<sup>2</sup>

**Inter illa primam est, quod mediante perspicillo à die 15. Decemb. Anni 1612. invenerim & viderim fixam vel stellam quandam admirandae figura, qualem in toto coelo deprehendere no possum.**

---

<sup>1</sup>This quote has been taken from the translation of Hafez (2010) with italics and explanations as found therein.

<sup>2</sup>Marius (1988) gives the original Latin text as well as a German translation. The English text was translated by the author of this thesis from the German text.

The first observation consists in discovering and observing with the help of the telescope since December 15th, 1612, a star or a fixed star of such a remarkable shape, which I cannot find anywhere else on the sky.

Hence, Marius was aware that this object was something different from any other he could observe. He then went on to describe in more detail what he saw:

**Absque instrumento cernitur ibidem quaedam quasi nubecula; at cum instrumento nulla videntur stellae distinctae, ut in nebula cancri & alijs stellis nebulosis, sed saltem radij albicantes, qui qui propiores sunt centro eò clariores evadunt, in centro est lumen obtusum & pallidum, in diametro quartam fere gradus partem occupat. Similis fere splendor apparet, si àtonginquo candela ardens per cornu pellucidum de nocte cernatur; non absilimis esse videtur Cometae illi, quem Tycho Brahe Anno 1586 observavit.**

Without instrument you see there something like a nebula; but with the telescope you do not see individual stars, like in the cloud in Cancer or other stellar clouds, but only shimmering rays that become brighter the closer they are to the center. In the center, there is a weak and faint brilliance with a diameter of about a quarter of a degree. A quite similar brilliance is seen when you observe a burning candle from a large distance through a simmering piece of horn. The nebula seems not dissimilar to the comet observed by Tycho Brahe in 1586.

Marius did not feel qualified enough to give an interpretation of what this peculiar object might be:

**An autem nova sit nec ne, certo affeverare nequeo, dispiciant & judicent id alij.**

If this star is a new one or not, I cannot state for sure; others may judge and determine this.

Another century later, Charles Messier included this object into his catalog of nebulae (Messier, 1781) as the 31st entry, hence the galaxy is referred to as Messier 31 or M31. It is possible that in the late 18th century William Herschel already made reference to the different stellar populations of the bulge and disk of the galaxy by noting the red color of the nucleus of M31 (Ferne, 1970). In 1847, G.P. Bond was the first one to see dark lanes in the northwestern part of the galaxy (Wilson, 1899), but the true spiral structure was not seen until Roberts (1888) took a long exposure photograph of M31. He thought that it was a solar system “condensing” from the nebular phase into the central star and the surrounding planets, with the neighboring dwarf galaxies M32 and NGC 205 already condensed planets. Huggins & Miller (1864) found that the spectrum was different from other nebulae and more similar to stellar spectra, which led Wilson (1899) to claim

that M31 was a “sidereal system” in formation, which in time would become something similar to our own Milky Way, with stars aligned along the spiral arms of the galaxy. In 1885, the so far only Supernova was observed in M31, SN1885A (Hartwig, 1885), which occurred in the bulge region and was later identified to be of type Ia (van den Bergh, 1994). Scheiner (1899) took a 7.5 hour exposure spectrum of M31 and noted that the spectrum was very similar to the spectrum of the sun, concluding that “the previous suspicion that the spiral nebulae are star clusters is now raised to a certainty.”

The first velocity measurement of M31 was obtained by Slipher (1914), measuring a mean velocity of  $v = -300 \text{ km s}^{-1}$ . This high approaching velocity puzzled Slipher and he speculated that the nebula might have encountered a dark “star” that might also have triggered the “peculiar nova” SN1885A. Pease (1918) produced the first rotation curve of M31 along the major and minor axis and measured the axis ratio  $q = 0.25$ , corresponding to an inclination of  $i = 76^\circ$ .

The long-standing issue of the real nature of the spiral nebulae, if they are just nebulae inside the Milky Way or galaxies in their own right, was settled by Hubble (1925) who discovered Cepheids in M31 and M33 and thus measured the distances to these two galaxies, thereby proving that these two spiral nebulae are indeed distant galaxies.

Baade (1944) resolved individual stars in the central region of M31, proving that it is made out of stars right to the very center. The rotation curve of M31 was further refined by Mayall (1951) and Rubin & Ford (1970). Argyle (1965) produced the first two-dimensional velocity map from HI data.

## 1.2 Spectroscopy of M31

After the groundbreaking scientific work mentioned above, a huge number of spectroscopic observations have been performed on M31, of which I will list a few selected highlights.

Stellar kinematics of the bulge were obtained by McElroy (1983), but Saglia et al. (2010, hereafter S10) showed that his stellar velocity dispersions were severely underestimated.

Bender et al. (2005) focused on the very central regions of M31 in order to investigate the black hole dynamics, they found that M31 hosts a triple nucleus.

For the ionized gas. Rubin & Ford (1971) found that  $\text{H}\alpha$ , while concentrated in a thin rotating disk, shows deviations from axisymmetry. Similarly, Pellet (1976) observed  $\text{H}\alpha$  and  $[\text{NII}]\lambda\lambda 6548, 6583$  and found that the gas is asymmetric along the major axis. Jacoby et al. (1985) produced flux maps in a broad  $\text{H}\alpha + [\text{NII}]$  filter and in  $[\text{OIII}]\lambda 5007$ , seeing a spiral structure in the central region, which was more face-on than the overall disk of M31. Boulesteix et al. (1987) in  $[\text{NII}]$  and Ciardullo et al. (1988) in  $\text{H}\alpha + [\text{NII}]$  basically observed the same. S10 also measured ionized gas, observing that the rotation of  $[\text{OIII}]\lambda 5007$  on large scales is fairly regular, while in the inner bulge, the situation becomes more complicated,

even showing gas counter-rotation near the minor axis, possibly coming from a minor merger.

By far the most observations have been done in the neutral gas with the HI 21cm line. Kent (1989) found that the kinematics of ionized gas and the neutral gas largely agree along the major axis. Brinks (1983) didn't find neutral gas in the inner 500 pc and claimed this is because gas so close to the central region in the galaxy is mostly ionized. Roberts & Whitehurst (1975) were the first to observe that the disk plane of M31 is warped, which was later confirmed by Brinks & Burton (1984). They claimed that the warp is symmetric and therefore cannot be the result of a possible interaction with the companion galaxy M32. Braun (1991) made a more detailed investigation of the HI morphology and kinematics, using data from Brinks & Shane (1984) for the inner galaxy and the wide-field coverage by Emerson (1974) for the outer parts. They found that the inner 2 kpc disk is tilted by  $15^\circ$  with respect to the outer disk, while a trailing two-arm spiral explains the gas morphology well. However, in the inner 5 kpc the spiral is distorted elliptically with apparently the same orientation as the possible triaxiality of the bulge. Braun (1991) thought that the main driver of the spiral was M32. A full map in HI was created by Chemin et al. (2009). The gas is axisymmetric except for the innermost regions, which are less inclined than the average disk, whereas the outermost regions appear more inclined, pointing to a strong warp in the HI disk. Multiple gas components are found, sometimes up to five kinematically distinct ones, with the main one corresponding to a rotating gas disk and the others being due to warps, which project low velocities from outer regions into the center. Braun et al. (2009) also produced an HI map, finding that unlike other galaxies, in which the gas mass is dominated by molecular gas at small radii, the gas in M31 is dominated by atomic gas at all radii. Working with the images of Braun et al. (2009), Corbelli et al. (2010) tested cosmological models of structure formation with M31's rotation curve. They fitted a tilted ring model to the HI data from 8 to 37 kpc and proved the existence of a dark halo.

M31 has also been observed in molecular gas. A comprehensive survey of the whole galaxy has been done by Nieten et al. (2006). The molecular gas is concentrated in filamentary arms coinciding with dust lanes in optical images. Melchior et al. (2000) reported a first discovery of CO in the bulge of M31, subsequently, Melchior & Combes (2011), Melchior & Combes (2013) and Melchior & Combes (2016) investigated the center in more detail. Melchior & Combes (2011) found that for a few pointings, the molecular lines showed two separate peaks, split by up to  $260 \text{ km s}^{-1}$ , and an outflow of ionized gas in the circumnuclear 75 pc. These velocities do not match the velocities of the ionized gas or the HI.

With the development of spectrographs with integral field units (IFUs), it has become possible to obtain optical spectra not only along one slit direction, but over a two-dimensional area. The availability of the IFU spectrograph VIRUS-W

(Fabricius et al., 2012a) has led us to observe the Andromeda galaxy M31, building on the observations by S10. A major motivation for us was to investigate if M31 harbors a bar, which will be further discussed below.

### 1.3 General properties of M31

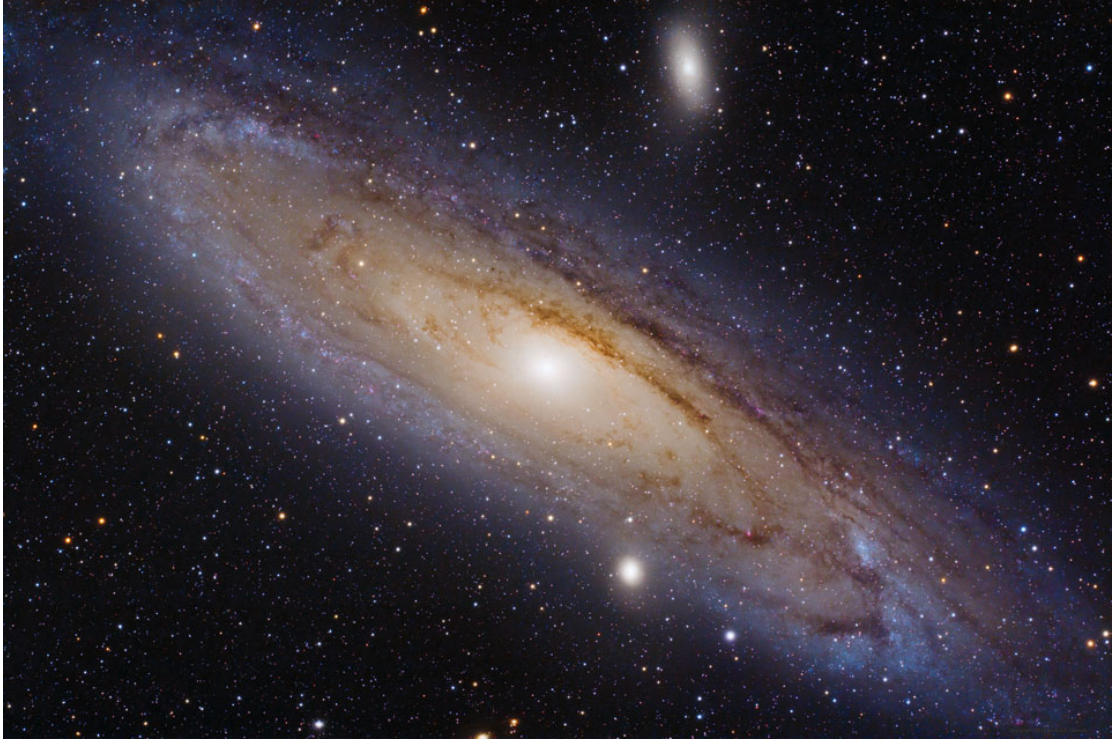


**Figure 1.1:** Optical image of M31, taken from the website Astronomy Picture of the Day<sup>3</sup>. North is up and east is to the left.

The Andromeda galaxy, an optical image is shown in figure 1.1, is the nearest large galaxy to our own Milky Way, at a distance of  $D = 780 \pm 40$  kpc (de Grijs & Bono, 2014). It is one of the few galaxies that are blueshifted instead of redshifted, with the heliocentric velocity  $v_{helio} = -300 \pm 4$  km s<sup>-1</sup> relative to the solar system and the galactocentric velocity of  $v_{gal} = -122 \pm 8$  km s<sup>-1</sup> with respect to the Milky Way as a whole (de Vaucouleurs et al., 1991). It is a spiral galaxy, classified as an unbarred SA(s)b galaxy by de Vaucouleurs et al. (1991). However, in this thesis, we will present evidence that M31 is indeed a barred galaxy. The position angle of the disk is  $PA_{disk} = 38^\circ$  (de Vaucouleurs, 1958), the PA of the bulge is slightly offset at  $PA_{bulge} = 48^\circ$  (S10). The inclination of the galaxy is  $i = 77^\circ$  (Corbelli et al., 2010), with the western side of the galaxy being the near side (Henderson, 1979). The bulge has a Sérsic index of  $n = 2.2 \pm 0.3$  (Courteau et al., 2011), therefore just falling in the range for classical bulges with  $n > 2$  (Fisher & Drory,

<sup>3</sup><http://apod.nasa.gov/apod/ap130626.html>

2008). From its morphology, the bulge is seen as a classical bulge (Kormendy & Kennicutt, 2004). Beaton et al. (2007) see that the bulge is actually boxy in the outer part, therefore it has been termed a “classical bulge with pseudobulge trimmings” (Mould, 2013). M31 is about as massive as the Milky Way, the mass inside 300 kpc is  $M_{300} = 1.4 \pm 0.4 \times 10^{12} M_{\odot}$  (Watkins et al., 2010). Davidge et al. (2012) give a nice review over the star formation history of M31, listing star formation rates of  $0.3 M_{\odot} yr^{-1}$  (Tabatabaei & Berkhuijsen, 2010),  $0.4 M_{\odot} yr^{-1}$  (Barnby et al., 2006) and  $0.6 M_{\odot} yr^{-1}$  (Kang et al., 2009). These values are only about a third of the star formation rate in the Milky Way, which is estimated to be 0.68 - 1.45  $M_{\odot} yr^{-1}$  (Robitaille & Whitney, 2010) or 1.9  $M_{\odot} yr^{-1}$  (Boissier & Prantzos, 1999). The specific star formation rate in M31 is similar to that in nearby red disk galaxies, like the lenticular galaxy NGC 5102 (Davidge et al., 2012). The disk of the Andromeda galaxy is about 2.4 times larger and twice as massive as that of the Milky Way, however, its gas fraction is only half of the one in the Milky Way disk (Yin et al., 2009). M31 hosts a supermassive black hole of  $M_{BH} = 1.4_{-0.3}^{+0.9} \cdot 10^8 M_{\odot}$  (Bender et al., 2005), which has ultra-weak nuclear activity (del Burgo et al., 2000). M31 appears to be similar to other local spiral galaxies, considering its rotation velocity and brightness, as well as the angular momentum of the disk and the metallicity in the galaxy outskirts. It seems to be a much more typical spiral galaxy than the Milky Way, probably owing to its more turbulent past with several mergers (Hammer et al., 2007). Table 1.1 gives an overview over M31’s properties.

**Table 1.1:** Properties of M31

Position of the center <sup>a</sup> (J2000.0)	RA: 00h 42min 44.3503s DEC: +41° 16' 08.634"
Classification <sup>b</sup>	SA(s)b
Inclination <sup>c</sup>	77°
Disk Position angle <sup>d</sup>	38°
Bulge Position angle <sup>e</sup>	48°
Distance <sup>f</sup>	$0.78 \pm 0.04$ Mpc
Heliocentric radial velocity <sup>b</sup>	$-300 \pm 4$ km s <sup>-1</sup>
Galactocentric radial velocity <sup>b</sup>	$-122 \pm 8$ km s <sup>-1</sup>

<sup>a</sup> Evans et al. (2010)

<sup>b</sup> de Vaucouleurs et al. (1991)

<sup>c</sup> Corbelli et al. (2010)

<sup>d</sup> de Vaucouleurs (1958)

<sup>e</sup> S10

<sup>f</sup> de Grijs & Bono (2014)

## 1.4 The bar in M31

A large fraction of disk galaxies in the local universe is barred, ranging from about 50% in the optical (Barazza et al., 2008) to about 60% to 70% in the infrared (Eskridge et al., 2000; Menéndez-Delmestre et al., 2007). It is now thought that global instabilities in the disk lead to the formation of bars, forming the bar

quickly (Sellwood & Wilkinson, 1993; Sellwood, 2013). The modes for the bar are like standing waves in a cavity, with the reflections happening at the center and at the corotation radius (Toomre, 1981). An alternative scenario is that in the inner parts of galaxies, eccentric orbits have the tendency to align themselves, which builds the bar slowly by orbit trapping (Lynden-Bell, 1979). Bars are a disk phenomenon, they are not related to ellipticals, despite a somewhat similar appearance (Kormendy & Kennicutt, 2004). While the Milky Way was originally thought of as unbarred, it is now widely accepted that it contains a bar (Dehnen, 2002). Recently, signs for a bar have also been detected in the innermost parts of the third large spiral galaxy in the Local Group, M33 (Hernández-López et al., 2009).

A bar is not easily detected in M31 because of its high inclination of  $77^\circ$ . This is too high to see a bar directly in the image, but too low to recognize its shape above and below the stellar disk, as is possible in an edge-on view (Athanasoula & Beaton, 2006). It is still possible, however, to detect a bar in a galaxy with such an inclination, Kuzio de Naray et al. (2009) investigated the galaxy NGC 2683, which has a similar inclination to M31 ( $i \approx 78^\circ$ ), by looking at ionized gas velocities and the overall morphology of the galaxy.

According to Stark & Binney (1994), there are three strong arguments for a bar in M31.

1. There is a twist in the inner isophotes in the bulge with respect to the outer disk, first seen by Lindblad (1956). He was subsequently the first one to claim that M31 has a bar. These twists cannot be reproduced by a rotationally symmetric distribution of stars (Stark, 1977).
2. The velocities of the HI gas are not symmetric about the minor axis (Rubin & Ford, 1971).
3. The ionized gas has the appearance of a spiral pattern, which is rounder than the appearance of the disk, as seen by Jacoby et al. (1985), Boulesteix et al. (1987) and Ciardullo et al. (1988).

Stark (1977) showed that the features measured by Lindblad (1956) can be explained by a family of bar models. Stark & Binney (1994) narrowed down these models by simulating the velocities of the gas in this potential.

Berman (2001) simulated the gas velocities in a barred potential that was derived using the method of Stark (1977) and they are in agreement with the non-circular gas velocities in the inner disk. According to Gordon et al. (2006), this model explains the morphology of dust in M31, with spiral arms emerging from the bar. However, the fact that the two prominent dust rings do not share the same center, which also does not coincide with the optical center of M31, led Block et al. (2006) to propose a different scenario, where these rings were not created by a bar, but instead are shock waves due to the collision of M32 with M31.

Athanasoula & Beaton (2006) tested four different bar models and qualitatively compared the velocities to HI kinematics from Rubin & Ford (1970), Brinks

& Shane (1984) and Brinks & Burton (1984), and the overall morphology to observations in the near infrared by Beaton et al. (2007). They found that in order to explain the boxy appearance of the isophotes in Beaton et al. (2007), a classical bulge needs to be present.

A boxy/peanut-shaped (B/P) bulge is thought to evolve naturally after a bar has formed in a galaxy. Over time, part of the bar goes through a buckling phase, which is a short, but violent vertical instability not long after bar formation (Combes & Sanders, 1981; Combes et al., 1990; Raha et al., 1991; Merritt & Sellwood, 1994). The instability bends out of the plane of the disk, then settles back to the plane, but the energy is distributed to smaller spatial scales and to higher stellar velocity dispersion, thereby thickening the bar (Raha et al., 1991). The buckled part of the bar is the B/P bulge, the part that has not buckled is the thin or flat bar. While this buckling phase is frequently seen in simulations, it has only recently been detected in observations by Erwin & Debattista (2016) for two local spiral galaxies.

The fact that the boxy isophotes in Beaton et al. (2007) do not coincide with the disk argues for a misalignment of the bar and disk major axis, with the bar position angle at about  $45^\circ$  (Athanasoula & Beaton, 2006). According to this model, there are four separate components in M31, from the innermost to the outermost:

1. A classical spherical bulge in the center,
2. a B/P bulge, which is the inner thicker part of the bar,
3. a thin bar, this is the outer part of the bar, and
4. a disk.

The bar, or triaxial bulge, as it is often called in these papers, seen by Lindblad (1956), Stark (1977) and Stark & Binney (1994), is the B/P bulge from Athanasoula & Beaton (2006). While the arguments for a bar in Athanasoula & Beaton (2006) are mostly qualitative, Blaña et al. (submitted, hereafter B16) did a more quantitative comparison, testing 84 different models and comparing them to IRAC  $3.6\mu\text{m}$  photometry from Barmby et al. (2006), HI kinematics from Chemin et al. (2009) and Corbelli et al. (2010), as well as stellar kinematics from S10 and data from this thesis. Again, they rule out solutions which do not have a classical bulge. In the best model for M31 by B16, plotted in figure 1.2, the B/P bulge contains 2/3 of the bulge mass, while the classical bulge contains 1/3. The position angle of the bar is  $PA_{bar} = 55.7^\circ$ , which is  $17.7^\circ$  more than the disk position angle of  $PA=38^\circ$ . The length of the bar is  $1000''$  intrinsically, projected onto the sky with M31's orientation and inclination, it becomes  $600''$ .

Matias Blaña is currently using the made-to-measure code NMAGIC (de Lorenzi et al., 2007) to fit the stellar kinematics presented in this thesis to build a better bar model.

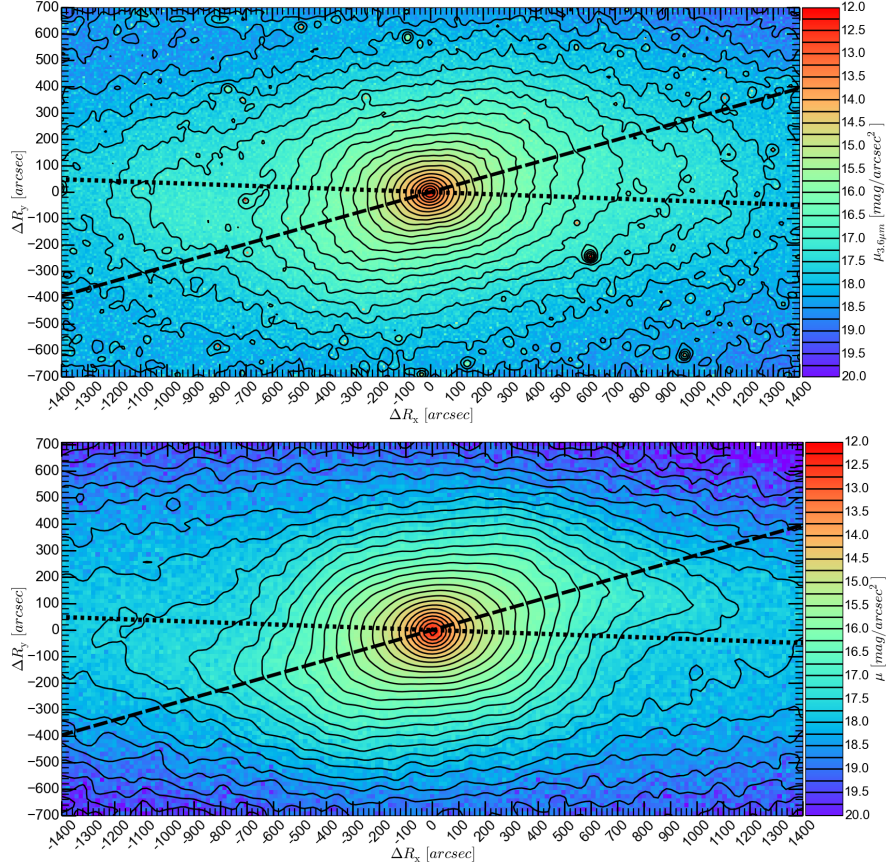


**Figure 1.2:** The bar model by B16. In the upper panel, the photometry of an IRAC  $3.6\mu\text{m}$  image observed by Barmby et al. (2006) is plotted. B16 constructed an N-body model with a bulge, a bar and a disk. The isophotes of the model are plotted in the lower panel. The lines with the short dashes is the disk major axis, the line with the long dashes is the orientation of the bar.

## 1.5 Outline of the thesis

This thesis is structured as follows: In chapter 2, our observations of M31 are described, as well as the data reduction and the methods used to fit the kinematics. Chapter 3 then presents the results for the stellar kinematics and chapter 4 the ones for the gas kinematics and morphology. Subsequently, the fitting of absorption line indices is illustrated in chapter 5, as well as the comparison to simple stellar population models. In chapter 6, the stellar kinematics are decomposed into a bulge and a disk component. From the decomposition, a galaxy model consisting of a bulge and a disk is constructed. The stellar populations measured on this model are then compared to the ones measured on the actual data. We conclude in chapter 7 and give an outlook on future projects with the obtained dataset.



# Chapter 2

## Observations and data reduction

### 2.1 Observations

#### 2.1.1 The IFU spectrograph VIRUS-W

The research presented in this thesis was carried out with the IFU spectrograph VIRUS-W (Fabricius et al., 2012a; Fabricius, 2012) mounted on the 2.7m telescope at the McDonald observatory. It is a fiber-based IFU spectrograph, a picture of the optical components can be seen in the left panel of figure 2.1. The integral-field unit consists of 267 fibers which are arranged in a rectangular hexagonal dense-pack scheme (Barden et al., 1998) with a filling factor of 1/3, shown in the lower panel of figure 2.1. The field-of-view of the instrument is  $105'' \times 55''$  at the 2.7m telescope, with the long edge of the fiberhead aligned along the east-west axis. Each fiber covers a circle with diameter  $3.2''$  on sky. The actual spectrograph has two different resolution modes, each realized with a Volume Phase Holographic grating. We use the high-resolution mode, where the grating has a line frequency of 3300 lines per millimeter and a resolution of  $R \approx 9000$ , which corresponds to an instrumental dispersion of  $\sigma_{inst} = 15 \text{ km s}^{-1}$ . By changing the grating angle, the blaze function can be adjusted so that the throughput for a specific wavelength range is optimized. For our observations, we adjusted the grating angle to  $35.3^\circ$  after some testing to get moderately high throughput at the wavelength of  $H\beta$  at  $4861 \text{ \AA}$ , with the maximum of the throughput being between  $4900 \text{ \AA}$  and  $5100 \text{ \AA}$ . The complete wavelength range is  $4802 \text{ \AA}$  to  $5470 \text{ \AA}$ . The properties of VIRUS-W are summarized in table 2.1, which also gives the emission and absorption lines in this range, the names of the absorption features are taken from Trager et al. (1998).

**Table 2.1:** VIRUS-W characteristics

Field of view	105'' x 55''
Fiber diameter on sky	3.6''
Filling factor	1/3
Instrumental dispersion	15 km s <sup>-1</sup>
Spectral range	[4802 - 5470] Å
Spectral features in this range	H $\beta$ ; [OIII] $\lambda\lambda$ 4959, 5007; Fe5015; Mgb; [NI] $\lambda\lambda$ 5198, 5200; Fe5270; Fe5335; Fe5406

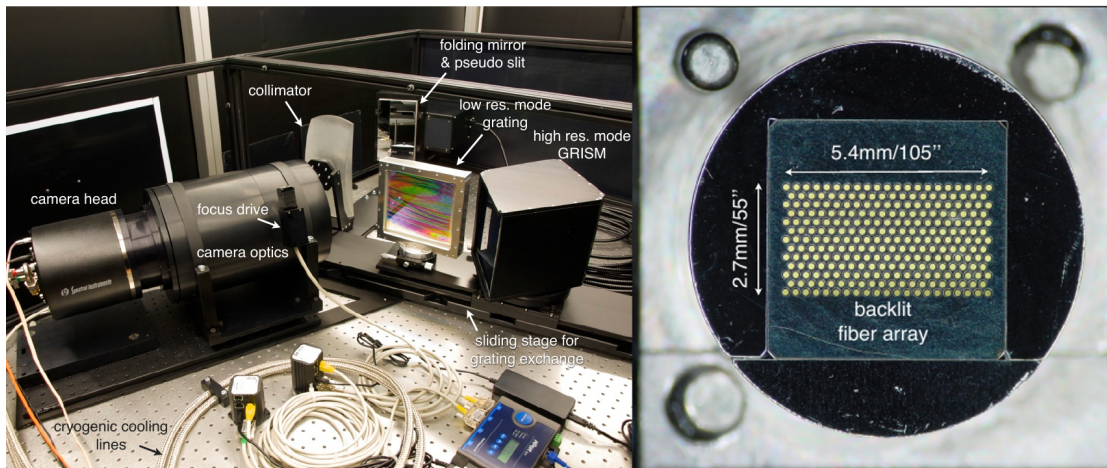


**Figure 2.1:** The VIRUS-W IFU spectrograph. *Left panel:* Inside view of the VIRUS-W spectrograph. *Right panel:* View of the fiberhead. The images are taken from Fabricius et al. (2012a).

### 2.1.2 Description of the observations

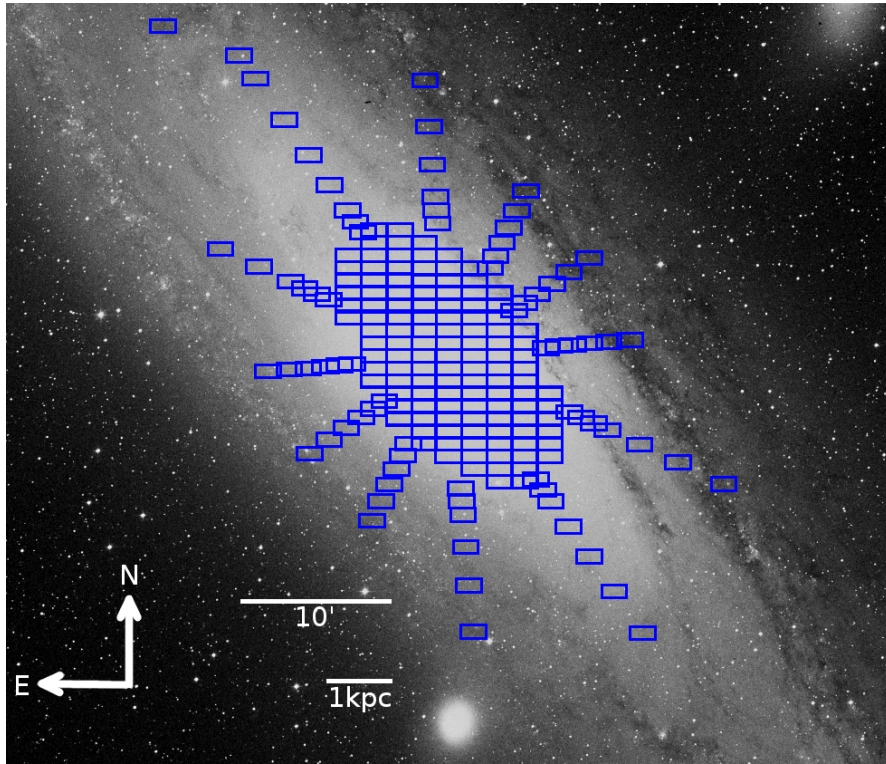


**Figure 2.2:** Observed pointings of M31 overlaid on a Digitized Sky Survey<sup>1</sup> V-band image.

We observed 198 pointings in four separate observing runs, in October 2011, October 2012, February 2013 and August 2013. The positions of all observed pointings are shown in figure 2.2, their central coordinates are listed in table A.4. This dataset is the most detailed spectroscopic survey of the center of M31 yet.

The observations consist of a completely covered area and six arms extending further out. The angles of these arms are  $35^\circ$  (approximately the disk major axis),  $65^\circ$ ,  $95^\circ$ ,  $125^\circ$  (approximately the disk minor axis),  $155^\circ$  and  $185^\circ$ . The completely covered region corresponds to the area where the bulge dominates the overall light emission (Kormendy & Bender, 1999). Therefore, all pointings in the completely covered area will be called “bulge pointings” and the ones in the arms “disk pointings”. Along the major axis, we reach approximately one disk scalelength of  $r_h = 24' = 5.3$  kpc (Courteau et al., 2011). We do not dither our observations, because we want to cover a large area of M31 with as few pointings as

<sup>1</sup>The image has been taken from [http://archive.stsci.edu/cgi-bin/dss\\_form](http://archive.stsci.edu/cgi-bin/dss_form). The Digitized Sky Surveys were produced at the Space Telescope Science Institute under U.S. Government grant NAG W-2166. The images of these surveys are based on photographic data obtained using the Oschin Schmidt Telescope on Palomar Mountain and the UK Schmidt Telescope. The plates were processed into the present compressed digital form with the permission of these institutions. ©1995 by the Association of Universities for Research in Astronomy, Inc.

possible. We observed each galaxy pointing with an exposure time of 10 minutes, except for M31\_107, which is only observed for 5 minutes, because it covers the bright nucleus of M31, where sufficient signal-to-noise values are already reached with this shorter exposure time. Before and after each galaxy pointing, we nodded the telescope away from the galaxy to a sky position, which was exposed for 5 minutes. The seeing varied between 1.3'' and 3.0'' during the observations.

In addition to these pointings of M31, we also observed one photometric standard star each night, these stars are listed in table A.1. These were observed for one or two minutes, depending on the observing conditions and their apparent brightness. Once per observation run we also targeted an open cluster for astrometric purposes, these clusters are listed in table A.2, they were observed with 6 sub-dithered observations, with each sub-dither being exposed for 3 minutes.

In the evening and morning of each observation night, calibration frames were taken.

To estimate the intrinsic noise of the detector, we obtained 11 bias frames with zero exposure time. Then, in order to trace the fiber positions on the detector and to compensate for fiber-to-fiber variation of the throughput, we took flatfields with the inner side of the telescope dome. Every observation night, we took 11 flats in the morning and the same number in the evening, the exposure time was estimated automatically by the observation software. For the wavelength calibration, a Hg and a Ne spectral lamp are were up to lighten the inside of the dome, which was then observed with the telescope. We took 5 of these arc frames every morning and evening.

### 2.1.3 Data reduction

The data reduction follows the standard procedure for VIRUS-W as described in Fabricius et al. (2014). It uses the `fitstools` package (Gössl & Riffeser, 2002) and the `Cure` pipeline developed for HETDEX (Hill et al., 2004).

First, master biases, flats and arcs are created by taking the mean of the individual images for each morning and evening. The master bias frames are subtracted from all other frames.

`Cure` traces the fiber positions on the master flat frames and then extracts the positions of the spectral line peaks along these traces in the master arc frames. To model the distortion and the spectral dispersion, a two-dimensional seventh degree Chebyshev polynomial is used. The resulting model transforms between pixel positions on the detector and fiber-wavelength pairs and vice-versa.

For the wavelength calibration, 27 lines are used, they are listed in table A.5.

Having traced the fiber positions and calibrated the wavelengths, the spectra are now extracted from the science frames by walking along the trace positions and averaging the values in a 7 pixel wide aperture. The extraction is performed in  $\ln(\lambda)$ -space, the step width corresponds to  $10 \text{ km s}^{-1}$ .

Because the different observing runs took place in different months of the year, we also have to correct during the extraction for the relative motion of the earth

around the sun. We use the web-tool by Edward Murphy<sup>2</sup> based on an algorithm described in Meeks (1976) to calculate the relative velocity of the Earth towards M31 at the time of the observation. For each absorption run, we use the value for the mean date of the observation run. We calculate the correction relative to the run in October 2011, because for that run, the correction is  $c_{Oct11} = 0 \text{ km s}^{-1}$ . The correction for the run in October 2012 is  $c_{Oct12} = -3.6 \text{ km s}^{-1}$ , for the run in February 2013 it is  $c_{Feb13} = 19.1 \text{ km s}^{-1}$  and for the run in August 2013 it is  $c_{Aug13} = -28.1 \text{ km s}^{-1}$ .

The flatfield frames are extracted in the same way as the data frames. Initially, the fiber to fiber throughput variation and the vignetting are corrected by dividing the spectra  $S(i, \lambda)$  in one pointing,  $i$  being the fiber number and  $\lambda$  the wavelength, by the median flux for each wavelength  $M_F(\lambda)$ .

$$SF(i, \lambda) = \frac{S(i, \lambda)}{M_F(\lambda)} \quad (2.1)$$

The resulting spectrum does still exhibit the rather strong variation of sensitivity as function of wavelength, that is due to the strongly peaked diffraction efficiency of the VPH grating. This would complicate the later throughput calibration. Therefore, in the next step the spectra are divided by the mean flat field spectrum  $F(\lambda)$  where the mean is taken across all fibers at each wavelength. The spectrally flatfielded value is then:

$$SFF(i, \lambda) = \frac{S(i, \lambda)}{F(\lambda)} \quad (2.2)$$

An example of the flatfielding process is shown in figure 2.3.

The two sky exposures that bracket each science exposure are averaged and cleaned for cosmics. To increase the S/N value, the signal of 20 neighboring fibers is averaged in a moving window, while the routine gets rid of outliers by  $\kappa$ - $\sigma$  clipping. These cleaned sky frames are then scaled to the exposure time of the science frames and subtracted.

An example for an object frame after the data reduction can be seen in figure 2.4.

The method to determine the correct astrometry is adapted from Adams et al. (2011). Because the galaxy pointings do not contain bright stars on which the astrometry can be determined, we use instead the stars observed by the guider camera of the telescope to keep the telescope pointed at the right position. This means that the position of the field-of-view of the guider camera relative to the field-of-view of the spectrograph itself has to be accurately determined. The relative positions of the two can be seen in figure 2.5. For this, the observations of the open clusters listed in table A.2 are used. The datacubes are collapsed to produce the projected view on sky. An example of such a collapsed datacube for the open cluster M37 is plotted in figure 2.6. The RA and DEC positions of the stars in

<sup>2</sup><https://www.astro.virginia.edu/~emm8x/utlils/vlsr.html>

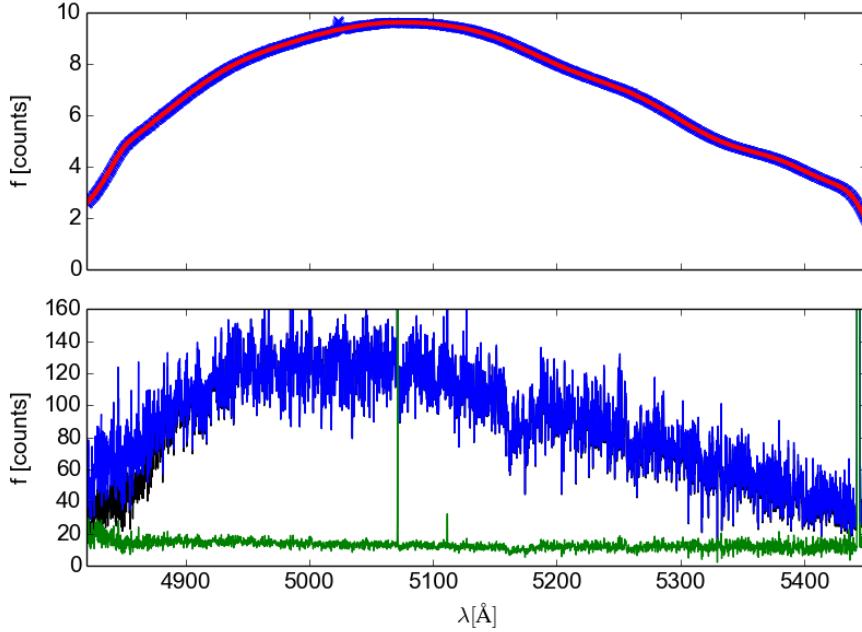


**Figure 2.3:** An example plot for the flatfielding of a spectrum. Top panel: A spectrum from a flatfield observation. Blue is the median flatfield  $M_F(\lambda)$ , the hump at 5020 Å is the Littrow ghost. Red is a smoothed version of the median where the Littrow ghost has been removed. Bottom panel: The input spectrum (black), the flatfielded spectrum (blue) obtained by applying equation 2.1 and the spectrally flatfielded spectrum (green) obtained with equation 2.2. The black and the blue spectrum are almost identical, except at short wavelengths.

the open cluster are loaded from the 2MASS catalog (Skrutskie et al., 2003). For the stars in the guider frames that were taken during the observation of the open cluster, the coordinates are also loaded from the catalog. The stars seen by the guider camera have relative coordinates in the guider image. A finder chart for the guider camera is plotted in figure 2.7. These finder charts are created before the observation for each pointing, simulating the field-of-view of the guider camera. Each star is assigned a coordinate in the image. The coordinate of the star that is used for guiding is written down during the observations. When calculating the astrometric solution, the relative coordinates of the guider star and its RA and DEC coordinates are compared to the RA and DEC coordinates of the stars in the collapsed datacube of the open cluster observation. The astrometric solution contains the relative position of the guider field-of-view to the spectrograph field-of-view. Having calculated this for the open cluster, we are now able to convert for every pointing the relative coordinates of the guider star to the RA and DEC coordinates of the fibers of the pointing. In this way, we calculate the coordinates of every fiber in each pointing of M31. The accuracy of this method was estimated by Adams et al. (2011) to be 0.21", much less than the fiber diameter of VIRUS-W with 3.2". The coordinates for the central fiber of each observation of M31 are the ones that are tabulated in table A.4 as the coordinates for each

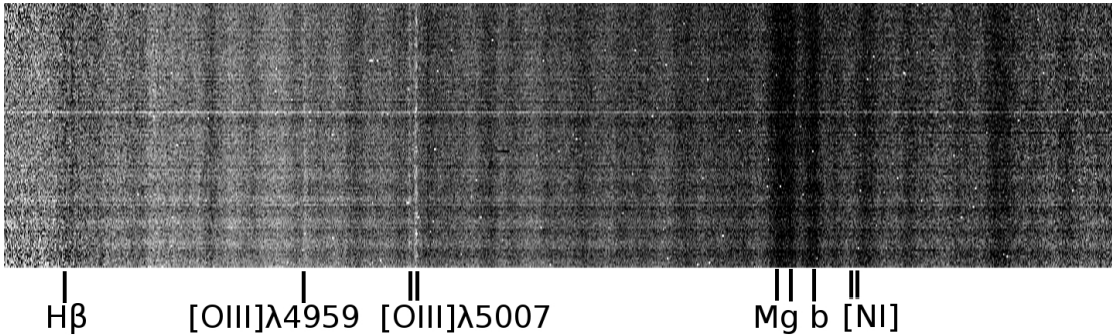


**Figure 2.4:** The image of one pointing after data reduction and cropping. The positions of  $H\beta$ , the  $[OIII]$  and  $[NI]$  lines (in emission) are marked, as well as the Mg b triplet (in absorption). The  $[NI]$  lines are very faint and not distinguishable from the background. The line  $[OIII]\lambda 5007$  shows two distinct peaks. This will be discussed in chapter 4.

pointing. The coordinates are converted to distance in arcseconds relative to the coordinate listed for pointing M31\_107.

Because of different observing conditions during the different runs and the underlying brightness profile of M31 itself, some of the pointings are noisier than others. The median flux above the sky  $S$  for each spectrum is plotted in figure 2.8. The overall distribution reproduces the brightness distribution of the galaxy, the pointing with low value to the south-east of the center (M31\_050 in table A.4) had cloudy observing conditions, therefore the flux values are low. The spectra are then binned together to get above a signal-to-noise ratio of  $S/N \approx 30$ , using the Voronoi-binning method by Cappellari & Copin (2003). This reduces the initial number of 52,866 spectra to 7563 binned ones, with the binning scheme plotted in figure 2.9. Figure 2.10 shows the number of fibers assigned to each bin. In the inner part of the galaxy, each bin corresponds to one fiber. This is true out to approximately  $140''$  along the major axis and  $100''$  along the minor axis. Outside, the number of fibers per bin gradually rises, until reaching a maximum of 345 fibers in the outermost pointings along the western arm of the minor axis. M31\_050 is also visible in this map, because of its low signal, more fibers have to be binned together.

The signal-to-noise map resulting from the binning scheme is shown in figure 2.11. In the very center,  $S/N$  is high, outside of the center it remains relatively constant.

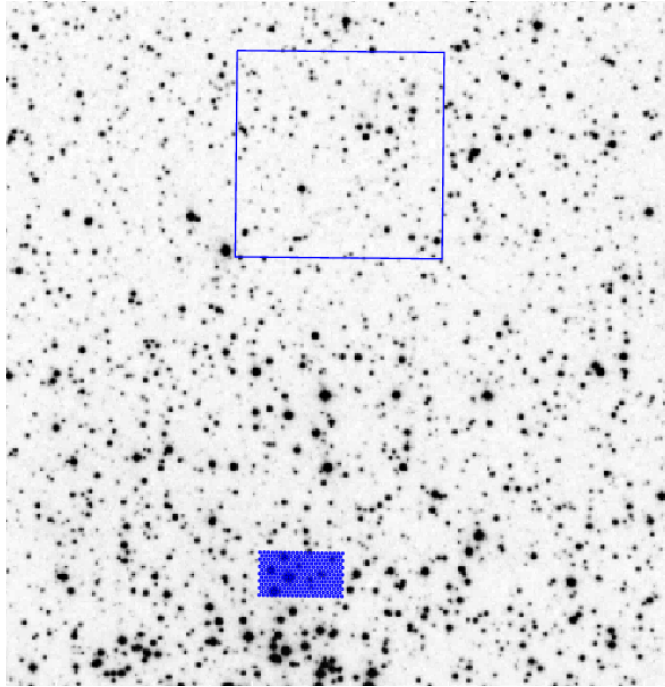


**Figure 2.5:** The relative positions of the field-of-view of the guider camera (large square) and the field-of-view of the spectrograph (small rectangle made of circles for the individual fibers) for the observation of M37

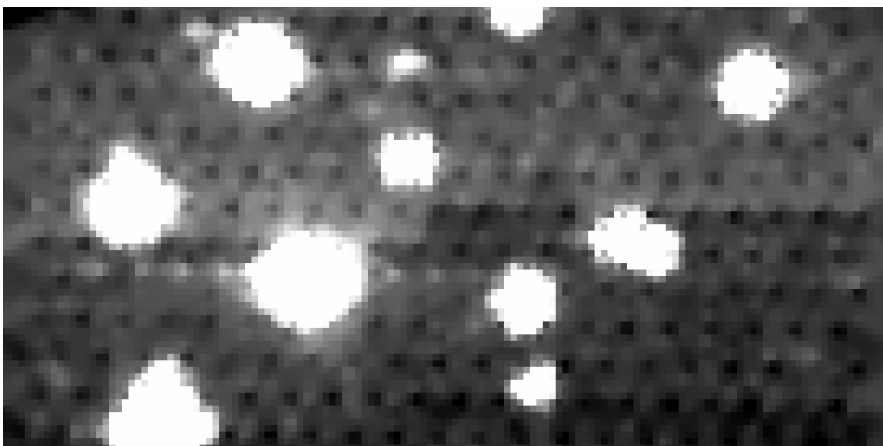


**Figure 2.6:** Collapsed data cube for M37.



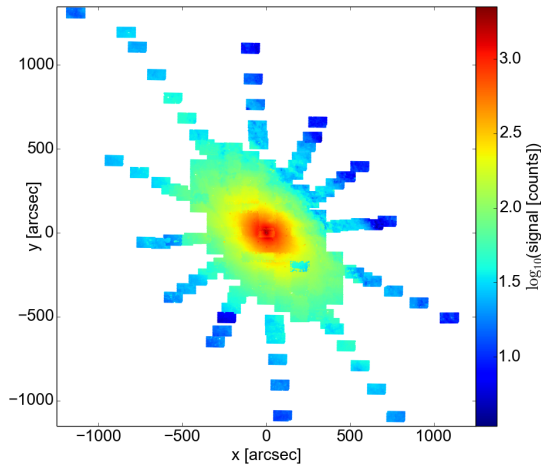


**Figure 2.8:** Map of the median flux for each spectrum.

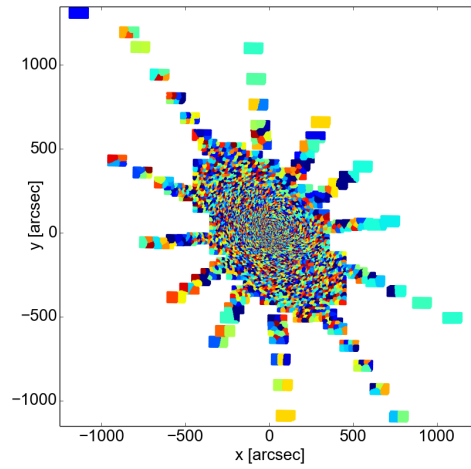


**Figure 2.9:** Map of the bins with a random color assigned to each bin.

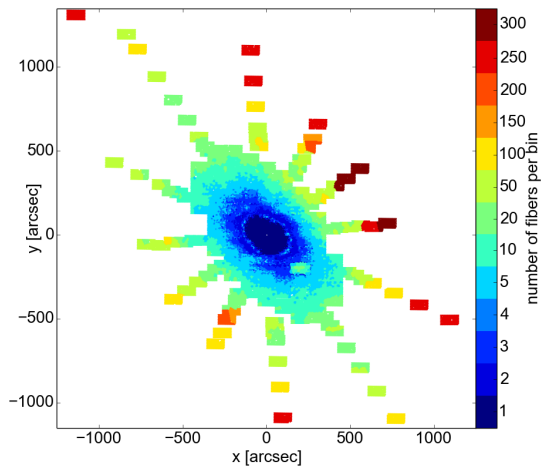


**Figure 2.10:** Map of the number of fibers per bin.

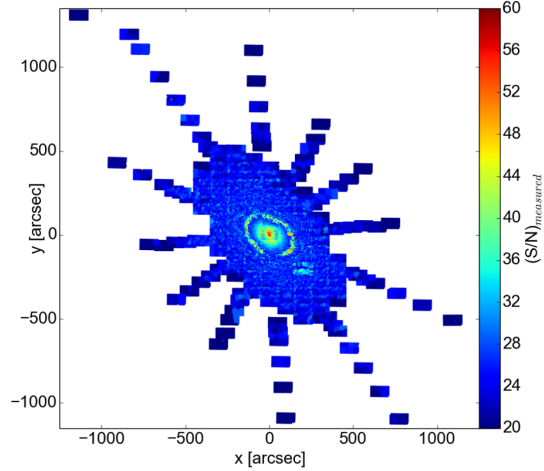


**Figure 2.11:** Map of the binned signal-to-noise ratio.

## 2.2 Obtaining the kinematics

### 2.2.1 Fitting the stellar kinematics with pPXF

The kinematics is measured using the routines pPXF (penalized PiXel Fitting) by Cappellari & Emsellem (2004) and GANDALF (Gas AND Absorption Line Fitting) by Sarzi et al. (2006). GANDALF uses pPXF as its first step. pPXF fits the stellar kinematics by broadening a weighted sum of template star spectra with a line-of-sight velocity distribution (LOSVD). We use spectra from 41 kinematic standard stars obtained with VIRUS-W. They are listed in table A.3. The information about the stars is taken from the ELODIE (Prugniel et al., 2007) and LICK (Worthey et al., 1994) catalogs. The coordinates come either from the ELODIE catalog or van Leeuwen (2007), using the SIMBAD interface (Wenger et al., 2000).

pPXF fits the stellar kinematics by approximating a galaxy spectrum  $G(x)$  with a model galaxy spectrum  $G_{mod}(x)$  (Cappellari & Emsellem, 2004). The pixel coordinate corresponds to the logarithm of the wavelength:  $x = \ln(\lambda)$ .

To construct  $G_{mod}(x)$ , each individual spectrum  $T_k$  of the  $K$  template spectra is convolved with the broadening function  $\mathcal{B}(x) = \mathcal{L}(cx)$ , where  $\mathcal{L}(v)$  is the LOSVD and  $c$  is the speed of light. The convolution for each template spectrum  $T_k$  gets assigned a weight  $w_k$ .

The sum of all weighted convolutions is multiplied by a multiplicative Legendre polynomial  $\mathfrak{P}(x) = \prod_{l=1}^L a_l P_l(x)$ , which removes any large-scale shape differences between the observed stellar and galactic spectra (Kelson et al., 2000). The galaxy model spectrum is thus represented as:

$$G_{mod}(x) = \prod_{l=1}^L a_l P_l(x) \cdot \left( \sum_{k=1}^K w_k [\mathcal{B} * T_k](x) \right) \quad (2.3)$$

We tested several different values of  $L$ . When  $L$  is too low, the overall shape of the spectra is not well approximated, when it is too high, noise features are fitted. In the end, we settle on  $L = 9$ .

The LOSVD is expanded as a Gauss-Hermite series following van der Marel & Franx (1993) and Gerhard (1993):

$$\mathcal{L}(v) = \frac{\exp\left(-\frac{(v-\langle v \rangle)^2}{2\sigma^2}\right)}{\sigma\sqrt{2\pi}} \left[ 1 + \sum_{m=3}^M hm \cdot H_m\left(\frac{v-\langle v \rangle}{\sigma}\right) \right] \quad (2.4)$$

$H_m$  are the Hermite polynomials and  $hm$  the Gauss-Hermite coefficients, the sum is broken off after  $M$  entries. pPXF only looks at the Gauss-Hermite moments  $h3$  and  $h4$ .

In figure 2.12, some model Gauss-Hermite functions are plotted.  $h3$  determines the asymmetric deviations from a pure Gaussian and  $h4$  the symmetric ones. For negative  $h3$ , the peak velocity of the Gauss-Hermite function is larger than the one for the pure Gaussian, whereas for positive  $h3$  it is the opposite. The wings are

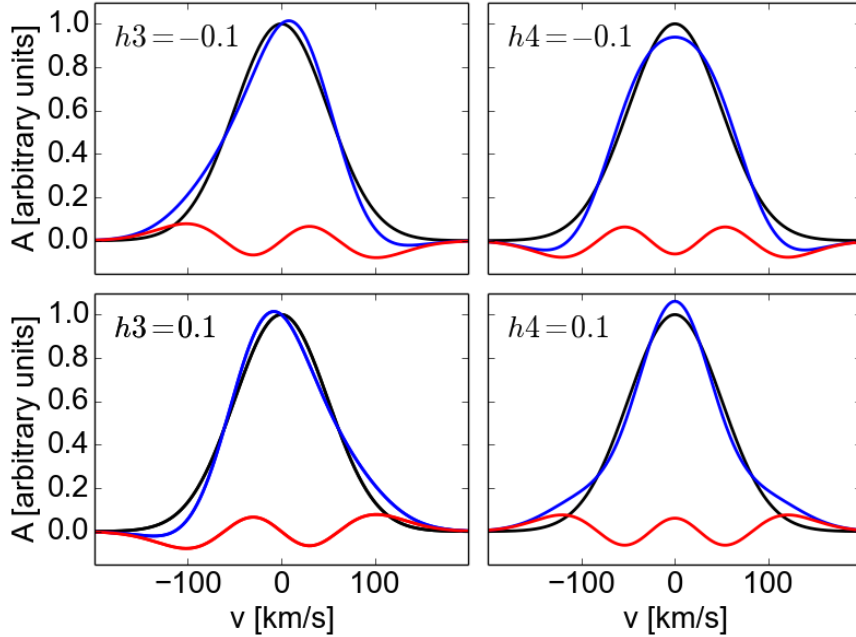


**Figure 2.12:** A plot of different Gauss-Hermite functions. In all panels, a Gaussian with  $v = 0 \text{ km s}^{-1}$  and  $\sigma = 50 \text{ km s}^{-1}$  is drawn in black, the Gauss-Hermite function in blue and the difference between the two, i.e. the higher-order part of the Gauss-Hermite function, in red. On the left panels,  $h4 = 0$  with  $h3 = -0.1$  in the upper figure and  $h3 = 0.1$  in the lower one. On the right,  $h3 = 0$  and  $h4 = -0.1$  in the upper panel and  $h4 = 0.1$  in the lower one. This plot has been adapted from [Bender et al. \(1994\)](#).

asymmetric, with the one on the side of the velocity peak being steeper. Positive  $h4$  values result in an LOSVD with a narrower core but larger wings, negative  $h4$  lead to a broader flat-top function.

### 2.2.2 Fitting the emission lines with GANDALF

The kinematics of the ionized emission lines are fitted with **GANDALF** ([Sarzi et al., 2006](#)), which uses **pPXF** to fit the stellar kinematics as its first step. The emission lines present in our wavelength range are  $H\beta$  at  $\lambda = 4861 \text{ \AA}$ , the doublet at  $[\text{OIII}]\lambda\lambda 4959, 5007$  and the doublet at  $[\text{NI}]\lambda\lambda 5198, 5200$ . The emission lines are treated as Gaussian functions. At each fitting step, their amplitudes, velocities and velocity dispersions are fitted. In the case of the  $[\text{OIII}]$  and  $[\text{NI}]$  doublets, each component gets assigned the same mean velocity and width. The relative strengths of the two lines in the doublet are fixed by the ratio of the corresponding transition probabilities ([Sarzi et al., 2006](#)).

The  $[\text{OIII}]\lambda 4959$  line is the forbidden atomic transition  $^1\text{D}_2 \rightarrow ^3\text{P}_1$ , while  $[\text{OIII}]\lambda 5007$  is  $^1\text{D}_2 \rightarrow ^3\text{P}_2$  ([Bowen, 1927](#)). The ratio of the amplitudes of these two values is ([Oh et al., 2011](#)):

$$\frac{A(4950)}{A(5007)} = 0.35 \quad (2.5)$$

[NI] $\lambda$ 5198 is the transition  $^4S_{3/2} \rightarrow ^3D_{3/2}$ , [NI] $\lambda$ 5200 is  $^4S_{3/2} \rightarrow ^3D_{5/2}$  (Gurzadyan, 1997). Their ratio is fixed in GANDALF to:

$$\frac{A(5200)}{A(5198)} = 0.7 \quad (2.6)$$

The H $\beta$  and [NI] lines cannot be measured confidently without first constraining their kinematics because contamination as a result of template mismatch can still be important. Additionally, there are several metal absorption lines near H $\beta$ , mostly from Fe and Cr at about 4870 Å, which complicate the independent measurement of the H $\beta$  emission line. The [NI] lines are usually quite weak, it is almost never possible to constrain their kinematics alone. Furthermore, these two lines are close to the continuum region that is generally matched worst by templates because of an enhancement in the Mg/Fe ratio that is not observed in stars in the solar neighborhood, where the template spectra are taken from (Sarzi et al., 2006). Therefore, the kinematics are fitted on the [OIII] lines, using the stronger one of the doublet, [OIII] $\lambda$ 5007.

The fitting routine runs the following steps:

1. The spectral regions within  $\pm 200$  km/s around the emission lines are masked.
2. The stellar continuum is fitted using pPXF.
3. The mask for the [OIII] doublet is lifted.
4.  $v_{gas}$ ,  $\sigma_{gas}$  and the coefficients of the multiplicative polynomial are fitted simultaneously.
5. The convolved stellar templates are multiplied with the polynomial.
6. The best linear combination of stellar templates and the [OIII] emission-line template is then determined. The fitted weight of the emission-line template is the amplitude  $A_{gas}$ .
7. The masks on H $\beta$  and [NI] are lifted.
8. The coefficients of the multiplicative polynomial are fitted, while  $v_{OIII}$  and  $\sigma_{OIII}$  are kept fixed.
9. The amplitudes for H $\beta$ , [OIII] and [NI] are fitted while keeping  $v_{OIII}$  and  $\sigma_{OIII}$  from before and also using it for H $\beta$  and [NI].

In figure 2.13, a fit with GANDALF to a spectrum is plotted.

### 2.2.3 Fitting double lines with GANDALF

After fitting every spectrum with GANDALF, we find that the gas lines are more complicated and need to be treated with more care than what has been presented in the previous section. In some spectra, like the one plotted in figure 2.13, we see only one emission line, while in others, each emission line, which means also both emission lines of a doublet, has two peaks. We modify GANDALF to fit two components for each line, this is achieved by adding a second Gaussian template for the second [OIII] peak. This second template consists, like the first, of one Gaussian for [OIII] $\lambda$ 5007 with amplitude 1 and one for [OIII] $\lambda$ 4959 with amplitude 0.35. We also add a second  $H\beta$  template and a second [NI] template. The initial guesses for the gas velocities have to be slightly different for the two components, otherwise GANDALF does not fit separate components. An example of a fit with two lines is shown in figure 2.14. Here, the two lines have almost the same amplitude and are clearly separated. This is not always seen so clearly, there are also cases when one line is stronger than the other, see figure 2.15, or where the two lines are almost blended together, see figure 2.16, or where there is only line clearly visible with a skewed line shape, that can, however, be described by the combination of two lines, see figure 2.17. We have to come up with a way that reliably fits all these different double line features and at the same time treat the cases correctly where only one line is present, since if we let GANDALF fit two line components all the time, it will give wrong results when only one line is present, often fitting a peak that in reality is only noise. So we modify the program further to sometimes fit one component and sometimes fit two components, depending on initial guesses we are feeding the program.

In order to get these initial guesses, we apply the following method: First, we cross-correlate a model spectrum only consisting of the [OIII] $\lambda$ 5007 line with each spectrum. A schematic view of this is shown in figure 2.18. The program then fits the resulting cross-correlation function with a set of gaussians. These gaussians all have the same dispersion of  $\sigma = 20 \text{ km s}^{-1}$  and their mean velocities are  $40 \text{ km s}^{-1}$  apart. The program now changes the amplitudes of the individual Gaussians to get the best approximation of the input cross correlated spectrum. We tell the program to only pick the Gaussian with the largest amplitude to have an estimate for the one-component fit and the one with the largest amplitude plus the one with the second largest amplitude for the two component estimate. These two plots are shown in figure 2.19 for the spectrum shown in figure 2.14. If the amplitude of the second component is less than 0.25 times the amplitude of the first one, we decide to take the initial guess with only one component. We use the mean velocities of the Gaussians as the initial guesses for GANDALF, letting it fit one line for the cases where we have found only one line and letting it fit two lines where we have found two lines.

After a first iteration, we check all fits manually, update the initial guesses for the spectra where the fit failed and let GANDALF fit a second iteration. This second iteration results in 85 % of the spectra being fitted correctly, the rest is left out of the analysis.

### 2.2.4 Error calculation

GANDALF estimates formal  $1\sigma$  errors on all quantities that are measured. In order to check if these formal errors are reliable, we run a Monte-Carlo simulation on 6 binned spectra. For each of our test bins, we take the bestfit spectrum that GANDALF gives out and randomly add Gaussian noise onto it, with the width  $\sigma_{Gauss}$  being the noise value we measure for the original spectrum for this bin. In this way, we produce 100 representations for each of the 6 investigated bins. For bin 7232, which is the one plotted in figure 2.14, the original spectrum, the bestfit spectrum and three representations of the bestfit spectrum with random noise are shown in figure 2.20. The 100 representations of the spectrum with random noise are fitted with GANDALF. For each of the measured quantities, the results for the 100 different representations are put into a histogram, which is fitted with a Gaussian. The mean value and the  $1\sigma$  value of this histogram are compared to the measured value. For bin 7232, these values are tabulated in table 2.2. Since

**Table 2.2:** Quantities and errors measured with GANDALF and the Monte-Carlo simulation

Quantity		GANDALF	Monte Carlo simulation
$v_{star}$	$[km\ s^{-1}]$	$-426.5 \pm 3.5$	$-423.3 \pm 2.4$
$\sigma_{star}$	$[km\ s^{-1}]$	$116.4 \pm 3.6$	$111.8 \pm 2.5$
$h3_{star}$		$-0.02 \pm 0.02$	$-0.015 \pm 0.015$
$h4_{star}$		$-0.03 \pm 0.02$	$-0.03 \pm 0.015$
$v_{OIII}$	$[km\ s^{-1}]$	$-458.3 \pm 2.1$	$-458.4 \pm 1.5$
$\sigma_{OIII}$	$[km\ s^{-1}]$	$26.9 \pm 2.1$	$26.9 \pm 1.5$
$A_{OIII}$	$[ADU/pix]$	$4.0 \pm 0.2$	$4.1 \pm 0.2$
$A_{H\beta}$	$[ADU/pix]$	$2.2 \pm 0.3$	$2.3 \pm 0.2$
$A_{NI}$	$[ADU/pix]$	$0.2 \pm 0.2$	$0.27 \pm 0.15$
$v_{OIII,2}$	$[km\ s^{-1}]$	$-304.0 \pm 2.1$	$-304 \pm 1.5$
$\sigma_{OIII,2}$	$[km\ s^{-1}]$	$24.7 \pm 2.1\ km\ s^{-1}$	$24.5 \pm 1.5$
$A_{OIII,2}$	$[ADU/pix]$	$3.8 \pm 0.2$	$3.8 \pm 0.2$
$A_{H\beta,2}$	$[ADU/pix]$	$0.8 \pm 0.3$	$0.9 \pm 0.2$
$A_{NI,2}$	$[ADU/pix]$	$0.2 \pm 0.2$	$0.16 \pm 0.13$

the errors that are measured by GANDALF are comparable to the ones from the Monte-Carlo simulations, we use the ones from GANDALF.

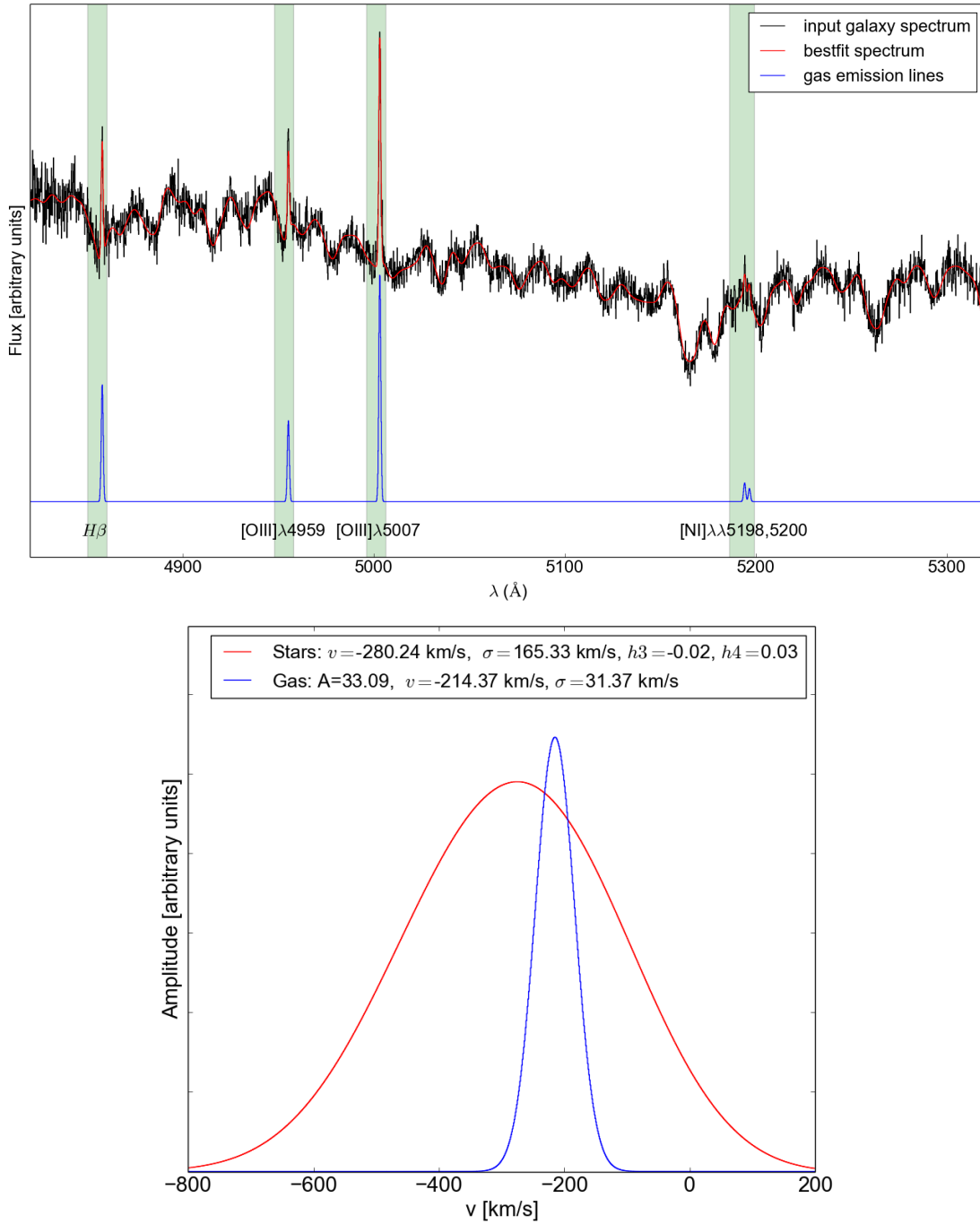


**Figure 2.13:** Upper panel: A spectrum from the bulge region. Black is the measured spectrum, red is the bestfit spectrum that GANDALF gives out, blue are only the fits to the gas emission lines. The green shaded areas are the regions where the gas emission lines are expected. Lower panel: The corresponding LOSVDs. Red is the LOSVD for the stars, blue is the one for the gas.

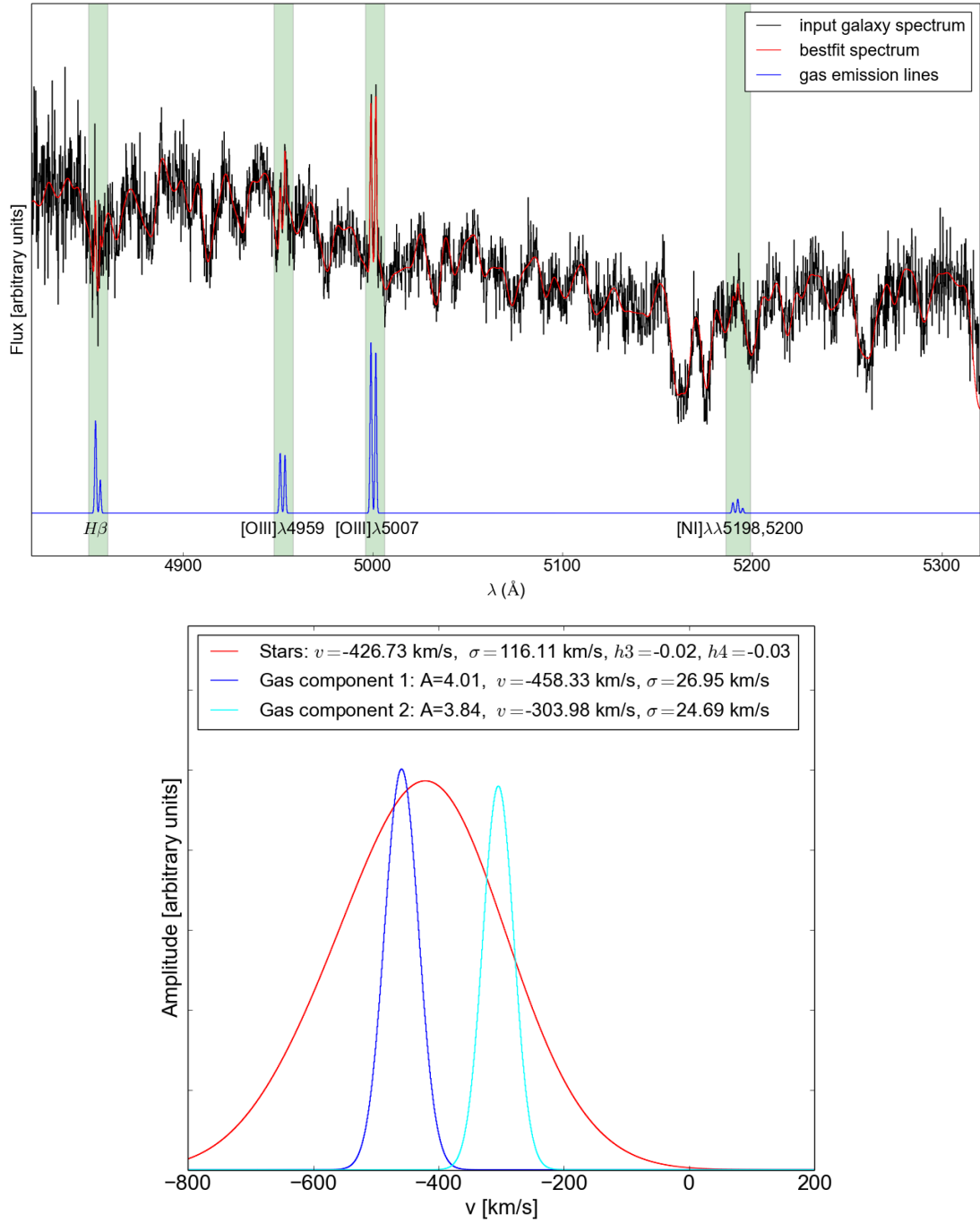


**Figure 2.14:** Upper panel: A spectrum from the outer edges of the bulge region where the emission lines are split into two lines with almost equal amplitudes. The colors are the same as in figure 2.13. Lower panel: The LOSVDs determined by GANDALF. Red is the LOSVD for the stars, blue is the LOSVD for the first gas line, cyan the one for the second gas line.

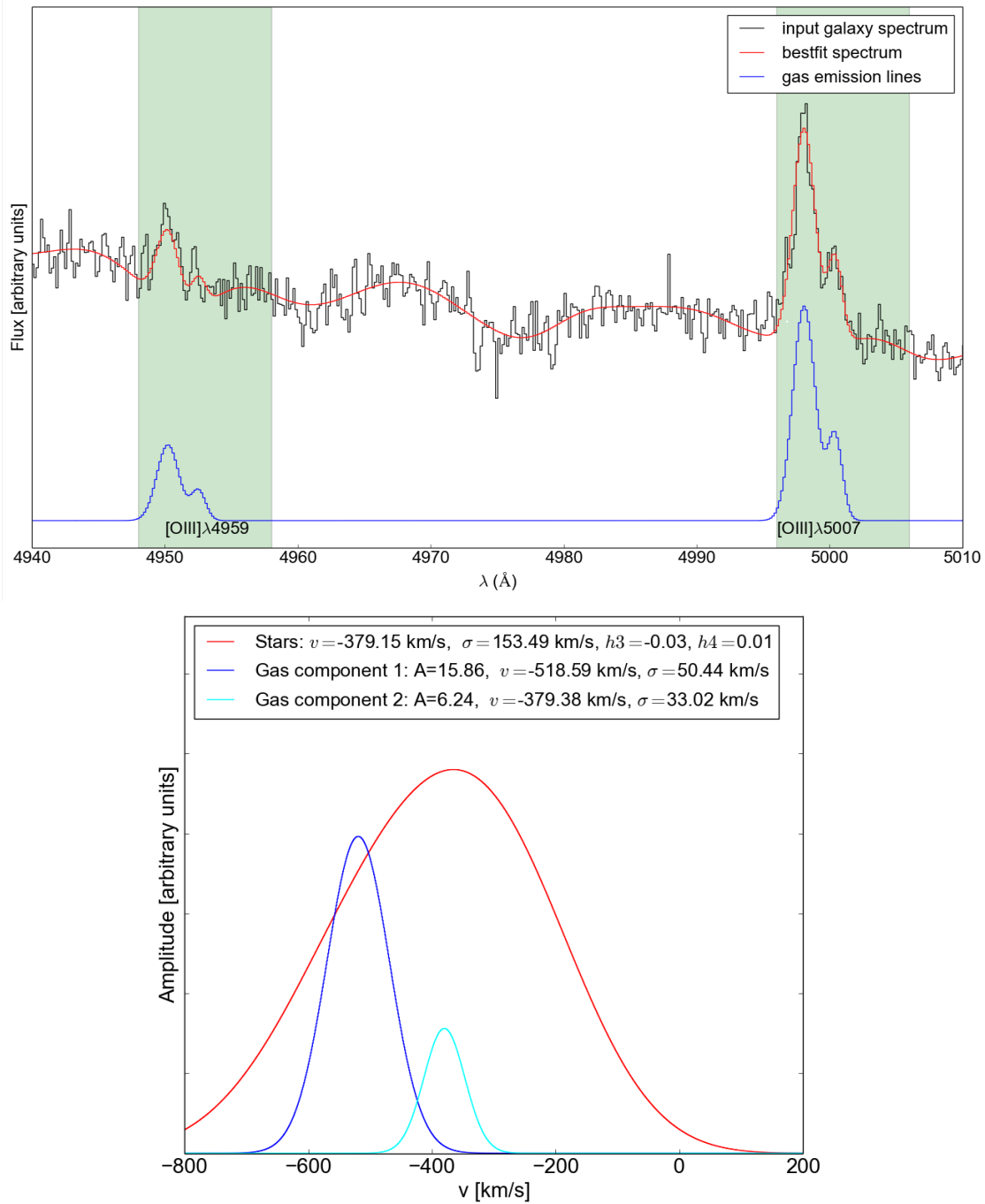


**Figure 2.15:** Upper panel: A spectrum from the bulge region where the emission lines are split, but one is stronger than the other. The colors are the same as in figure 2.13. Lower panel: The LOSVDs determined by GANDALF. The colors are the same as in the lower panel of figure 2.14.

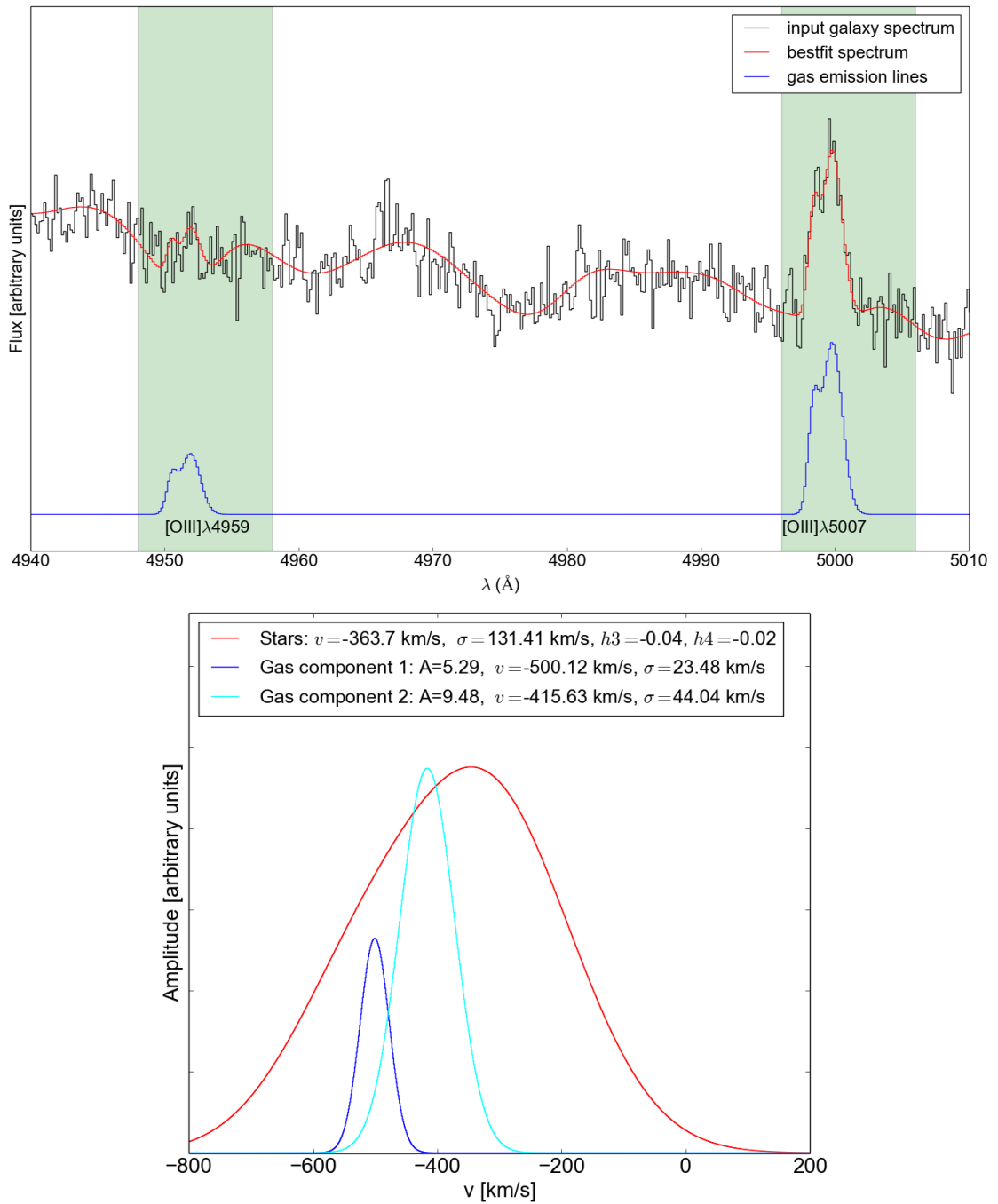


**Figure 2.16:** Upper panel: A spectrum from the bulge region where the emission lines are split, but are almost blended into one very broad line. The colors are the same as in figure 2.13. Lower panel: The LOSVDs determined by GANDALF. The colors are the same as in the lower panel of figure 2.14.

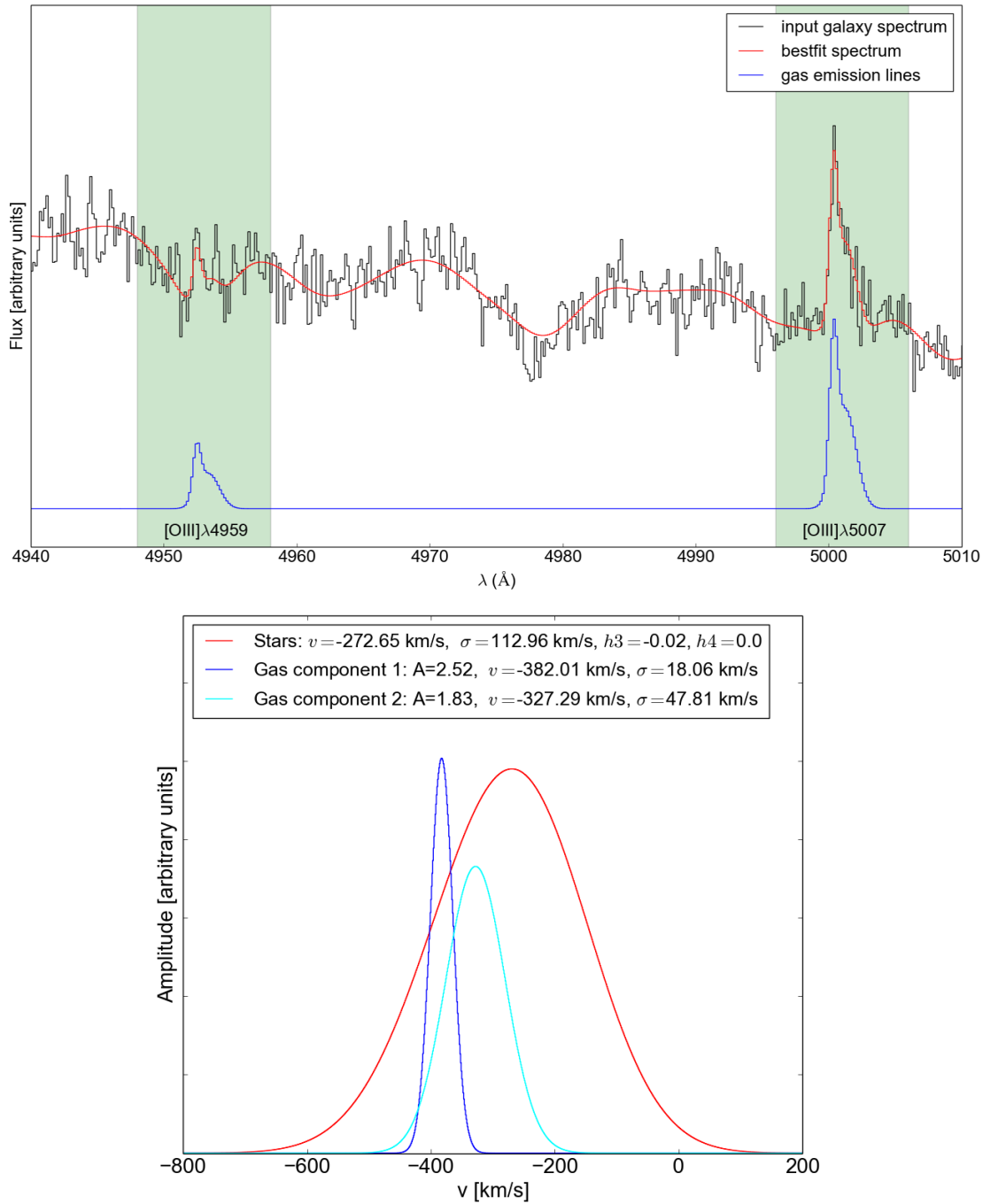


**Figure 2.17:** Upper panel: A spectrum from the bulge region where the emission line [OIII] $\lambda$ 5007 has a skewed shape that can be explained with the superposition of two Gaussian emission lines. The colors are the same as in figure 2.13. Lower panel: The LOSVDs determined by GANDALF. The colors are the same as in the lower panel of figure 2.14.

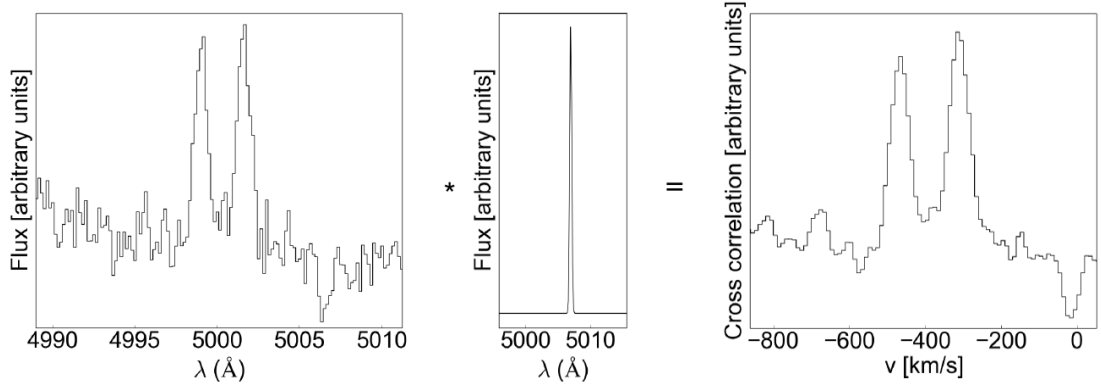


**Figure 2.18:** A schematic view of the cross correlation method. The measured spectrum for the bin from figure 2.13 (left) is convolved with a single Gaussian with the instrumental dispersion  $\sigma = 15 \text{ km s}^{-1}$  (middle). This results in the spectrum on the right, where the shift in velocity relative to [OIII] $\lambda$ 5007 is plotted on the x-axis.

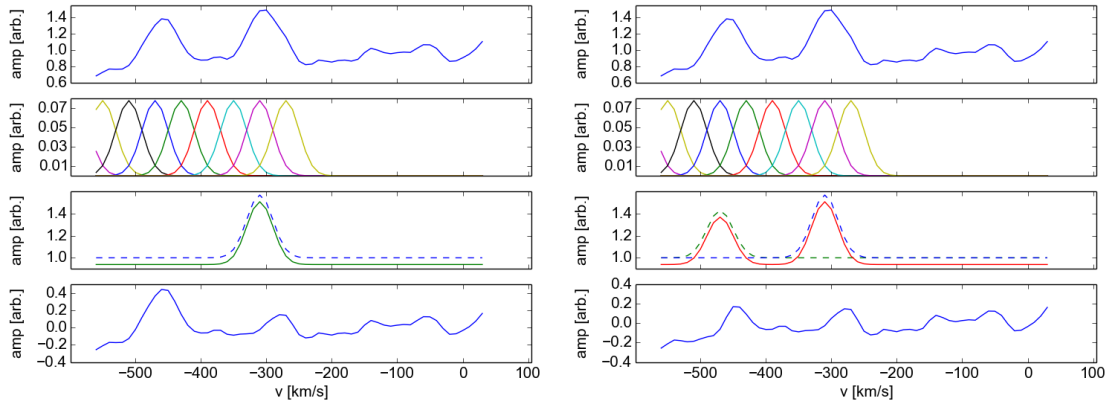


**Figure 2.19:** Fit to the cross correlation from figure 2.18 with one Gaussian (left) and two Gaussians (right). Top: Input cross correlated spectrum. Second from top: Different Gaussian functions, each with  $\sigma = 20 \text{ km s}^{-1}$ , their maxima are  $40 \text{ km s}^{-1}$  apart. Third from top in the left panel: The Gaussian with the highest amplitude. Third from top in the lower panel: The Gaussian with the highest amplitude (blue dashed line), the one with the second highest amplitude (green dashed line) and the sum of both (red). The dashed lines are slightly offset in the vertical direction for better visibility. Bottom: Residuals of upper panel minus the third panel. Along the y-axis, the amplitudes of the respective plots are shown in arbitrary units.

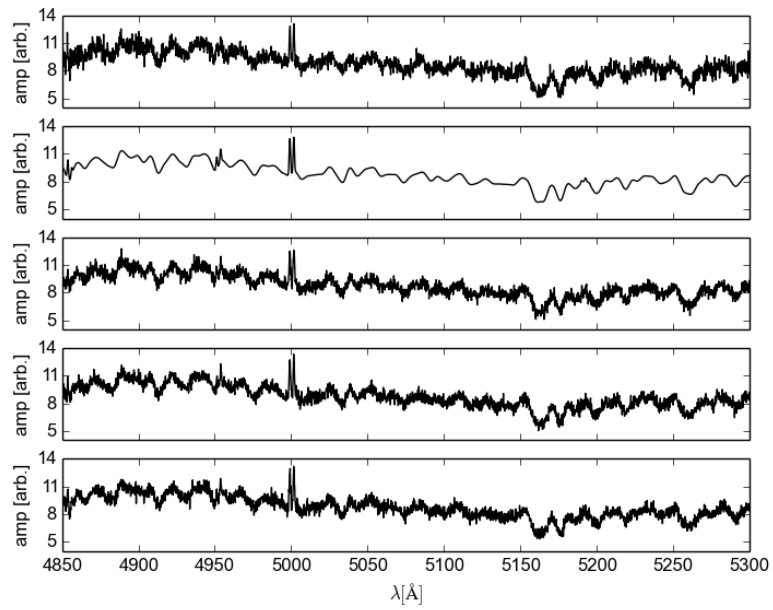


**Figure 2.20:** Top: Original spectrum for bin 7232. Second from top: Bestfit spectrum after the fit with GANDALF. Three bottom panels: Bestfit spectrum with added random Gaussian noise with  $\sigma_{Gauss}=0.36$ .

## 2.3 Photometric model image

For several tasks presented later in this thesis, we also need to compare the kinematics to photometry, for this, we construct a photometric model image. First, we look at a photometric bulge-disk decomposition along the major axis by [Kormendy & Bender \(1999\)](#). In this decomposition, the bulge is fitted with a Sérsic-profile ([Sersic, 1968](#)), see equation 2.7.

$$I(r) = I_e \exp \left\{ -b_n \left[ \left( \frac{r}{r_e} \right)^{1/n} - 1 \right] \right\} \quad (2.7)$$

$I_e$  is the intensity at the effective or half-light radius  $r_e$ , which encloses half the total galaxy light.  $n$  is called the Sérsic index,  $b_n$  is set to such a value that the light inside the half-light radius is exactly half the total light of the bulge. The disk is fitted with an exponential function, compare equation 2.8.

$$I(r) = I_0 \exp \left( -\frac{r}{h} \right) \quad (2.8)$$

The parameters of the fit are given in table 2.3, where instead of intensities, the values are tabulated as surface brightness  $\mu$ , which is related to the intensity via the equation:

$$\mu = -2.5 \log(I) \quad (2.9)$$

The profile of the decomposition is plotted in figure 2.21. Because this decomposition is only done on the major axis, we need to turn it into a model image to better compare it with our two-dimensional data. For that, we take an ellipse fit by [S10](#) on a K-band image of M31 from the 2MASS survey ([Jarrett et al., 2003](#)). The position angle (PA) and the ellipticity  $\epsilon = 1 - \frac{b}{a}$  of the ellipse fit are plotted in figure 2.22. These ellipse values are combined with the decomposition to build a model image, which is plotted in figure 2.23. Equivalent model images are also constructed for the fitted bulge and disk magnitudes from the decomposition. These are then used to calculate bulge-to-total (equation 2.10) and disk-to-total (equation 2.11) ratios for each bin by comparing the fluxes, the resulting  $\frac{B}{T}$  map is shown in figure 2.24.

$$\frac{B}{T} = \frac{f_{bulge}}{f_{tot}} = 10^{-0.4(\mu_{bulge} - \mu_{tot})} \quad (2.10)$$

$$\frac{D}{T} = \frac{f_{disk}}{f_{tot}} = 10^{-0.4(\mu_{disk} - \mu_{tot})} = 1 - \frac{B}{T} \quad (2.11)$$

The ellipse fit to the K-band image is used to build the model image because the K-band is less affected by dust than the V-band. To check if the model image is a good representation of the actual brightness distribution in M31, we look at the color profile between the model image and a near-infrared image. Unfortunately, the K-band image has problems with sky-subtraction, so colors obtained from a comparison would not be very reliable. Therefore, we choose another near-infrared

**Table 2.3:** Parameters of the bulge-disk decomposition

<b>Bulge</b>	
$r_e$	$313 \pm 43$ arcsec
$n$	$2.227 \pm 0.094$
$\mu_e$	$19.855 \pm 0.069$ mag/arcsec <sup>2</sup> , V
<b>Disk</b>	
$h$	$1723 \pm 164$ arcsec
$\mu_0$	$20.426 \pm 0.137$ mag/arcsec <sup>2</sup> , V

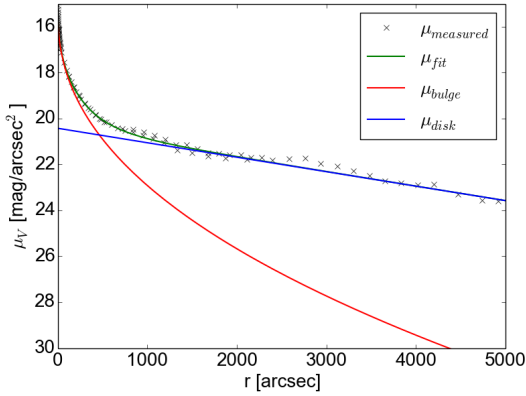
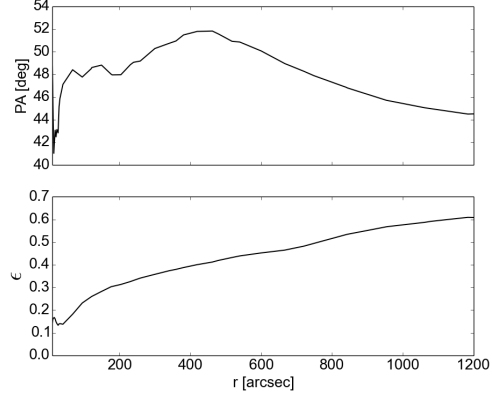
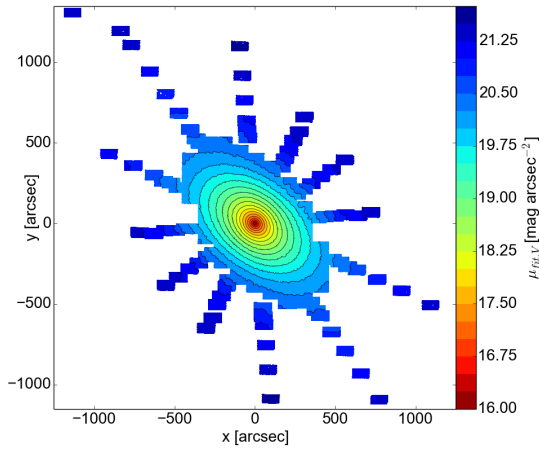
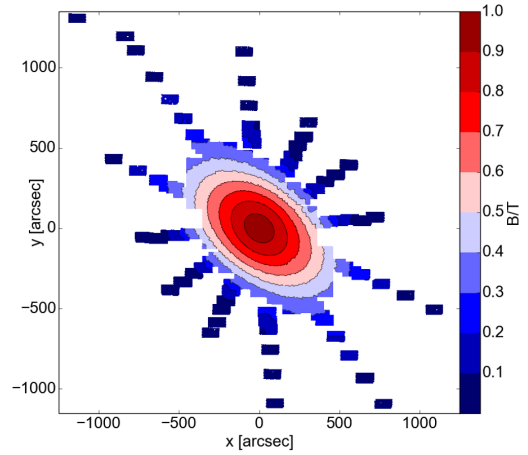
**Figure 2.21:** Decomposition along the major axis by [Kormendy & Bender \(1999\)](#): Total measured profile in V-band (crosses), fitted bulge (red), fitted disk (blue) and sum of both (green).**Figure 2.22:** Profiles of position angle and ellipticity of an ellipse fit by [S10](#) to a K-band image of M31 from the 2MASS survey ([Jarrett et al., 2003](#)), with the position angle (upper panel) and the ellipticity (lower panel) as functions of the major axis of the ellipses.

image to compare the model image to, an image from the **IRAC** instrument on the **Spitzer** space telescope in the  $3.6\mu m$  band from [Barnby et al. \(2006\)](#). In figure [2.25](#), we plot a map of the  $V - 3.6\mu m$  color. Over the bulge region, the color is relatively homogeneous, with a value of about 3.5. However, we see a "cross-shape" because the model image does not take into account diskiness and boxiness. In the disk region, the color values are lower, around 3.2.



**Figure 2.23:** Model image of M31, constructed by combining  $\mu_{fit}$  from figure 2.21 with the ellipse fit from figure 2.22.



**Figure 2.24:** The B/T-ratio from the model image. Bulge dominated regions are shaded red, while disk dominated regions are blue.

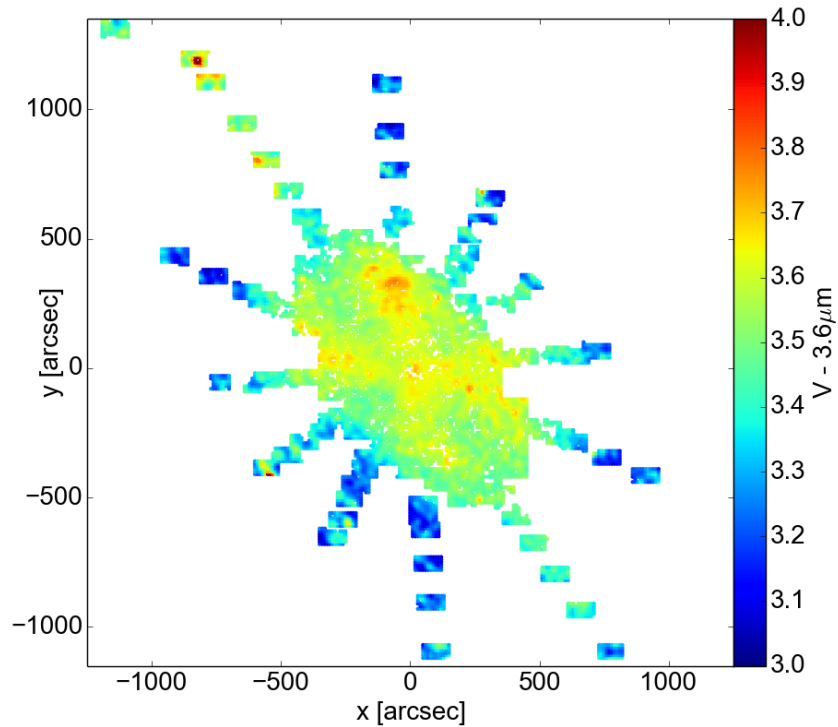


**Figure 2.25:** V-3.6 $\mu$ m color image determined from subtracting the IRAC 3.6 $\mu$ m image from Barmby et al. (2006) from the V-band model image.

## 2.4 Flux calibration

**Table 2.4:** Constants used for the flux calibration

---



---

$h = 6.626 \cdot 10^{-27}$ [erg s], Planck constant
$c = 2.998 \cdot 10^{10}$ [cm/s], speed of light
$A_{fiber} = \pi \cdot 1.6^2$ arcsec <sup>2</sup> = 8.0 arcsec <sup>2</sup> , area of one fiber on sky
$A_{eff} = \pi \cdot \left[ \left( \frac{270}{2} \right)^2 - \left( \frac{43}{2} \right)^2 \right]$ cm <sup>2</sup> = 55803 cm <sup>2</sup> ,
effective area of the telescope, area of main mirror minus area of secondary mirror
$gain = 1/1.61$ , instrumental gain of VIRUS-W [ $\frac{N_e}{ADU}$ ]
$cdelt_\lambda = 0.172$ , wavelength step for the linearly extracted spectra
$cdelt_{\ln\lambda} = 3.34 \cdot 10^{-5}$ , wavelength step for the logarithmically extracted spectra
$\lambda_{eff} = 5448$ Å, effective wavelength of the V-band filter (Bessell, 2005)
$\Delta_{eff} = 840$ Å, effective bandwidth of the V-band filter (Bessell, 2005)

---



---

We calibrate the flux of the measured spectra, which is a multi-step process. First, we convert the flux at every pixel  $i$  from analog-to-digital-units (ADUs) per pixel as given in the raw spectra to physical units [ $\frac{erg}{s \text{ cm}^2 \text{ \AA}}$ ]. The constants used for the calculations are tabulated in table 2.4. The reduced spectra are given in ADUs per pixel, so we now have to calculate “backwards” to get the actual photon energy. First, multiplying the ADUs with the gain gives the number of electrons.

$$f \left[ \frac{N_{electrons}}{pix} \right] = f \left[ \frac{ADU}{pix} \right] \cdot gain \quad (2.12)$$

Assuming that the number of electrons is the same as the number of photons (i.e. photon to electron conversion of 1), we have to multiply the number of photons with the energy per photon to get the energy in erg.

$$f \left[ \frac{erg}{pix} \right] = f \left[ \frac{ADU}{pix} \right] \cdot gain \cdot \frac{h \cdot c}{\lambda} \quad (2.13)$$

Because of the absorption in the atmosphere, the energy of photons arriving at the telescope has been diminished by the factor  $a = 10^{-0.4 \cdot AM \cdot X}$ , where  $AM$  is the airmass of the observation and  $X$  the absorption magnitude. In order to get the unabsorbed flux, we have to divide by  $a$ . With this, the equation becomes:

$$f \left[ \frac{erg}{pix} \right] = f \left[ \frac{ADU}{pix} \right] \cdot \frac{gain \cdot h \cdot c \cdot 10^{0.4 \cdot AM \cdot X}}{\lambda} \quad (2.14)$$

To calculate the energy per unit area, this is accomplished by dividing the incoming flux by the effective area of the telescope.

$$f \left[ \frac{erg}{\text{cm}^2 \text{ pix}} \right] = f \left[ \frac{ADU}{pix} \right] \cdot \frac{gain \cdot h \cdot c \cdot 10^{0.4 \cdot AM \cdot X}}{\lambda \cdot A_{eff}} \quad (2.15)$$

We want to obtain the energy per unit time, so we have to divide by the exposure time  $t_{exp}$ .

$$f \left[ \frac{\text{erg}}{s \text{ cm}^2 \text{ pix}} \right] = f \left[ \frac{ADU}{\text{pix}} \right] \cdot \frac{\text{gain} \cdot h \cdot c \cdot 10^{0.4 \cdot AM \cdot X}}{\lambda \cdot A_{eff} \cdot t_{exp}} \quad (2.16)$$

We also need the energy not per pixel but per Angstrom. For this, we have to divide by the number of Angstroms per pixel, which is the linear wavelength step  $cdelt_\lambda$ .

$$f \left[ \frac{\text{counts}}{\text{\AA}} \right] = f \left[ \frac{\text{counts}}{\text{pix}} \right] \cdot \frac{1}{\text{\AA}/\text{pix}} = f \left[ \frac{\text{counts}}{\text{pix}} \right] \cdot \frac{1}{cdelt_\lambda} \quad (2.17)$$

$$f \left[ \frac{\text{erg}}{s \text{ cm}^2 \text{ pix}} \right] = f \left[ \frac{ADU}{\text{pix}} \right] \cdot \frac{\text{gain} \cdot h \cdot c \cdot 10^{0.4 \cdot AM \cdot X}}{\lambda \cdot A_{eff} \cdot t_{exp} \cdot cdelt_\lambda} \quad (2.18)$$

The throughput of the instrument  $t(\lambda)$  diminishes the infalling photon flux.

$$f_{after} = f_{before} \cdot t(\lambda) \quad (2.19)$$

We want to get the infalling photon flux:

$$f_{before} = \frac{f_{after}}{t(\lambda)} \quad (2.20)$$

With this, the flux becomes:

$$f \left[ \frac{\text{erg}}{s \text{ cm}^2 \text{\AA}} \right] = f \left[ \frac{ADU}{\text{pix}} \right] \frac{\text{gain} \cdot h \cdot c \cdot 10^{0.4 \cdot AM \cdot X}}{\lambda \cdot A_{eff} \cdot t_{exp} \cdot cdelt_{\ln \lambda} \cdot t(\lambda)} \quad (2.21)$$

The way this is implemented in our case is that the instrumental throughput  $t(\lambda)$  is also multiplied with the atmospheric extinction, resulting in  $T(\lambda)$ .

$$T(\lambda) = 10^{-0.4 \cdot AM \cdot X} \cdot t(\lambda) \quad (2.22)$$

The full equation is then:

$$f \left[ \frac{\text{erg}}{s \text{ cm}^2 \text{ pix}} \right] = f \left[ \frac{ADU}{\text{pix}} \right] \cdot \frac{\text{gain} \cdot h \cdot c}{\lambda \cdot A_{eff} \cdot t_{exp} \cdot cdelt_\lambda \cdot T(\lambda)} \quad (2.23)$$

To get the flux also per arcsec<sup>2</sup>, you have to divide by  $A_{fiber}$ . The relative area of the fiber does not change in our case, because when binning together several fibers, the mean flux is used, so the effective area of a binned spectrum does not change.

$$f \left[ \frac{\text{erg}}{s \text{ cm}^2 \text{\AA} \text{ arcsec}^2} \right] = f \left[ \frac{ADU}{\text{pix}} \right] \frac{\text{gain} \cdot h \cdot c}{\lambda \cdot A_{eff} \cdot A_{fiber} \cdot t_{exp} \cdot cdelt_\lambda \cdot T(\lambda)} \quad (2.24)$$

For logarithmically binned spectra, the wavelength step is a logarithmic wavelength step, which is related to the real wavelength step by:

$$cdelt_\lambda = \lambda \cdot cdelt_{\ln \lambda} \quad (2.25)$$

In that case, the final energy becomes:

$$f \left[ \frac{\text{erg}}{\text{s cm}^2 \text{\AA}} \right] = f \left[ \frac{\text{ADU}}{\text{pix}} \right] \cdot \frac{\text{gain} \cdot h \cdot c}{\lambda \cdot A_{\text{eff}} \cdot t_{\text{exp}} \cdot \lambda \cdot c \text{delt}_{\ln \lambda} \cdot T} \quad (2.26)$$

When converting flat fielded logarithmically extracted data to flux, there is a special complication because the flat fielding also linearizes the spectrum, This can be explained in the following way: Evenly spaced pixels in log-space are unevenly spaced in linear space, the pixel size follows the relation:

$$d \ln(x) = \frac{1}{x} dx \quad (2.27)$$

The total flux is preserved when the flux is recalculated for the logarithmic scale.

$$f_x dx = f_{\ln x} d \ln(x) = f_{\ln x} \frac{1}{x} dx \quad (2.28)$$

During the flatfielding, the logarithmically spaced object spectrum is divided by the likewise logarithmically spaced flatfield spectrum.

$$\frac{f_{\ln x,1}}{f_{\ln x,2}} = \frac{f_{x,1} \cdot x_2}{f_{x,2} \cdot x_1} \quad (2.29)$$

$x_1$  and  $x_2$  are the same at every position for the two spectra, so they cancel out. The final ratio is then:

$$\frac{f_{\ln x,1}}{f_{\ln x,2}} = \frac{f_{x,1}}{f_{x,2}} \quad (2.30)$$

This means, that in our case, we have to treat the spectra as if they were linearly extracted, using equation 2.24.

For our observations, the throughput  $t(\lambda)$  for each night is determined by observing a photometric standard star each night, listed in table A.1. The observed spectra are compared with spectra from the literature (Oke, 1990; Le Borgne et al., 2003) to get the throughput for the particular observation night as a function of wavelength. An example for the calculation of the throughput is shown in figure 2.26 for the photometric standard star Feige 110. In our implementation, we apply the flux calibration after binning the spectra together. Since spectra from different observation dates are binned together, we calculate for each bin a mean throughput  $T(\lambda)$ . Since the airmass  $AM_i$  and the extinction  $X_i$  are also properties of the individual observations  $i$ , we take care of them in this step as well. For a bin built from  $N$  fibers  $i$ , the mean throughput is then:

$$T_{\text{bin}}(\lambda) = \frac{1}{N} \sum_i t_i(\lambda) \cdot 10^{-0.4 \cdot AM_i \cdot X_i} \quad (2.31)$$

This is then substituted into equation 2.24.

We also correct for differences in observing conditions between the different observations by comparing the integrated flux  $f_{\text{tot}}$  in one spectrum to the flux  $f_V$

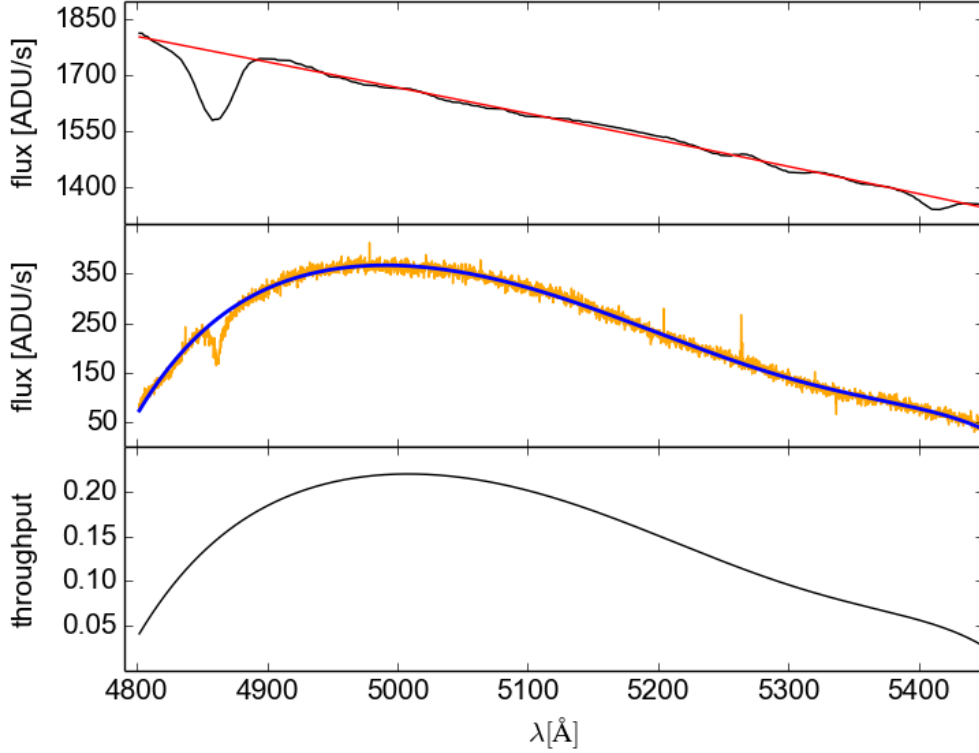


**Figure 2.26:** Example for the calculation of the throughput for an observation of the photometric standard star Feige 110. Top panel: Spectrum (black) and best fit to the spectrum (red) from Oke (1990) converted to ADU/s with the routine described in Müller (2014). Middle panel: Spectrum measured with VIRUS-W (orange) and best fit (blue). Bottom panel: The throughput obtained by dividing the best fit in the top panel by the best fit in the middle panel.

of the photometric model image from section 2.3 at the position of the spectrum.  $f_{tot}$  is calculated according to equation 2.33.

$$f_{tot} \left[ \frac{\text{erg}}{\text{s cm}^2 \text{ arcsec}^2} \right] = \int f \left[ \frac{\text{erg}}{\text{s cm}^2 \text{ \AA arcsec}^2} \right] d\lambda \quad (2.32)$$

$$= \sum f_i \left[ \frac{\text{erg}}{\text{s cm}^2 \text{ \AA arcsec}^2} \right] \cdot c\text{delt}_\lambda [\text{\AA}] \quad (2.33)$$

The flux in the model image is given in V-band magnitudes in the Vega system. These first have to be converted to AB magnitudes (Frei & Gunn, 1994):

$$V_{AB} = V_{Vega} - 0.044 \quad (2.34)$$

To convert the AB magnitudes into fluxes, the following equation by Oke & Gunn (1983) needs to be applied:

$$f_V \left[ \frac{\text{erg}}{\text{s cm}^2 \text{ arcsec}^2} \right] = \Delta\lambda_V \cdot \frac{c [\text{cm/s}]}{\lambda_{eff}^2 [\text{\AA}]} \cdot 10^{-0.4\mu} \cdot 10^{-0.4 \cdot 48.6} \cdot 10^8 \quad (2.35)$$

The integration over the shape of the V-band filter is replaced by multiplying with the bandwidth  $\Delta\lambda_V = 840 \text{ \AA}$ .  $\lambda_{eff}$  is the effective wavelength, which is for the V-band  $5448 \text{ \AA}$  (Bessell, 2005).  $f_{tot}$  and  $f_V$  are then divided by each other to get the correction factor  $c_{corr}$ .

$$c_{corr} = \frac{f_{tot}}{f_V} \quad (2.36)$$

To get the normalized result, the flux  $f(\lambda)$  of a spectrum has to be divided by  $c_{corr}$ , leading to the final equation 2.37:

$$f \left[ \frac{\text{erg}}{\text{s cm}^2 \text{ \AA arcsec}^2} \right] = f \left[ \frac{ADU}{pix} \right] \frac{\text{gain} \cdot h \cdot c}{\lambda \cdot A_{eff} \cdot A_{fiber} \cdot t_{exp} \cdot cdelt_\lambda \cdot T(\lambda) \cdot c_{corr}} \quad (2.37)$$

The V-band magnitudes converted to fluxes with equation 2.35 are plotted in figure 2.27, the integrated fluxes for each spectrum are plotted in figure 2.28 and the correction factors calculated with equation 2.36 in figure 2.29. To test if the flux calibration gives correct results, the fluxes corrected with equation 2.37 are integrated to get  $f_{ci}$  (figure 2.30), which is then compared to  $f_V$ . In figure 2.30,  $f_V/f_{ci}$  is plotted, it is  $\approx 1$  for the whole dataset, with small deviations coming from the integration process.

Kapala et al. (2015) observe five pointings in the outer regions of M31 with the PMAS instrument (Roth et al., 2005; Kelz et al., 2006). Their innermost pointing overlaps with our offset outermost pointing in the northwest. The relative positions can be seen in figure 2.32. In figure 2.33, we compare the spectrum of the PMAS pointing, which was independently flux calibrated and provided to us by Maria Kapala (private communication), with the flux calibrated VIRUS-W spectrum. Our data are higher by a factor of 2.4. This discrepancy can be explained by the fact that our pointing lies in a particularly dark region of M31, see the blue rectangle in figure 2.32. Comparing the brightness in the dark region with the surrounding bright regions, we get a mean flux difference of a factor of about 2.5. Our model image does not take the dark region into account, so we overcorrect our spectrum by this factor, which explains the discrepancy between our data and the one from PMAS.

In our implementation of the flux calibration, we apply the flux correction after GANDALF has already fitted the kinematics and the gas amplitudes. Therefore, we only need to correct the values for the amplitude  $A$  and the flux  $f$  that are given out. GANDALF fits the gas lines as the following Gaussians, which are not normalized:

$$G(v) = A \cdot \exp\left(-\frac{(v - v_0)^2}{2\sigma^2}\right) \quad (2.38)$$

To get the flux, we have to integrate over the line, which GANDALF also does internally. GANDALF uses the following equation for the redshift:

$$\lambda = \lambda_0 \exp(v/c) \quad (2.39)$$

This results in:

$$\frac{d\lambda}{dv} = \lambda_0 \exp\left(\frac{v}{c}\right) \frac{1}{c} \quad (2.40)$$

In order to get the correct flux, we have to integrate over equation 2.38 multiplied with  $\frac{d\lambda}{dv}$ :

$$f \left[ \frac{\text{erg}}{\text{s cm}^2} \right] = \int_{-\infty}^{\infty} A \left[ \frac{\text{erg}}{\text{s cm}^2 \text{Å}} \right] \exp\left(-\frac{(v - v_0)^2}{2\sigma^2}\right) dv \frac{d\lambda}{dv} \quad (2.41)$$

$$= A\sqrt{2\pi}\sigma \frac{d\lambda}{dv} \left[ \frac{\text{erg km}}{\text{s s cm}^2 \text{Å}} \right] \quad (2.42)$$

$$= A\sqrt{2\pi}\sigma \frac{\lambda_0}{c} \exp\left(\frac{v}{c}\right) \left[ \frac{\text{erg}}{\text{s cm}^2} \right] \quad (2.43)$$

As an example, the amplitude of  $H\beta$  is corrected in the following way for a random spectrum. First, the position of the  $H\beta$ -line of that spectrum is calculated from the velocity.

$$\lambda_{H\beta} = 4861 \cdot \left(1 + \frac{v}{c}\right) \quad (2.44)$$

This is then put into equation 2.37, without dividing by the fiber area:

$$A_{H\beta,corr} \left[ \frac{\text{erg}}{\text{s cm}^2 \text{Å}} \right] = A_{H\beta} \cdot \frac{\text{gain} \cdot h \cdot c}{\lambda_{H\beta} \cdot A_{eff} \cdot t_{exp} \cdot \text{cdelt}_\lambda \cdot T(\lambda_{H\beta}) \cdot c_{corr}} \quad (2.45)$$

The flux is then calculated by putting  $A_{H\beta,corr}$  into equation 2.43:

$$f_{H\beta,corr} \left[ \frac{\text{erg}}{\text{s cm}^2} \right] = \quad (2.46)$$

$$= A_{H\beta,corr} \left[ \frac{\text{erg}}{\text{s cm}^2 \text{Å}} \right] \cdot \sqrt{2\pi}\sigma_{H\beta} [\text{km/s}] \lambda_{H\beta} [\text{Å}] \frac{\exp\left(\frac{v_{H\beta} [\text{km/s}]}{c [\text{km/s}]}\right)}{c [\text{km/s}]} \quad (2.47)$$

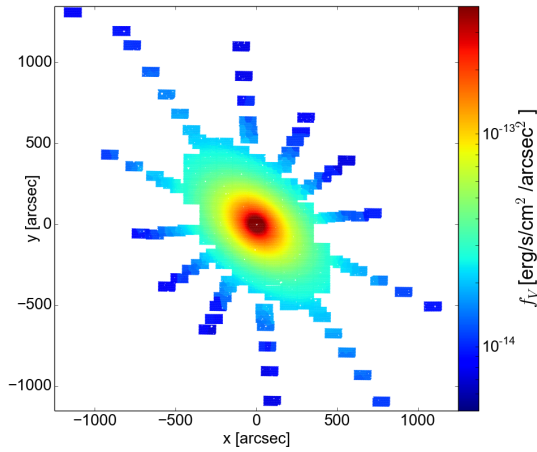


**Figure 2.27:** The model image converted to flux.

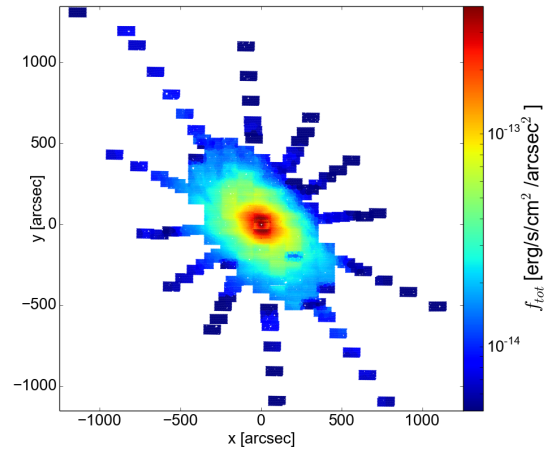


**Figure 2.28:** The integrated flux for each binned spectrum.

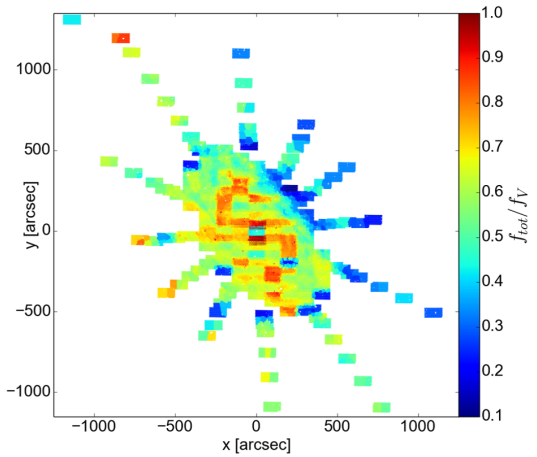


**Figure 2.29:** Map of the correction factors for each binned spectrum.

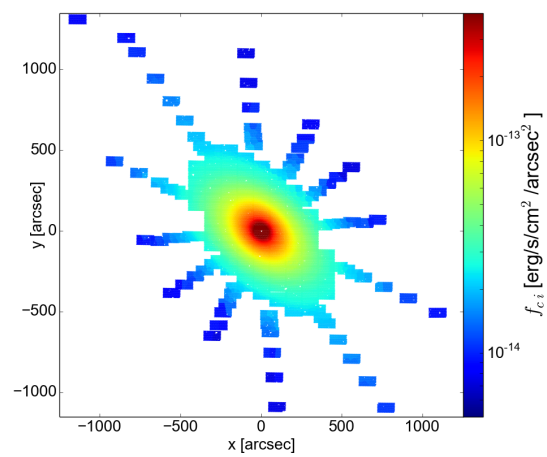


**Figure 2.30:** The integrated fluxes from the flux corrected spectra.

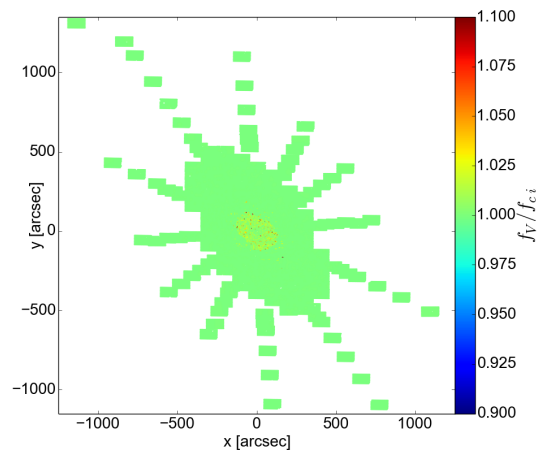


**Figure 2.31:** The model image fluxes from figure 2.27 divided by the integrated corrected fluxes from figure 2.30.

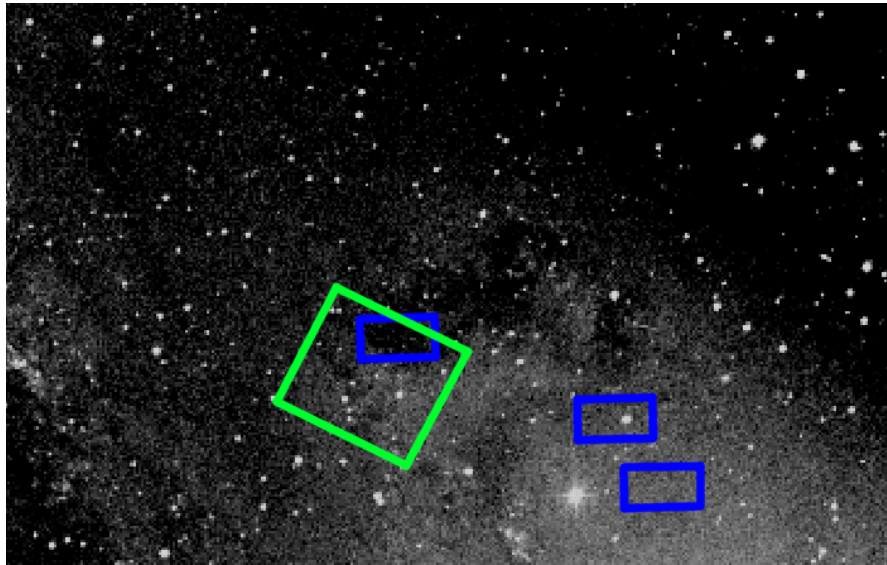


**Figure 2.32:** Position of the PMAS pointing (green) to the outermost VIRUS-W pointings in the northwest (blue).

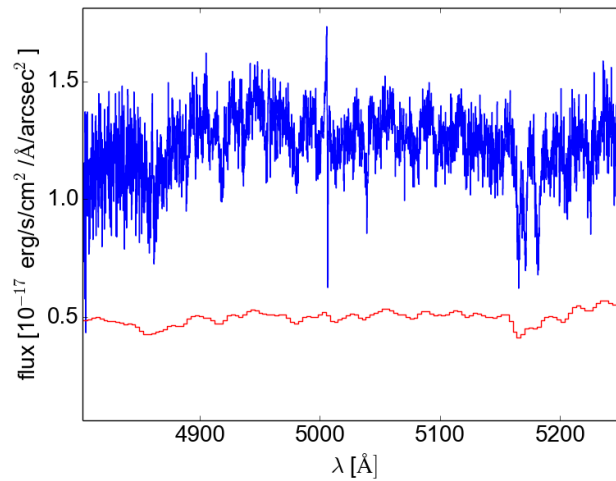


**Figure 2.33:** Comparison of PMAS spectrum by [Kapala et al. \(2015\)](#) (red) to spectrum from GANDALF to VIRUS-W data (blue).



# Chapter 3

## Bar signatures in the stellar kinematics

### 3.1 Description of the measured stellar kinematics

In this chapter, the stellar kinematics measured with GANDALF is presented. The stellar velocity map is plotted in figure 3.1, the heliocentric velocity of M31 ( $v_{sys} = -300$  km/s; de Vaucouleurs et al., 1991) has been subtracted. A schematic view of M31 based on Henderson (1979) is plotted in figure 3.2, with the naming of the receding and approaching sides of M31 taken from the stellar velocity map in figure 3.1. Overall, the stellar velocity field is regular, rotation is clearly visible. The velocities increase strongest along the major axis, with the highest velocity in the bulge region being  $v_{bulge,max} = 136 \pm 4$  km s<sup>-1</sup> in the outermost bulge pointing in the receding side and the lowest being  $v_{bulge,min} = -157 \pm 4$  km s<sup>-1</sup> on the opposite side. The “bulge region” is the region of M31 where the bulge-to-total ratio of the model image from section 2.3 is larger than 0.5, compare figure 2.24. The absolute maximum of the velocities is reached with  $v_{max} = 208 \pm 3$  km s<sup>-1</sup> in the outermost major axis disk pointing in the receding side, and the lowest value of  $v_{min} = -193 \pm 2$  km s<sup>-1</sup> already reached in the middle disk pointing and then roughly remaining at that value. The median velocity error is  $dv = 3.8$  km s<sup>-1</sup>. There are several asymmetries, which become more pronounced if the velocity is plotted logarithmically, as shown in figure 3.3. We compare the velocities with the ones measured by S10. They observe M31 with a longslit spectrograph along 6 directions, the slit positions are plotted in figure 3.4. We make cuts through our own velocity maps along the slit directions of S10 and compare them with their data in figure 3.5. Our velocities agree within 5% with the ones by S10, except for the minor axis on the near side (positive radii in figure 3.5), where the deviation is about 30%.

The stellar velocity dispersion of M31 is plotted in figure 3.6.

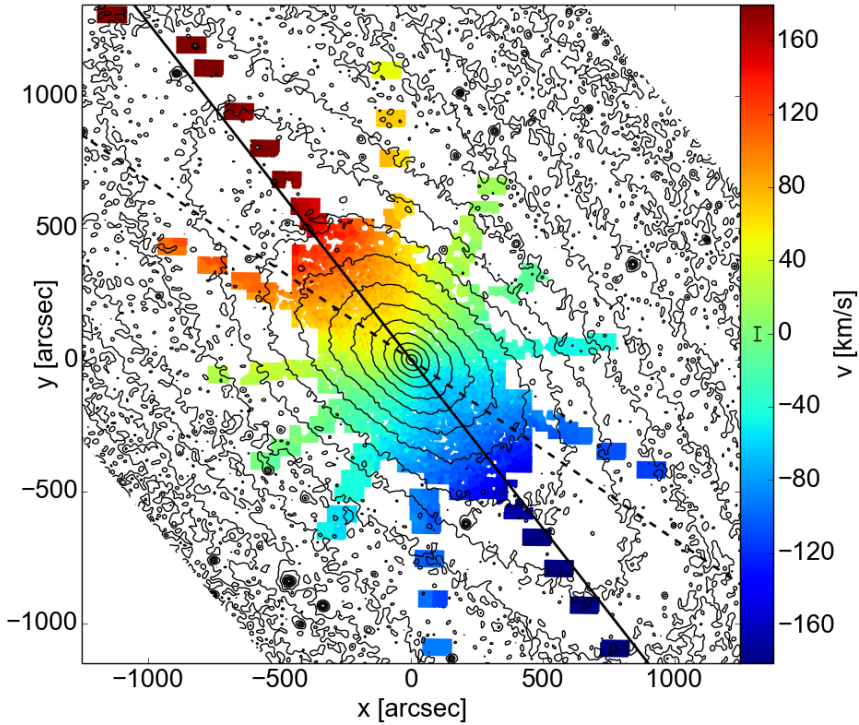


**Figure 3.1:** Map of the stellar velocity corrected for the systemic velocity of M31. The solid straight line is the disk major axis at  $PA_{disk}=38^\circ$ , the dashed straight line is the bar major axis at  $PA_{bar}=55.7^\circ$  from B16. The contours are the surface brightness of the IRAC  $3.6\mu\text{m}$  image by Barmby et al. (2006).

The maximum value is  $\sigma_{max} = 188 \pm 5 \text{ km s}^{-1}$ , located at a distance of  $46''$  from the center, the minimum value is  $\sigma_{min} = 55 \pm 4 \text{ km s}^{-1}$ , in the outermost northern disk pointing at  $x=-100''$  and  $y=1100''$ . The mean velocity dispersion for the whole dataset is  $\sigma_{mean} = 116 \pm 4 \text{ km s}^{-1}$ , considering only the bulge region it is  $\sigma_{mean,bulge}=137 \pm 4 \text{ km s}^{-1}$ , in the disk it is considerably lower with  $\sigma_{mean,disk}=103 \pm 4 \text{ km s}^{-1}$ . The disk velocity dispersion is still quite high, which is in agreement with what Fabricius et al. (2012b) have found for other disk galaxies. We compare our measured  $\sigma$  map with the data from S10 in figure 3.7. Overall, our data agree well with the measurements of S10, but we do not reproduce the central spike in  $\sigma$  that is caused by the supermassive black hole, because we lack resolution in the very central regions. The overall agreement is within 4%. The higher moments  $h3$  and  $h4$  of the LOSVD are also fitted by GANDALF. In figure 3.8, the third moment  $h3$  is plotted. To highlight the regions of correlation and anti-correlation, we also show a plot of  $sign(v \cdot h3)$  in figure 3.9. In the central  $50''$ ,  $h3$  has values of about  $\pm 0.05$ . Further out, the values drop to about  $\pm 0.02$ , before rising at the edges of the bulge region to  $\pm 0.08$ . In the bulge, the mean absolute value in the bulge region is  $|h3_{bulge}| = 0.026 \pm 0.022$ . In the disk, the values are higher, the mean absolute disk value is  $|h3_{disk}| = 0.035 \pm 0.026$ . Along the major axis, the values are highest, here, the mean absolute value is  $|h3_{major}|$

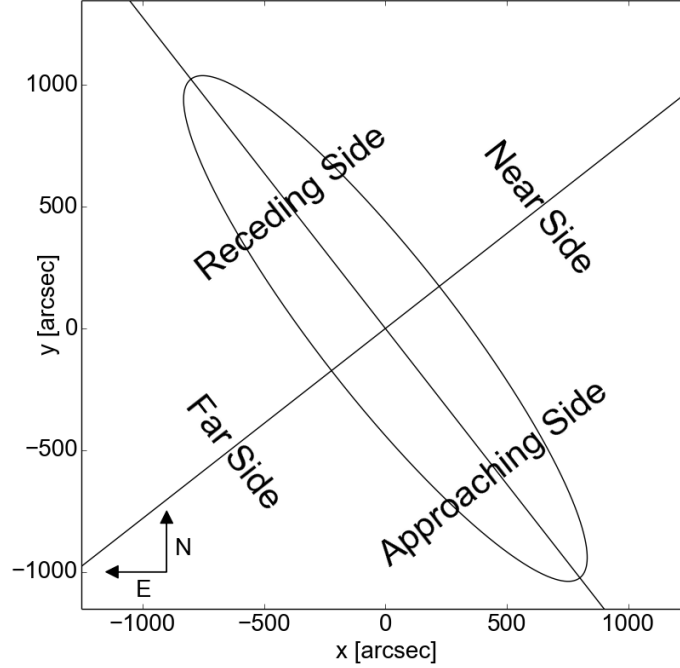


**Figure 3.2:** Schematic view of M31. A generic ellipse with ellipticity  $\epsilon = 0.78$  is plotted, this corresponds to an inclination angle of  $i = 77^\circ$ , the major axis has position angle  $PA = 38^\circ$ . The half of the galaxy to the west of the major axis is closer than the other side (Henderson, 1979).

$= 0.07 \pm 0.02$ . The maximum and minimum values of the whole map are also along the major axis, being  $h3_{max} = 0.14 \pm 0.02$  and  $h3_{min} = -0.16 \pm 0.02$ . Our measurements reproduce the longslit cuts by S10, the comparison is plotted in figure 3.10. The standard deviation of the difference between our values and the ones by S10 is 2%–2.7%, which agrees with the root mean square value of the error of the VIRUS-W values.

In figure 3.11, the Gauss-Hermite moment  $h4$  is plotted. The mean value over the whole dataset is  $|h4| = 0.02$ , with the minimum  $h4_{min} = -0.15$  and the maximum  $h4_{max} = 0.25$ . In the central  $100''$ , the mean value is  $h4_{central} = 0.009 \pm 0.02$  and the mean absolute value is  $|h4_{central}| = 0.02$ . Further out along the major axis, the values of  $h4$  become lower, in regions at radii  $r > 100''$  and  $r < 120''$  perpendicular to the major axis, the mean value is  $h4_{outer\ bulge} = -0.003$ . Along the minor axis, the values of  $h4$  are generally higher, in regions that have a distance to the major axis of more than  $120''$ , the mean value is  $|h4_{minor}| = 0.03$ . Along the major axis, the  $h4$  is higher in the northern half of the galaxy, having a mean value of  $h4_{major,north} = 0.04$ , in the southern part it is  $h4_{major,south} = -0.005$ . In figure 3.12, we compare our measurements to the values from S10. Again, we find good agreement, the standard deviation of the difference between our values and the ones by S10 is 2%, which agrees with the root mean square of the error of the VIRUS-W values.

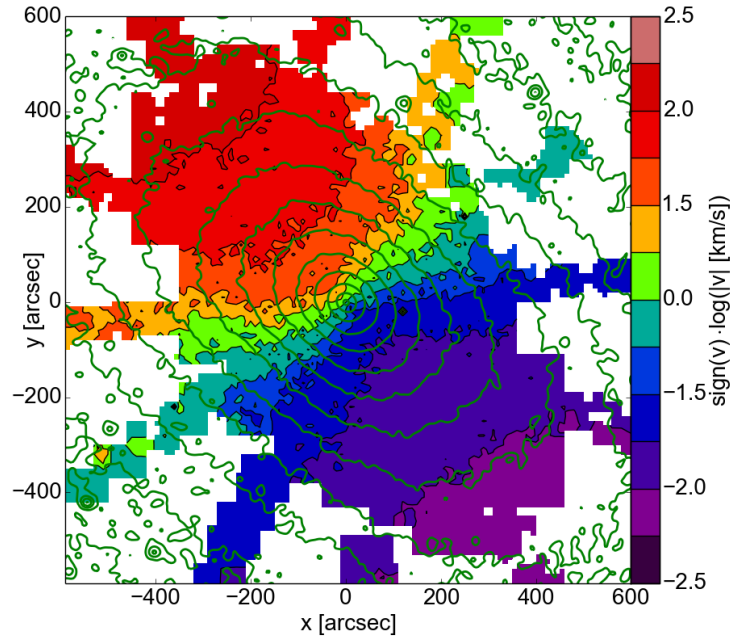


**Figure 3.3:** Plot of  $\text{sign}(v) \cdot \log(|v|)$ . The magenta contours are from the IRAC  $3.6\mu\text{m}$  image.

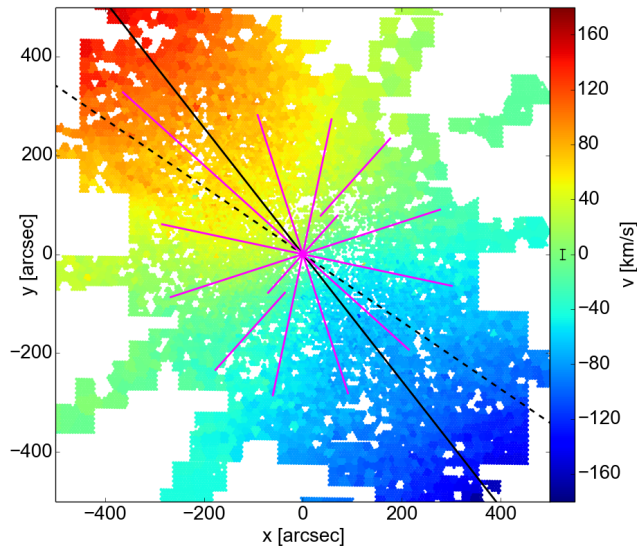


**Figure 3.4:** Velocity map with disk major axis (PA= $38^\circ$ , solid black line), the bar major axis (PA= $55.7^\circ$ , dashed black line) and the slit positions by S10 (magenta). They are PA= $48^\circ$  (the bulge major axis), PA= $78^\circ$ , PA= $108^\circ$ , PA= $138^\circ$  (the bulge minor axis), PA= $108^\circ$  and PA= $18^\circ$ , all angles measured east from north. The line in the colorbar is the median errorbar of the velocities.

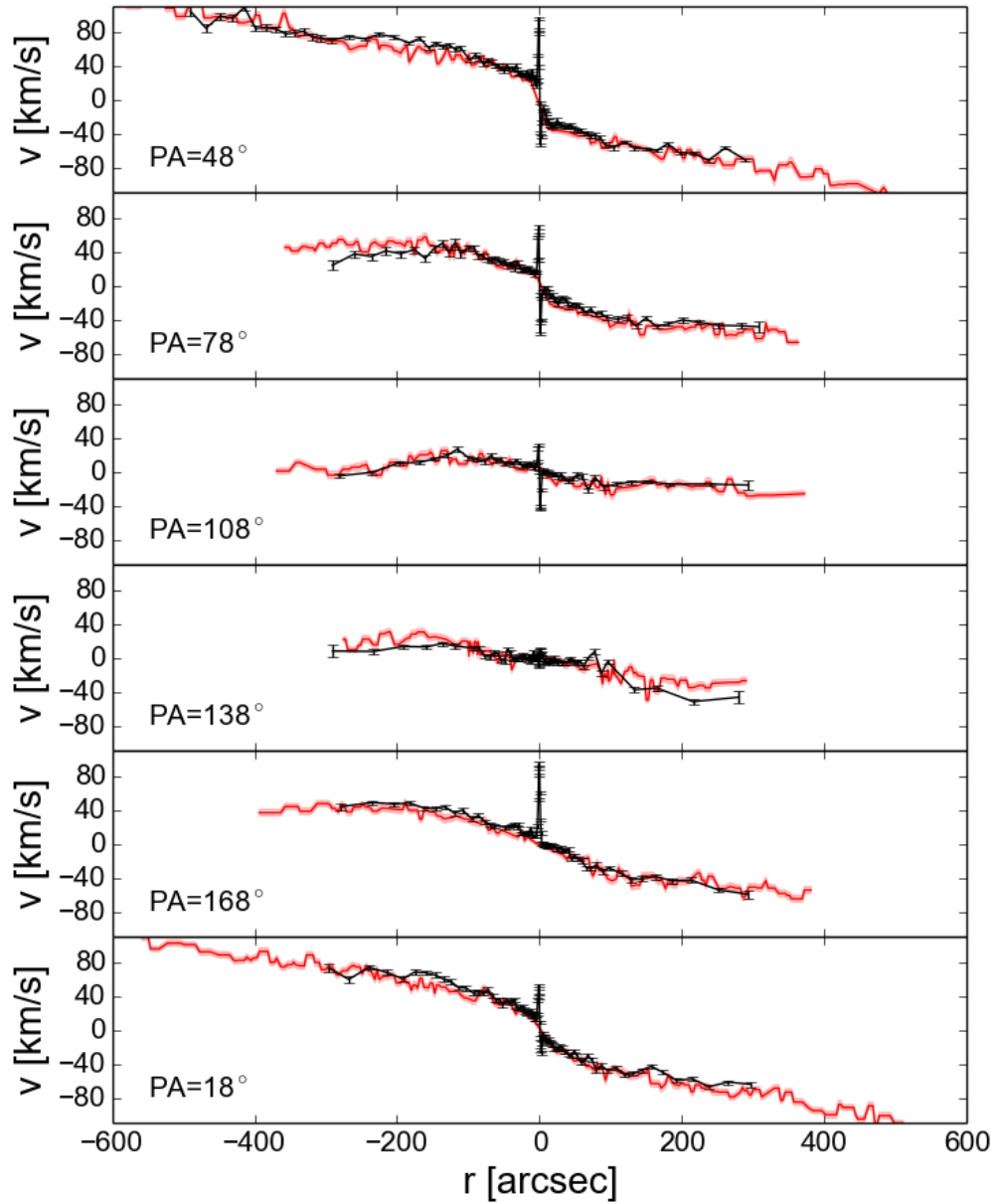


**Figure 3.5:** Comparison of our velocities with the ones from S10. Black are the velocities measured by S10, red are cuts through our velocity maps along the same directions.

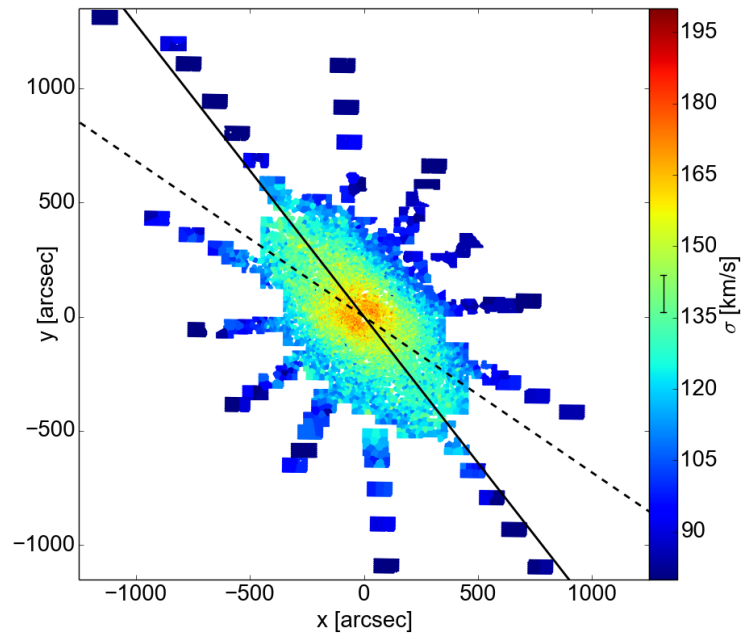


**Figure 3.6:** Stellar velocity dispersion map with the disk major axis with  $PA_{disk}=38^\circ$  (solid line) and the bar major axis with  $PA_{bar}=55.7^\circ$ . The line in the colorbar is the median errorbar of the velocity dispersion.

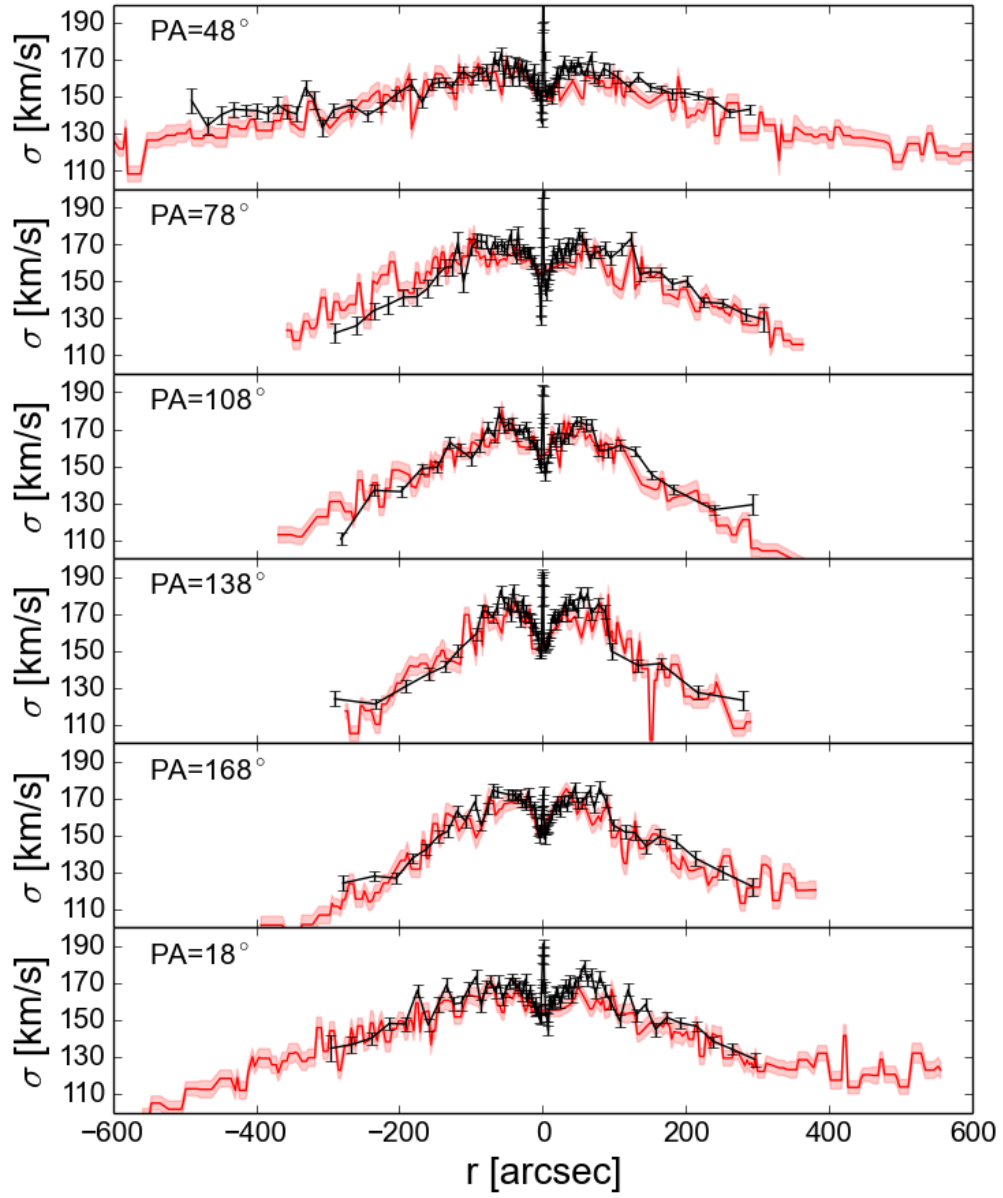


**Figure 3.7:** Comparison of our velocity dispersions with the ones from S10. Black are the values measured by S10, red are cuts through our velocity dispersion maps along the same directions.

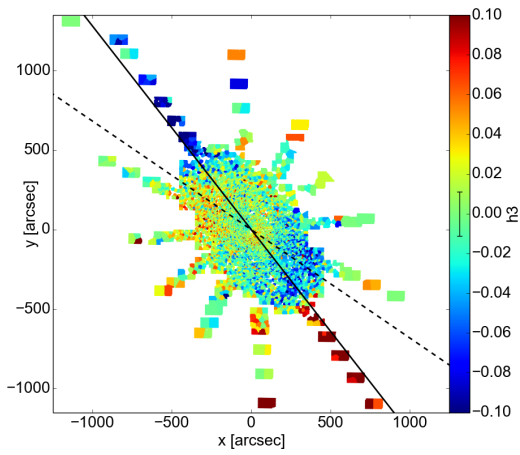


**Figure 3.8:** Map of  $h_3$ , the third moment of the Gauss-Hermite series. The lines are analogous to figure 3.6.

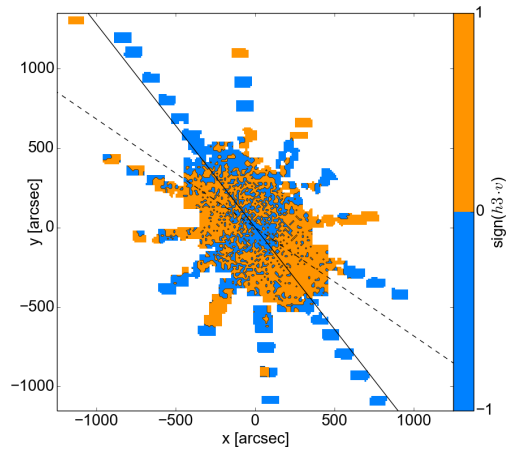


**Figure 3.9:** Correlation between the stellar velocity and  $h_3$ . Plotted is  $\text{sign}(h_3 \cdot v)$ , with the disk and bar major axis from figure 3.6.

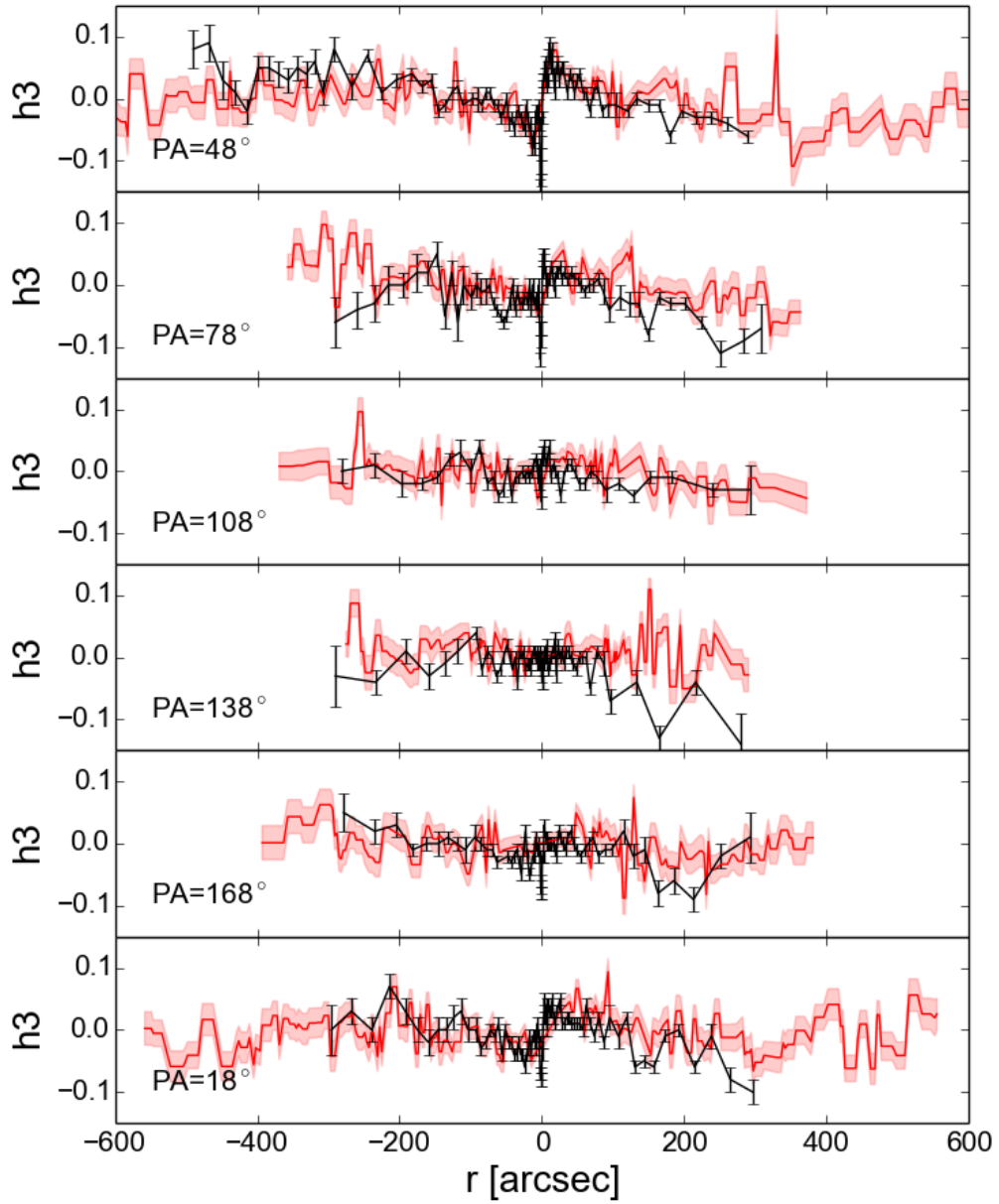


**Figure 3.10:** Comparison of the measured  $h3$  values with the ones from S10. Black are the values measured by S10, red are cuts through our maps along the same directions.

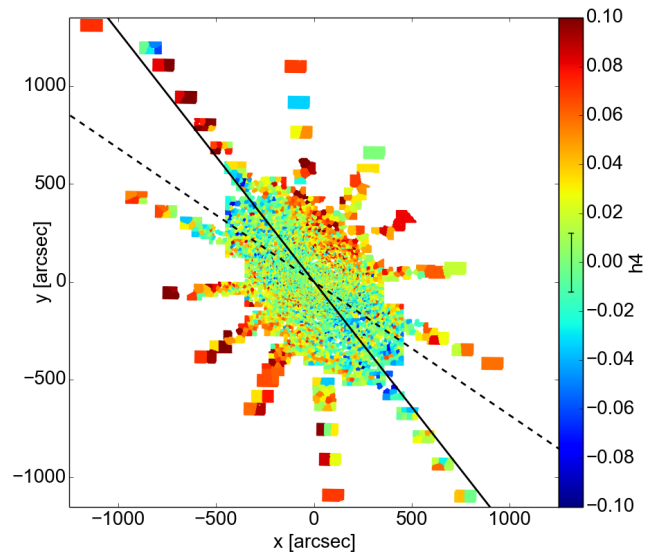


**Figure 3.11:** Map of  $h_4$ , the fourth moment in the Gauss-Hermite series. The lines are analogous to figure 3.6.

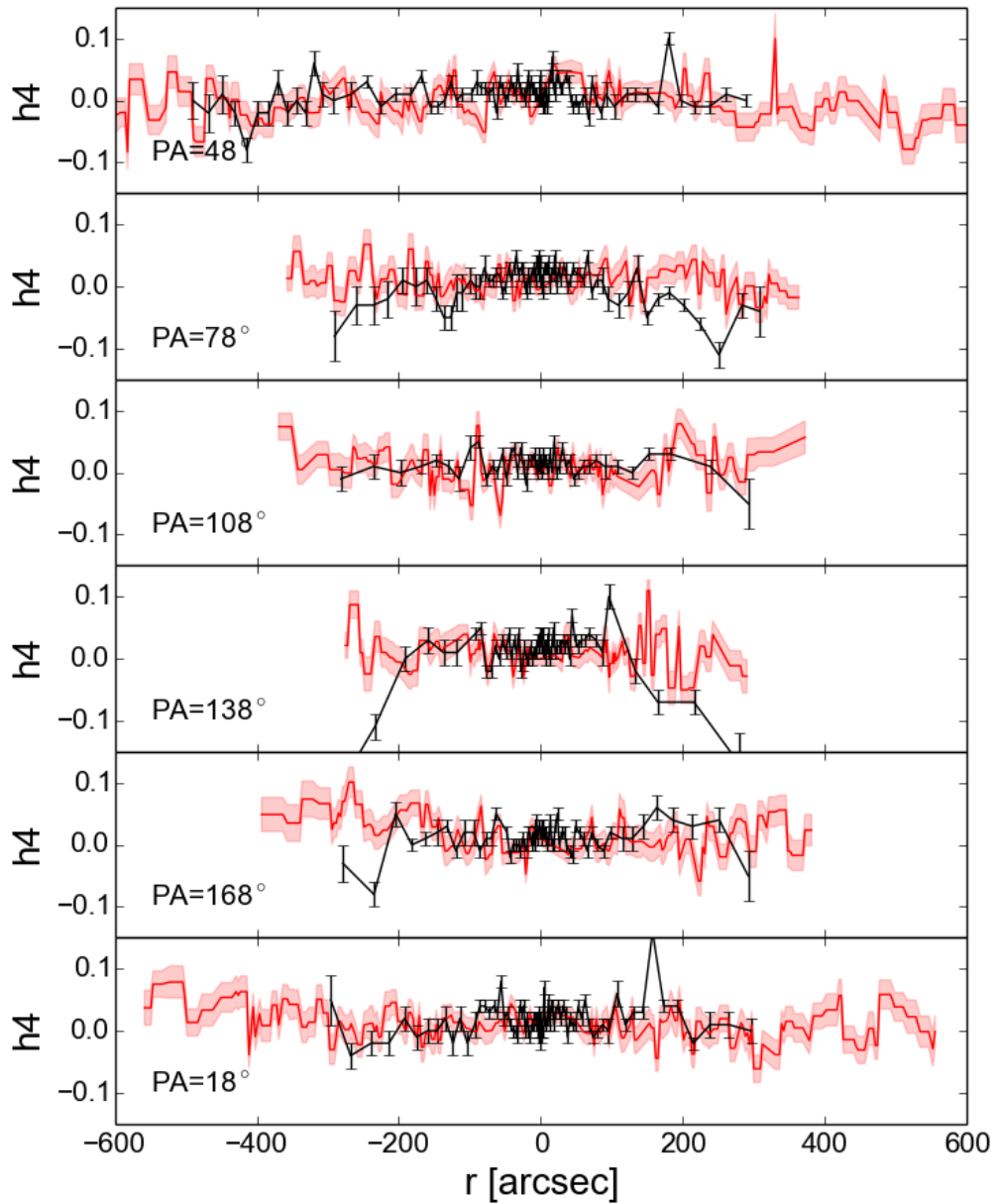


**Figure 3.12:** Comparison of the measured  $h_4$  values with the ones from S10. Black are the values measured by S10, red are cuts through maps along the same directions.

## 3.2 Bar signatures in the kinematics

A bar leaves certain signatures in the kinematics of the stars. Bureau & Athanassoula (2005) modeled several bars, with different strengths and viewing angles. Stark & Binney (1994), Athanassoula & Beaton (2006) and B16 all claim that the bar in M31 is neither viewed end-on nor side-on, but instead at an intermediate angle. The kinematic profiles measured by Bureau & Athanassoula (2005) for a strong bar model viewed at an intermediate angle of  $45^\circ$  are plotted in figure 3.13. The special signatures of a bar are a "double-hump" structure in the velocity, a plateau at intermediate radii and a drop in the center in the velocity dispersion and minima in the higher moments  $h_3$  and  $h_4$ . These were theoretically predicted by Bureau & Athanassoula (2005) and measured on several barred galaxies by Chung & Bureau (2004). In figure 3.14, the equivalent plot with our

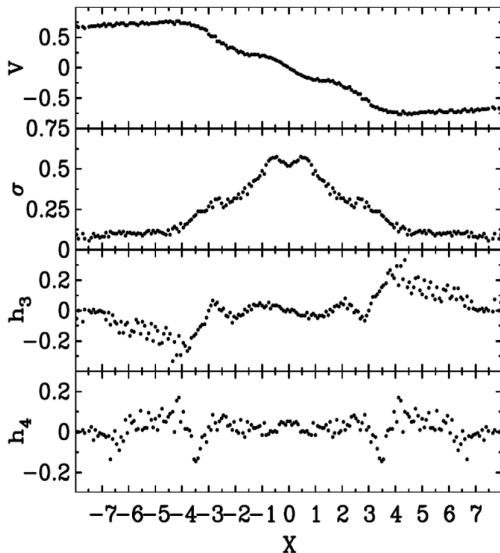


**Figure 3.13:** The stellar kinematics of a bar model by Bureau & Athanassoula (2005). The cuts are made along the disk major axis, with the bar at an intermediate angle of  $45^\circ$  to that axis.

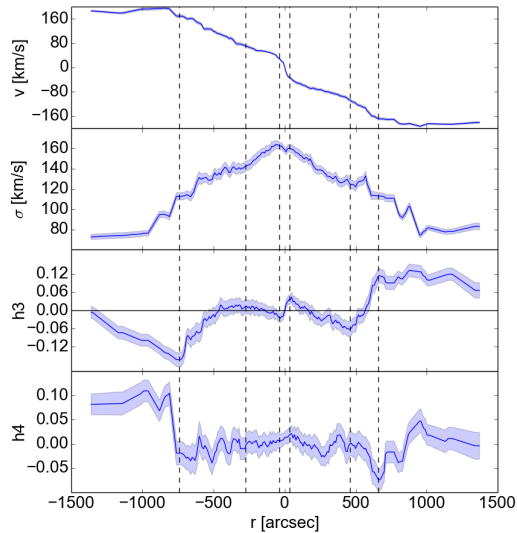


**Figure 3.14:** Cuts through the stellar kinematic maps from VIRUS-W along the disk major axis (PA= $38^\circ$ ). In the third panel, the horizontal line is  $h_3=0$ . The vertical dashed lines are the lines where  $h_3$  has a local maximum or minimum.

measured data is plotted. Our cuts show several of the features that are visible in the schematic view of figure 3.13, they are generally more pronounced for positive radii, which corresponds to the receding side of M31. The "double hump" can be seen, the absolute value of the velocity rises to  $70 \text{ km s}^{-1}$  at  $35''$ , before remaining relatively constant until  $350''$  on the left and  $460''$  on the right, before reaching  $160 \text{ km s}^{-1}$  at  $-750''$  on the left and at  $660''$  on the right. Such double-hump structures can be explained by the presence of a bar. The first "hump" is related to the orbits of the stars that are parallel to the bar. The radius at which the rotation curve becomes flat marks the beginning of an inner ring structure caused

by the bar (Bureau & Athanassoula, 2005). The overall structure becomes weaker if the bar is viewed more side-on (Bureau & Athanassoula, 2005). In the plot in figure 3.15, we compare our measurement to the model by B16, which models the bar with a length of  $r = 600''$  and the position angle  $\text{PA}_{\text{bar}} = 55.7^\circ$  projected on sky. Our data agree very well with the model.

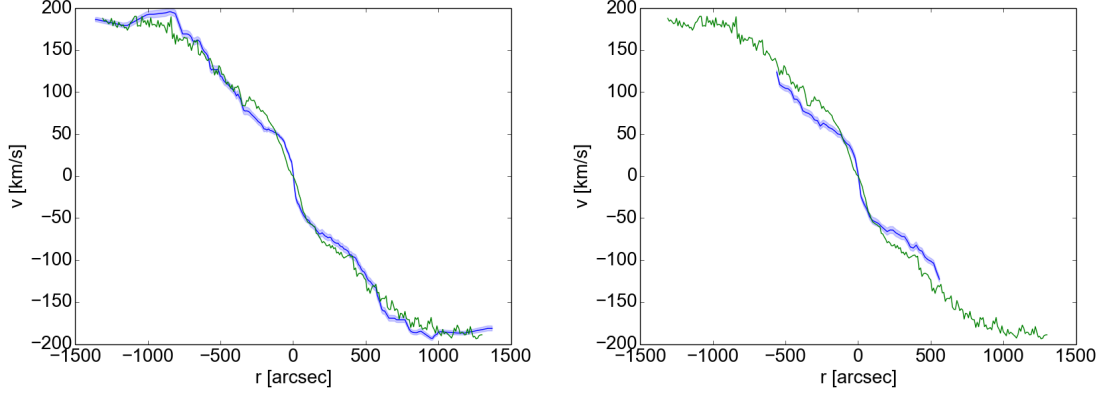


**Figure 3.15:** Cuts through the measured velocity map from figure 3.1 (blue) and the modeled velocity map by B16 (green), cut along the major axis of the disk ( $\text{PA}_{\text{disk}}=38^\circ$ ) on the left and along the bar model by B16 ( $\text{PA}_{\text{bar}}=55.7^\circ$ ) on the right.

The measured kinematic maps are fitted with the routine `kinemetry` (Krajinović et al., 2006) to get the kinematic position angle. `kinemetry` fits isovelocity contours to the velocity field, analogous to fitting isophotes on photometric images. The position angle found by `kinemetry` is compared to the photometric one from the ellipse fit described in section 2.3. The comparison is plotted in figure 3.16. The two angles are misaligned by  $10^\circ$  to  $20^\circ$ , with the kinematic position angle separating from the photometric one at about  $50''$ . The photometric PA then stays constant at  $48^\circ$ , which is why that value was determined as the bulge PA in S10. The kinematic PA deviates further and further from it, reaching the minimum value of  $32^\circ$ , which is lower than the disk PA ( $38^\circ$ ), at  $300''$ . S10 measured their data out to this radius, and in this inner region, our measurement agrees with theirs. Beyond that, the photometric PA has a maximum at  $52^\circ$  at  $435''$ , before it declines again and reaches the bulge PA at  $750''$ . The kinematic position angle stays roughly constant until  $600''$ , then rises slowly until reaching  $37^\circ$ , which is almost the disk PA, at  $800''$ . This means that the kinematics in this outer region trace the disk kinematics. Misalignments between kinematic and photometric position angles are a sign for triaxiality (Binney, 1985; Franx et al., 1991) and bars in disk galaxies (Falcón-Barroso et al., 2006). Barrera-Ballesteros et al. (2014) measure misalignments between photometric and kinematic position angles for 80 galaxies from the CALIFA survey. They find that the barred galaxies have slightly higher misalignments. In figure 3.17, the misalignment is shown as function of stellar mass of the galaxies. The values for M31 are higher than for the unbarred galaxies and are within the range of the barred ones.

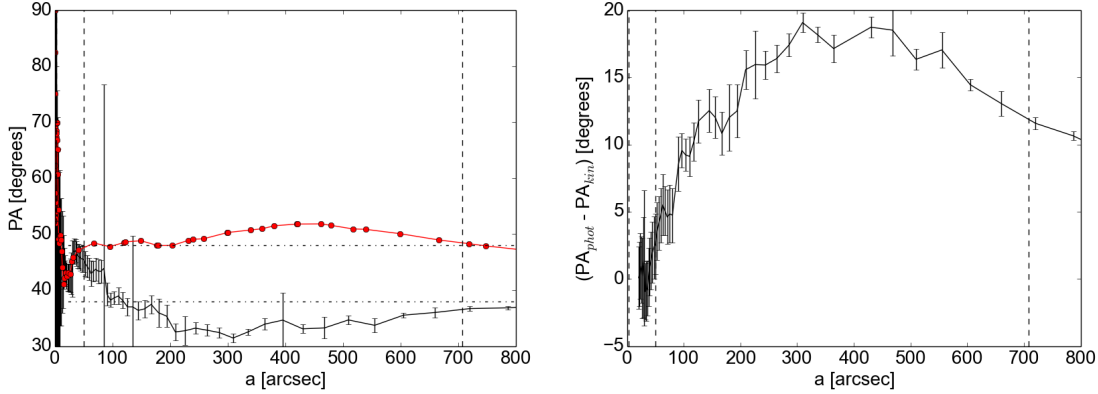


**Figure 3.16:** Left: Comparison between the photometric (red) and the kinematic (black) position angle as function of semimajor-axis. Right: The difference  $PA_{phot} - PA_{kin}$ . The photometric position angle is taken from the ellipse fit to the K-band image from figure 2.22, the kinematic one from the fit with `kinemetry` to the stellar velocity field from figure 3.1. The horizontal dash-dotted lines are the disk position angle at  $PA_{disk} = 38^\circ$  and the bulge position angle at  $PA_{bulge} = 48^\circ$ . The vertical lines denote the extent of the circular classical bulge and the boxy bulge from Beaton et al. (2007).

The cut along the disk major axis through the velocity dispersion map in figure 3.14, shows that  $\sigma$  has two off-centered maxima, with a slight drop of about  $8 \text{ km s}^{-1}$  in between. Bureau & Athanassoula (2005) claim that such minima can also be caused by the bar, because the orbits parallel to the bar become more circular and thus lower the dispersion. The bar model by Bureau & Athanassoula (2005) in figure 3.13 also has this central minimum in  $\sigma$ , however, it is much stronger than in the measurement. Further out,  $\sigma$  drops to  $140 \text{ km s}^{-1}$  at  $400''$ , before staying roughly constant out to  $600''$  and then dropping to  $80 \text{ km s}^{-1}$  at  $950''$ . These plateaus are also seen as signs for a bar.

In figure 3.18, cuts through the velocity dispersion map along the disk major axis and the bar major axis are plotted, compared to the profiles from the bar model by B16. The agreement along the disk major axis is not perfect along the disk major axis (left panel in 3.18), but it is good along the bar major axis (right panel in 3.18).

The  $h3$  profile in figure 3.14 shows that  $h3$  changes sign several times. The maxima and minima in the  $h3$  correspond to the points where the slope of the velocity profile changes, this corresponds to the behavior of the simulations by Bureau & Athanassoula (2005) and has also been observed in barred galaxies (Fisher, 1997; Chung & Bureau, 2004; Falc3n-Barroso et al., 2006; Ganda et al., 2006). In the outer regions,  $h3$  is anti-correlated to  $v$ , see also in figure 3.9, which is the expected behavior for disky structures in a galaxy (Binney & Tremaine, 1987; Bender et al., 1994; Fisher, 1997; Binney & Tremaine, 2008).

In the central  $30''$ ,  $h3$  is again anti-correlated to the velocity. This could mean that a disky structure is also present at the center, potentially explaining the slight drop in velocity dispersion. A decoupled core would show a similar behavior in  $h3$ , but this is not supported by the velocities. The radial extent of this central anti-

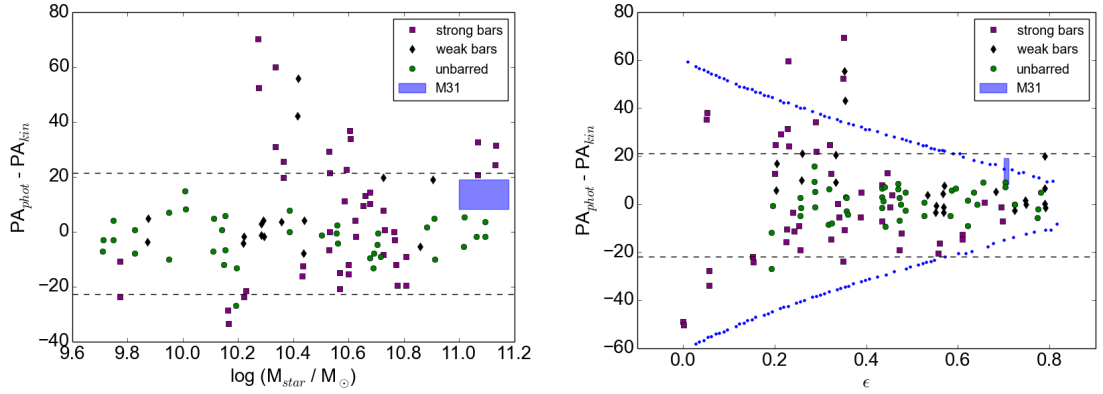


**Figure 3.17:** The mean kinematic misalignment of M31 compared to results from the CALIFA survey. The datapoints for strongly barred (purple), weakly barred (black) and unbarred galaxies are taken from Barrera-Ballesteros et al. (2014). The dashed lines denote the  $2\sigma$  dispersion of their sample. The blue rectangle represents M31, with the lower limit for the misalignment being the mean difference ( $8.31^\circ$ ) and the maximum being the largest kinematic misalignment in figure 3.16 ( $19.07^\circ$ ). The total stellar mass of M31 ( $10\text{--}15 \cdot 10^{10} M_\odot$ ) is taken from Tamm et al. (2012). The blue points in the plot with ellipticity display the projection effect of a bar that is  $60^\circ$  away from the disk in the plane of the galaxy. This is almost the same as what B16 measure in their model ( $55.7^\circ$ ).

correlation corresponds roughly to the rapidly rising part of the rotation curve, a behavior that is also seen in other disk galaxies (Chung & Bureau, 2004) and interpreted as a decoupled inner disk. In between the two anti-correlated regions,  $h3$  becomes correlated with the velocity, which is taken by Bureau & Athanassoula (2005) to be a sign for a bar. The correlation means that there are more stars rotating faster than the circular velocity in projection, which can only be achieved by elongated motions. However, the correlation does not necessarily have to be caused by a bar, it can also be caused by the superposition of an axisymmetric bulge component embedded in a rotating disk, depending on the bulge-to-disk ratio. If the bulge is brighter than the disk, the main velocity that is seen is mainly the bulge, with the disk creating a tail of high-velocity material (van der Marel & Franx, 1993; Bureau & Athanassoula, 2005).

In figure 3.19, cuts along disk and bar major axis through the  $h3$  maps are compared to corresponding cuts of the models by Blaña et al. (in prep.), who improve on the models by B16 by fitting the measured stellar kinematics with the made-to-measure code NMAGIC (de Lorenzi et al., 2007). The measured and modeled values agree well, except for the anti-correlation in the center, which is not reproduced by the model.

The  $h4$  profile in figure 3.14 is relatively constant, with the exception of a minimum at  $670''$ , where  $h4$  drops from 0 to  $-0.7$ . This minimum corresponds to the radius where  $h3$  reaches its maximum. On the opposite side, the drop in  $h4$  at  $-750''$  is not as pronounced. B/P bulges often show dips in the very center in  $h4$  (Debattista et al., 2005; Méndez-Abreu et al., 2008), however, this only applies

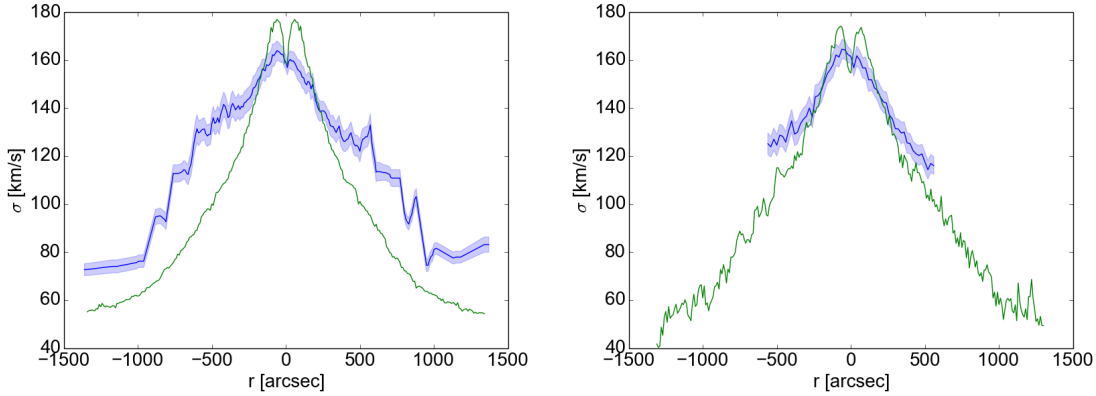


**Figure 3.18:** Cuts through the velocity dispersion map from figure 3.6 along the major axis of the disk ( $PA_{disk}=38^\circ$ ) on the left and along the suggested bar model by B16 ( $PA_{bar}=55.7^\circ$ ) on the right. The blue lines are the observations and the green lines the ones from the bar model by Blańa et al. (submitted).

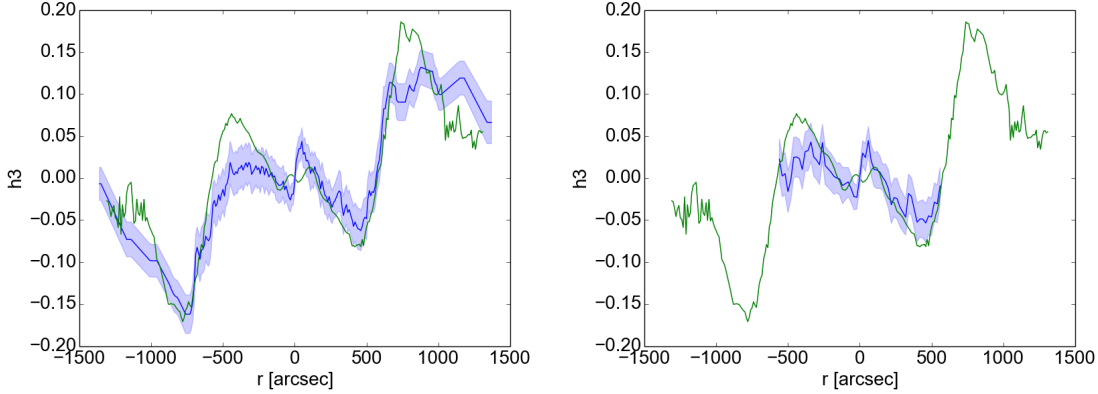


**Figure 3.19:** Cuts through the  $h3$  map from figure 3.8 along the major axis of the disk ( $PA_{disk}=38^\circ$ ) on the left and along the bar major axis ( $PA_{bar}=55.7^\circ$ ) by B16 ( $PA_{bar}=55.7^\circ$ ). The blue lines are the observations and the green lines the ones from the bar model by Blańa et al. (in prep.).

to low inclinations of  $i < 30^\circ$ . It is therefore not surprising that we do not see a drop in  $h4$  in M31. In figure 3.20, cuts along disk and bar major axis are again compared to cuts by Blańa et al. (in prep.). Our values are offset from the ones by Blańa et al. (in prep.), but they display similar features, like the minima at about  $700''$  and the subsequent increase further out. The models by Blańa et al. (in prep.) have not been finalized and for future iterations, the agreement will certainly improve.

In conclusion, the stellar kinematics we measure for M31 support the presence of a bar that is neither observed end-on nor side-on, but at an intermediate angle. This is corroborated by comparing the measured kinematics to the models by B16 and Blańa et al. (in prep.), which are constructed with such an intermediate bar.

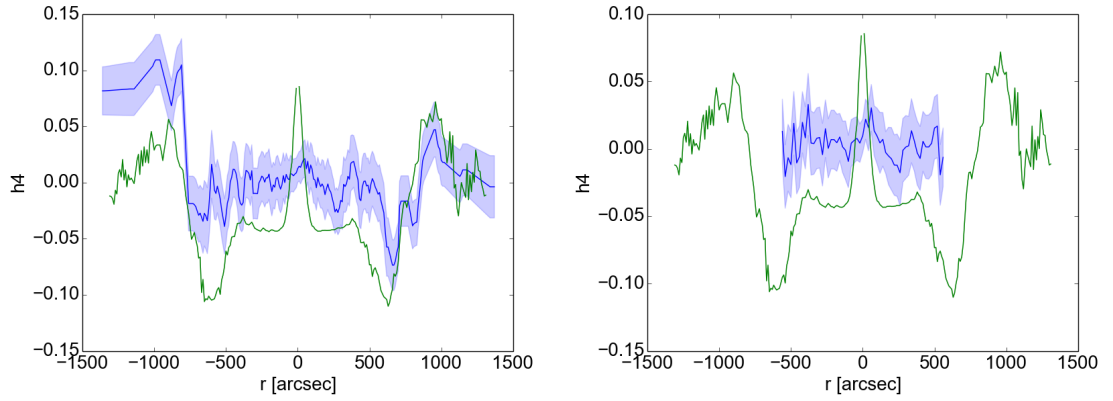


**Figure 3.20:** Cuts through the  $h4$  map from figure 3.11 along the major axis of the disk ( $PA_{disk}=38^\circ$ ) on the left and along the suggested bar model by B16 ( $PA_{bar}=55.7^\circ$ ). The blue lines are the observations and the green lines the ones from the bar model by Blaña et al. (in prep.).



# Chapter 4

## Bar signatures in the kinematics and morphology of the ionized gas

In this chapter, the kinematics of the ionized gas is presented. The motions of the gas are more complicated than the ones of the stars from chapter 3, which is usually seen in disk galaxies (e.g. Falc3n-Barroso et al. (2006); Ganda et al. (2006)), because contrary to the dissipationless stars, the gas can also lose energy through radiation. The dense gas traced by ground-state CO and HI transitions is most likely to have settled onto closed orbits via hydrodynamic interactions. Associated with this dense gas are regions of ionized gas (Stark & Binney, 1994), which is then seen in the optical emission lines.

### 4.1 Gas velocities

#### 4.1.1 Description

As mentioned in chapter 2, we see in about half of the investigated binned spectra two gas components, which we sort according to their velocities. The velocity map of the first component, which is the faster one of the two, is plotted in figure 4.1, the one of the second component in figure 4.2. The first gas component has a median absolute value of  $\overline{|v_{[OIII,1]}|} = 162 \pm 5 \text{ km s}^{-1}$ . The maximum value is  $v_{[OIII,1],max} = 294.7 \pm 4.5 \text{ km s}^{-1}$  at the coordinates  $(-220'', 281'')$ , at  $360''$  from the center along the disk major axis in the receding side. The minimum value is  $v_{[OIII,1],min} = -340 \pm 3.0 \text{ km s}^{-1}$  at the coordinates  $(25'', -100'')$ , which is at about  $100''$  south of the center in the approaching side. Since this is much closer than the maximum value, a general asymmetry becomes apparent. Apart from that, there is a spiral structure in the innermost  $100'' \times 100''$  and a large ‘‘S-shape’’ between the approaching and receding gas velocities.

For the second component, the median absolute value is significantly lower than for the first component, with  $\overline{|v_{[OIII,2]}|} = 73.2 \pm 5.5 \text{ km s}^{-1}$ . The maximum value is  $v_{[OIII,2],max} = 183.8 \pm 5.2 \text{ km s}^{-1}$  at the coordinates  $(-190'', 280'')$ , which is in the same region as the maximum for the first component. The minimum value is

$v_{[OIII,2],min} = -240.2 \pm 3.8 \text{ km s}^{-1}$ , at the coordinates  $(65'', -170'')$ , at  $182''$  from the center along the disk major axis in the receding side. This again corresponds to a region of low velocities in the first component. The overall shape of the velocity field for the second component is similar to the first, but an arm of approaching velocities is extending further into the region of receding velocities, while on the western edge of the bulge, an arm has velocities of about zero, this arm seems to be unconnected to the kinematics of the rest of this component.

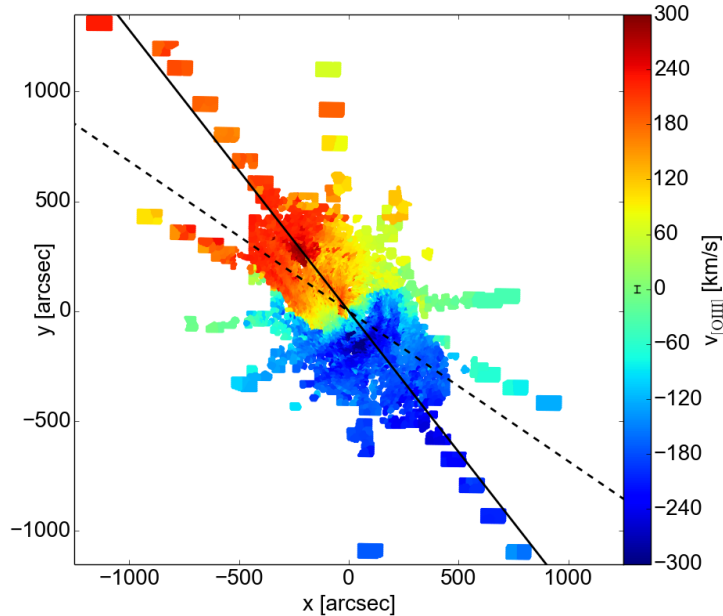


**Figure 4.1:** Velocity map of the first gas component, being the faster one of the two. The solid line is the disk major axis ( $PA_{disk}=38^\circ$ ) and the dashed line the bar major axis ( $PA_{bar}=55.7^\circ$ ). The line in the colorbar is the median error of the dataset.

The first component shows clear rotation to the very innermost radii, which is in contrast to the claims of Melchior & Combes (2011), who compile ionized gas measurements from Saglia et al. (2010) and del Burgo et al. (2000) and state that there is no rotation at all in the central  $40'' \times 40''$  and almost the whole dataset is blueshifted.

As with the stellar kinematics, we compare the gas kinematics to the data from S10. The comparison plot is shown in figure 4.3. Generally, the first component agrees with the values from S10. For large radii, the velocity from S10 often lies between both velocity components. This is somewhat expected, because S10 does not resolve the two components, so they measure a broader Gaussian, which incorporates both thin Gaussians from the two components. This broader Gaussian has of course a mean value that is in between the two thin ones, which is then adopted as the velocity.

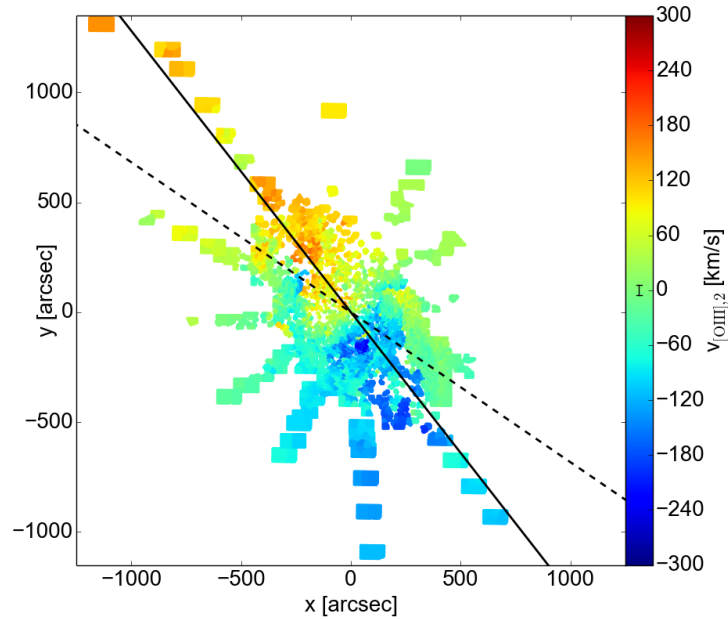


**Figure 4.2:** Velocity map of the second gas component, being the slower one of the two. The lines are analogous to figure 4.1.

### 4.1.2 Discussion

As mentioned above, both velocity maps display an S-shape in the line of zero velocity. This S-shape is stronger than the twist in the stellar velocity field. Such S-shaped twists in the gas velocity are usually signs for bars, they are seen in many barred galaxies, like NGC 1068 (Emsellem et al., 2006), NGC 1300 (Peterson & Huntley, 1980), NGC 2683 (Kuzio de Naray et al., 2009), NGC 3386 (García-Barreto & Rosado, 2001) and NGC 5448 (Fathi et al., 2005).

The spiral in the very center of the velocity map corresponds to a region with a higher dust concentration, see figure 4.4.

The region of very low velocities at the edge of the bulge on the near side of the galaxy could be produced by a large scale warp in the gas. Such a warp can project small velocities from further out into the line-of-sight (Melchior & Combes, 2011). Like for the stellar kinematics, we use `kinemetry` to measure the kinematic position angle of the first [OIII] component, the profiles are plotted in figure 4.5. We use this value to look at the misalignment between the photometric and the gas kinematic position angle and compare it to what has been observed in other galaxies, the comparison with the CALIFA survey is shown in figure 4.6. As with the misalignment between the photometric position angle and the stellar kinematic position angle, M31 lies more towards the barred galaxies.

In figures 4.8, 4.9 and 4.10, position-velocity diagrams are plotted for the gas. We show the gas kinematics in this way to compare with similar diagrams from measurements and simulations of neutral gas, e.g. Chemin et al. (2009) and Athanassoula & Beaton (2006). The coordinate system for these diagrams is shown in figure 4.7. The r-axis is parallel to the disk major axis along PA=38°. At

each r-coordinate, all points perpendicular to the major axis are plotted. They are color coded, depending on their distance to the major axis along the perpendicular coordinate  $d$ . Values on the far side of the major axis are shown in blue, values on the near side in red. The maximum and minimum values for  $d$  in the colorbar are shown as dash-dotted lines in figure 4.7. In figure 4.8, the position-velocity diagram is plotted for both velocity components, figure 4.9 shows only the first component and figure 4.10 the second one. In this way, differences between the two components become immediately apparent. In the first component, there is a prominent steep band of velocities in the center. The peak is more pronounced on the approaching side of the galaxy. On the receding side, the velocities stay more or less constant once they reached the plateau. The second component also shows the same main feature as the first component, but it is less pronounced and much wider. A cloud of points on the right of the center is prominent in the second component, this is the arm of zero velocity visible in figure 4.2. To the left of the center, there is an almost flat band of negative velocities, this is the zone of approaching velocities on the eastern side of the bulge in figure 4.2. There is also a second minimum for these velocities. The position-velocity diagram is similar to position-velocity diagrams from models of barred galaxies, like the one by Athanassoula & Beaton (2006), shown in figure 4.11. A very steep inner branch can be seen, which consists of the velocities of the innermost streaming motions, while the outer flatter branches are due to material further out (Athanassoula & Beaton, 2006).

Figure 4.12 shows a cut along the disk major axis ( $PA=38^\circ$ ), averaging the values within an aperture of width  $40''$ . The stellar velocity rises slowly to about  $200 \text{ km s}^{-1}$  at  $830''$ . The first component of the gas has a much steeper rise, reaching  $200 \text{ km s}^{-1}$  already at  $70''$ . The second component shows a more erratic behavior, somewhat mimicking the first component, reaching  $120 \text{ km s}^{-1}$  at  $60''$  in the receding half and at  $130''$  in the approaching one. The black continuous curve is the circular velocity predicted by the N-body model by B16. The dashed black line is the gas velocity from the model of Berman (2001), which simulates a triaxial bulge in M31. The overall shape of the first gas component is very similar to this triaxial bulge model, especially the fact that the velocity reaches a peak, then stays constant and rises to a second peak. However, it is asymmetric, for the approaching side of M31 this happens much closer to the center than for the other side. In Berman's model, the triaxial bulge has a position angle of  $PA_{\text{triaxial}} = 53^\circ$ , which is close to the bar position angle  $PA_{\text{bar}} = 55.7^\circ$  by B16.

In the neutral gas HI, Chemin et al. (2009) find regions with sometimes up to five different gas components. The velocity maps for all these components look very similar and have basically the same regular pattern. Chemin et al. (2009) present a cut through the velocities along the major axis, to which we compare our velocity values, see figure 4.13. The component that is steep in the center and has large velocities further out tracks the main HI component, while Chemin et al. (2009) claim that the flatter slope is due to slower gas in the outer HI disk that is projected into the central areas due to warps in the HI disk. However,

Athanassoula & Beaton (2006) present an older HI PV-diagram by Brinks & Shane (1984), which has the same shape as the one by Chemin et al. (2009). They say that this shape with the steep and the shallow branches is due to the bar. In figure 4.13, I overplot the position-velocity diagram by Chemin et al. (2009) over the full position-velocity diagram from figure 4.8. The central arms of the VIRUS-W position-velocity diagram trace the main HI disk well. The fact that the inner slope is less steep for the HI data is because of the lower resolution of the HI data.

A galaxy with similar inclination ( $i \approx 78^\circ$ ) as M31, which has also a B/P bulge, is NGC 2683 (Kuzio de Naray et al., 2009). Investigating the  $H\alpha$  velocity field, they see S-shaped twists and claim the presence of a bar at a position angle of  $5^\circ$  higher than the disk position angle. The position-velocity diagram they measure does not have the “bow tie” appearance of the one in M31, but it looks like two nested parallelograms, see figure 4.14. The fact that this PV-diagram looks different from the one in M31 led Melchior & Combes (2011) to claim that the interpretation of Athanassoula & Beaton (2006) of the bar in M31 is wrong and the ring structures are only due to the collision of M31 with M32 suggested by Block et al. (2006). However, the bar in NGC 2683 is only at an angle of  $6^\circ$  to the major axis, so it is seen quite side-on, whereas the bar in M31 is at an angle of  $17^\circ$  to the major axis, it is seen more end-on. Bars seen more end-on lead to a bow-shape in the position-velocity diagrams and bars seen side-on to the parallelogram shape (Bureau & Athanassoula, 2005), leading Kuzio de Naray et al. (2009) to speculate that the bar in M31 is seen more end-on than the one in NGC 2683. However, they caution that also underlying differences between the two galaxies, like the presence of dust or the density of the gas, could influence the shape of the position-velocity diagram, urging for further modeling to settle this issue.

Melchior & Combes (2011) measured molecular emission lines in CO with two peaks, in Melchior & Combes (2016) sometimes even three. In figure 4.15, we plot the double components from Melchior & Combes (2011) together with our own velocity fields for the two components. While the approaching velocity in CO corresponds very well with the velocities we measure in the [OIII], the receding velocities measured in CO are off by about 100 km/s.

Melchior & Combes (2011) try to explain the double CO components with a tilted ring model, see figure 4.16, coming from the collision model by Block et al. (2006). An inner disk which is at an inclination of  $43^\circ$ , i.e. more face-on than the disk of M31, is surrounded by an inner ring. The velocity structure this ring model would then create is plotted in figure 4.17, where it is compared to the velocity field of the first [OIII] component. The second component is not compared, because it is not detected in the region corresponding to the simulated velocity field. Comparing the simulated and the measured velocities, it becomes clear that they agree fairly well in the innermost part, but further out the line of zero velocity is more strongly twisted in the simulated velocity field. The velocity profiles extracted from the simulated velocity fields by Melchior &

Combes (2011) consist of a very broad component, which is blueshifted and a narrow one, which is redshifted, the blueshifted part comes from the inner disk and the redshifted part from the ring. The spectrum they model for a double-peaked region is compared in figure 4.18 to a corresponding VIRUS-W spectrum. The measured VIRUSW [OIII] components both roughly have the same width, so the scenario of Melchior & Combes (2011) does not predict the actual shape of our measured [OIII] spectrum.

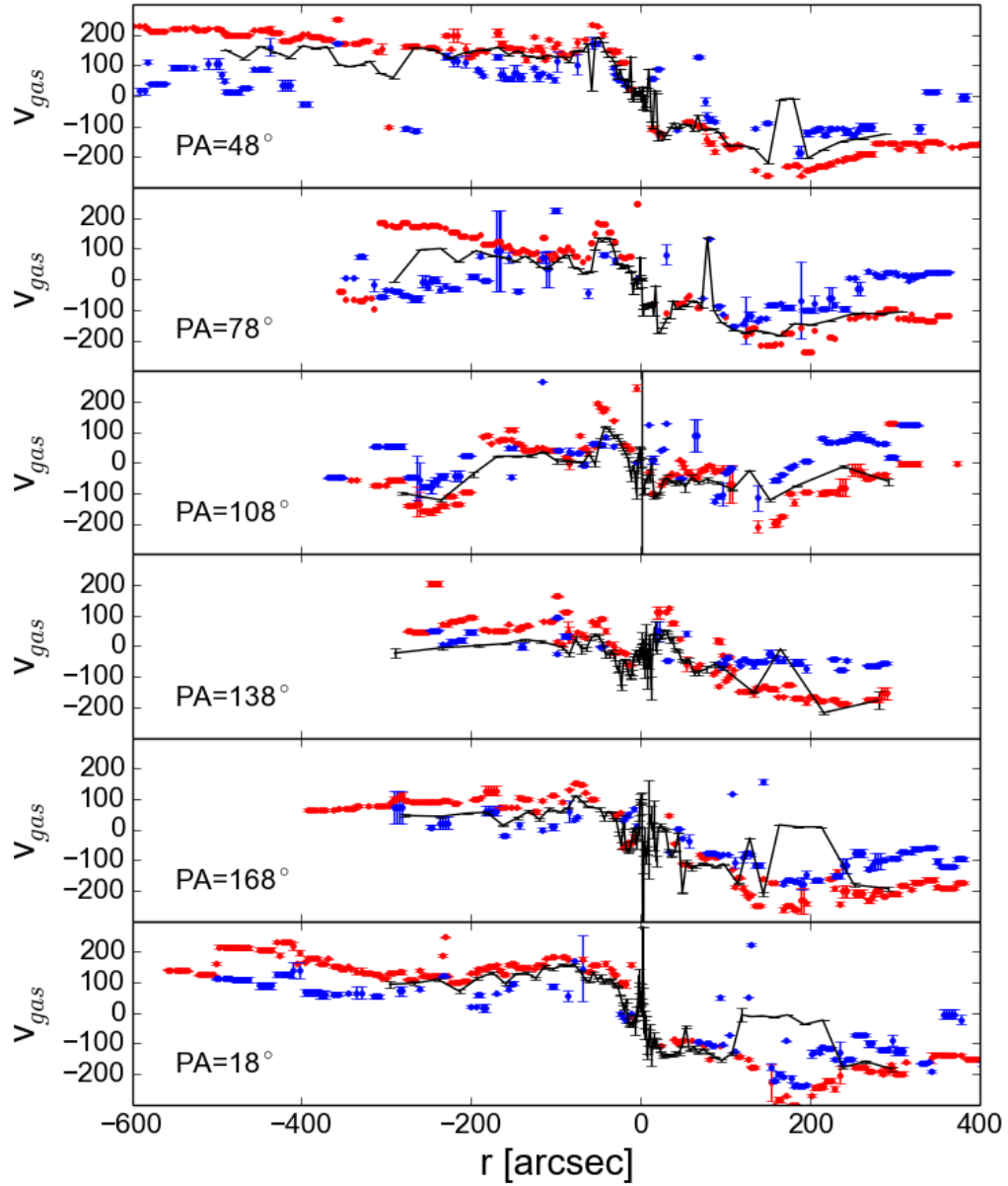


**Figure 4.3:** Comparison of our gas velocities with the ones from S10. Black are the velocities measured by S10, red are cuts through the first gas component from figure 4.1 and blue the cuts through the second component from figure 4.2.

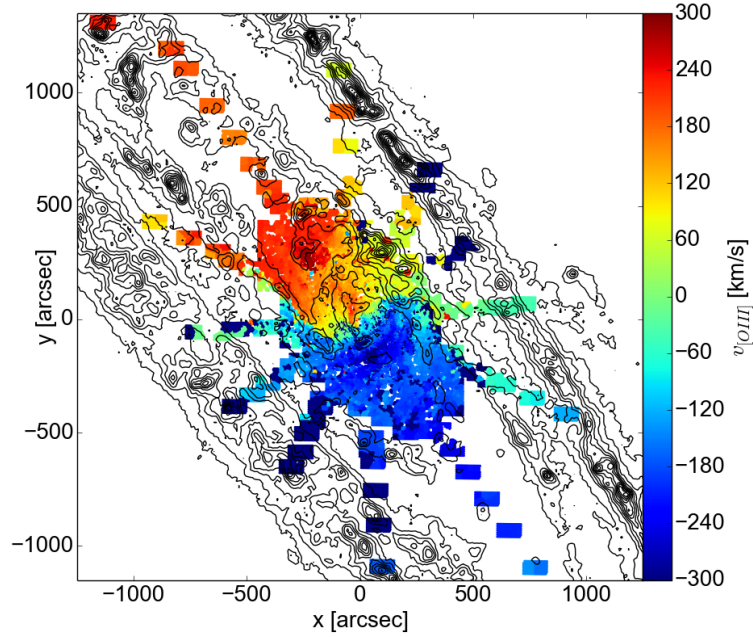


**Figure 4.4:** The velocity map of the first gas component from figure 4.1 overlaid with contours from Herschel observations at  $250 \mu m$ .

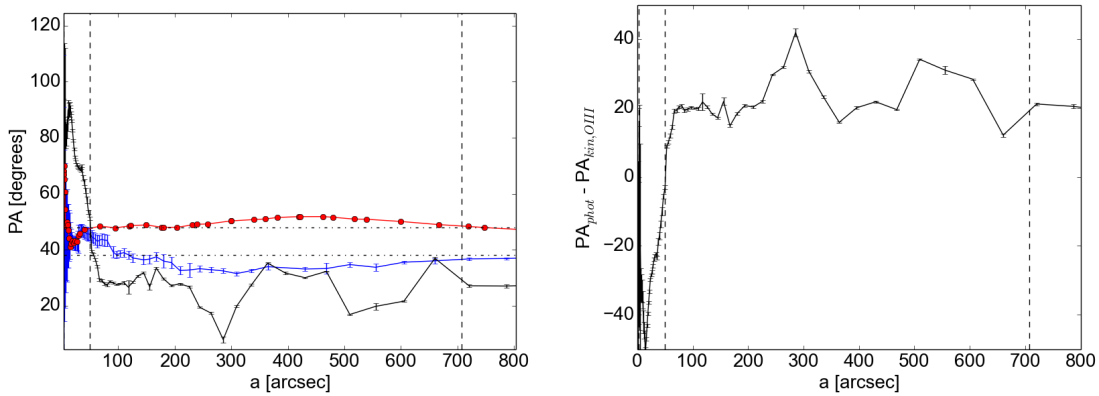


**Figure 4.5:** Left: Comparison between the photometric position angles for the stars (red), the kinematic position angle of the stars (blue) and the kinematic (black) position angle for the first ionized gas component. Right: The difference between the photometric position angle and the kinematic position angle for the gas. The photometric position angle is taken from the ellipse fit to the K-band image from figure 2.22, the kinematic one from the fit with `kinemetry` to the gas velocity field from figure 4.1. The horizontal dash-dotted lines are the disk position angle at  $PA_{disk} = 38^\circ$  and the bulge position angle at  $PA_{bulge} = 48^\circ$ . The vertical lines denote the extent of the circular classical bulge and the boxy bulge from Beaton et al. (2007).

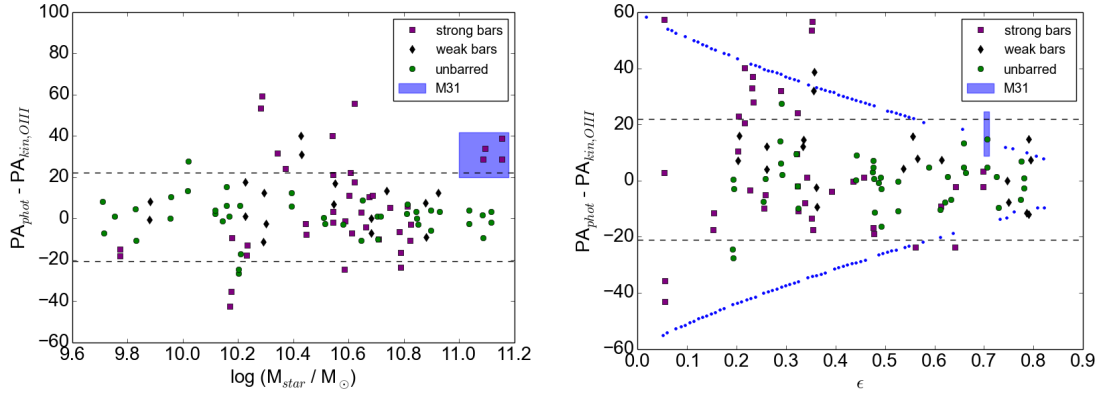


**Figure 4.6:** The mean kinematic misalignment of M31 compared to the CALIFA survey. The datapoints for strongly barred (purple), weakly barred (black) and unbarred galaxies are taken from Barrera-Ballesteros et al. (2014). The dashed lines denote the  $2\sigma$  dispersion of their sample. The blue rectangle represents M31, with the lower limit for the misalignment being the mean difference ( $8.31^\circ$ ) and the maximum being the largest kinematic misalignment in figure 4.5 ( $19.07^\circ$ ). The stellar mass of M31 ( $10\text{--}15 \cdot 10^{10} M_\odot$ ) is taken from Tamm et al. (2012). The blue points in the plot with ellipticity display the projection effect of a bar that is  $60^\circ$  away from the disk in the plane of the galaxy. This is almost the same as the value from B16 ( $55.7^\circ$ ).

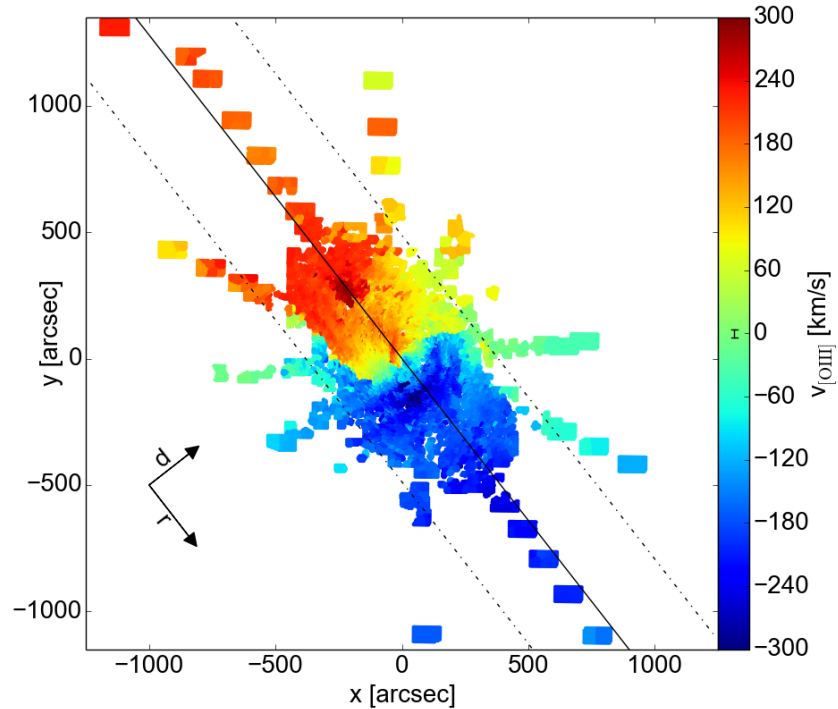


**Figure 4.7:** Same as figure 4.1, overplotted with the major axis in black and two dash-dotted lines at distances of  $-300''$  and  $+300''$  to the major axis, which are the boundaries of the colorbar in figure 4.8. The arrows in the lower left indicate the direction of  $r$  and  $\phi$  in that figure.

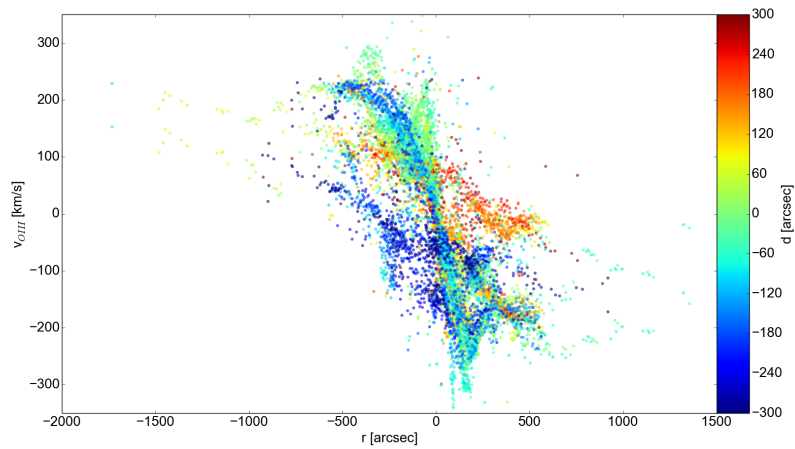


**Figure 4.8:** The position-velocity diagram projected onto the major axis, the x-axis is the distance along the major axis, the y-axis is the velocity and the color represents the perpendicular distance to the major axis. The axes are given in figure 4.7.

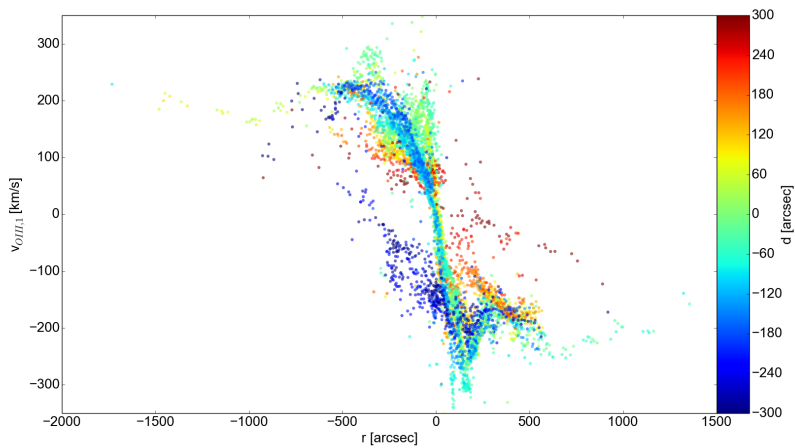


**Figure 4.9:** Similar to figure 4.8, only the first component is plotted.

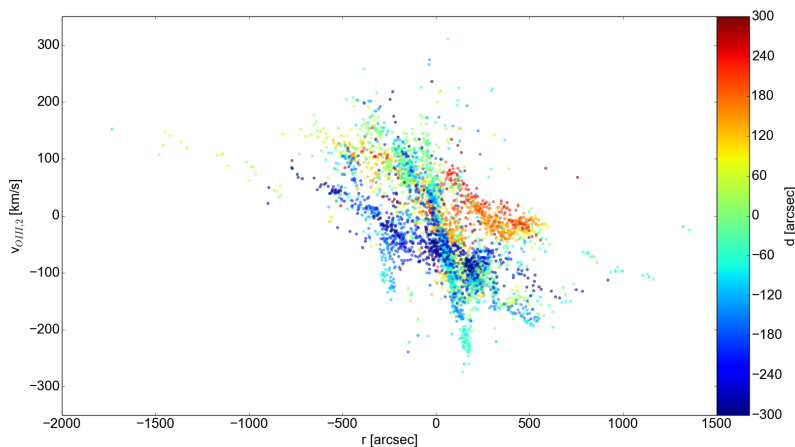


**Figure 4.10:** Similar to figure 4.8, only the second component is plotted.

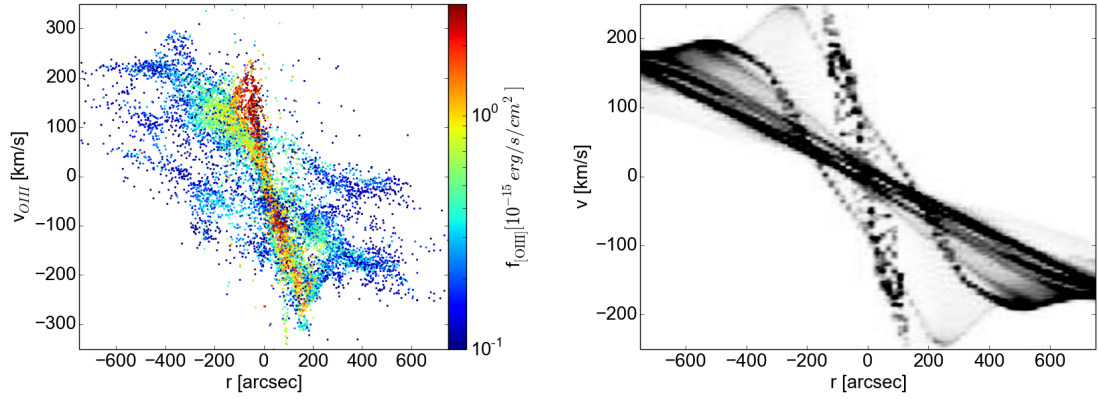


**Figure 4.11:** Comparison of position-velocity diagram of both [OIII] components (left) with theoretic model by Athanassoula & Beaton (2006) (right). In this model, the angle between the disk and the bar is at  $60^\circ$  in the plane of the disk, which is similar to  $PA_{bar} = 55.7$  by B16. The color in the left panel are the flux values of the [OIII] gas, which are described in more detail below in section 4.3.

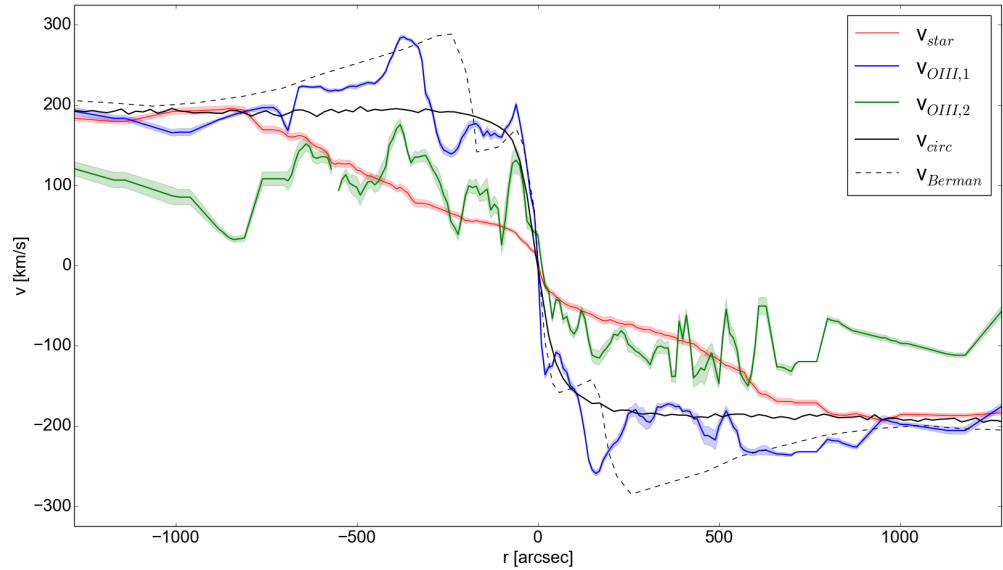


**Figure 4.12:** Cut through the velocity maps along the major axis within an aperture of  $40''$ . The red line is a cut through the stellar velocity (figure 3.1), the blue is a cut through the first velocity component (figure 4.1), green the second velocity component (figure 4.2). The solid black line is the circular velocity from the barred N-body model by B16, the black dashed line is the velocity for the triaxial bar model by Berman (2001).

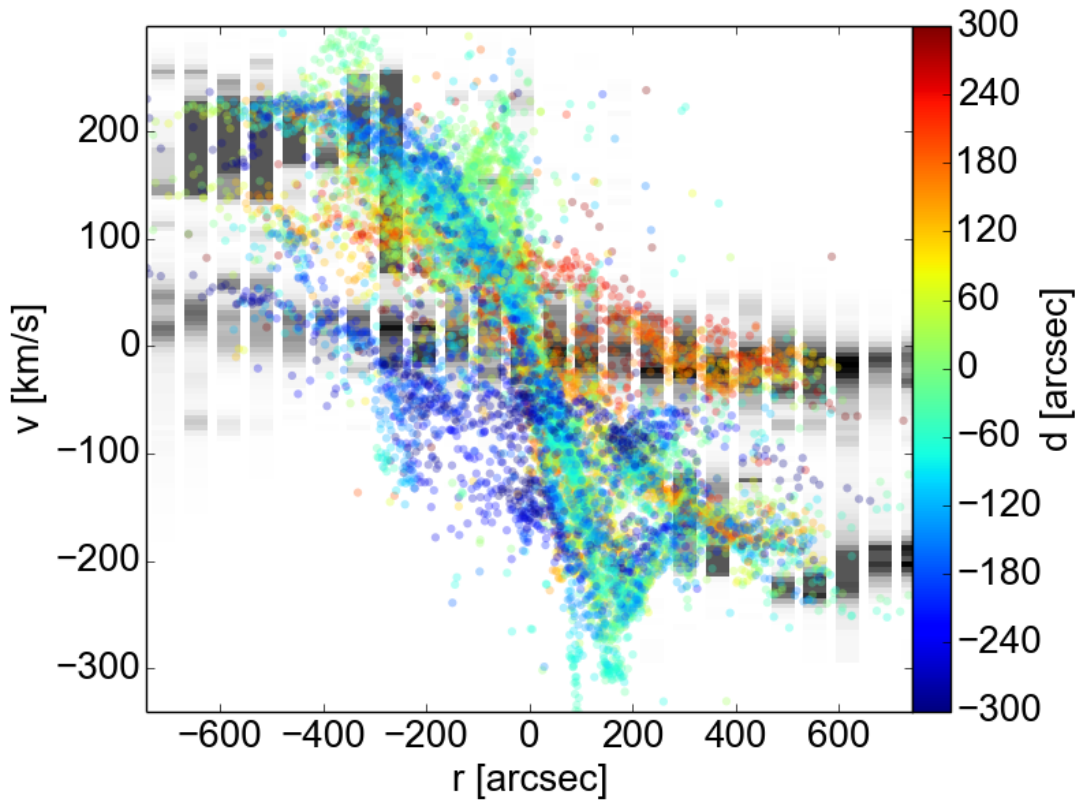


**Figure 4.13:** Position-velocity diagrams of the HI component (grey) and the full position-velocity diagram from figure 4.8.

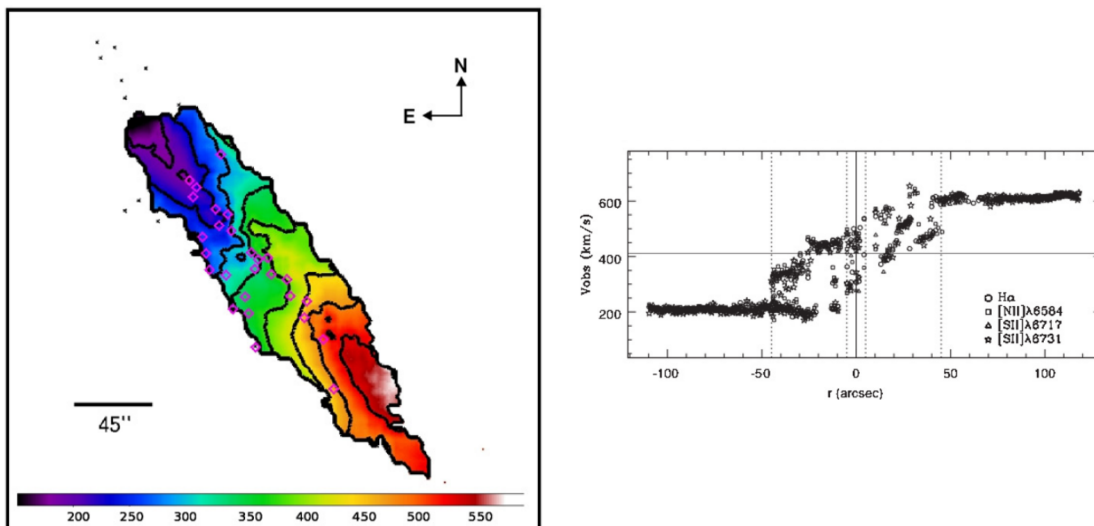


**Figure 4.14:** Velocity field (left) and position-velocity diagram (right) of NGC 2683 (Kuzio de Naray et al., 2009).

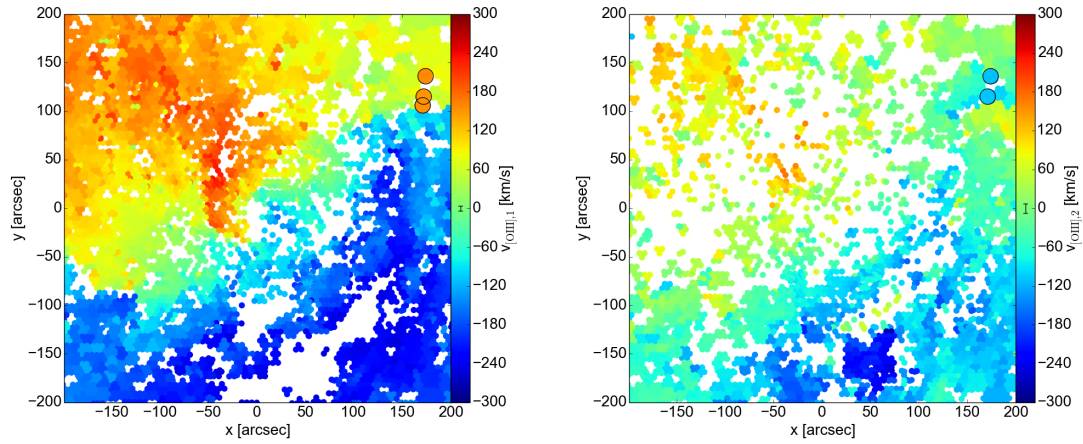


**Figure 4.15:** Left panel: Comparison of the first [OIII] component with the first component in CO. Right: Comparison of the second [OIII] component with the second component of CO. The velocity maps are zoomed versions of figures 4.1 and 4.2. Pointings in CO from Melchior & Combes (2011) are marked with circles. While the second CO component agrees with the second gas component, the first one does not.

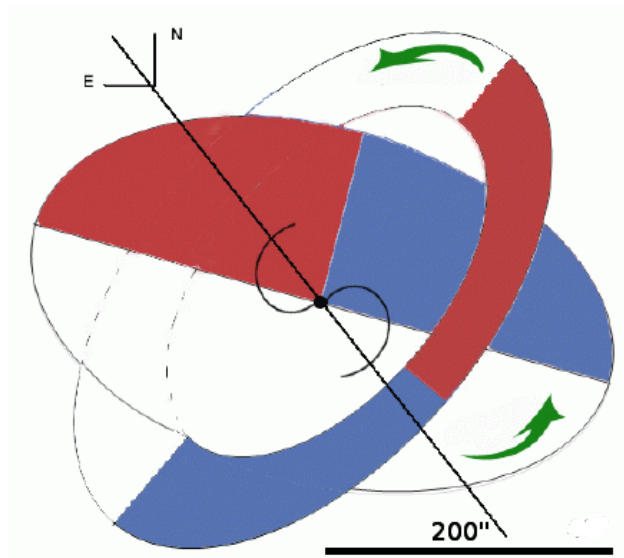


**Figure 4.16:** Ring model by Melchior & Combes (2011) to explain the double lines in the CO. The inner disk has  $PA=70^\circ$  and inclination  $i=77^\circ$ . The ring is superimposed with similar inclination and position angle  $PA=-35^\circ$ . The straight line is the major axis of the main galaxy disk with  $PA=35^\circ$ . The near sides of the two components are colored, red corresponds to receding parts and blue to approaching ones.

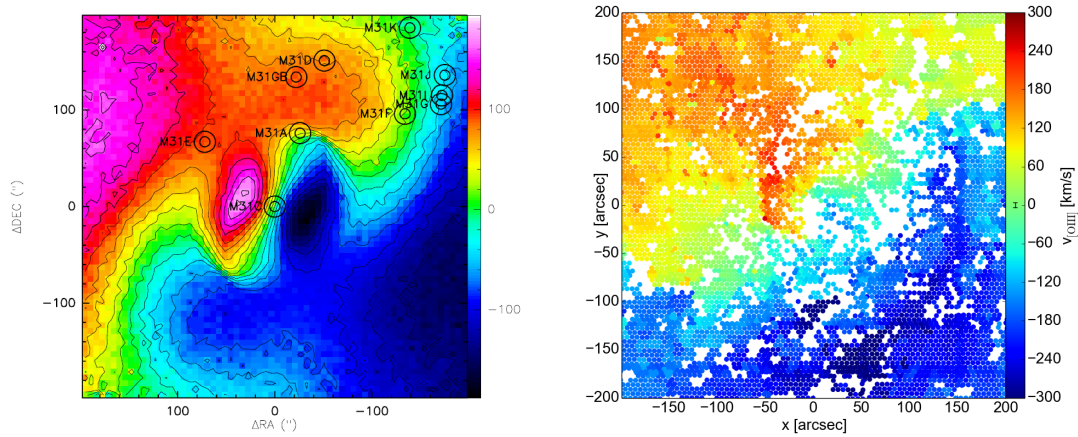


**Figure 4.17:** Simulated velocity field created by the ring model from Melchior & Combes (2011) (left) and velocity field of the first component from figure 4.1. The three CO pointings plotted in figure 4.15 are marked as M31G, M31I and M31J in this plot. The radial extent is  $200''$  from the center in each direction.

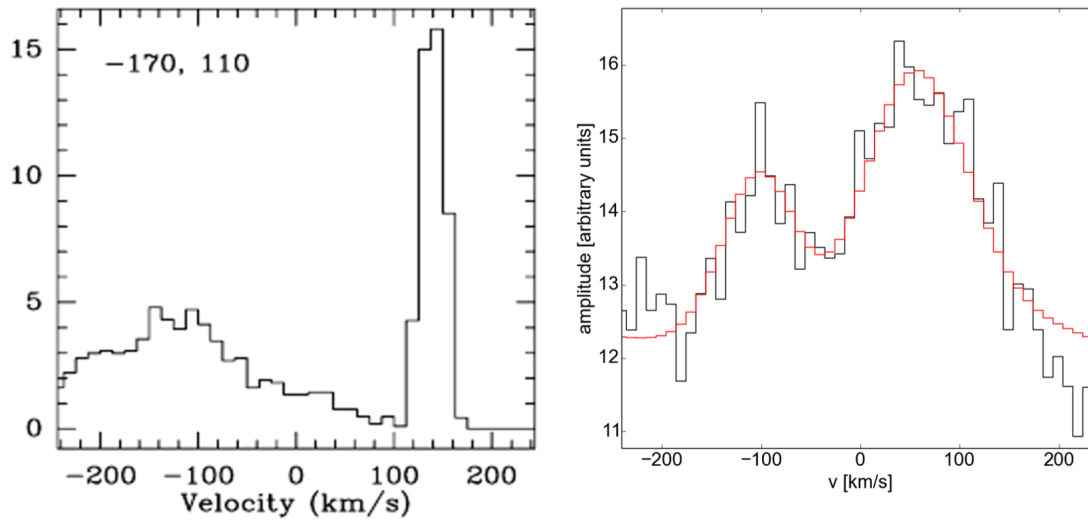


**Figure 4.18:** Spectrum extracted from the simulated velocity field for the ring model at the position of the double line in CO by Melchior & Combes (2011) (left) compared to measured [OIII] velocity profile at the same position (right), with the black line being the measured spectrum and red the best fit by GANDALF. On the x-axis, the velocity relative to the systemic velocity is plotted.

## 4.2 Velocity dispersion

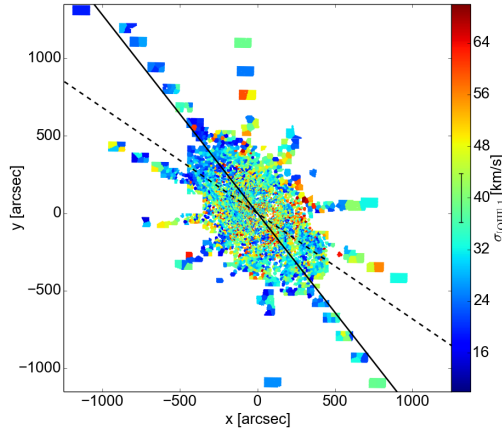


**Figure 4.19:** Velocity dispersion of the first gas component. The lines are the disk major axis at  $PA_{disk}=38^\circ$  (solid) and the bar major axis at  $PA_{bar}=55.7^\circ$ . The median error of the values is given in the colorbar.

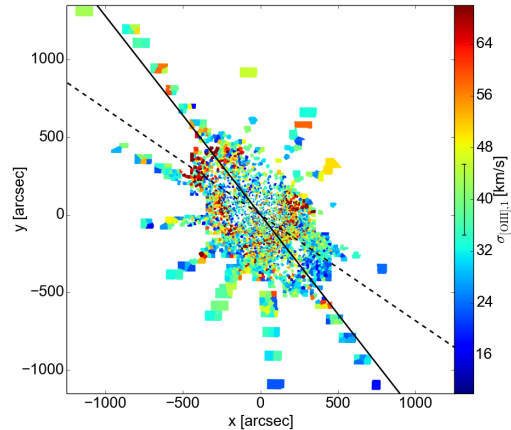


**Figure 4.20:** Velocity dispersion of the second gas component. The lines correspond to the ones in figure 4.19.

The velocity dispersion of the first component, plotted in figure 4.19, is low near the northern end of the bulge along the major axis, where the velocities are high. There seems to be a spiral structure where  $\sigma$  is higher. The  $\sigma$  values of the second component in figure 4.20 are generally higher, especially in the arm of negative velocities on the near side, but also in a zone of comparatively high velocities just south of the minor axis. The area at the northwestern edge of the bulge with low  $\sigma$  in the first component has high values in the second component. The arm of zero velocity in the southwest is not fully distinguishable in the velocity dispersion, but its  $\sigma$  is in general low. We do not compare our values with the ones by S10, because of the different instrumental resolutions ( $\sigma_{inst,VIRUSW} = 15 \text{ km s}^{-1}$  and  $\sigma_{inst,S10} = 69 \text{ km s}^{-1}$ ).

## 4.3 Gas fluxes

The fluxes of  $H\beta$ ,  $[OIII]\lambda 5007$  and  $[NI]\lambda 5198$  are plotted in figures 4.21 to 4.29. In figure 4.21, we show the line flux of the first and second  $H\beta$  line. The corresponding fluxes for  $[OIII]\lambda 5007$  are shown in figure 4.24, and the ones for  $[NI]\lambda 5198$  in figure 4.27. We also add the fluxes of the two line components together in figures 4.23, 4.26 and 4.29. The first component is usually brighter than the second component.  $H\beta$  and  $[OIII]$  show the same general behavior with a spiral pattern in the center. Especially prominent is an arm in the southwest for the first component. The  $H\beta$  emission is lower than the one in  $[OIII]$ . The  $[NI]$  is much fainter than either the  $H\beta$  or the  $[OIII]$ , no clear pattern can be seen there apart from the fact that

it becomes brighter in the center. The overall filamentary appearance of the gas morphology could be either due to heating by shocks or supernovae of type Ia (Jacoby et al., 1985).

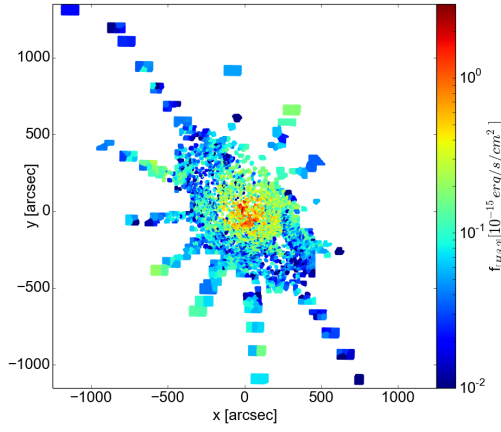
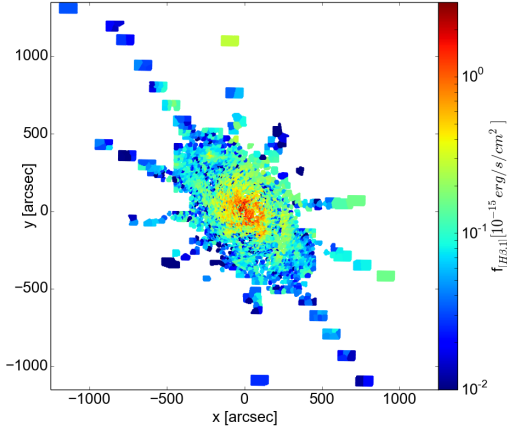


**Figure 4.21:** Flux of first  $H\beta$  component. The median error is  $0.01 \cdot 10^{-15}$  [erg/s/cm<sup>2</sup>]. **Figure 4.22:** Flux of second  $H\beta$  component. The median error is  $0.01 \cdot 10^{-15}$  [erg/s/cm<sup>2</sup>].

In figures 4.23, 4.26 and 4.29, we plot the sum of the fluxes for component 1 and component 2. The pattern that is visible for [OIII] and  $H\beta$  is very similar to the one seen by Jacoby et al. (1985) in a  $H\alpha + [\text{NII}]$  filter and in [OIII], by Boulesteix et al. (1987) in [NII] and by Ciardullo et al. (1988) in  $H\alpha + [\text{NII}]$ . The latter is plotted in figure 4.30 together with our own data. The structure aligned along the major axis in the center could be an inner disk that is projected due to M31's inclination and orientation into the elongated shape we see (Jacoby et al., 1985). The inner spiral pattern seems to be tipped to a lower inclination with respect to the outer part, which according to Jacoby et al. (1985) can be caused by a non-axisymmetry, like a bar, and cannot be explained by axisymmetric features alone.

In figure 4.31, we plot the combined [OIII] flux with the expected flux from a generic bar model by Athanassoula & Beaton (2006). The plot in Athanassoula & Beaton (2006) is originally given as a face-on view, it has been scaled to the deprojected bar length of  $1000''$  and rotated to the orientation of  $\text{PA}_{\text{bar}} = 55.7^\circ$  given by B16. It has also been flipped along the bar axis, since the model in Athanassoula & Beaton (2006) is rotating clockwise, while the one in B16 is rotating anticlockwise. The distances perpendicular to the disk major axis have been multiplied with  $\cos(i)$ , where  $i$  is the inclination of M31. Comparing the measured fluxes to the ones in the model, you see that the fluxes in the measurement are oriented more along the minor axis of the disk, while the ones of the model are more elongated along the major axis. However, the dark red regions in the measured [OIII] morphology could well correspond to the dark red regions in the innermost part of the model by Athanassoula & Beaton (2006), being the streamlined gas closest to the center.

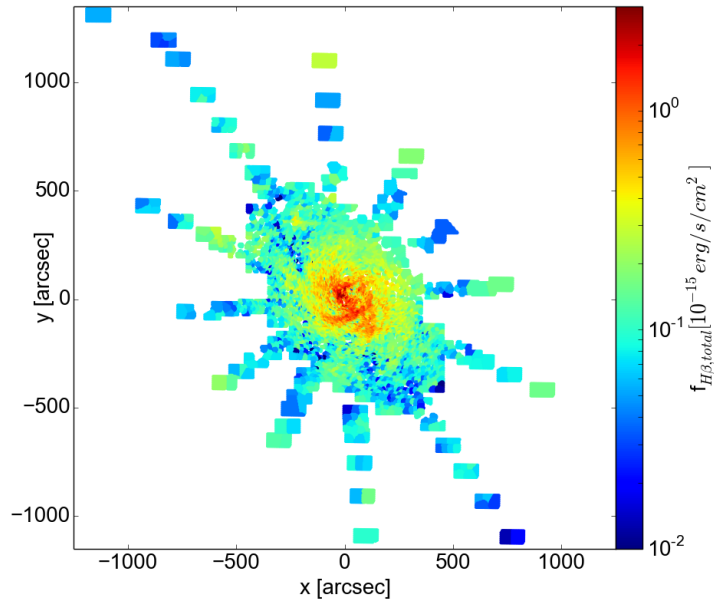


**Figure 4.23:** Flux of both  $H\beta$  components combined. The median error is  $0.02 \cdot 10^{-15}$  [erg/s/cm<sup>2</sup>].

The fact that the structure in the central region is aligned along the minor axis, almost perpendicular to the position of the assumed bar, led [Block et al. \(2006\)](#) to conclude that this ring structure is not caused by a bar, but by the collision of M31 with M32, which also caused a “split” of the so-called 10-kpc ring, which is a structure appearing further out in the gas. Their simulation for the gas fluxes in the central regions is shown in figure 4.32. While the collision model is in better agreement with the ring structure, it has lower flux inside the ring, whereas in our flux maps, as well as the ones by [Jacoby et al. \(1985\)](#), [Boulesteix et al. \(1987\)](#) and [Ciardullo et al. \(1988\)](#), there is a high flux present there.

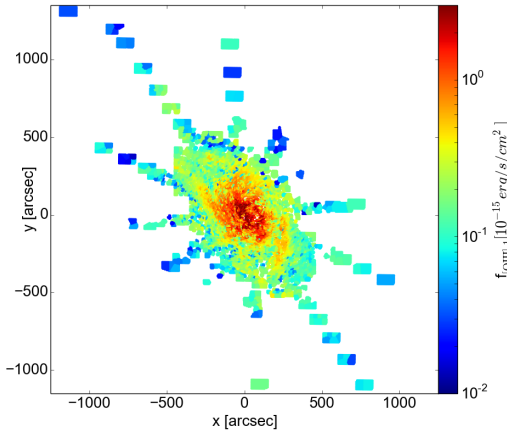


**Figure 4.24:** Flux of first [OIII] component. The median error is  $0.01 \cdot 10^{-15}$  [erg/s/cm<sup>2</sup>].

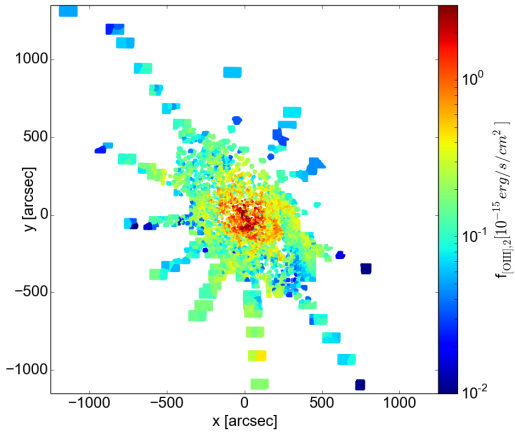


**Figure 4.25:** Flux of the second [OIII] component. The median error is  $0.01 \cdot 10^{-15}$  [erg/s/cm<sup>2</sup>].

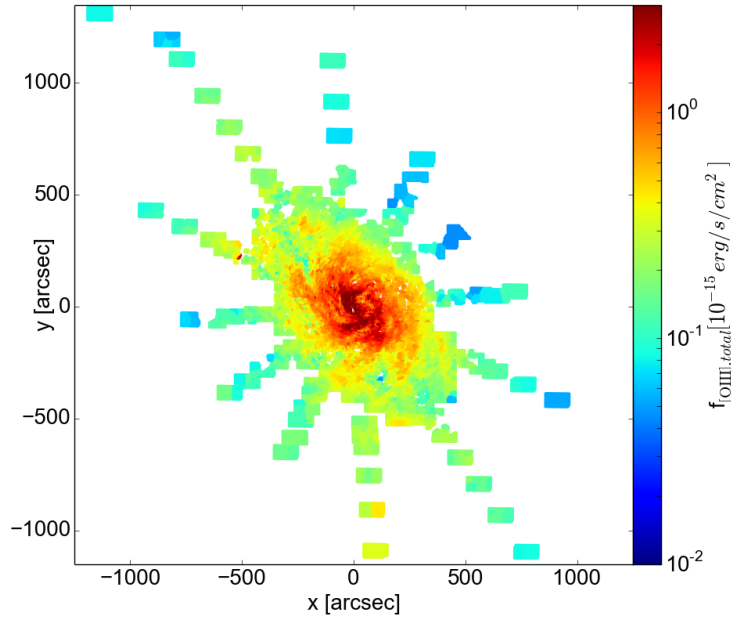


**Figure 4.26:** Sum of the flux of the two [OIII] components. The median error is  $0.02 \cdot 10^{-15}$  [erg/s/cm<sup>2</sup>].

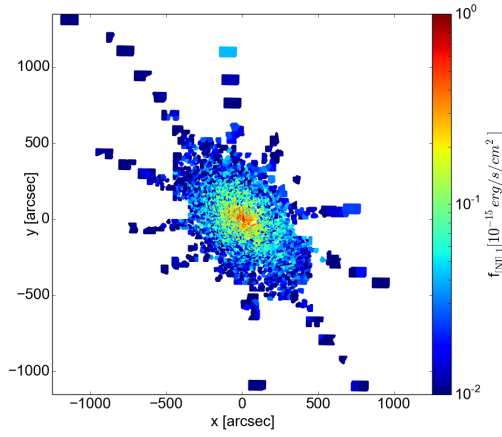


**Figure 4.27:** Flux of the first [NI] component. The median error is  $0.01 \cdot 10^{-15}$  [erg/s/cm<sup>2</sup>].

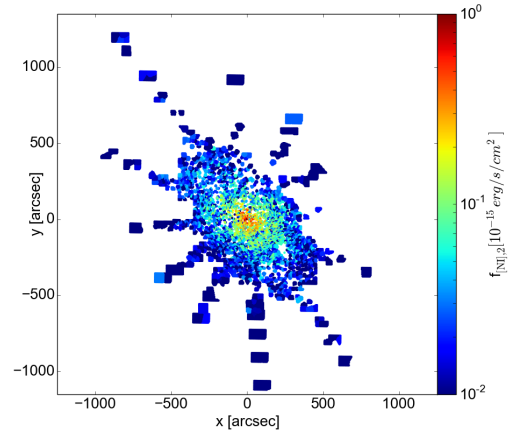


**Figure 4.28:** Flux of the second [NI] component. The median error is  $0.01 \cdot 10^{-15}$  [erg/s/cm<sup>2</sup>].

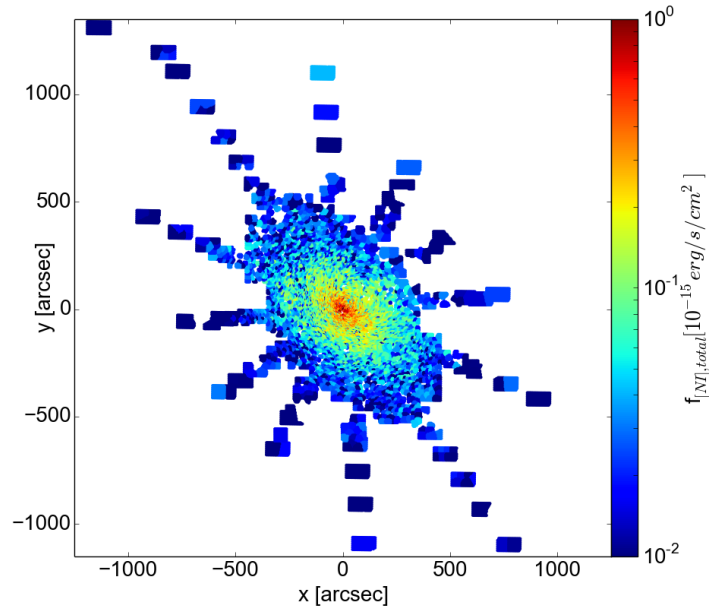


**Figure 4.29:** Total flux of the two [NI] components. The median errorbar is  $0.01 \cdot 10^{-15}$  [erg/s/cm<sup>2</sup>].

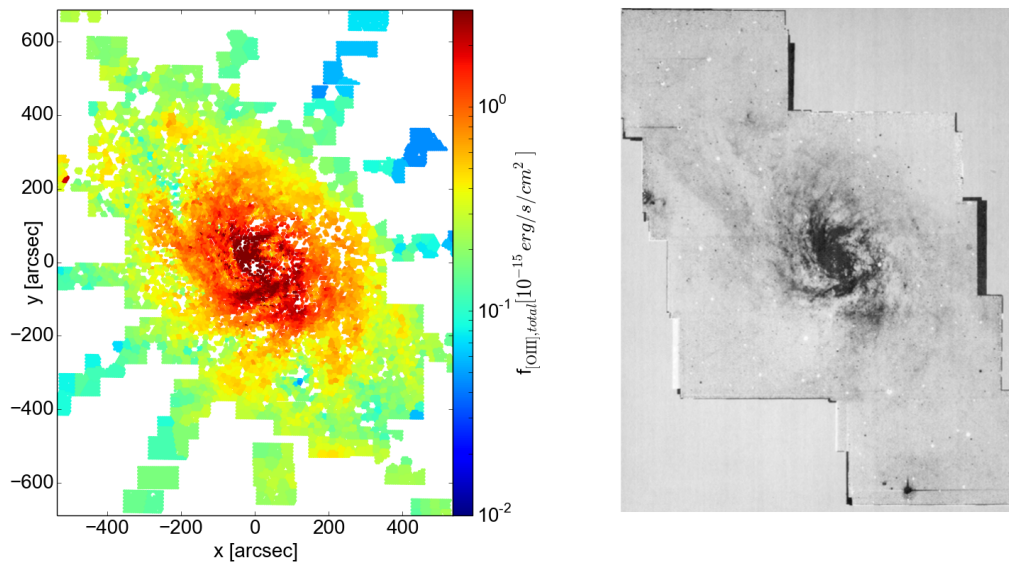


**Figure 4.30:** Comparison of a zoom into figure 4.26 (left), compared to an image of  $\text{H}\alpha + [\text{NII}]$  image by Ciardullo et al. (1988) (right).

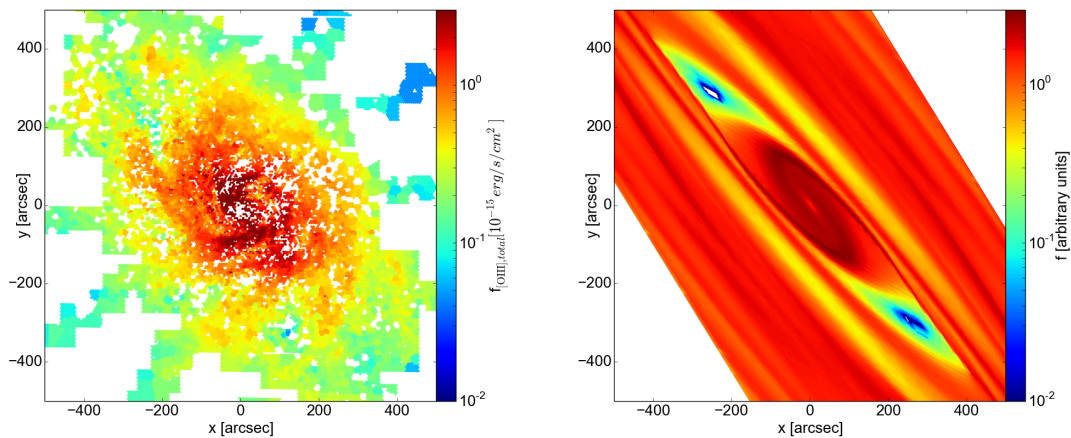


**Figure 4.31:** Comparison of the combined  $[\text{OIII}]$  flux, which is a zoom into figure 4.26 (left) and the flux expected from the response of the gas to a barred potential, adapted from the model given in Athanassoula & Beaton (2006) (right).

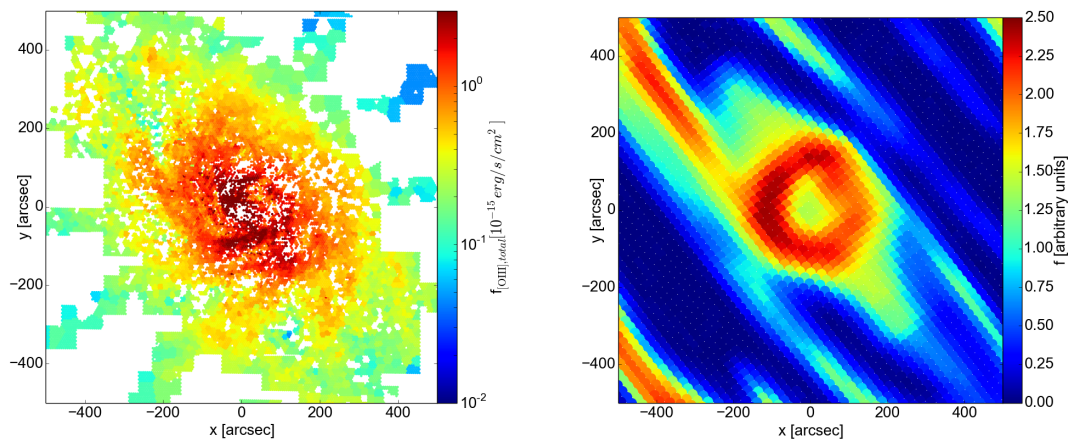


**Figure 4.32:** Comparison of the combined [OIII] flux, which is a zoom into figure 4.26 (left) and the flux expected from the collision of M31 with M32, adapted from the plot in Block et al. (2006) (right).

## 4.4 Ionization mechanisms of the gas

In order to investigate which mechanisms are responsible for ionizing the gas, diagnostic diagrams are used, which compare the ratios of line fluxes of different emission lines. The most widely utilized of these diagrams compares  $[OIII]\lambda 5007/H\beta$  to  $[OI]\lambda 6300/H\alpha$  (Veilleux & Osterbrock, 1987). Since we don't have  $H\alpha$  or  $[OI]\lambda 6300$  in our observed wavelength range, we cannot use this standard diagnostic diagram. Sarzi et al. (2010) devised alternative diagnostic diagrams for the SAURON spectrograph (Bacon et al., 2001), which has a similar wavelength range as VIRUS-w. This diagram compares  $[OIII]\lambda 5007/H\beta$  to  $[NI]\lambda\lambda 5198, 5200/H\beta$ . The  $[NI]$  lines are usually present in partially ionized regions in gaseous nebulae, which are photo-ionized by a spectrum containing high-energy photons, but they are absent in HII regions, where  $H\beta$  and  $[OIII]\lambda 5007$  arise. The Sarzi diagram is plotted for both  $[OIII]$  components in figure 4.33. The diagnostic diagrams for both components look very similar, there is also no systematic offset between the inner and the outer regions. Neither component lies in the regions where ionization happens via starbursts. Most of the points lie in the region where the ionization is due to shocks in the gas. These shocks could be triggered by the bar, like the shock regions and streamlines in figure 4.31.

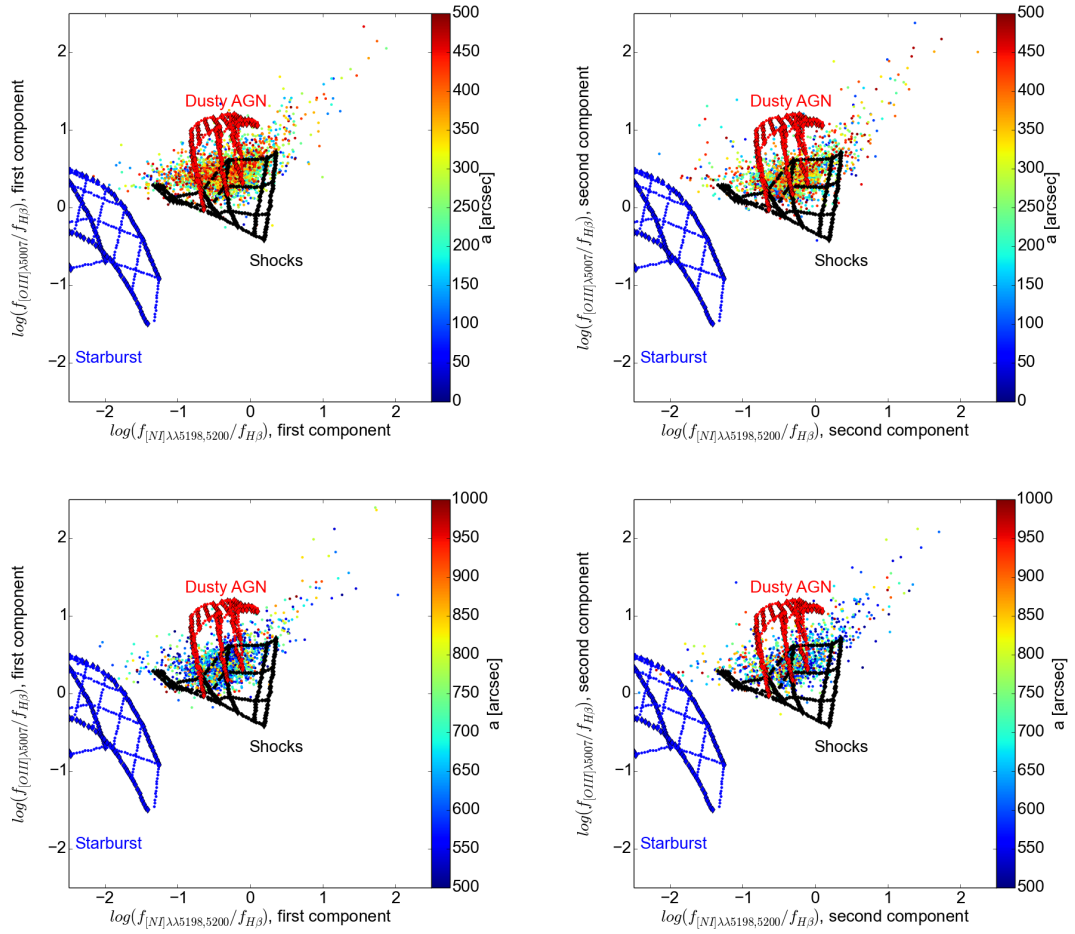


**Figure 4.33:**  $[\text{NI}]/\text{H}\beta$  versus  $[\text{OIII}]\lambda 5007/\text{H}\beta$  for the inner part of the first gas component (upper left), the outer part of the first gas component (lower left), the inner part of the second gas component (upper right) and the outer part of the second gas component (lower right). Color coded is the distance to the center, where the distances have been corrected for the inclination of the galaxy. The contours are regions where the ionization happens via starbursts (blue), shocks (black) and AGNs (red). These have been taken from Sarzi et al. (2010).

## 4.5 Conclusion

In conclusion, the gas kinematics is more complicated than the stellar kinematics, with the spectral lines often displaying two peaks, leading to two components. Both components display rotation, with one of them being faster than the other. The overall shape of the kinematics of the gas agrees with simulations of gas in a barred potential. The fluxes of the two components have the overall appearance of a spiral with lower inclination than the galaxy. This tilting of the gas structure could have been caused by a bar. The shape of the fluxes also shows similarities with the gas responses to a bar potential.

However, to further investigate this, a simulation of gas particles in a barred model for M31 is needed, the kinematics and the morphology of the gas in this model can then be compared to the measurement.

# Chapter 5

## Stellar populations

In this chapter, we will present the measurement of absorption line strengths in the Lick/IDS system (Burstein et al., 1984; Faber et al., 1985; Burstein et al., 1986; Worthey et al., 1994). These will then be compared to simple stellar population models to obtain the age, metallicity and  $\alpha$ /Fe-overabundance of the stellar populations.

### 5.1 Lick indices

We measure Lick indices on emission corrected spectra, using the band definitions of Trager et al. (1998). The indices that fall into our spectral range are H $\beta$ , Mg b and the iron indices Fe5015, Fe5270, Fe5335 and Fe5406, they are listed in table 5.1. To measure the indices, the emission lines fitted by GANDALF are subtracted from the spectra. The emission subtracted spectra are broadened to the resolution of the Lick spectra  $\sigma_{Lick} = 220$  km/s. The mean flux value in each continuum window is calculated, the values are connected and define a pseudocontinuum. The Lick indices are then the integral over the normalized difference between the spectrum  $F_I(\lambda)$  and the pseudocontinuum  $F_C(\lambda)$  in the index window:

$$Index = \int_{\lambda_1}^{\lambda_2} \left( \frac{F_C(\lambda) - F_I(\lambda)}{F_C(\lambda)} \right) d\lambda \quad (5.1)$$

In figure 5.1, a convolved spectrum is shown with the windows for the index Mg b.

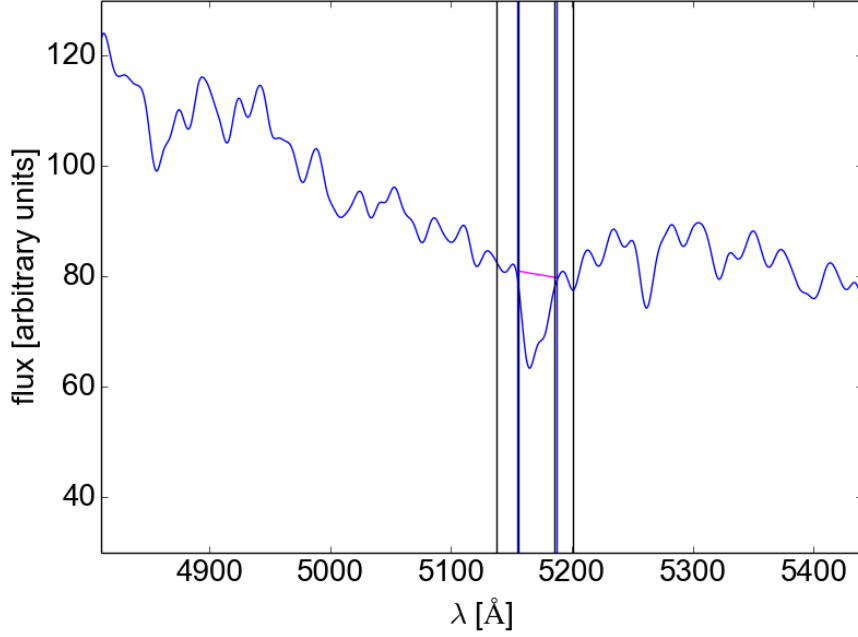


**Figure 5.1:** The windows of the Lick index Mg b overlaid over a typical emission corrected spectrum broadened to a resolution of  $\sigma_{Lick} = 220$  km/s. The blue vertical lines are the borders of the index window, the areas between the red and the black lines are the continuum windows. The magenta line is the pseudocontinuum, connecting the mean fluxes in the continuum windows.

**Table 5.1:** Definitions of the Lick indices used in our analysis, table taken from [Trager et al. \(1998\)](#). The last column indicates which elements are measured by the index. The abundance of the species without parentheses is directly proportional to the index value, the abundance for the ones in parentheses are inversely proportional.

Name	Index Bandpass [Å]	Pseudocontinua [Å]	Element Measured
H $\beta$	4847.875 – 4876.625	4827.875 – 4847.875 4876.625 – 4891.625	H $\beta$ , (Mg)
Fe5015	4977.750 – 5054.000	4946.500 – 4977.750 5054.000 – 5065.250	(Mg), Ti, Fe
Mgb	5160.125 – 5192.625	5142.625 – 5161.375 5191.375 – 5206.375	Mg, (C), (Cr)
Fe5270	5245.650 – 5285.650	5233.150 – 5248.150 5285.650 – 5318.150	Fe, C, (Mg)
Fe5335	5312.125 – 5352.125	5304.625 – 5315.875 5353.375 – 5363.375	Fe, (C), (Mg), Cr
Fe5406	5387.500 – 5415.000	5376.250 – 5387.500 5415.000 – 5425.000	Fe

Errors on the index measurements are estimated using a Monte-Carlo approach. For each spectrum, 1000 representations with added random Gaussian noise are created, with the width of the Gaussian being the noise value of the individual spectra.

The resulting maps for the Lick indices are plotted in figures 5.2 to 5.7, they have been smoothed with a two-dimensional Gaussian filter with  $\sigma = 10''$  in order to reduce the noise in the maps and make the trends clearer.  $H\beta$  in figure 5.2 has a median value of  $H\beta = 1.70 \pm 0.08 \text{ \AA}$ , with a maximum value of  $H\beta_{max} = 3.9 \pm 0.2 \text{ \AA}$  in the outermost pointing in the near side at  $PA = -25^\circ$ , and the minimum value of  $H\beta_{min} = 1.1 \pm 0.1 \text{ \AA}$  in the innermost disk pointing at  $PA = 185^\circ$ . The overall distribution of the  $H\beta$  values is asymmetric, with higher values on the near side and lower values on the far side of the galaxy. From visual inspection of the map, we decided to separate the map into two halves, one to the north and west of a line with  $PA_{sep} = 50^\circ$ , subsequently called the upper half, and one south and east of it, the lower half. The angle  $PA_{sep}$  is similar to the bar angle  $PA_{bar} = 55.7^\circ$  from B16. In the upper half, the median value is  $H\beta_{upper} = 1.68 \pm 0.08 \text{ \AA}$ , with maximum value  $H\beta_{max,upper} = 3.9 \pm 0.2 \text{ \AA}$  and minimum value  $H\beta_{min,upper} = 1.3 \pm 0.1 \text{ \AA}$ . In the lower half, the median value is  $H\beta_{lower} = 1.57 \pm 0.08 \text{ \AA}$ , with  $H\beta_{max,lower} = 2.7 \pm 0.1 \text{ \AA}$  and  $H\beta_{min,lower} = 1.1 \pm 0.1 \text{ \AA}$ . In the bulge region, defined as the region where the bulge-to-disk ratio of the model image from section 2.3 is larger than 0.5, the values are in general lower than in the disk with  $H\beta_{bulge} = 1.61 \pm 0.07 \text{ \AA}$ , with  $H\beta_{max,bulge} = 1.86 \pm 0.09 \text{ \AA}$  and  $H\beta_{min,bulge} = 1.41 \pm 0.08 \text{ \AA}$ , compared to  $H\beta_{disk} = 1.75 \pm 0.09 \text{ \AA}$ , with  $H\beta_{max,disk} = 3.6 \pm 0.2 \text{ \AA}$  and  $H\beta_{min,disk} = 1.1 \pm 0.1 \text{ \AA}$ . In figure 5.8, we compare cuts through our data to the values by S10. While the individual measurements sometimes deviate, the overall trends are similar, with the overall agreement being within 10%. As in the comparison plots of the stellar velocity dispersion in chapter 3, we don't reproduce the spike in the very center, because we lack resolution there.

The Mg b index, as an  $\alpha$ -element important for the measurement of the  $\alpha/Fe$ -overabundance, is plotted in figure 5.3. The overall appearance of the map has higher values along the position angle  $PA_{sep} = 50^\circ$ , roughly the direction where the bar is expected. The median value is  $Mg\ b = 4.0 \pm 0.1 \text{ \AA}$ , with  $Mg\ b_{max} = 4.5 \pm 0.09$  in the very center and  $Mg\ b_{min} = 2.0 \pm 0.3 \text{ \AA}$  in the outermost disk pointing at  $PA = 5^\circ$ . We define a bar region, where the distance to a line with  $PA_{sep}$  is larger than  $270''$  and where the distance along  $PA_{sep}$  is smaller than  $600''$ , which is the projected bar length in B16. This region is overplotted as a rectangle in figure 5.3. Measuring the values inside that region, we get  $Mg\ b_{bar} = 4.1 \pm 0.1 \text{ \AA}$ , with  $Mg\ b_{bar,max} = 4.4 \pm 0.8 \text{ \AA}$  and  $Mg\ b_{bar,min} = 3.7 \pm 0.1 \text{ \AA}$ . Outside of this region, the values are lower, with  $Mg\ b_{out} = 3.7 \pm 0.1 \text{ \AA}$ , with  $Mg\ b_{out,max} = 4.4 \pm 0.1 \text{ \AA}$  along the disk major axis and  $Mg\ b_{outer,min} = 2.0 \pm 0.3 \text{ \AA}$  for the outermost pointing along  $PA = 5^\circ$ . In figure 5.9, we compare our data again to the values from S10. Here, the agreement is better than for  $H\beta$ , the values agreeing within 3%.

The iron indices are also elongated along the bar direction, but the edge of the bar area is not as sharp as for the Mg b index. The index Fe5015 in figure

5.4 has a median value of  $\text{Fe}5015 = 4.7 \pm 0.2 \text{ \AA}$ , with  $\text{Fe}5015_{max} = 5.7 \pm 0.2 \text{ \AA}$  for the middle disk pointing along the southern disk major axis and the minimum at  $\text{Fe}5015_{min} = 2.7 \pm 0.5 \text{ \AA}$  in the outermost disk pointing along  $\text{PA}=5^\circ$ , where also Mg b had its lowest value. For the bar region, defined in the same way as for Mg b, the values are  $\text{Fe}5015_{bar} = 4.8 \pm 0.2 \text{ \AA}$ , with  $\text{Fe}5015_{bar,max} = 5.2 \pm 0.1$  and  $\text{Fe}5015_{bar,min} = 4.5 \pm 0.2$ . Outside the bar region, we get  $\text{Fe}5015_{out} = 4.5 \pm 0.2 \text{ \AA}$ , with  $\text{Fe}5015_{out,max} = 5.7 \pm 0.2 \text{ \AA}$  and  $\text{Fe}5015_{out,min} = 2.7 \pm 0.5 \text{ \AA}$ . The comparison with S10 in figure 5.10 shows an agreement within 7%.

For Fe5270 in figure 5.5, we measure  $\text{Fe}5270 = 2.7 \pm 0.1 \text{ \AA}$ , with  $\text{Fe}5270_{max} = 3.2 \pm 0.2 \text{ \AA}$  at the middle disk pointing along the southern disk major axis and  $\text{Fe}5270_{min} = 0.64 \pm 0.34 \text{ \AA}$  at the outermost disk pointing along  $\text{PA}=5^\circ$ . For the bar region, the median value is  $\text{Fe}5270_{bar} = 2.7 \pm 0.1 \text{ \AA}$ , with  $\text{Fe}5270_{bar,max} = 2.9 \pm 0.1 \text{ \AA}$  and  $\text{Fe}5270_{bar,min} = 2.4 \pm 0.1 \text{ \AA}$ . Outside the bar, the values are  $\text{Fe}5270_{out} = 2.5 \pm 0.2 \text{ \AA}$ ,  $\text{Fe}5270_{out,max} = 3.3 \pm 0.2 \text{ \AA}$  at the outermost disk pointing at  $\text{PA}=275^\circ$  and  $\text{Fe}5270_{out,min} = 0.64 \pm 0.34 \text{ \AA}$ . Comparing again with S10 in figure 5.11, we get an agreement to within 5%.

Looking at Fe5335 in figure 5.6, the median value we get is  $\text{Fe}5335 = 2.5 \pm 0.1 \text{ \AA}$ , with  $\text{Fe}5335_{max} = 3.1 \pm 0.3 \text{ \AA}$  at the outermost disk pointing at  $\text{PA}=185^\circ$ , and the minimum value  $\text{Fe}5335_{min} = 1.5 \pm 0.1 \text{ \AA}$  near to the center. In the bar region, the values are  $\text{Fe}5335_{bar} = 2.5 \pm 0.1 \text{ \AA}$ , with  $\text{Fe}5335_{bar,max} = 3.0 \pm 0.2 \text{ \AA}$  for the disk pointing at  $(900'', -400'')$  and  $\text{Fe}5335_{bar,min} = 1.5 \pm 0.1 \text{ \AA}$ , being again the minimum value in the center. Outside the bar, the values are  $\text{Fe}5335_{out} = 2.4 \pm 0.2 \text{ \AA}$ , with  $\text{Fe}5335_{out,max} = 3.1 \pm 0.3 \text{ \AA}$  and  $\text{Fe}5335_{out,min} = 1.4 \pm 0.2 \text{ \AA}$  in the bulge region along the minor axis. Comparing again with S10 in 5.12, we get an agreement to within 8%.

For Fe5406 in figure 5.7, the measured values are  $\text{Fe}5406 = 1.6 \pm 0.1 \text{ \AA}$ , with  $\text{Fe}5406_{max} = 3.7 \pm 0.3 \text{ \AA}$  at the outermost disk pointing at  $\text{PA}=5^\circ$ , and the minimum value  $\text{Fe}5406_{min} = 0.0 \pm 0.2 \text{ \AA}$  at the outermost disk pointing along  $\text{PA}=275^\circ$ . The bar region, which is a bit more patchy than for the other iron indices, has the values  $\text{Fe}5406_{bar} = 1.6 \pm 0.1 \text{ \AA}$ , with  $\text{Fe}5406_{bar,max} = 2.0 \pm 0.1 \text{ \AA}$  and  $\text{Fe}5406_{bar,min} = 1.3 \pm 0.1 \text{ \AA}$ . Outside the bar, the values are  $\text{Fe}5406_{out} = 1.5 \pm 0.1 \text{ \AA}$ ,  $\text{Fe}5406_{out,max} = 3.7 \pm 0.3 \text{ \AA}$  and the minimum  $\text{Fe}5406_{out,min} = 0.0 \pm 0.2 \text{ \AA}$ . The agreement with the cuts by S10 in 5.13 is 6%.

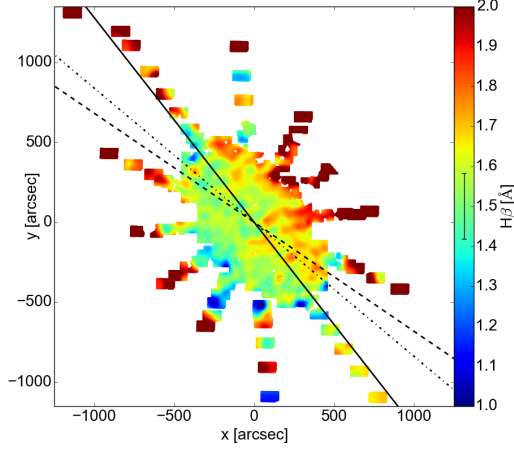


**Figure 5.2:** Map of the Lick index  $H\beta$  with the disk major axis (solid line), the bar major axis (dashed line) and the angle  $PA_{sep} = 50^\circ$  (dash-dotted line). The median errorbar is plotted in the colorbar.

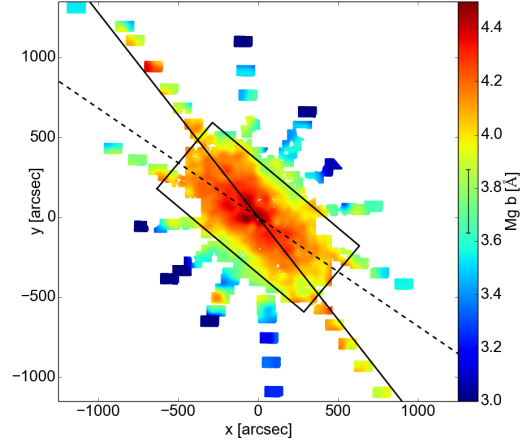


**Figure 5.3:** Map of the Lick index  $Mg\ b$  with the disk major axis (solid line), the bar major axis (dashed line) and the bar region as defined in the text (rectangle). The median errorbar is plotted in the colorbar.

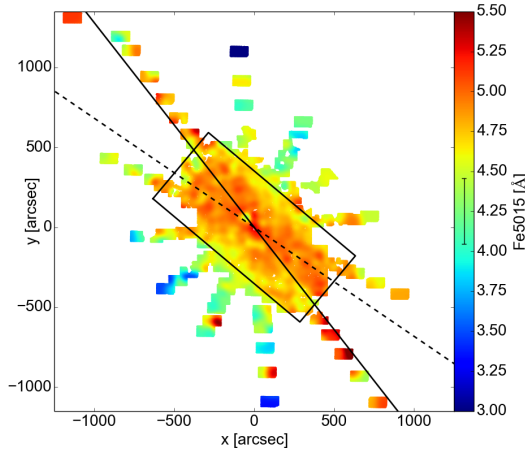


**Figure 5.4:** Map of the Lick index  $Fe5015$ , the lines are the same as in figure 5.3.

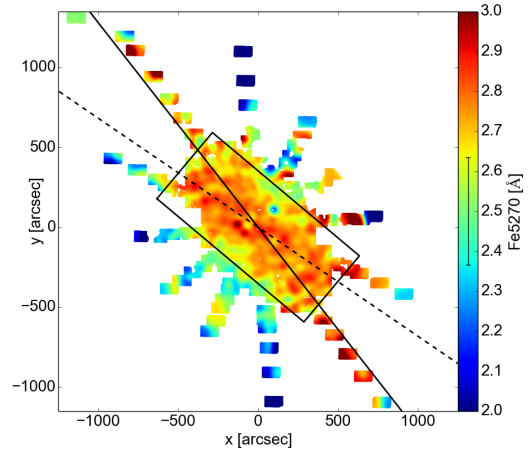


**Figure 5.5:** Map of the Lick index  $Fe5270$ , the lines are the same as in figure 5.3.

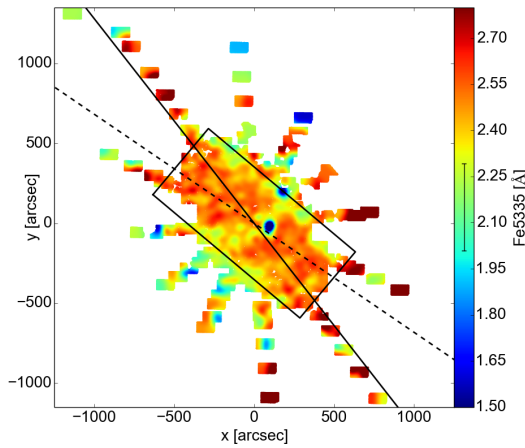


**Figure 5.6:** Map of the Lick index  $Fe5335$ , the lines are the same as in figure 5.3.

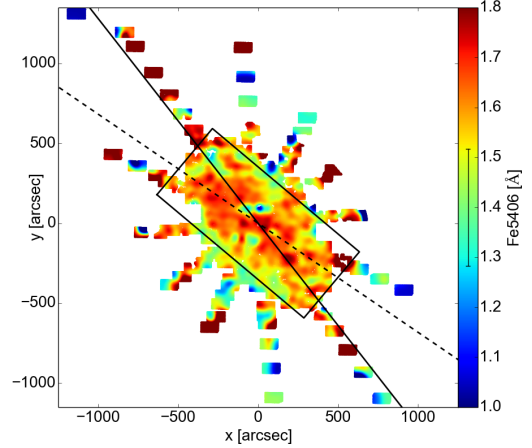


**Figure 5.7:** Map of the Lick index  $Fe5406$ , the lines are the same as in figure 5.3.

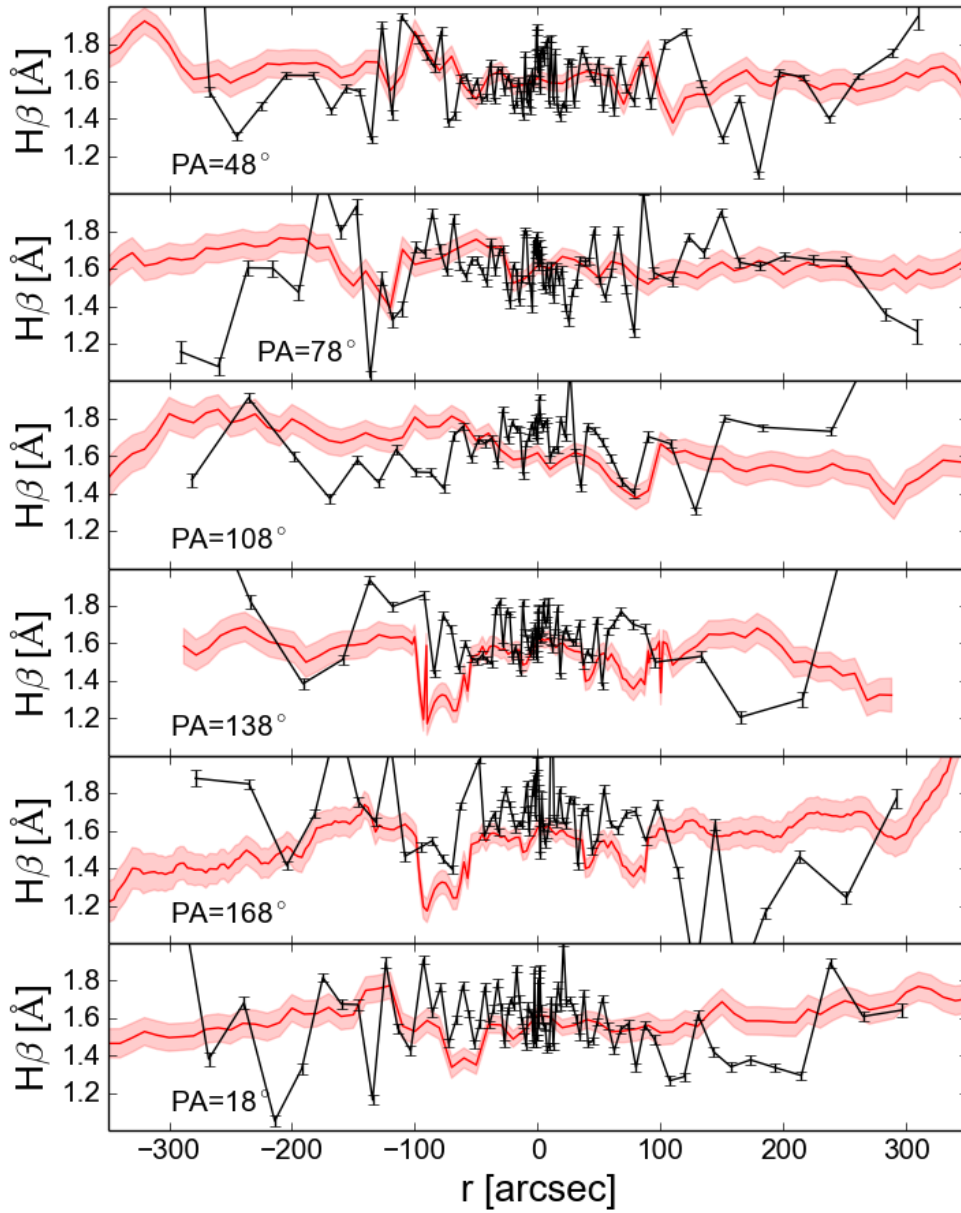


**Figure 5.8:** Cuts through the  $H\beta$  map from figure 5.2 (red) compared to data from S10 (black).

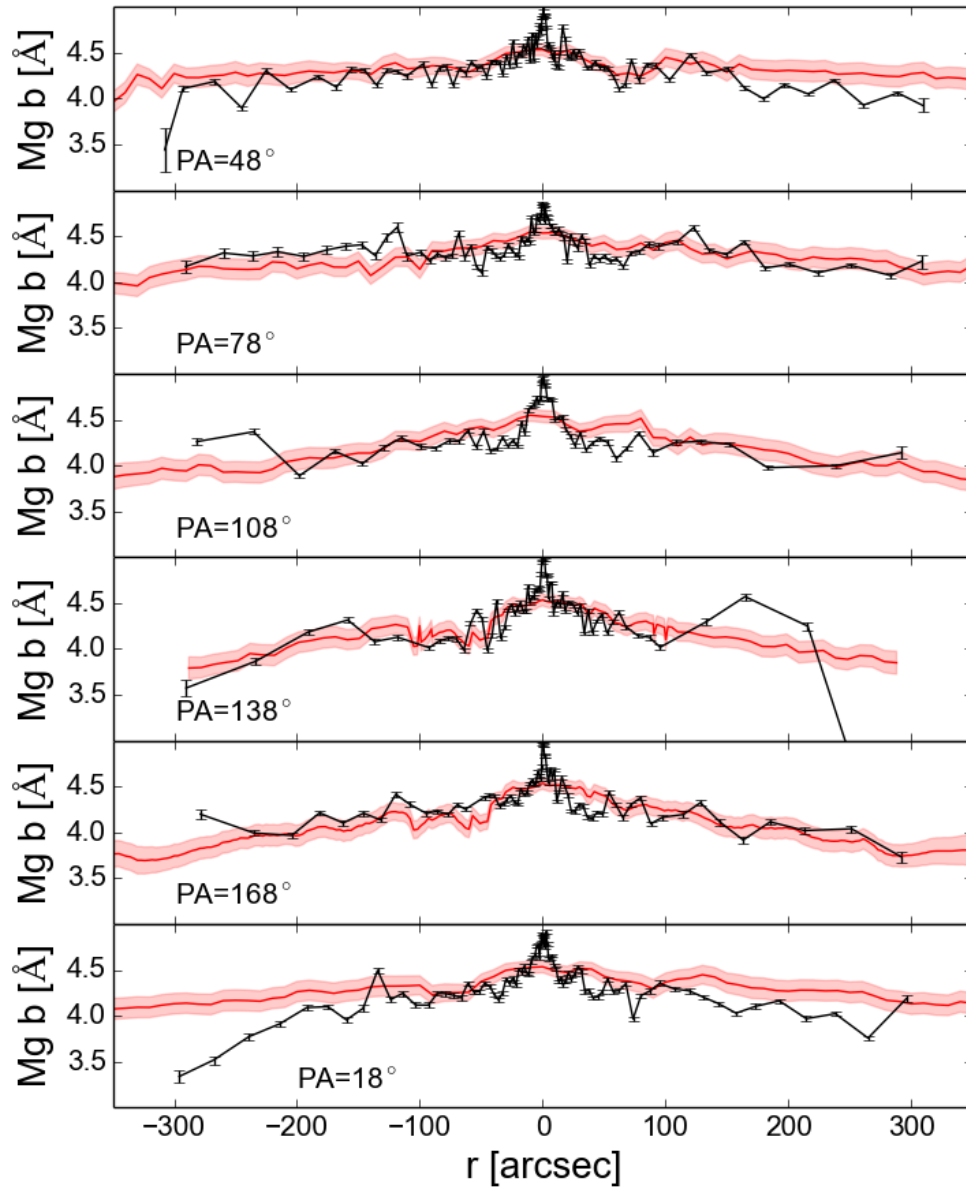


**Figure 5.9:** Cuts through the Mg b map from figure 5.3 (red) compared to data from S10 (black).

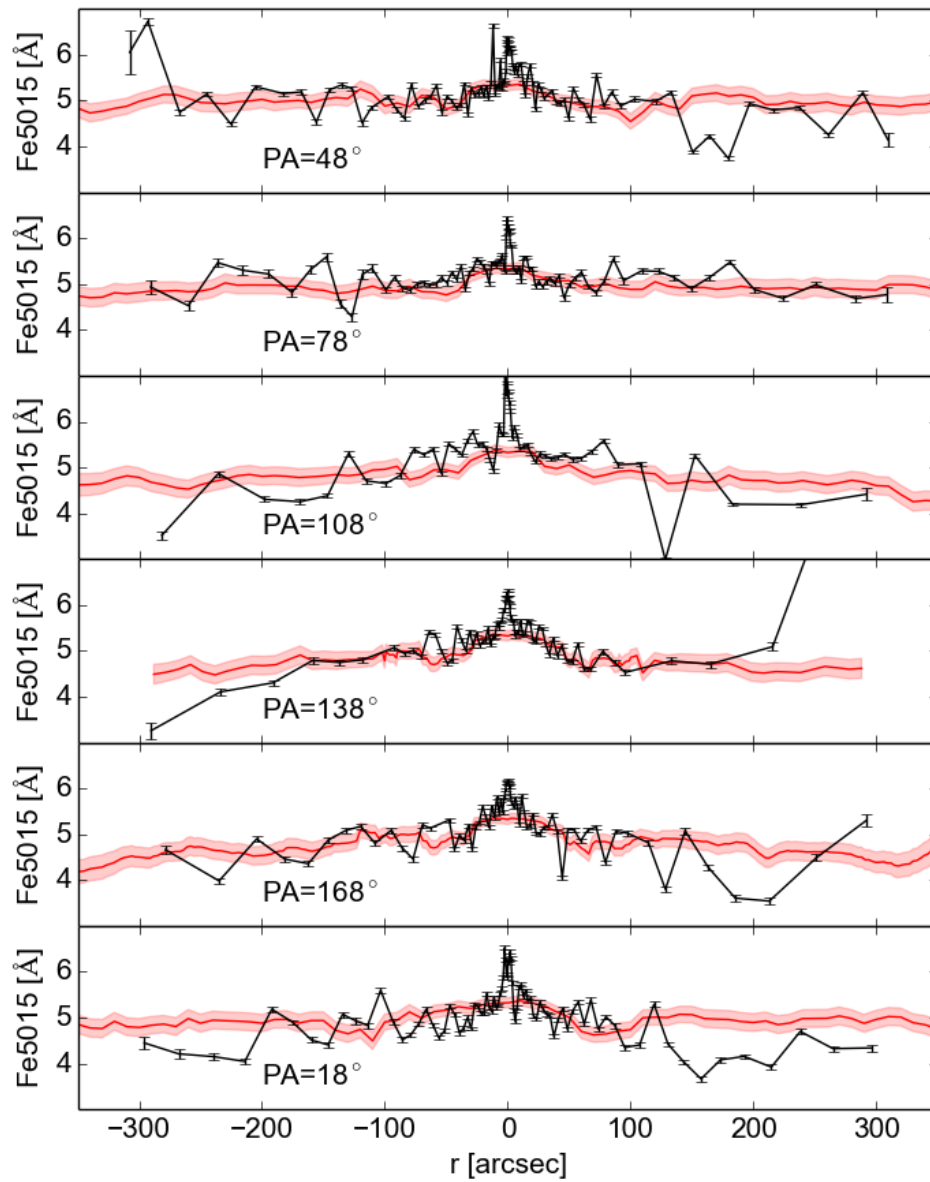


**Figure 5.10:** Cuts through the Fe5015 map from figure 5.4 (red) compared to data from S10 (black).

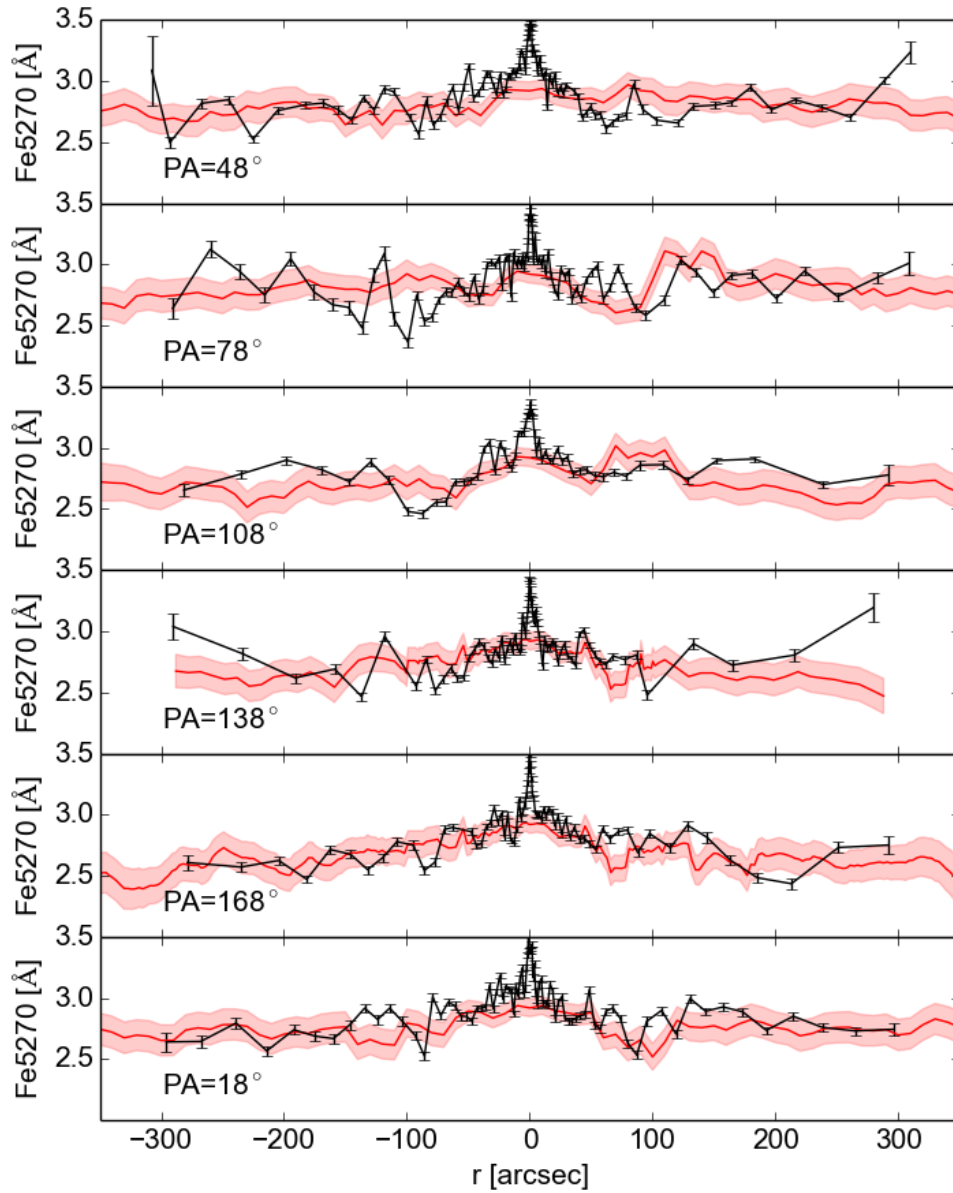


**Figure 5.11:** Cuts through the Fe5270 map from figure 5.5 (red) compared to data from S10 (black).

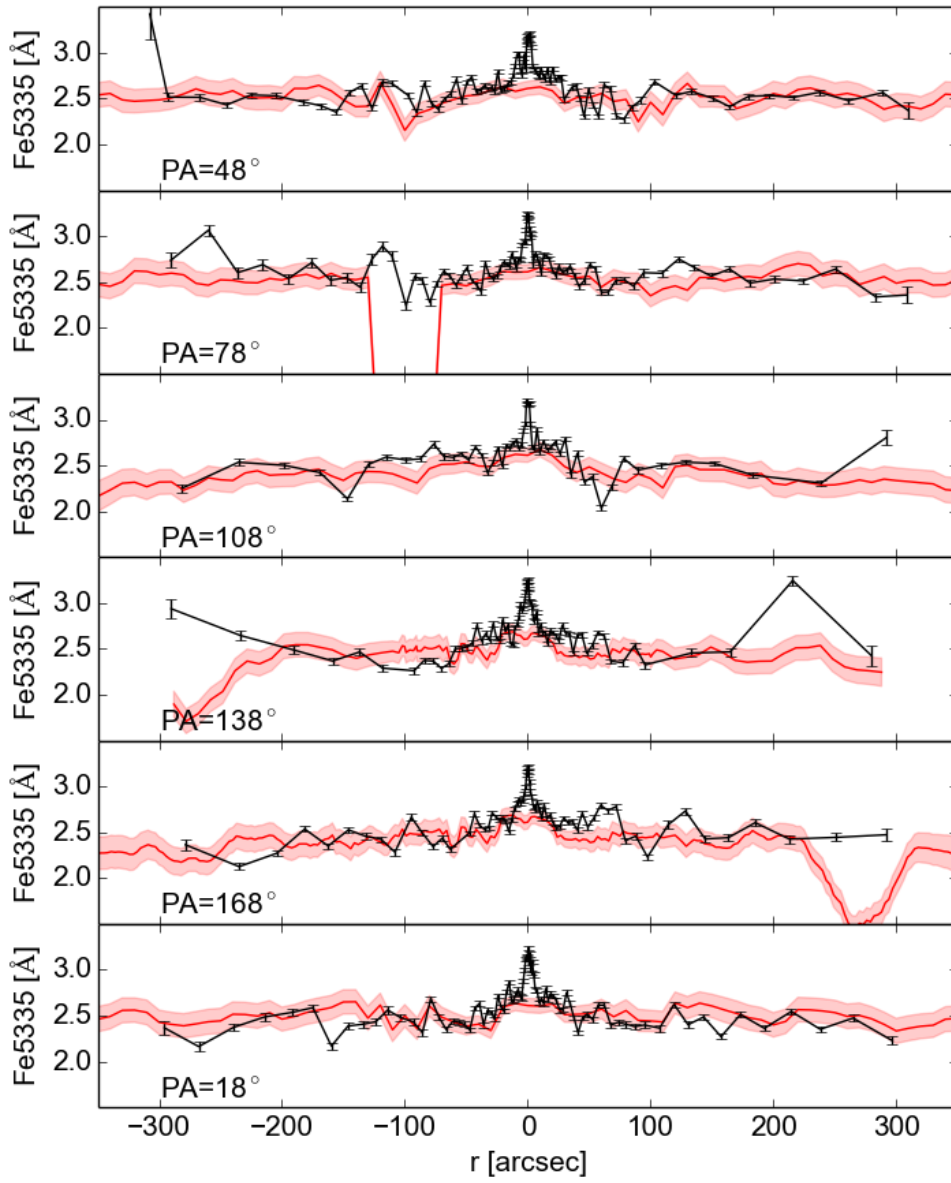


**Figure 5.12:** Cuts through the Fe5335 map from figure 5.6 (red) compared to data from S10 (black).

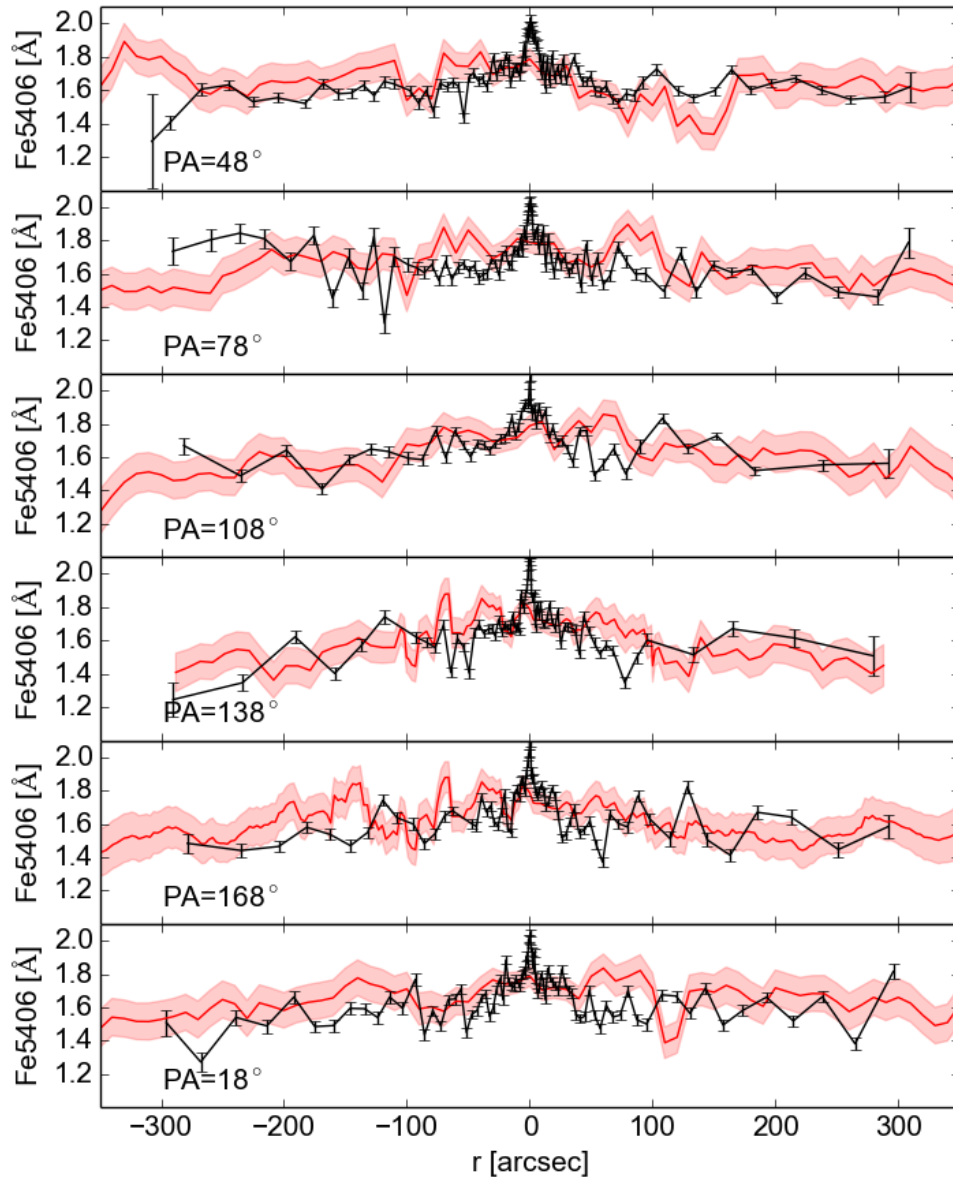


**Figure 5.13:** Cuts through the Fe5406 map from figure 5.7 (red) compared to data from S10 (black).

## 5.2 Stellar population analysis

We adopt the method by S10 to measure stellar population properties. We assume that a spectrum of M31 is well represented by one single stellar population, which is chemically homogeneous and in which all stars have the same age.

For these populations we take simple stellar population (SSP) models from Maraston (1998, 2005), which are combined with a Kroupa (2001) initial mass function and models for  $\alpha$ /Fe-overabundance by Thomas et al. (2003). For the SSP models, the spectral line indices are calculated, as well as the values of their stellar age, their metallicity  $[Z/H]$  and the  $\alpha$ /Fe-overabundance.

The metallicity is defined as  $[Z/H] = \log(Z/Z_\odot) - \log(H/H_\odot)$ , i.e. the total abundance of heavy elements with respect to hydrogen, normalized to solar values. The  $\alpha$ /Fe-overabundance is analogous to  $[Z/H]$ :  $[\alpha/Fe] = \log(\alpha/\alpha_\odot) - \log(Fe/Fe_\odot)$ .  $\alpha$ -elements are created by successive capture of  $\alpha$  particles and therefore separated by a step of 2 in atomic number in the periodic table.  $\alpha$ -elements are released into the interstellar medium on a timescale of  $\approx 10^7$  years by supernovae of type II, which also produce Fe, but the bulk of Fe is released by supernovae of type Ia on longer timescales of  $\approx 10^9$  years (Nissen, 2013). Therefore, the  $\alpha$ /Fe is indicative of how long ago star formation has taken place. From the absorption line indices we measure, only Mg is an  $\alpha$ -element.

The measured Lick indices are compared to the Lick indices in the models. Where the best agreement is found, the model values of age,  $[Z/H]$  and  $\alpha$ /Fe are then taken as the values for the measurements.

### 5.2.1 Measurements

Since the original models by Maraston (1998, 2005) are relatively coarse, they are interpolated onto a finer grid, ranging in age from 0.1 to 15.0 *Gyr* with a stepsize of 0.1 *Gyr*, in metallicity from -2.25 to 0.67 with a stepsize of 0.07, and in  $\alpha$ /Fe-overabundance from -0.3 to 0.5 with a stepsize of 0.05.

The measured Lick index value for binned spectrum  $n$  is compared to the ones in the model grid. For each gridpoint  $i$ ,  $\chi^2(i)$  is calculated.

$$\chi_n^2(i) = \Delta H\beta_n(i)^2 + \Delta Mg b_n(i)^2 + \Delta Fe5270_n(i)^2 + \Delta Fe5335_n(i)^2 + \Delta Fe5406_n(i)^2 \quad (5.2)$$

$\Delta Index(i)^2$  is:

$$\Delta Index(i)^2 = \left( \frac{Index_{measured,n} - Index_{grid}(i)}{dIndex_{measured,n}} \right)^2 \quad (5.3)$$

The index Fe5015 is excluded from the analysis, because of a systematic offset between the measurements and the grid model values. The grid index  $i$  for which  $\chi^2(i)$  is minimal is determined and the values for age  $age_{fit}(i)$ , metallicity  $[Z/H]_{fit}(i)$  and overabundance  $(\alpha/Fe)_{fit}(i)$  are then taken as the values for

the stellar populations. The errors are estimated by quoting the range of values for which  $\chi_n^2 - \min(\chi_n^2) \leq 1$ . Since we do not extrapolate the SSP model grids, sometimes the minimum value is right at the edge of the grid.

The resulting maps of the Lick indices from the SSP models are plotted in figures 5.14 to 5.18. The agreement between the measured and the SSP values is worst for Fe5270, with the median relative difference being 5%, and best for Mg b, where it is better than 1%.

The age obtained from the SSP modeling is plotted in figure 5.19. Like the map of  $H\beta$  in figure 5.2, the overall distribution is asymmetric, with lower values in the upper half relative to the disk major axis and higher ones in the lower half. The median age value is  $\text{age} = 11.2 \pm 1.2$  Gyr, with a maximum  $\text{age}_{max} = 15.0 \pm 0.2$  Gyr in the inner disk pointings in the lower half, and a minimum value of  $\text{age}_{min} = 0.72 \pm 0.05$  Gyr in the outermost disk pointing at  $\text{PA}=335^\circ$ . In the upper half, the median age is  $\text{age}_{upper}=10.4 \pm 1.2$  Gyr, with the maximum  $\text{age}_{upper,max}=14.9 \pm 0.4$  Gyr in the second to outermost disk pointing along  $\text{PA}= 5^\circ$  and the minimum at  $\text{age}_{upper,min}=0.72 \pm 0.05$  Gyr at the outermost pointing along  $\text{PA}= 335^\circ$ . In the lower half, the values are higher, with  $\text{age}_{lower}=11.9 \pm 1.1$  Gyr, with the maximum  $\text{age}_{upper,max}=15.0 \pm 0.2$  Gyr in the disk pointing at  $(-206'', -484'')$  and the minimum value  $\text{age}_{min}=1.84 \pm 0.3$  Gyr at the outermost disk pointing along  $\text{PA}= 65^\circ$ . Comparing bulge and disk, the bulge has the values  $\text{age}_{bulge}=11.4 \pm 1.2$  Gyr, with  $\text{age}_{bulge,max}=13.9 \pm 0.9$  Gyr and  $\text{age}_{bulge,min}=6.7 \pm 1.4$  Gyr. The bar region, defined in the same way as before for the Lick indices, has almost identical values. The age in the disk is slightly lower,  $\text{age}_{disk}=10.9 \pm 1.1$  Gyr, with  $\text{age}_{disk,max}=15.0 \pm 0.2$  Gyr and  $\text{age}_{disk,min}=0.72 \pm 0.05$  Gyr.

The comparison of our age measurements with the measurements by S10 are plotted in 5.22. While there is much scatter, in general both datasets agree within the errors. The younger population that S10 find in the innermost 5 arcseconds is not seen in our data, because we don't have the spatial resolution that far in.

The metallicity in figure 5.20 clearly shows an elongation along the bar position angle, like the Mg b and the iron indices. From a visual inspection, the angle along which the values are elongated seems to be  $\text{PA}=50^\circ$ . The median value is  $[Z/H] = 0.03$ , with the median errorbar 0.06. The maximum metallicity is  $[Z/H]_{max} = 0.65 \pm 0.02$  in the disk pointing at  $(600'', 50'')$  and the minimum is  $[Z/H]_{min} = -0.30 \pm 0.06$  in the outermost pointing along the minor axis on the near side. For the bar region, the values are  $[Z/H]_{bar} = 0.05$ , with the median errorbar being 0.05, with the maximum  $[Z/H]_{bar,max} = 0.21 \pm 0.04$  in the very center and the minimum  $[Z/H]_{bar,min} = -0.10 \pm 0.04$  at the edges of the bar region. Outside the bar region, the values are  $[Z/H]_{out} = -0.03$  with the median errorbar 0.06. The maximum metallicity is  $[Z/H]_{out,max} = 0.65 \pm 0.02$  and the minimum  $[Z/H]_{out,min} = -0.30 \pm 0.06$ . In figure 5.23, the comparison of our data with the data from S10 is shown. The values agree to within 10%.

The  $\alpha/\text{Fe}$ -overabundance map is plotted in figure 5.21.  $\alpha/\text{Fe}$  stays relatively constant over the whole area, neither showing the overall asymmetry of the age

map nor the elongation of the metallicity along the bar. The median value is  $\alpha/\text{Fe} = 0.21 \pm 0.04$ , the maximum value is  $\alpha/\text{Fe}_{max} = 0.5 \pm 0.01$  at the disk pointing at  $(730'', 60'')$ , the minimum is  $\alpha/\text{Fe}_{min} = -0.25 \pm 0.05$  in the outermost disk pointing at  $(-320'', -650'')$ . In the bulge region, the median value is  $\alpha/\text{Fe}_{bulge} = 0.21 \pm 0.03$  with the maximum value  $\alpha/\text{Fe}_{bulge,max} = 0.33 \pm 0.04$  and the minimum value  $\alpha/\text{Fe}_{bulge,min} = 0.08 \pm 0.03$ . In the disk, the median value is very similar with  $\alpha/\text{Fe}_{disk} = 0.20 \pm 0.04$ , but the maximum and minimum values are more extreme, with  $\alpha/\text{Fe}_{disk,max} = 0.5 \pm 0.01$  and the minimum value  $\alpha/\text{Fe}_{disk,min} = -0.25 \pm 0.05$ . In figure 5.24, we show the comparison of our data to the one by S10. Our values mostly agree within the errorbars.

### 5.2.2 Discussion

As shown above, the old age in the bulge is in agreement with S10 within the errors. They find a single uniform bulge population of ages higher than 12 Gyr, while our median bulge value is  $\text{age}_{bulge} = 11.4 \pm 1.2$  Gyr. We do not detect the young population in the central  $5''$ , because we do not resolve it. The values for metallicity that we measure agree with the ones from S10 and are higher than the ones by Sarajedini & Jablonka (2005), who obtain a mean metallicity similar to the solar metallicity. Gregersen et al. (2015) calculate the metallicity using observed individual red giant branch stars outside  $R \approx 720''$ . They measure a decline of the metallicity outside that radius, which is not seen in our data. However, they assume a constant age of 4 Gyr for their data, which is significantly lower than the ages we measure at  $R \approx 720''$ . The fact that the gradient of the metallicity is less steep along the bar major axis is another hint for a bar, since bars tend to flatten the index gradients (Seidel et al., 2016).

Cuts through the metallicity maps along the bar major axis from B16 (PA=55.7°) and the minor axis (PA=145.7°) are plotted in figure 5.25. The profile along the bar minor axis is steeper than along the bar major axis, with the major axis profile changing slope at roughly  $0.13 r_{bar}$ , with  $r_{bar}=600''$  taken from B16. This is also seen in the sample of 16 large barred galaxies by Seidel et al. (2016). We fit gradients to the major and minor axis profiles from figure 5.25, plotted in figure 5.26. The gradients are similar to the results from Seidel et al. (2016). A comparison of the values is tabulated in table 5.2.

	Seidel et al. (2016)	this work
major axis gradient [dex/kpc]	$0.03 \pm 0.07$	$-0.035 \pm 0.007$
minor axis gradient [dex/kpc]	$-0.20 \pm 0.04$	$-0.21 \pm 0.01$

**Table 5.2:** Major and minor axis gradients by Seidel et al. (2016) and our own data.

In figure 5.27, we compare our gradients to the ones compiled by Seidel et al. (2016) for barred and unbarred galaxies. The measured gradient along the minor axis is very similar to values measured in barless galaxies or along the minor axis of barred galaxies. The gradient along the major axis is larger than that, therefore

implying that M31 indeed is barred. However, the gradient is at the lower edge of the distribution of the major axis gradients of the sample of barred galaxies. This can be explained by the fact that we do not sample the whole bar region with our observations and that therefore we do not measure the gradient over the whole bar length.

The very central values of the stellar populations that we measure for M31 are similar to what is seen in other galaxies. Figure 5.28 shows the stellar population values averaged in the central 250 pc for a list of galaxies compiled by [Thomas & Davies \(2006\)](#). For M31, 250 pc correspond to 66". M31 does not stand out compared to the other galaxies, while for instance the Milky Way is clearly offset in the plots.

To conclude, we can say that the age has predominantly high values in the bulge, with some drops in the disk and the  $\alpha/Fe$  is homogeneous. However, high values in metallicity are clearly elongated along the direction where the bar is expected, being a further hint for its presence.

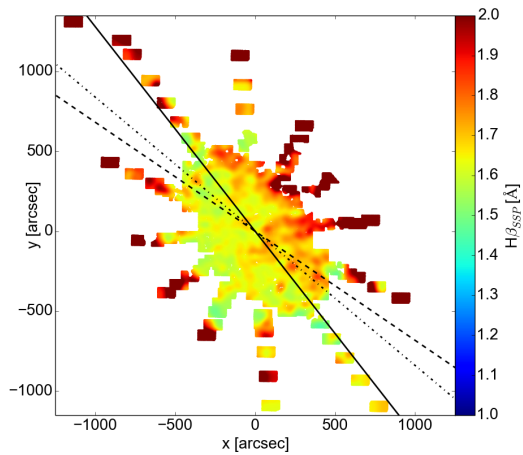


**Figure 5.14:** Map of the SSP Lick index  $H\beta$ , the lines are the same as in figure 5.2.

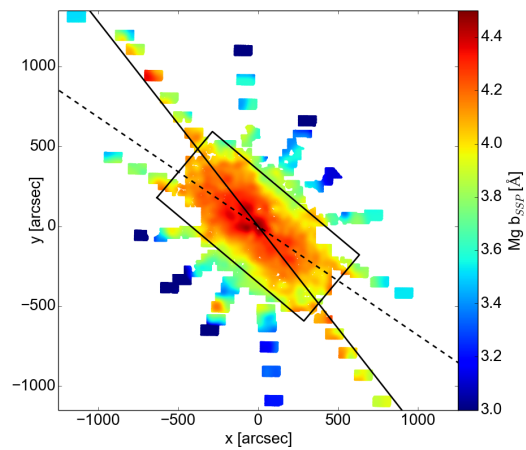


**Figure 5.15:** Map of the SSP Lick index  $Mg\ b$ , the lines are the same as in figure 5.14, the box is the bar region as defined in the text.

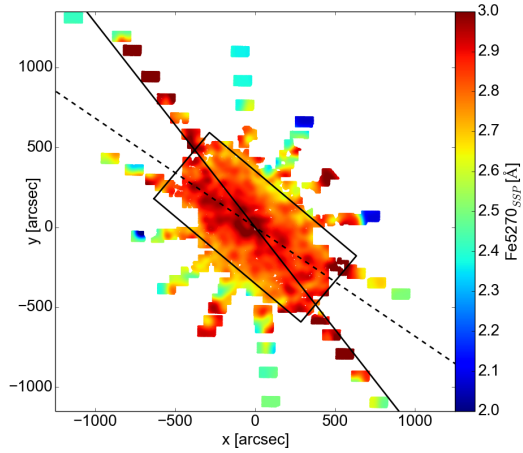


**Figure 5.16:** Map of the SSP Lick index  $Fe5270$ , the lines are the same as in figure 5.15.

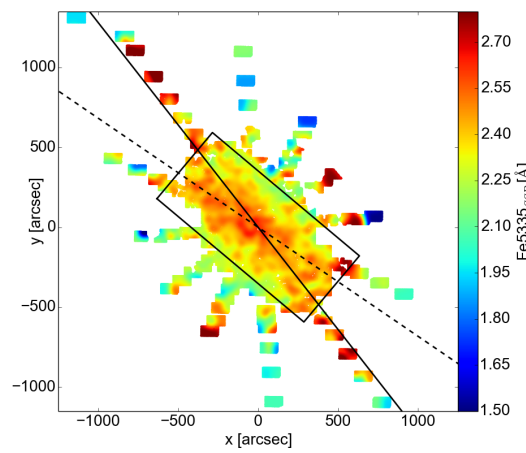


**Figure 5.17:** Map of the SSP Lick index  $Fe5335$ , the lines are the same as in figure 5.15.

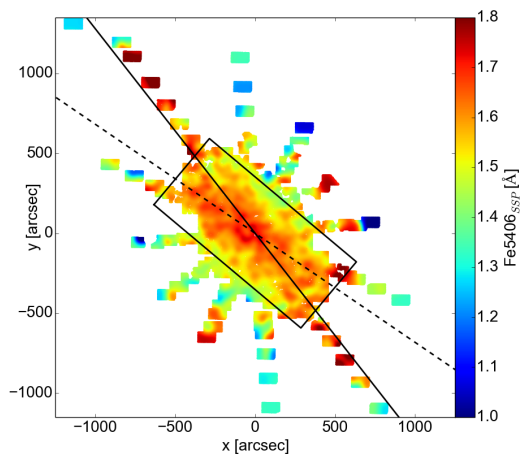


**Figure 5.18:** Map of the SSP Lick index  $Fe5406$ , the lines are the same as in figure 5.15.

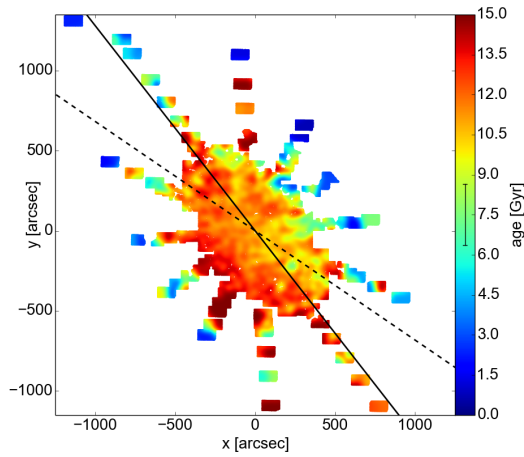


**Figure 5.19:** Age map with the disk major axis (solid), the bar major axis (dashed) and the median errorbar of the dataset (in the colorbar).

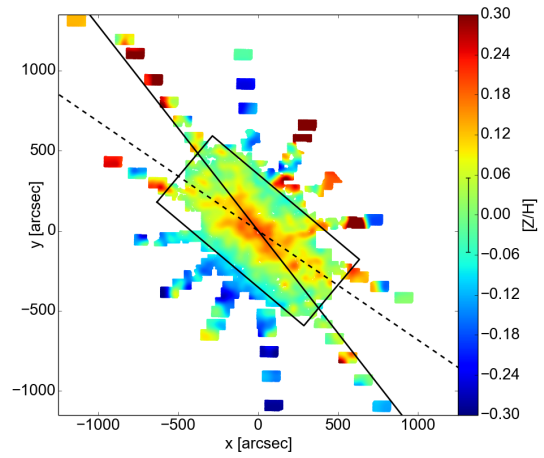


**Figure 5.20:** Metallicity map, the lines are analogous to the ones in figure 5.1.

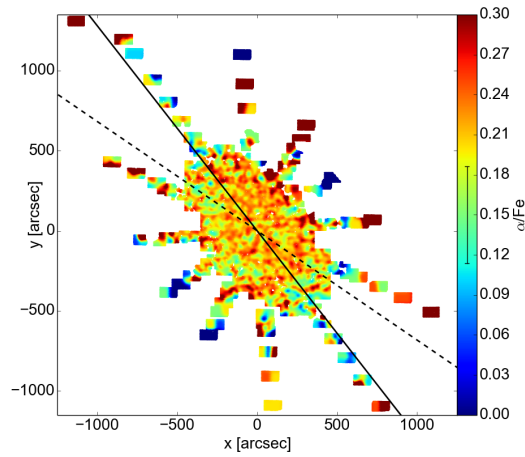


**Figure 5.21:**  $\alpha/Fe$ -overabundance map, the lines are the same as in 5.19.

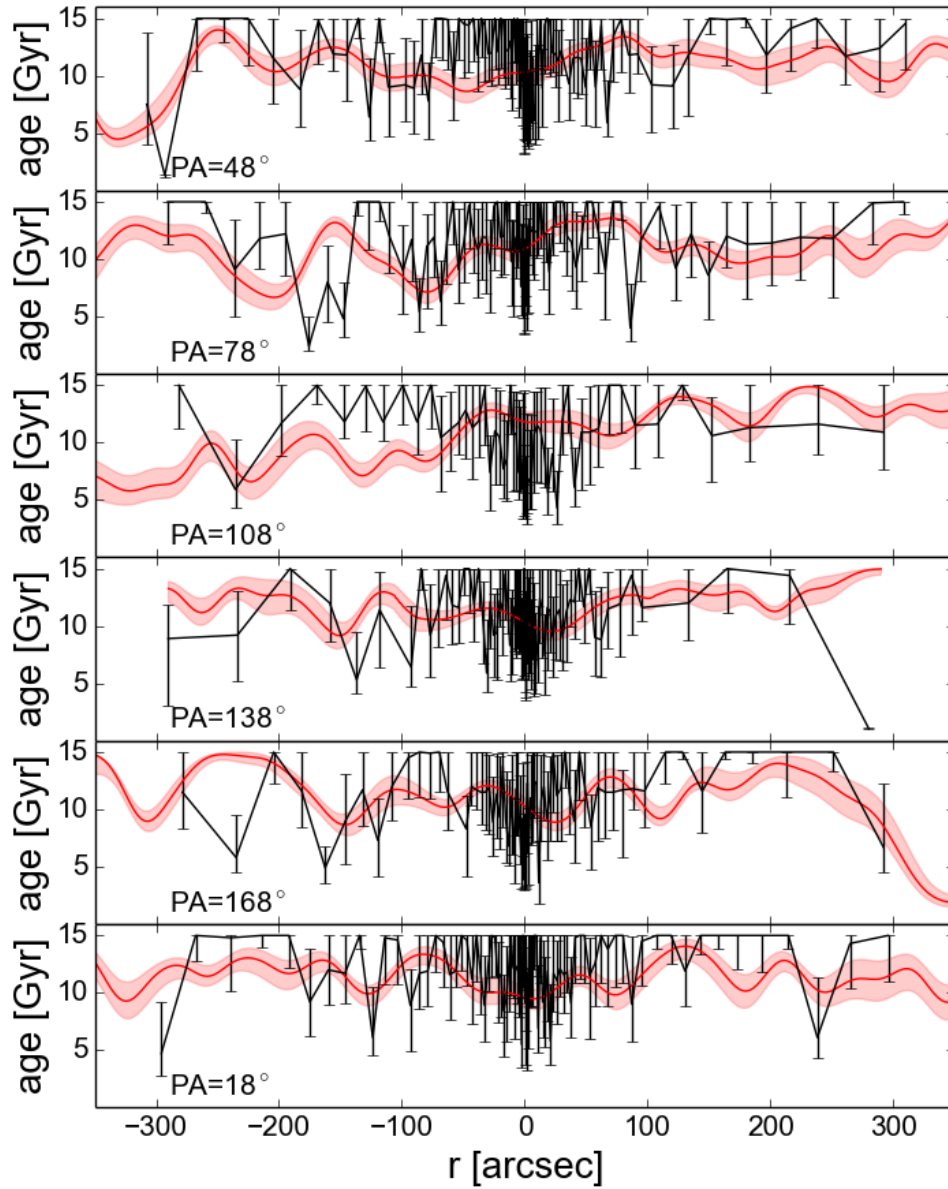


**Figure 5.22:** Cuts through our age measurements (red) compared to data from S10 (black).

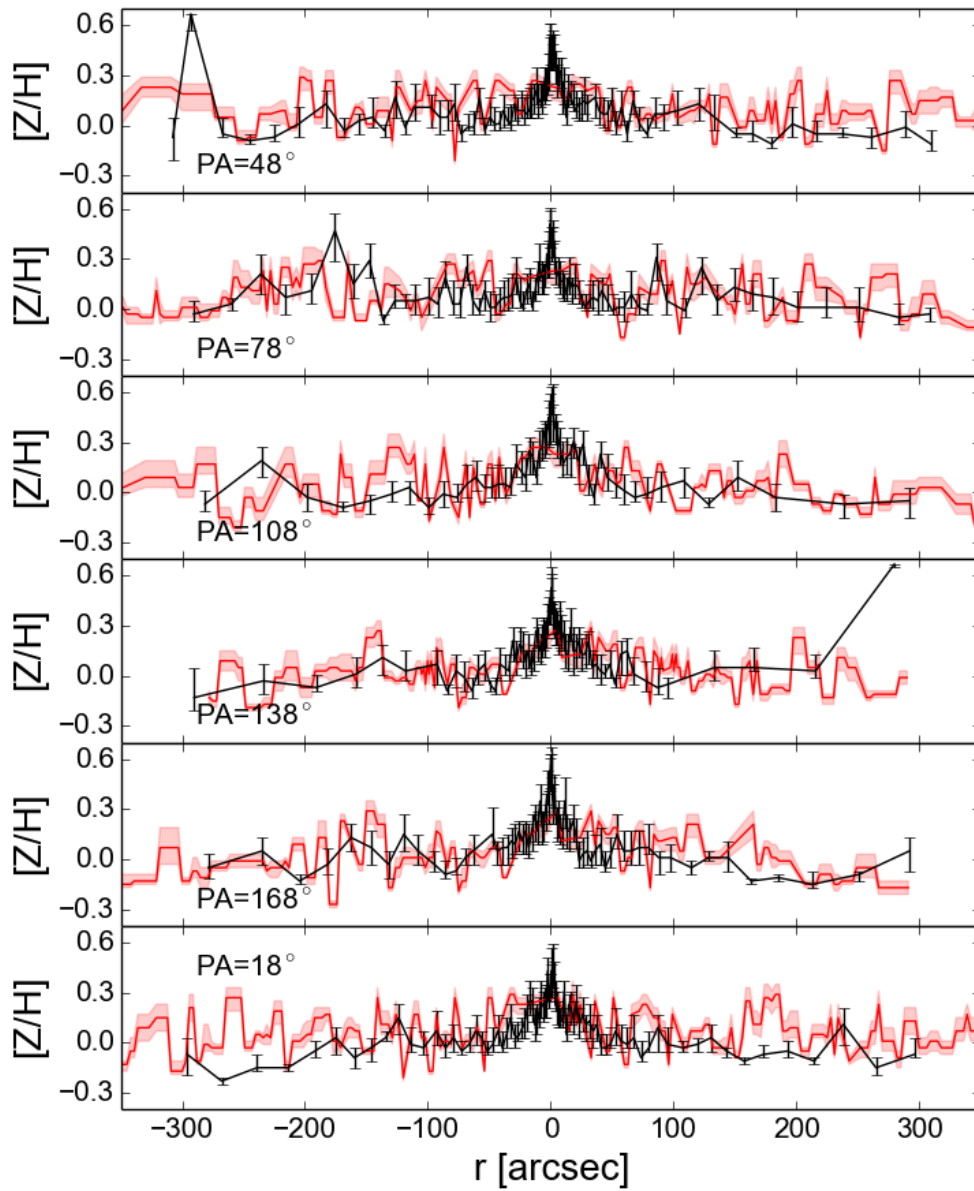


**Figure 5.23:** Cuts through our metallicity measurements (red) compared to data from S10 (black).

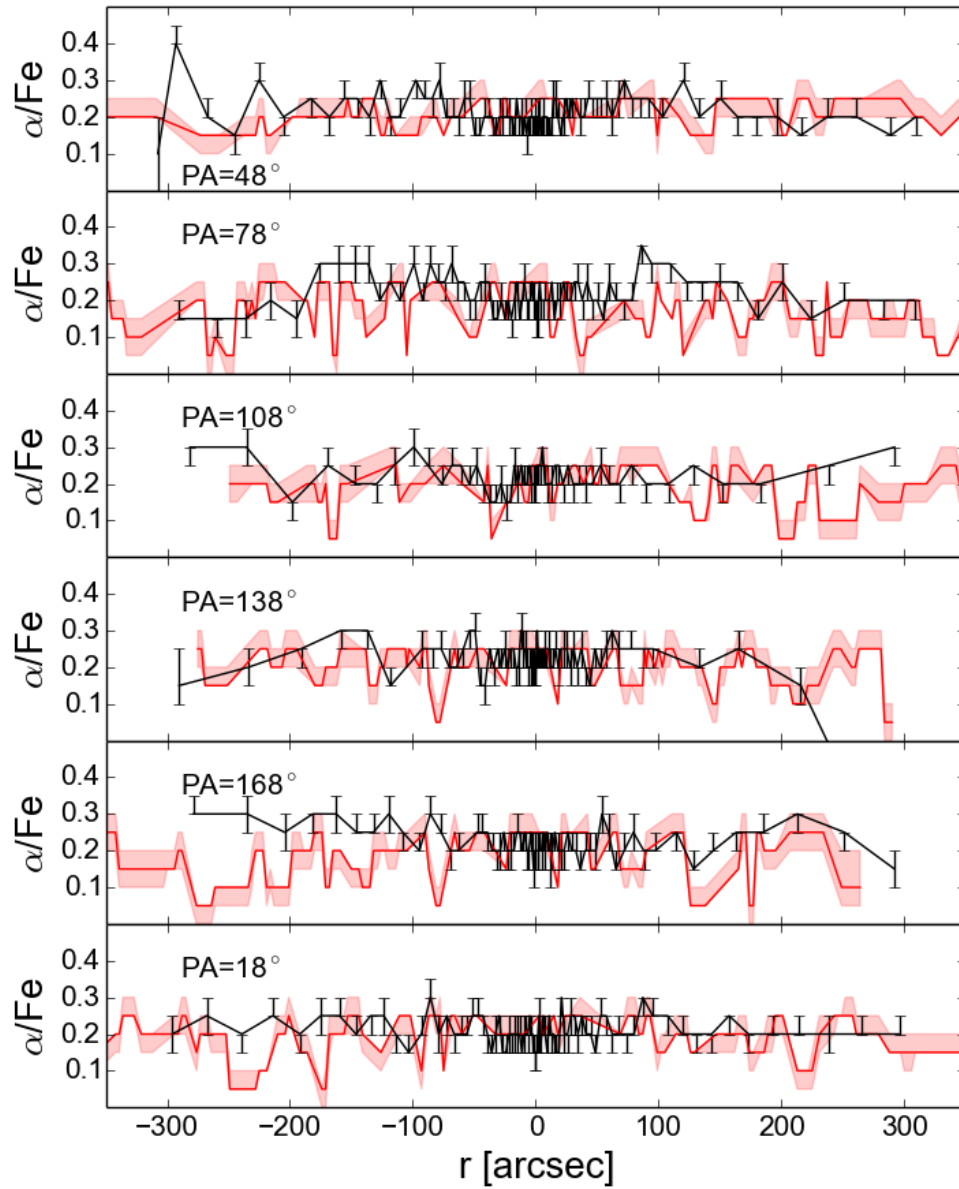


**Figure 5.24:** Cuts through our  $\alpha/\text{Fe}$  measurements (red) compared to data from S10 (black).

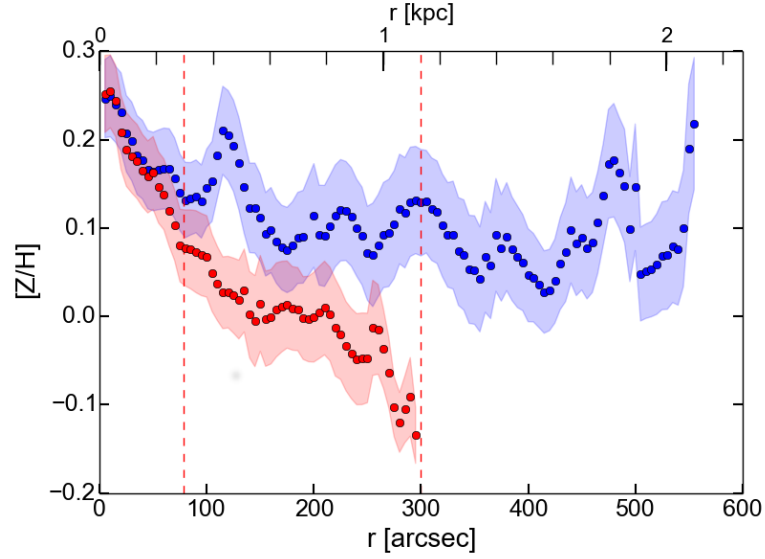


**Figure 5.25:** The metallicity profile along the bar at position angle  $PA_{bar}=55.7^\circ$  (blue) and at the bar minor axis (red). The dashed lines are  $0.13 r_{bar}$  and  $0.5 r_{bar}$ , with  $r_{bar} = 600''$ . The values are taken from B16.

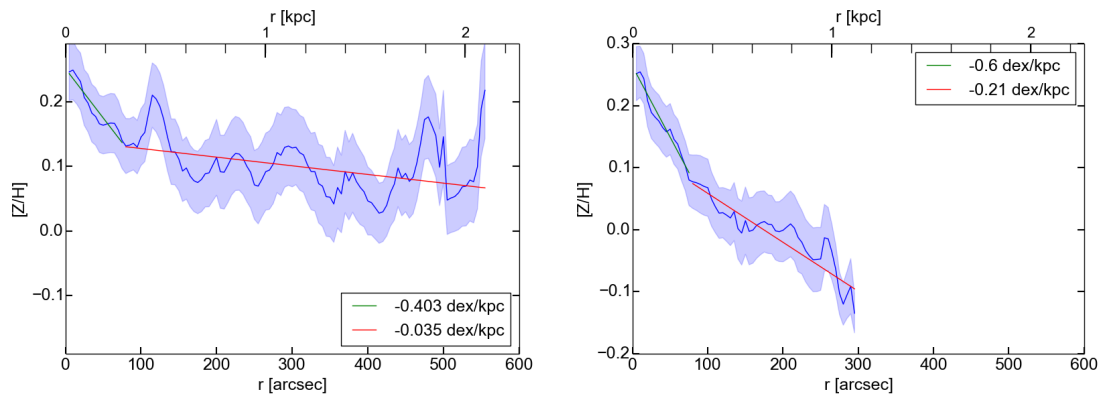


**Figure 5.26:** Fits to the profiles along the bar major axis at  $PA_{bar}=55.7^\circ$  (left) and the minor axis (right).

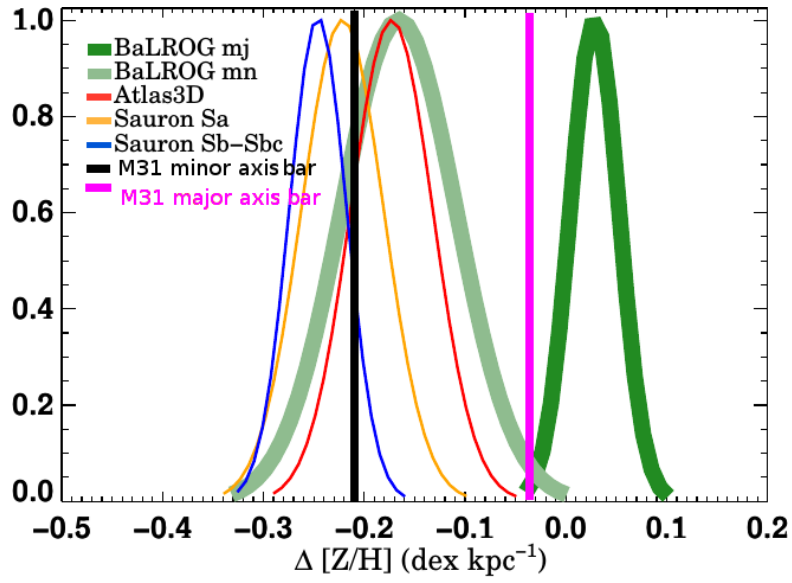


**Figure 5.27:** Comparison of the metallicity gradients measured along the major axis (magenta) and the minor axis (black) to other galaxies compiled by Seidel et al. (2016), the BaLROG galaxies are barred galaxies, galaxies from Atlas3D are ellipticals and Sauron Sa and Sb-Sbc galaxies are barless disk galaxies. The distributions have all been normalized to 1.

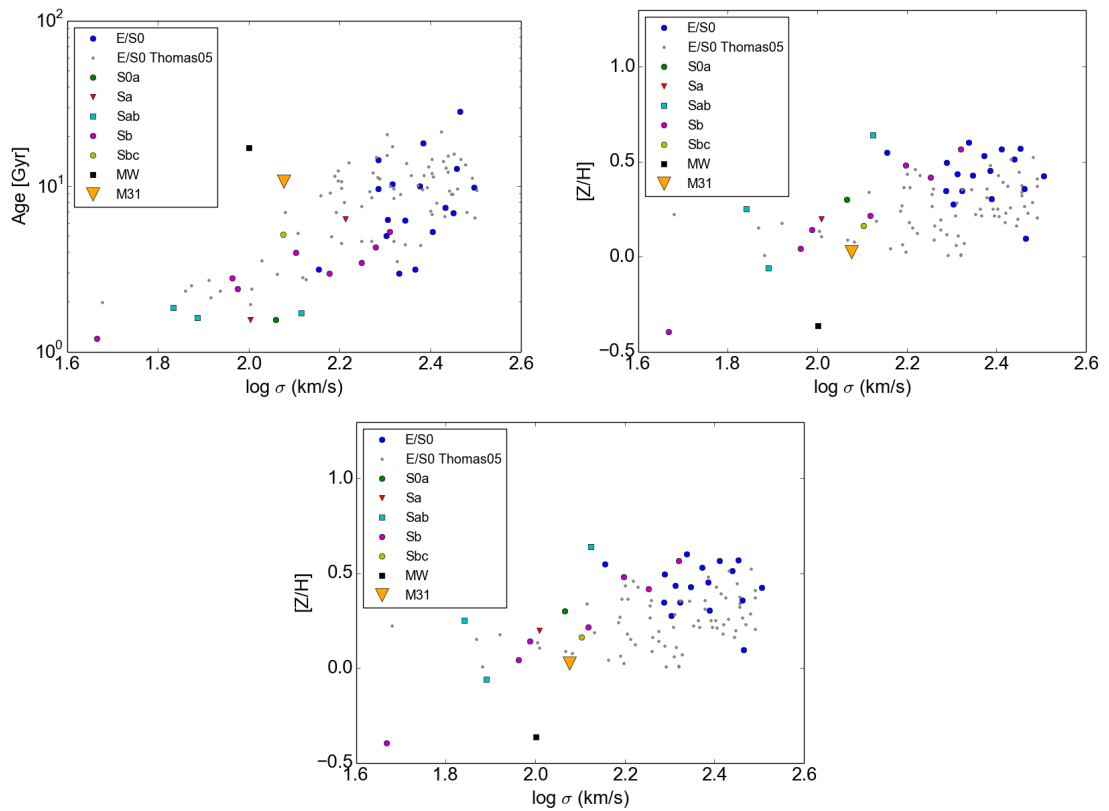


**Figure 5.28:** Comparison of stellar population values in the central 66'' with other galaxies compiled by [Thomas & Davies \(2006\)](#).



# Chapter 6

## Kinematic Decomposition

In the previous chapters, we have seen that the stellar kinematics, the gas kinematics and the metallicity are indicative of a bar in M31. However, the age map is homogeneous and does not show a trend along the bar.

In this chapter, we will investigate if it is possible to see similar stellar population trends as the measured ones in a model with only disk and bulge, i.e. without a bar. The stellar kinematics will be decomposed into a bulge and a disk component. This decomposition will be used to broaden a model bulge and a model disk spectrum, which will be combined according to the bulge-to-total ratio from the model image from section 2.3. On this combined model, Lick indices and stellar populations will be measured and compared to the observed stellar populations.

### 6.1 Fit of the LOSVD with two Gaussians

Since pPXF does a parametric fit, we essentially have for each bin the following parameters:

$$v, dv, \sigma, d\sigma, h3, dh3, h4, dh4 \quad (6.1)$$

From these, we then build the measured LOSVD:

$$\mathcal{L}(v) = \frac{\exp\left(\frac{(v-\langle v \rangle)^2}{2\sigma^2}\right)}{\sigma\sqrt{2\pi}} \left[ 1 + \sum_{m=3}^4 hm H_m\left(\frac{v-\langle v \rangle}{\sigma}\right) \right] \quad (6.2)$$

Errors on the LOSVDs are measured with a Monte Carlo method. For each bin  $i$ , 1000 LOSVDs are created, with the parameters for the LOSVD taken randomly from the intervals  $v_i \pm dv_i$ ,  $\sigma_i \pm d\sigma_i$ ,  $h3_i \pm dh3_i$  and  $h4_i \pm dh4_i$ .

For each velocity  $v$ , the error  $d\mathcal{L}(v)$  is then the standard deviation of all Monte Carlo LOSVD representations at this velocity.

An example LOSVD with errors, taken from a bin in the outer bulge region, is shown in figure 6.1.

These LOSVDs are fitted with the model fitting function  $\mathcal{F}(v)$ , which is the sum

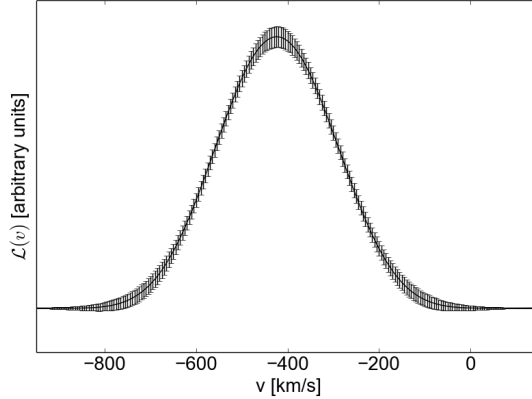


**Figure 6.1:** Example LOSVD, from a bin at the outer edge of the bulge. The LOSVD has been calculated from the values  $v$ ,  $\sigma$ ,  $h3$  and  $h4$  fitted with GANDALF. The errors have been determined with a Monte-Carlo simulation, see text.

of two Gaussians,  $\mathcal{B}(v_{bulge}, \sigma_{bulge})$  for the bulge and  $\mathcal{D}(v_{disk}, \sigma_{disk})$  for the disk.

$$\mathcal{F}(v) = \frac{B}{T} \cdot \mathcal{B}(v_{bulge}, \sigma_{bulge}) + \frac{D}{T} \cdot \mathcal{D}(v_{disk}, \sigma_{disk}) \quad (6.3)$$

For each spectrum, the  $\frac{B}{T}$  and  $\frac{D}{T}$  values are taken from the model image from section 2.3. The fit is done using a Markov-Chain-Monte-Carlo (MCMC) algorithm with the python package `pyMC`<sup>1</sup>, the code was adapted from the website of Mat Kelcey<sup>2</sup>. Several other fitting methods were tried, all giving similar results. We focused on the MCMC method because it gives an estimate of the errors. A Markov chain is a stochastic process where given the present state, past and future states are independent (Gelman & Lopes, 2006). A MCMC algorithm samples the parameter space by performing a random walk.

Our routine uses equation 6.3. The parameters  $v_{bulge}$ ,  $\sigma_{bulge}$ ,  $v_{disk}$  and  $\sigma_{disk}$  are taken randomly from uniform distributions. The values for the velocities are taken from the interval  $[-2000, 995]$  and the ones for the dispersions from  $[0, 400]$ . The routine uses  $v_{bulge}$ ,  $\sigma_{bulge}$ ,  $v_{disk}$  and  $\sigma_{disk}$  to calculate the function  $\mathcal{F}(v)$  and compares it to  $\mathcal{L}(v)$ . The chain steps through the parameter space in 100,000 steps and uses that to estimate the errors. Since the chain can start at a value far away from the actual best-fit value and can stay in that region of the parameter space for a long time, the errors can be skewed towards wrong values. Therefore, the first 50,000 representations are not used to estimate the errors.

For the LOSVD shown in figure 6.1, the sampled parameter space is plotted in figure 6.2. The problem of fitting an (almost) Gaussian LOSVD with two Gaussians is inherently degenerate, the routine converges on two different solutions most of the time. Sometimes, it finds only one and sometimes, it finds more than two, but that happens when the routine does not converge on a solution after the maximum number of representations. In figure 6.3, a map of the number of

<sup>1</sup><https://pypi.python.org/pypi/pymc>

<sup>2</sup>[http://matpalm.com/blog/2012/12/27/dead\\_simple\\_pymc](http://matpalm.com/blog/2012/12/27/dead_simple_pymc)

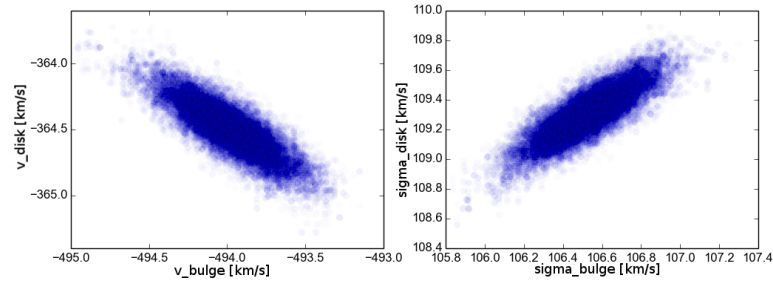


**Figure 6.2:** The sampled parameter space for the fit to the LOSVD plotted in figure 6.1.

solutions is shown. The other fitting methods that we tested also resulted in the

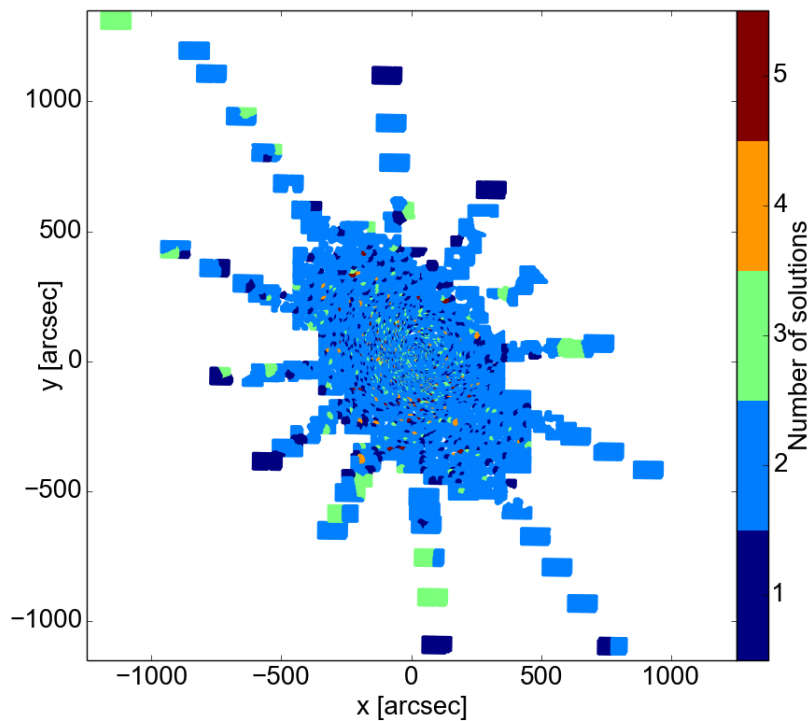


**Figure 6.3:** The number of solutions on which the fitting routine converges. For the large majority of bins, there are two solutions.

degenerate solutions. Examples of degenerate solutions are plotted in figures 6.4 and 6.5. In the example in figure 6.4, the two results are very similar and simply appear symmetric with respect to the mean velocity of the original LOSVD. For figure 6.5 they are different. In order to see how often both solutions appeared, we run the fitting routine 10 times for each bin, finding that the two solutions are found roughly equally often. We then sort them according to the value of their  $\chi^2$ .

$$\chi^2 = \sum \frac{(\mathcal{L}(v) - \mathcal{F}(v))^2}{d\mathcal{L}(v)^2} \quad (6.4)$$

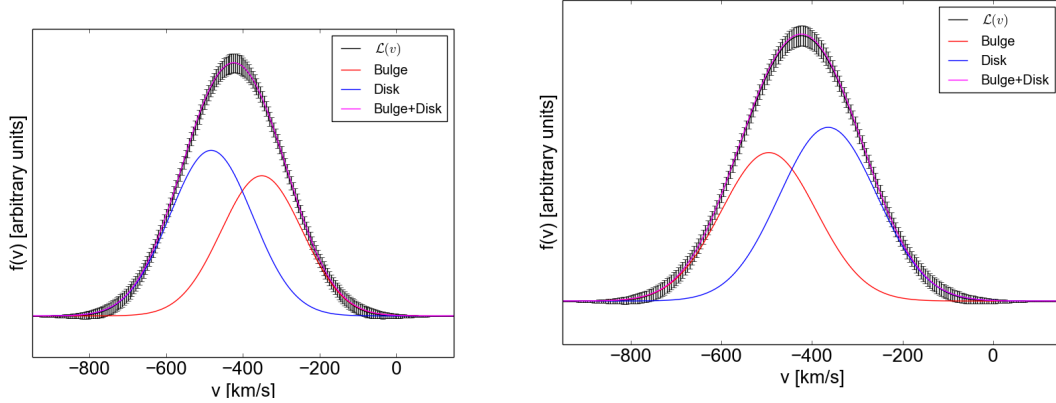


**Figure 6.4:** The two solutions for the LOSVD from figure 6.1. Plotted are  $\mathcal{L}(v)$  (black), the fitted bulge (red) and disk (blue) functions and the sum of bulge and disk (magenta). In the left panel, the fitted parameters are  $v_{bulge} = -351 \pm 7 \text{ km s}^{-1}$ ,  $\sigma_{bulge} = 106 \pm 5 \text{ km s}^{-1}$ ,  $v_{disk} = -483 \pm 6 \text{ km s}^{-1}$  and  $\sigma_{disk} = 108 \pm 5 \text{ km s}^{-1}$ , in the right panel, they are  $v_{bulge} = -495 \pm 7 \text{ km s}^{-1}$ ,  $\sigma_{bulge} = 105 \pm 5 \text{ km s}^{-1}$ ,  $v_{disk} = -364 \pm 6 \text{ km s}^{-1}$  and  $\sigma_{disk} = 108 \pm 5 \text{ km s}^{-1}$ . The bulge and disk fractions are  $\frac{B}{T} = 0.45$  and  $\frac{D}{T} = 0.55$ , respectively. The overall appearance of the bulge and disk gaussians appears symmetric. The  $\chi^2$  values (equation 6.4) are 22.56 and 22.58, respectively.

We call the one with lower  $\chi^2$  “solution 1” and the one with higher  $\chi^2$  “solution 2”. The kinematic maps for the two solutions are plotted in figures 6.6 and 6.7. A cut through the maps along the major axis (PA =  $38^\circ$ ) is plotted in figure 6.8.

Solution 1 and solution 2 look very similar in the maps, however somewhat complementary to each other. For example, it often appears that if solution 1 has a low  $v_{bulge}$  value, solution 2 will have a large one and vice versa. In the cuts in velocity, this becomes even more prominent, the velocities “oscillate”. This means that the solutions have not been sorted sufficiently, so we have to apply a two-step method. First, the solutions are sorted according to their  $\chi^2$ , like before. Then, we take a look at the velocity values. Since a bulge is dispersion dominated and a disk rotation dominated,  $v_{bulge}$  should be smaller than  $v_{disk}$ . So, if in one solution for one bin  $v_{bulge} < v_{disk}$ , but in the other we have  $v_{bulge} > v_{disk}$ , the former is sorted into solution 1 and the latter into solution 2. If both solutions show the same behavior, i.e. if in both cases,  $v_{bulge} < v_{disk}$  or  $v_{bulge} > v_{disk}$ , we keep the original sorting according to the  $\chi^2$  values. The velocity maps that result from this sorting algorithm are plotted in figures 6.9 and 6.10. We call these solutions “sorted solution 1” and “sorted solution 2”. A cut through the maps along the major axis is plotted in figure 6.11.

Now, the velocity maps look more regular. In sorted solution 1, the bulge almost has no rotation, while the disk shows the expected rotation pattern. In sorted solution 2, the bulge rotation pattern looks similar to cylindrical rotation, reminiscent of patterns seen in bulges that are spun up by galactic bars in edge-on galaxies (Saha et al., 2012). Here, the disk almost shows no rotation in the central region, but it does along the major axis in the outer regions. The velocity dispersion maps are more similar between sorted solution 1 and sorted solution 2,

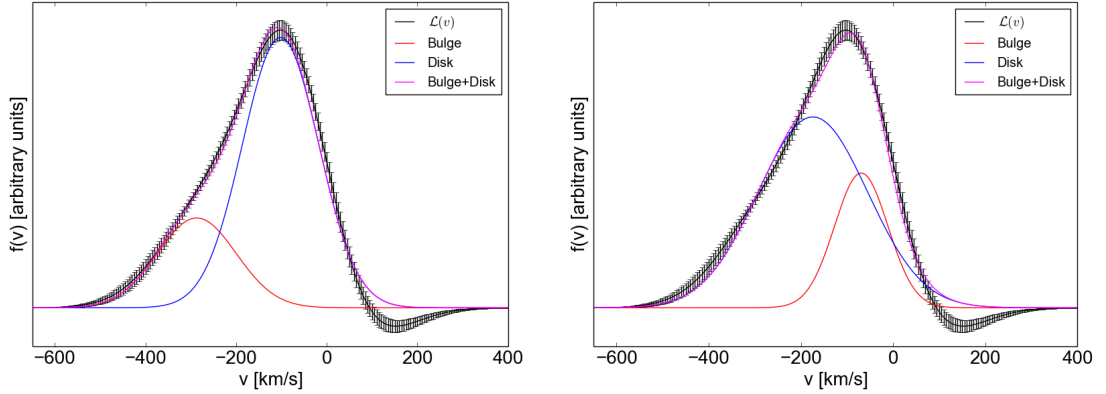


**Figure 6.5:** Two solutions shown for a different bin than the one in 6.4. In the left panel, the fitted parameters are  $v_{bulge} = -287 \pm 4 \text{ km s}^{-1}$ ,  $\sigma_{bulge} = 87 \pm 3 \text{ km s}^{-1}$ ,  $v_{disk} = -102 \pm 2 \text{ km s}^{-1}$  and  $\sigma_{disk} = 84 \pm 2 \text{ km s}^{-1}$ , in the right panel, they are  $v_{bulge} = -69 \pm 3 \text{ km s}^{-1}$ ,  $\sigma_{bulge} = 58 \pm 2 \text{ km s}^{-1}$ ,  $v_{disk} = -174 \pm 2 \text{ km s}^{-1}$  and  $\sigma_{disk} = 119 \pm 2 \text{ km s}^{-1}$ , the bulge and disk fractions are  $\frac{B}{T} = 0.26$  and  $\frac{D}{T} = 0.74$ , respectively. Here, the two solutions are not symmetric around the mean velocity of the LOSVD, unlike figure 6.4. The  $\chi^2$  values are 585.61 and 656.68. The fact that the LOSVD becomes negative is due to the  $h3$  and  $h4$  values for this LOSVD, this also explains the large  $\chi^2$  values.

$\sigma_{bulge}$  has a maximum in the center and then drops, this region of large  $\sigma_{bulge}$  is more regular for sorted solution 1.

When looking at the cuts in 6.11, sorted solution 1 represents a slowly rotating bulge with a rotation amplitude of  $50 \text{ km s}^{-1}$  and a fast rotating disk with  $200 \text{ km s}^{-1}$ . In the innermost regions, the velocity of the disk jumps to counter-rotating values, but this is because there,  $\frac{D}{T}$  is so low that it is not properly confined any more. In sorted solution 2, the bulge velocity profile slowly rises until  $500''$  before staying constant at a rotation amplitude of  $200 \text{ km s}^{-1}$ . The disk velocity fluctuates around zero until  $500''$ , before slowly rising with a similar slope as the bulge velocity. Since a disk always has to rotate, what we call the “disk” solution here is not a real disk. The separation between the two stays roughly constant at  $100 \text{ km s}^{-1}$ . The velocity dispersion profiles from figure 6.12 overall look very similar. Further out,  $\sigma_{disk}$  drops the same way as  $\sigma_{bulge}$  for sorted solution 1, while it stays roughly constant for sorted solution 2 at about  $100 \text{ km s}^{-1}$ . We reject this whole solution as unphysical.

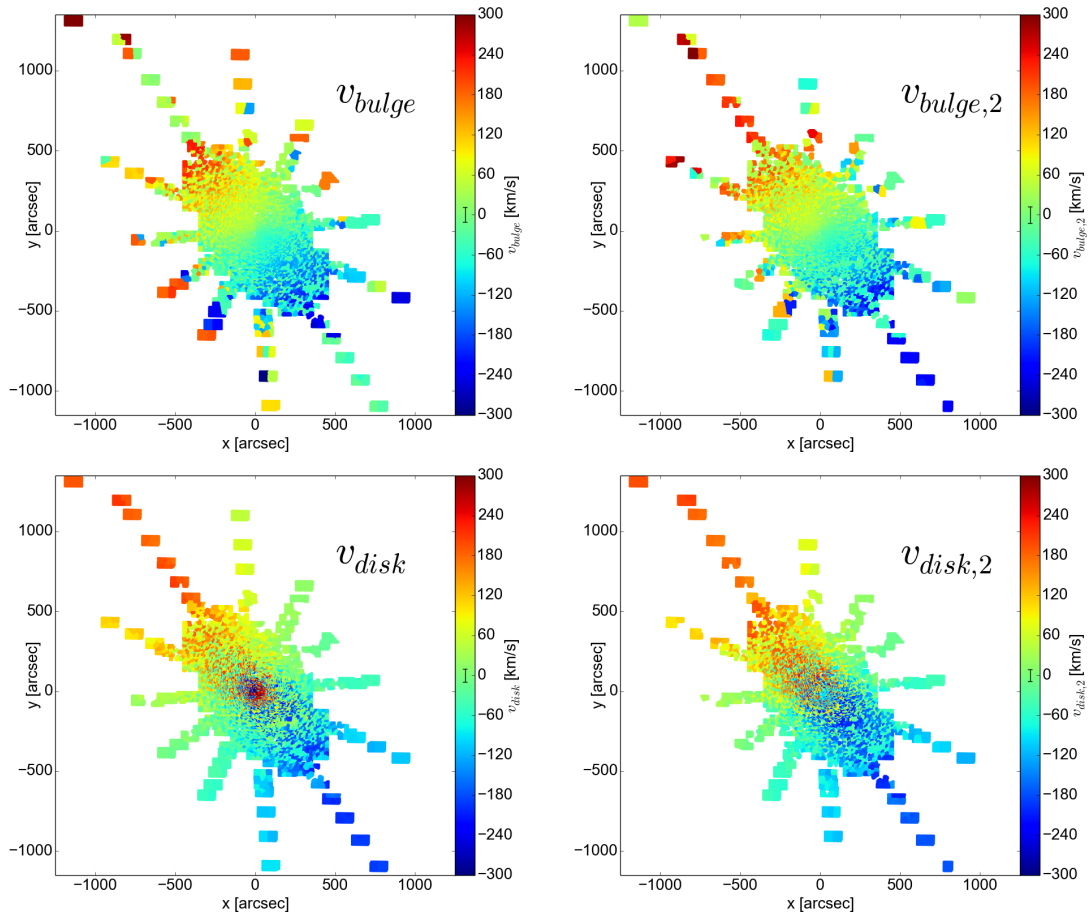


**Figure 6.6:** The velocity maps for the two solutions. The four maps are ordered as follows: The left column shows the velocities belonging to solution 1, the right column the ones belonging to solution 2, the upper row shows the bulge velocities and the lower one the disk velocities. The median errors are plotted into the colorbar.

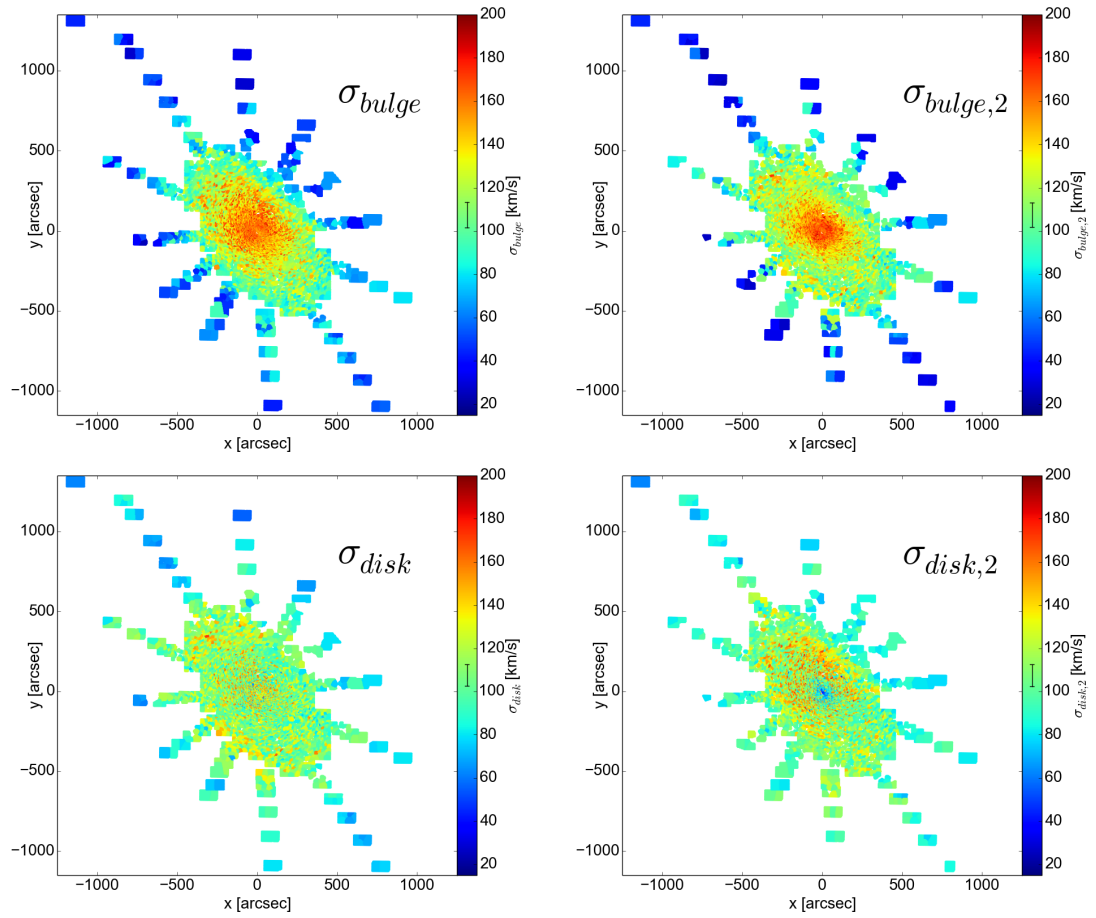


**Figure 6.7:** The velocity dispersion maps for the two solutions. The plot is analogous to figure 6.6.

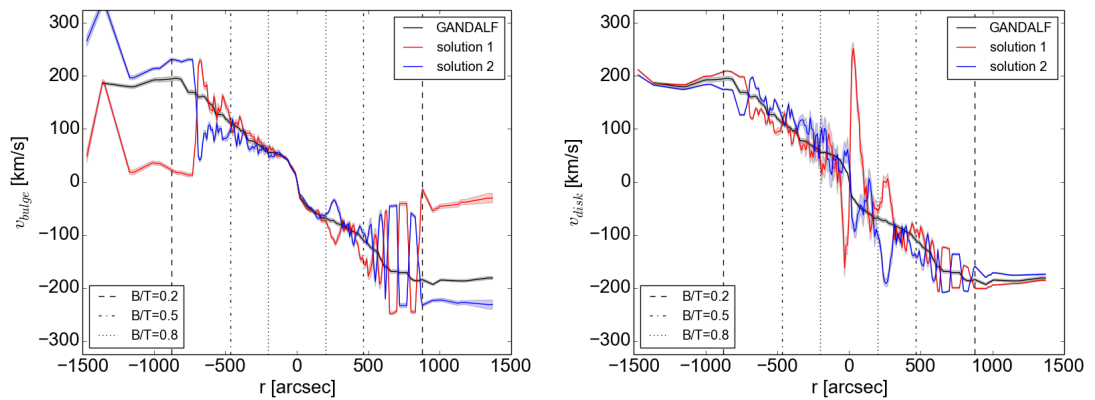


**Figure 6.8:** Cuts through the velocity maps in figure 6.6 along the disk major axis. In the left panel, the bulge velocities are shown for solution 1 (red) and solution 2 (blue). The black line is the stellar velocity profile from GANDALF. In the right panel, the same is plotted for the disk velocities.

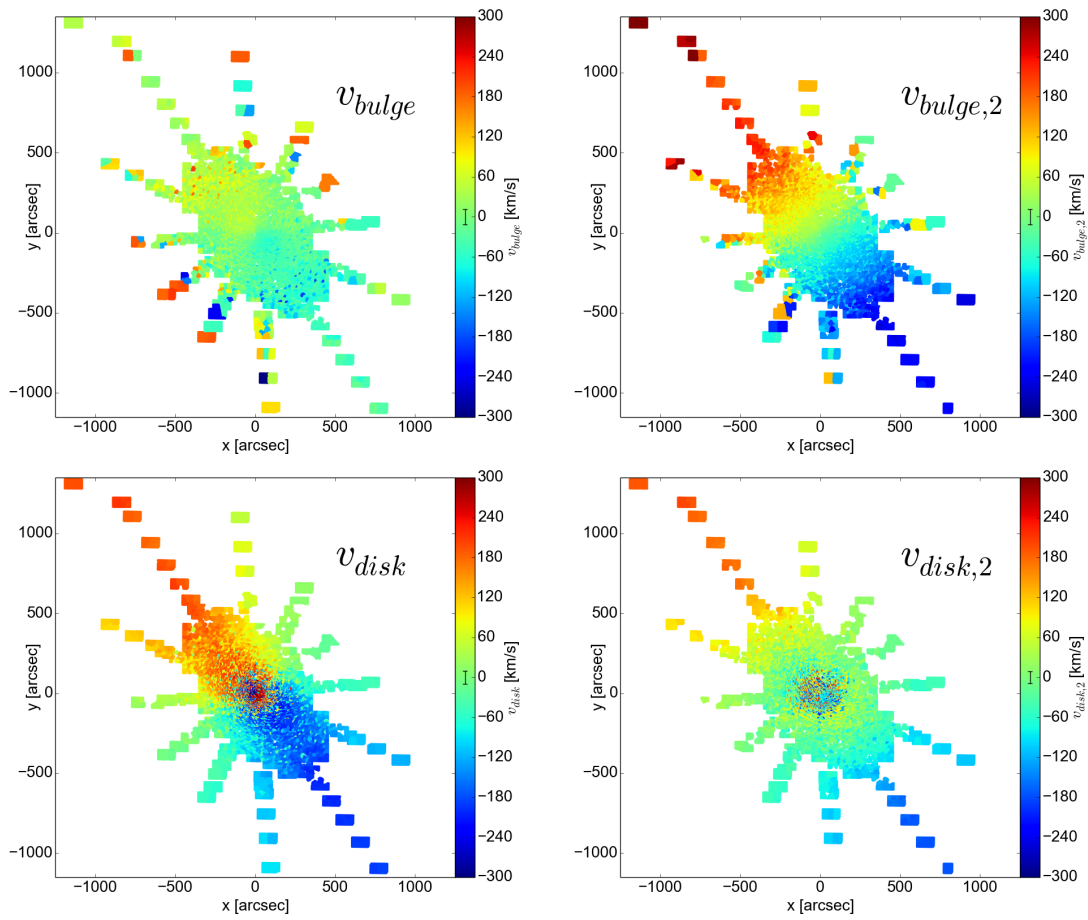


**Figure 6.9:** The velocity maps for the two sorted solutions. The plot is similar to figure 6.9.

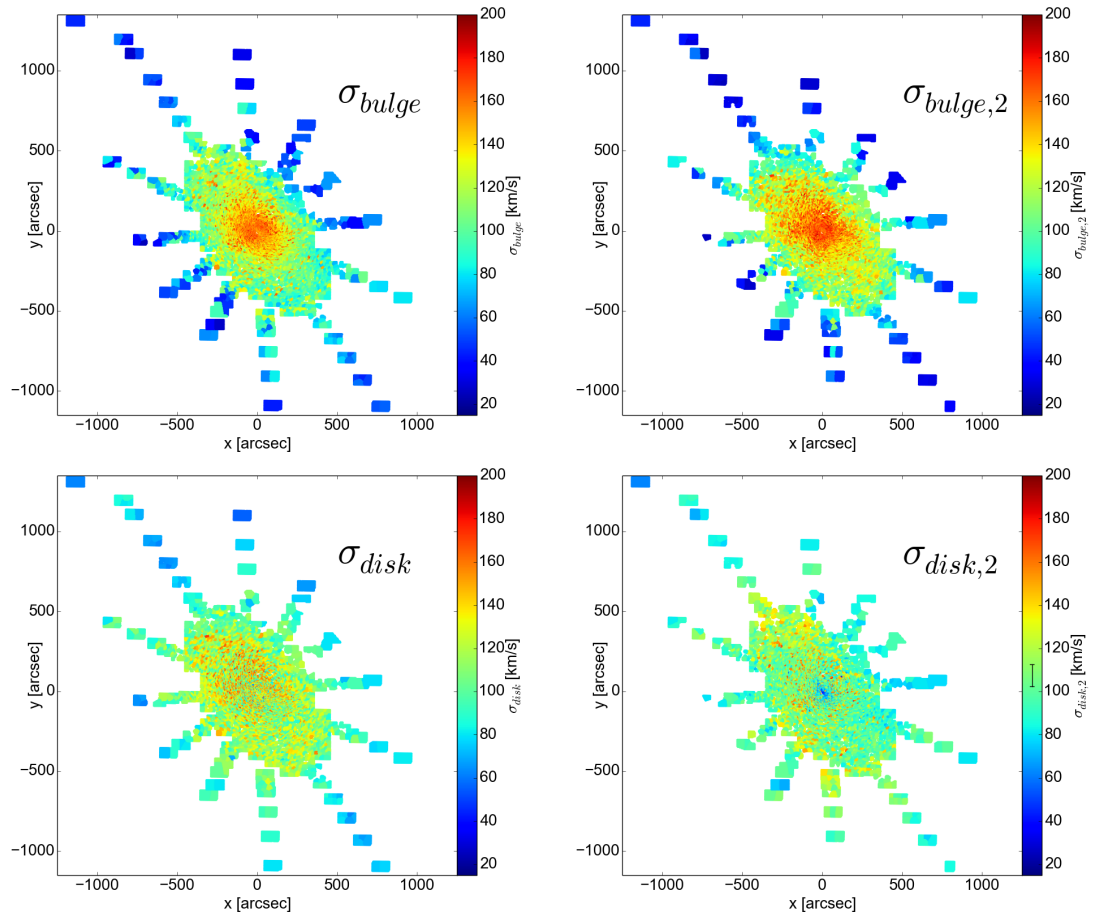


**Figure 6.10:** The velocity dispersion maps for the two sorted solutions. The plot is analogous to figure 6.7.

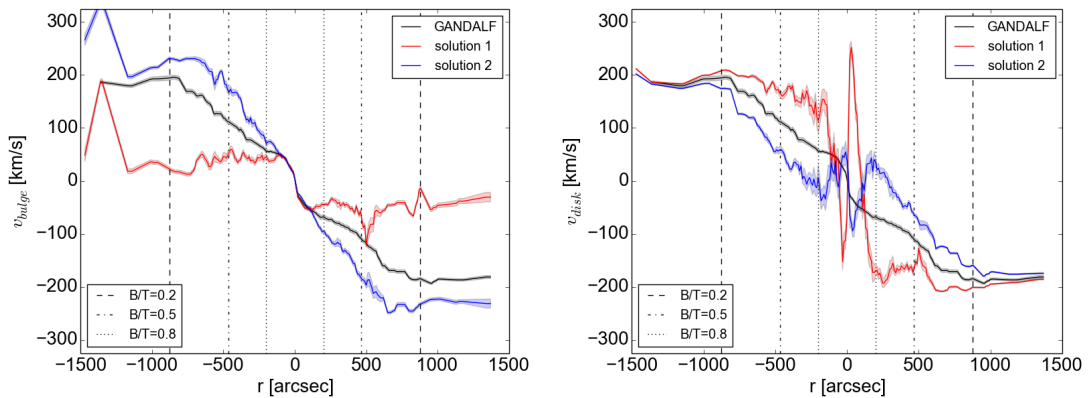


**Figure 6.11:** Cuts through the velocity maps in figure 6.9 along the disk major axis. The plot is similar to figure 6.8, the velocity profiles do not show the jumps any more.

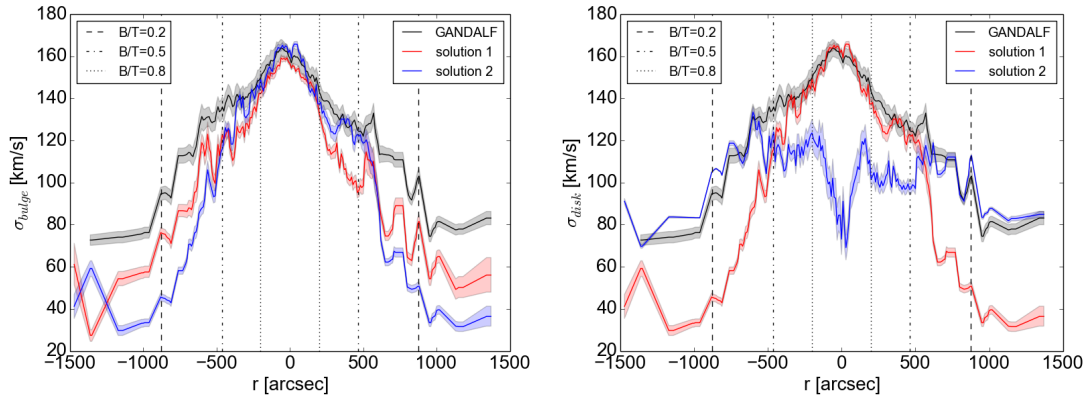


**Figure 6.12:** Cuts through the velocity dispersion maps in figure 6.10.

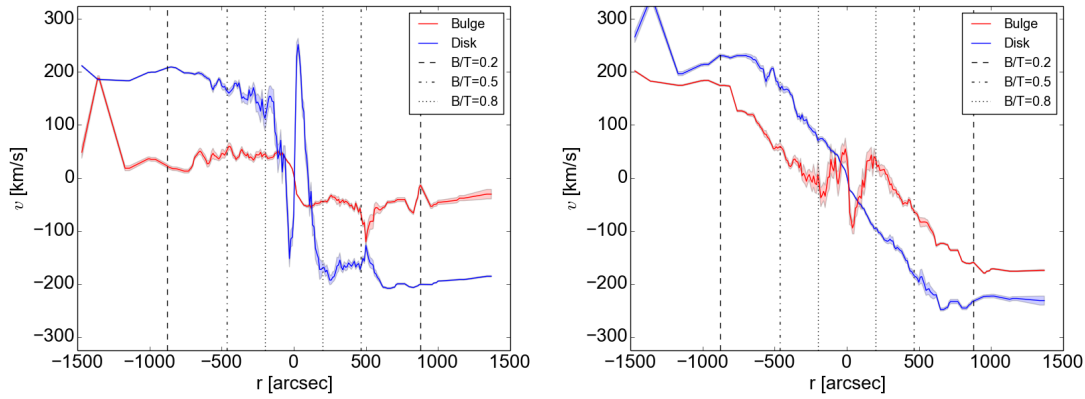


**Figure 6.13:** The velocity profiles from figure 6.11, re-arranged into the cuts from sorted solution 1 (left) and sorted solution 2 (right).

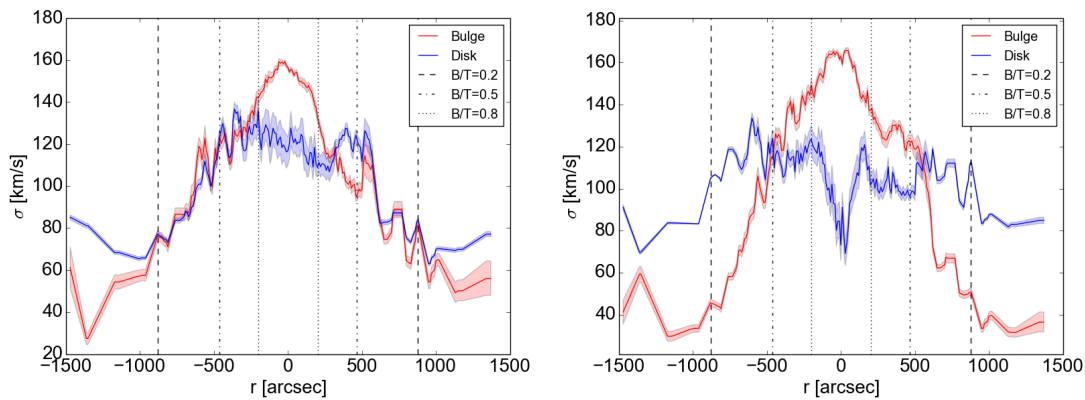


**Figure 6.14:** The velocity dispersion profiles from figure 6.12, re-arranged into the cuts from sorted solution 1 (left) and sorted solution 2 (right).

## 6.2 Test on N-body model

We also test our kinematic decomposition routine on the barred N-body model by B16.

Their model originally starts with a bulge and disk. Over time, a bar forms, which then buckles and forms the B/P bulge. In the end, the disk particles have buckled into the B/P bulge.

When fitting this model dataset with our kinematic decomposition routine, we also get two solutions most of the time, see figure 6.15. These solutions again

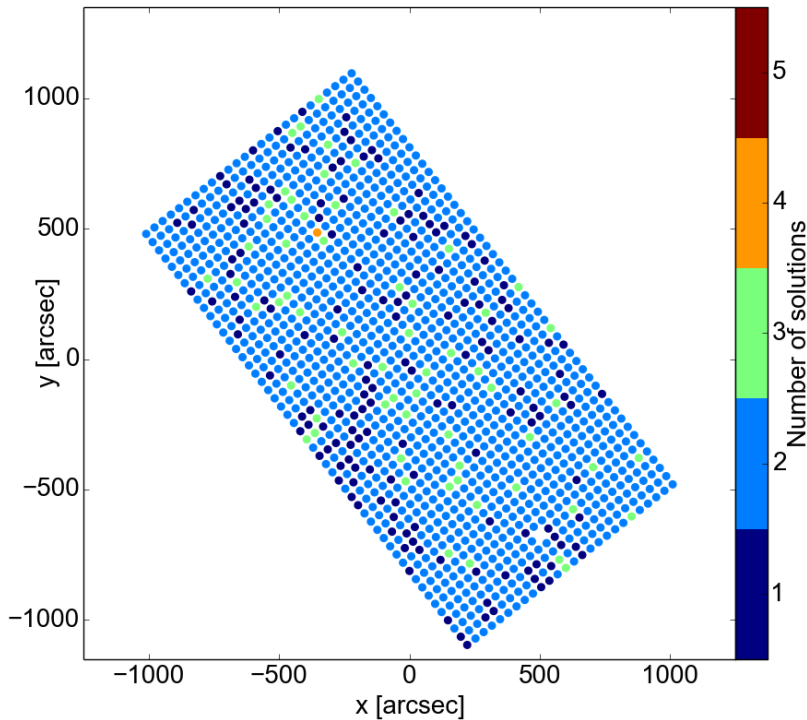


**Figure 6.15:** The number of solutions on which the fitting routine converges for the model by B16. For the large majority of bins, there are two solutions.

have to be sorted by velocity. The maps for the sorted solutions are plotted in figure 6.16 and the cuts in figure 6.18.

Qualitatively, we get the same results as before in the measured data, one solution combines a slowly rotating bulge with a fast rotating disk, while the other one is a combination of two cylindrically rotating structures. The result of this experiment is that even in a model where we know that no stellar disk is present, it is still possible to see a solution that resembles a disk with the kinematic decomposition. This means that the fact that we see such a solution in the M31 data does not necessarily mean that the disk is really present all the way into the center, as it is expected from a simple bulge and disk decomposition.

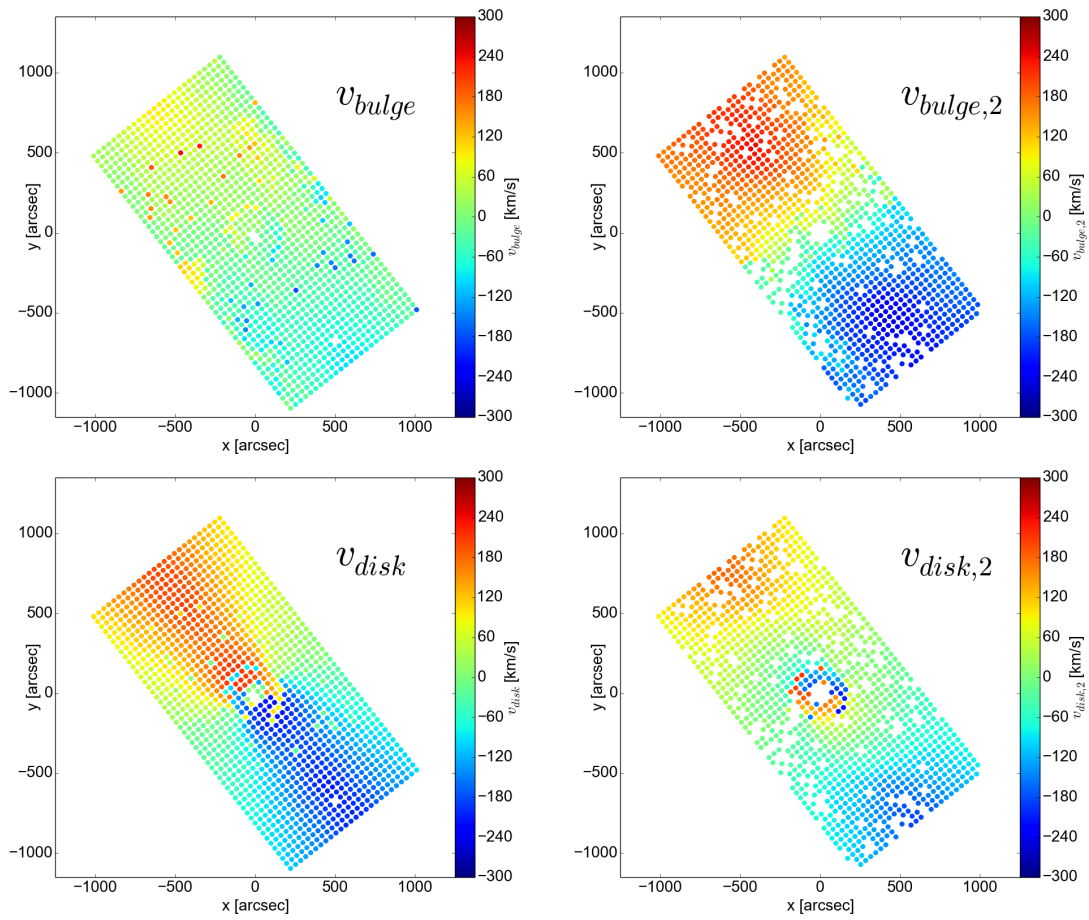


**Figure 6.16:** The sorted velocity maps for the N-body model by B16. The plot is similar to figure 6.9.

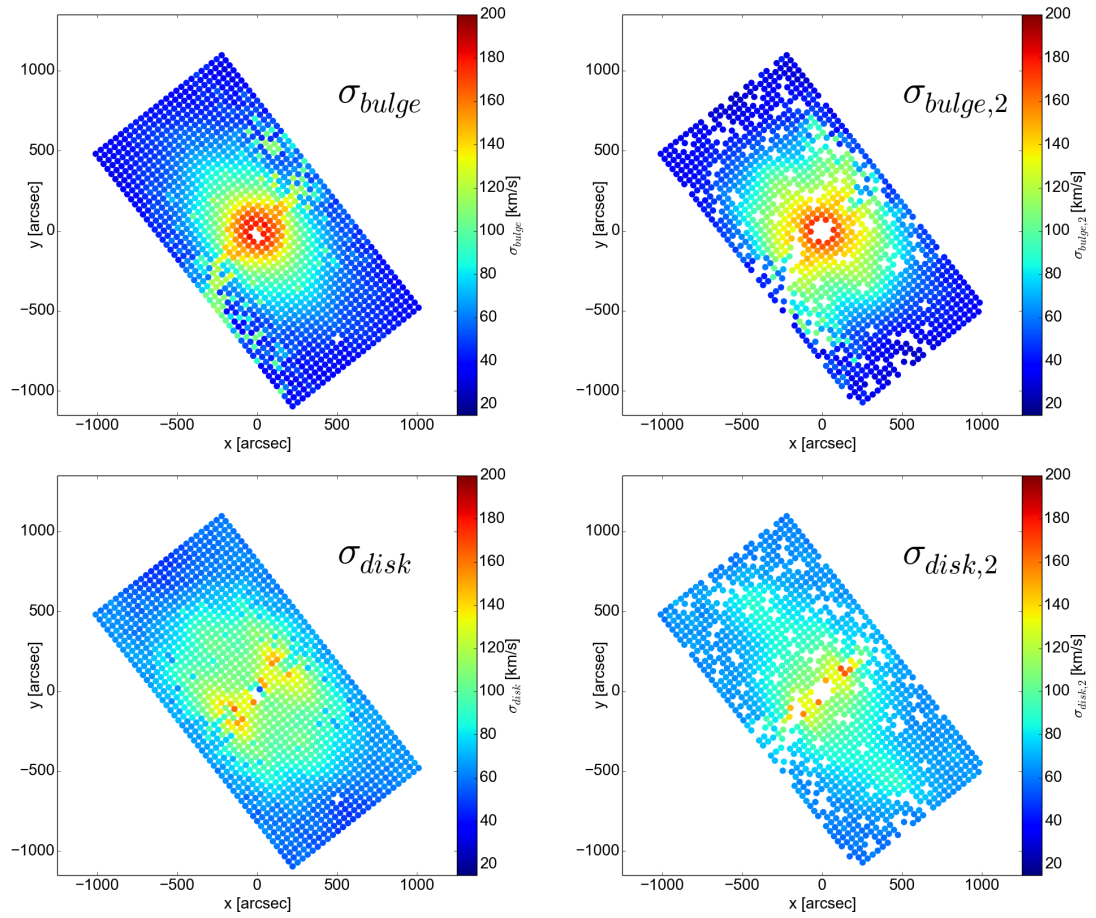


**Figure 6.17:** The sorted velocity dispersion maps for the N-body model by B16. The plot is similar to figure 6.10.

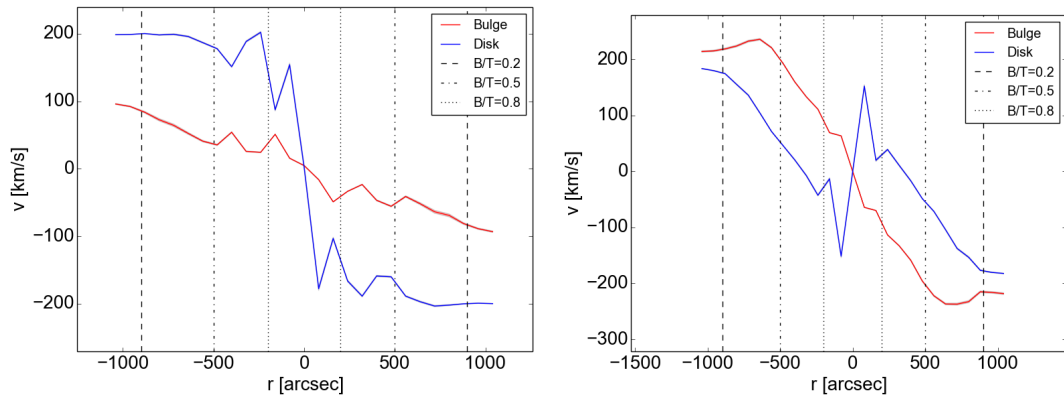


**Figure 6.18:** Cuts through the velocity maps in figure 6.16 along the disk major axis. The plot is analogous to figure 6.11.

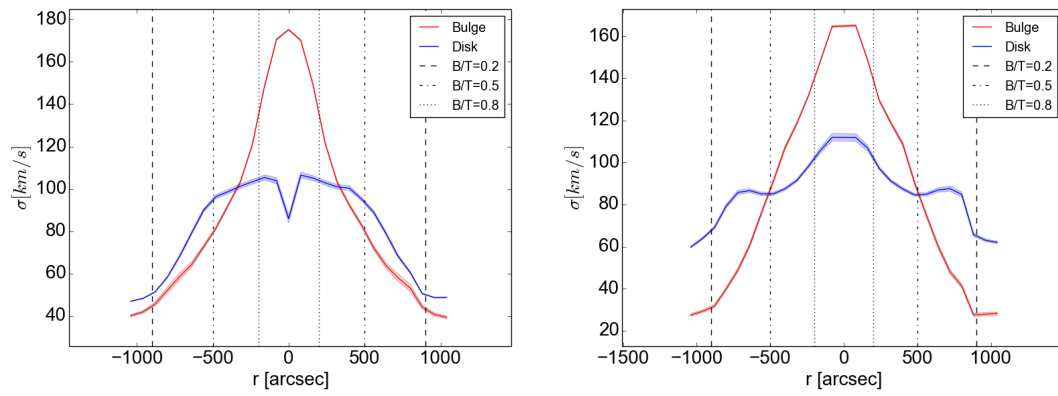


**Figure 6.19:** Cuts through the velocity dispersion maps in figure 6.17 along the disk major axis. The plot is analogous to figure 6.12.

## 6.3 Simple bulge and disk model

With the values for  $v_{bulge}$ ,  $v_{disk}$ ,  $\sigma_{bulge}$  and  $\sigma_{disk}$  from sorted solution 1, we now build a bulge and disk model. For this, we take a spectrum from the galaxy bulge and one from the galaxy disk. We choose one spectrum from the very center of M31 as the bulge spectrum and the outermost bin along direction PA=55° on the far side as the disk spectrum. Both spectra and their positions are plotted in figure 6.20. An intrinsic problem is that we want to have de-convolved model bulge and disk spectra, whereas the spectra from the observations are already convolved with the respective LOSVDs. In order to get de-convolved spectra, we fit both the bulge and the disk spectrum with pPXF to obtain the optical linear combinations of the template star spectra. For the fits, all 230 giants from the ELODIE catalog (Prugniel et al., 2007) are used, with their spectra having been broadened to the VIRUS-W resolution. The fits result in a model bulge and a model disk spectrum. The resulting non-broadened, non-redshifted spectra are plotted in figure 6.21. For each bin, the model bulge spectrum  $b(\lambda)$  and the disk spectrum  $d(\lambda)$  are then convolved with gaussians  $\mathcal{G}$  with  $v$  and  $\sigma$  from sorted solution 1 and weighted with  $\frac{B}{T}$  and  $\frac{D}{T}$  from the photometric model from section 2.3. The spectrum  $s_n(\lambda)$  for bin n is then:

$$s_n(\lambda) = \left(\frac{B}{T}\right)_n (b(\ln \lambda) * \mathcal{G}(v_{bulge}, \sigma_{bulge})) + \left(\frac{D}{T}\right)_n (d(\ln \lambda) * \mathcal{G}(v_{disk}, \sigma_{disk})) \quad (6.5)$$

The combined spectrum for an example bin is shown in figure 6.22.

### 6.3.1 Lick indices

On these combined model spectra, the Lick indices are measured with the method described in chapter 5. Maps of the are shown in figures 6.23 to 6.28. You can clearly see gradients in the indices that are similar to the gradients related to the  $\frac{B}{T}$  fractions, which are not seen in the measured Lick profiles. In figures 6.29 to 6.32, radial profiles are plotted, which have been averaged along the ellipses from the ellipse fit to the K-band image by S10. For H $\beta$  in figure 6.29, the model curve only agrees in the very center and in the very outermost points. This is because the H $\beta$  value in the disk spectrum is not representative of the actual mean disk value. However, the purpose of this exercise is to see if the homogeneity of the H $\beta$  value in the bulge is in agreement with a simple bulge/disk decomposition, which is clearly not the case.

In Mg b, both the bulge and the disk spectrum are representative of the averaged profiles, however, there seems to be a systematic offset of 0.3 to lower values in the models. This could be due to the fact that the raw spectra are not fitted directly, but first a kinematic fit is performed using the ELODIE spectra. The ELODIE spectra are giants taken from the disk region of the Milky Way and as such they are less  $\alpha$ /Fe abundant than the bulge spectrum which they should represent.

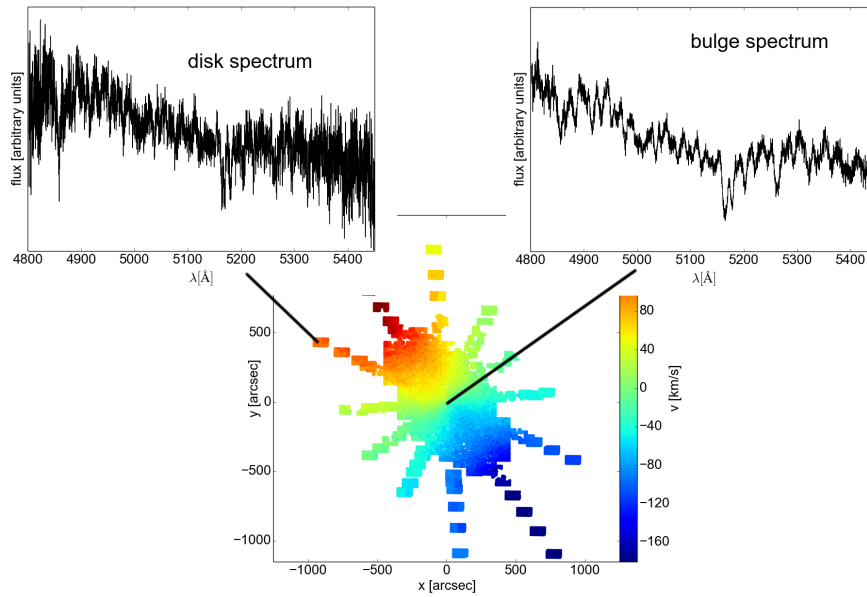


**Figure 6.20:** The bulge and the disk spectrum used for the model. The bulge spectrum is taken from the very center, the disk spectrum is the outermost bin along direction  $PA=55^\circ$  on the far side of the galaxy.

Fe5015 in figure 6.31 agrees fairly well in the regions where the disk dominates, because for these indices, the chosen disk spectrum is representative for the spectra in this region. For the bulge dominated parts of the profile, the profile of the model deviates from the fairly constant profile for the measured values. This is because the bulge profile is representative of the spike in the Fe indices in the very innermost values, which only extends for the innermost  $30''$ , whereas the bulge dominates out to  $460''$ . With the method of constructing the bulge and disk models, this spectrum is taken to be representative for the whole bulge region, therefore resulting in the much slower decline of the high values.

The behavior of the other iron indices is similar to the one of Fe5015.

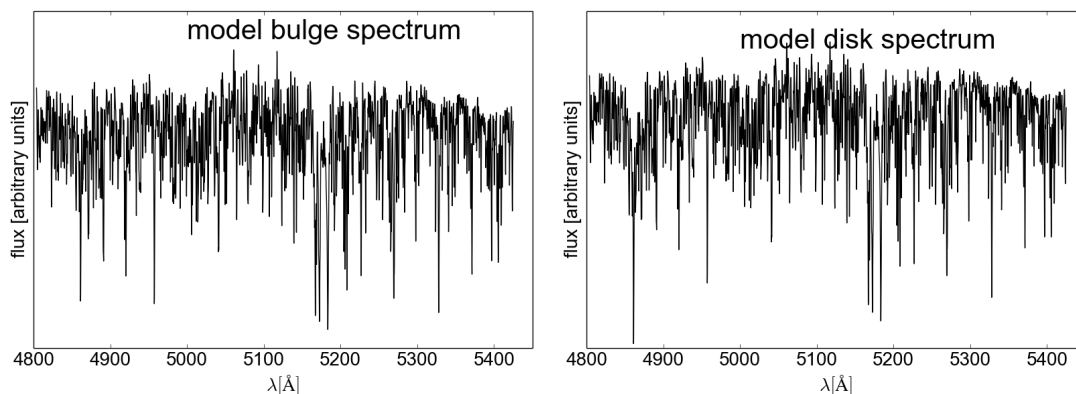


**Figure 6.21:** Continuum-normalized model bulge (left) and disk (right) spectra, obtained by deconvolving a pPXF fit to the raw bulge and disk spectra in figure 6.20.

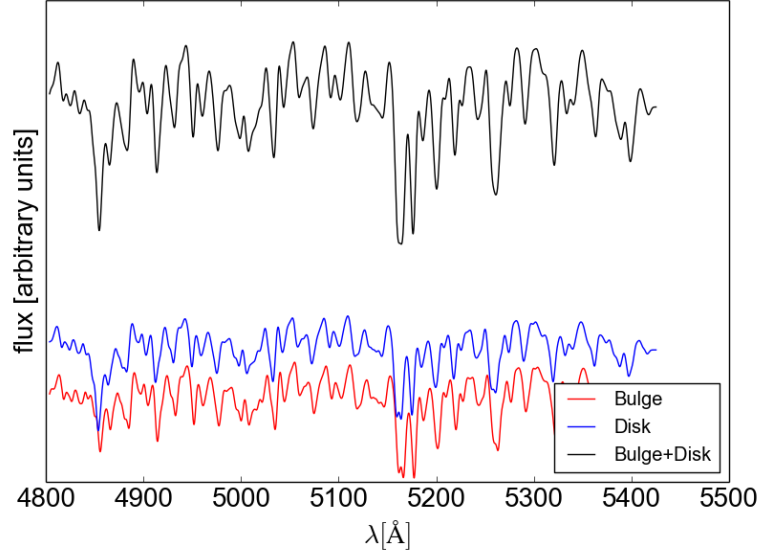


**Figure 6.22:** Model spectrum for the bin plotted in figure 6.4 with  $v_{bulge} = -351 \pm 7 \text{ km s}^{-1}$ ,  $\sigma_{bulge} = 106 \pm 5 \text{ km s}^{-1}$ ,  $v_{disk} = -483 \pm 6 \text{ km s}^{-1}$  and  $\sigma_{disk} = 108 \pm 5 \text{ km s}^{-1}$ . The bulge and disk fractions are  $\frac{B}{T} = 0.45$  and  $\frac{D}{T} = 0.55$ , respectively.

### 6.3.2 Population properties

We then fit age, metallicity and  $\alpha/Fe$  overabundance in a similar way as in chapter 5. Again, we leave out the Lick index Fe5015 from the fit. Since the spectra of the model image are already noise-free models, we do not estimate the statistical errors of the Lick indices with Monte-Carlo simulations. The fit of the stellar populations is done minimizing in the same way as in chapter 5, only that we set the errors to zero.

The resulting map for age is plotted in figure 6.35, a radial profile in figure 6.36. The ages of the stars are overall much younger than in the maps of the measured data. This is because the raw disk spectrum yields a very young age of  $T_{disk} = 1.8_{-0.2}^{+0.3}$  Gyr. However, the steep gradient in age would still be present, even if the used disk spectrum had a slightly higher age. Overall, it is fairly difficult to reproduce the constant age profile from the measurement with the simple bulge and disk model used here.

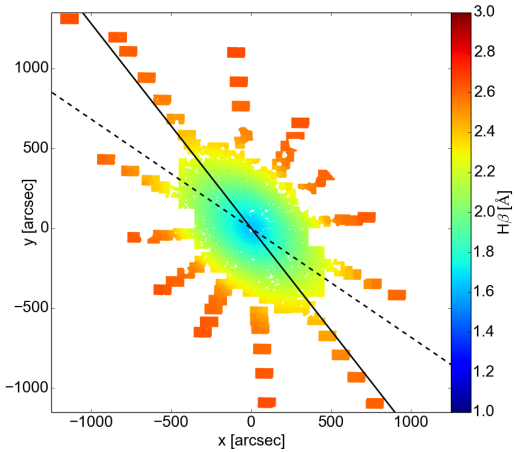


**Figure 6.23:** Lick index  $H\beta$  for the bulge and disk model with the disk major axis (solid line) and the bar major axis (dashed line).

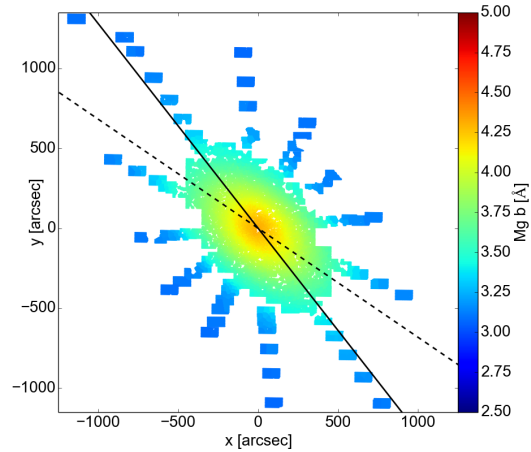


**Figure 6.24:** Lick index  $Mg\ b$  for the bulge and disk model. The lines are the same as in figure 6.23.

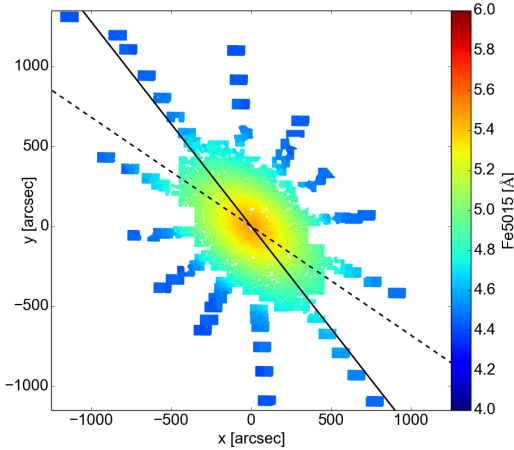


**Figure 6.25:** Lick index  $Fe5015$  for the bulge and disk model. The lines are the same as in figure 6.23.

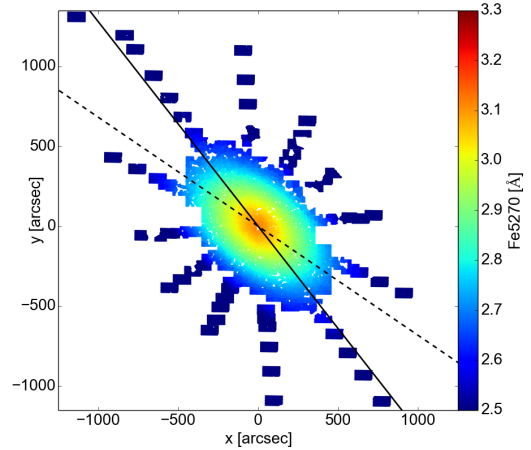


**Figure 6.26:** Lick index  $Fe5270$  for the bulge and disk model. The lines are the same as in figure 6.23.

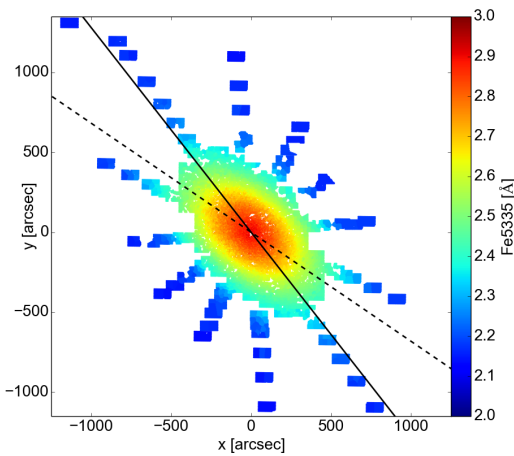


**Figure 6.27:** Lick index  $Fe5335$  for the bulge and disk model. The lines are the same as in figure 6.23.

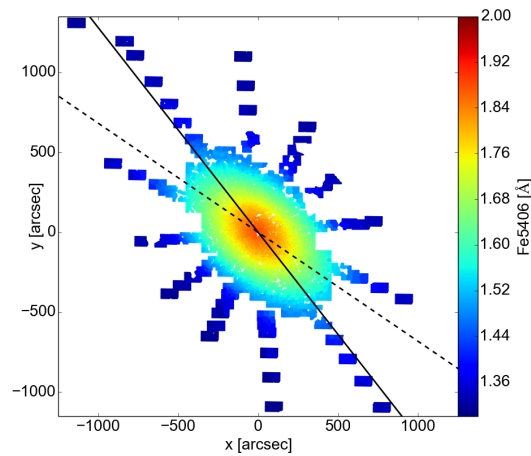


**Figure 6.28:** Lick index  $Fe5406$  for the bulge and disk model. The lines are the same as in figure 6.23.

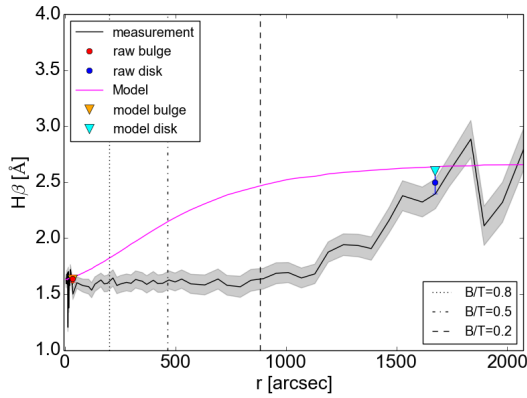


**Figure 6.29:** Profiles of the Lick index  $H\beta$ . Black is the measured profile from chapter 5, magenta is the profile from the model. The red and blue points denote the values that are measured for the raw bulge and the raw disk spectrum, respectively. The orange and cyan triangles are the values that are measured for the model spectra at the same positions.

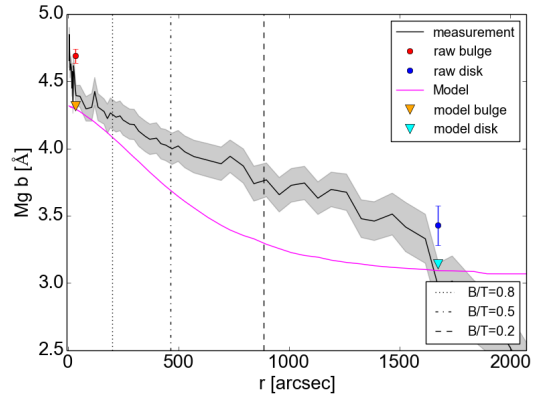


**Figure 6.30:** Profiles of the Lick index Mg b. The lines and points correspond to the ones in figure 6.29.

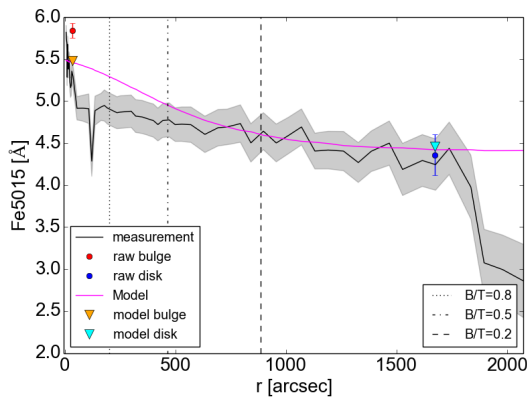


**Figure 6.31:** Profiles of the Lick index Fe5015. The lines and points correspond to the ones in figure 6.29.

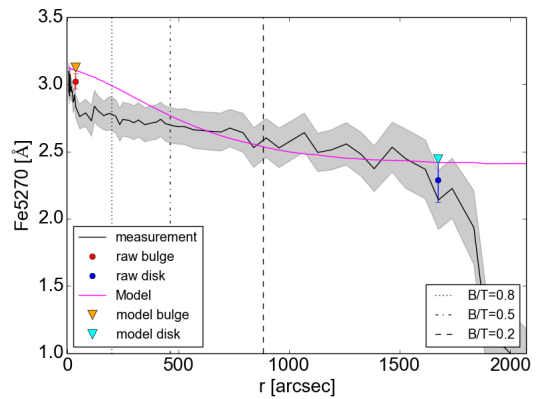


**Figure 6.32:** Profiles of the Lick index Fe5270. The lines and points correspond to the ones in figure 6.29.

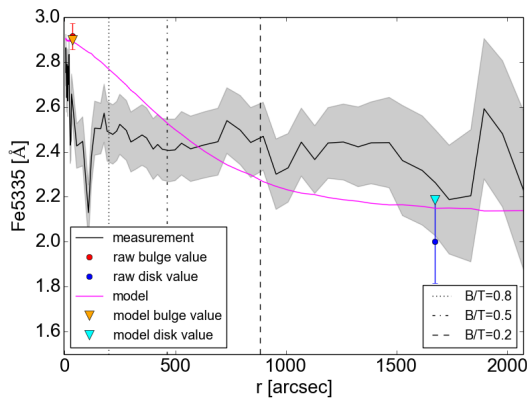


**Figure 6.33:** Profiles of the Lick index Fe5335. The lines and points correspond to the ones in figure 6.29.

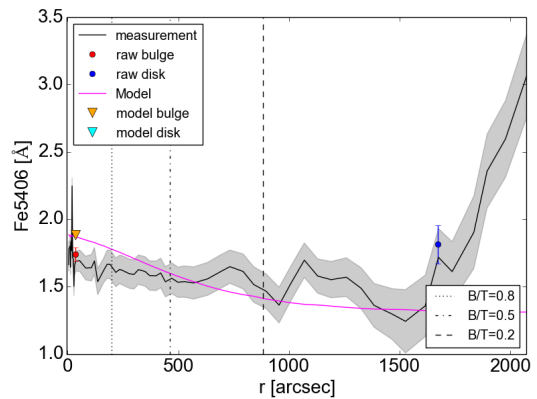


**Figure 6.34:** Profiles of the Lick index Fe5406. The lines and points correspond to the ones in figure 6.29.

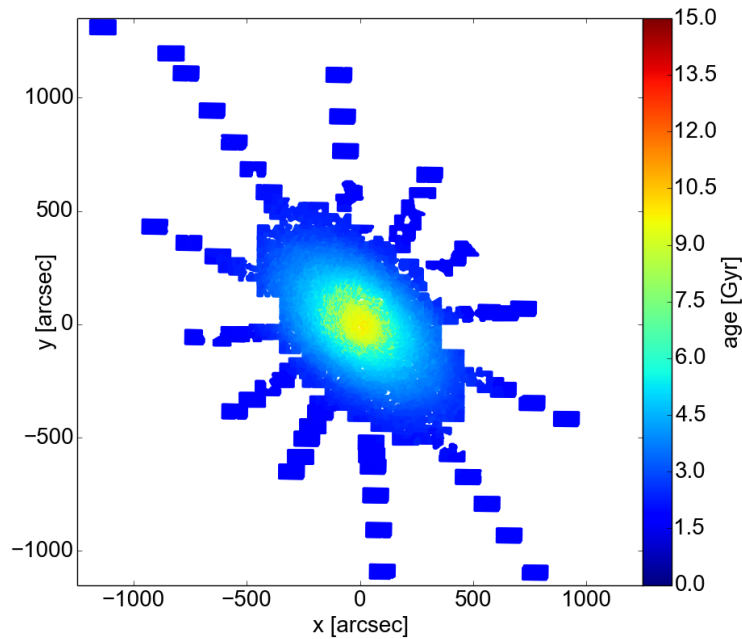


**Figure 6.35:** Age map for the bulge and disk model. Contrary to the measured values in figure 5.19, you can clearly see a gradient in age and the populations are much younger overall.

The metallicity map is plotted in figure 6.37, the profile in 6.38. The model metallicity is rounder than the one measured from the data in figure 5.20, because it traces the ellipticity of the K-band ellipse fit and not the elongation we see in the data that is caused by the bar.

We do not show the plot of the  $\alpha/Fe$ -overabundance, because the template stars used to produce the model bulge and model disk spectra are taken from the solar neighborhood and are therefore disk stars, which cannot reproduce  $\alpha/Fe$  in the bulge region.

This exercise was a first attempt to see if the measured stellar populations can be represented with a simple bulge and disk model, without having a bar. Despite the simplicity of the model, the following conclusion can be made: If an old bulge and a young disk are combined, the gradient in the age maps is clearly visible, which is not the case in the measurements. For the metallicity, we do not reproduce the elongated structure along the suspected bar major axis, instead, the metallicity map reproduces the simple bulge and disk decomposition from the model image, but this is expected. This further corroborates our belief that M31 can not be described by a simple bulge and disk model, but that another component is needed.

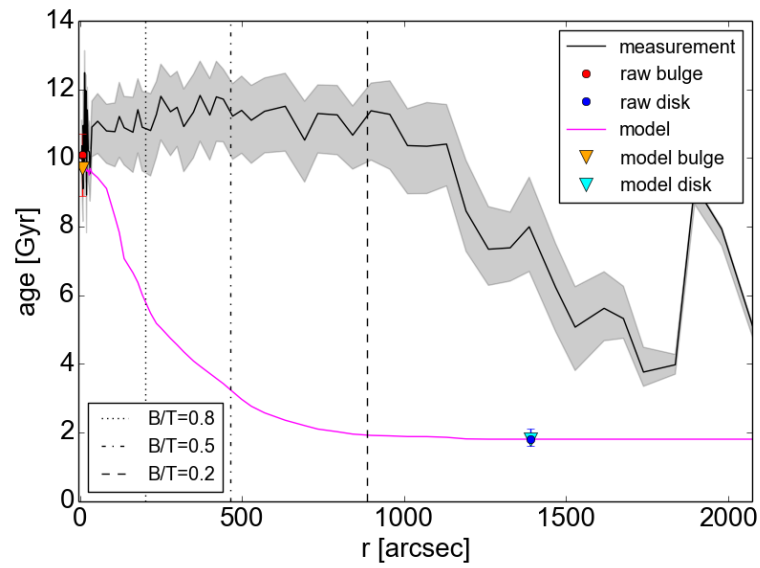


**Figure 6.36:** Comparison of the age profiles of the measured indices (black) and the model ages (magenta). The red point is the value of the original bulge spectrum, the blue one the one of the original disk spectrum. The orange triangle is the value for the model at that position and the cyan triangle the one for the disk position.

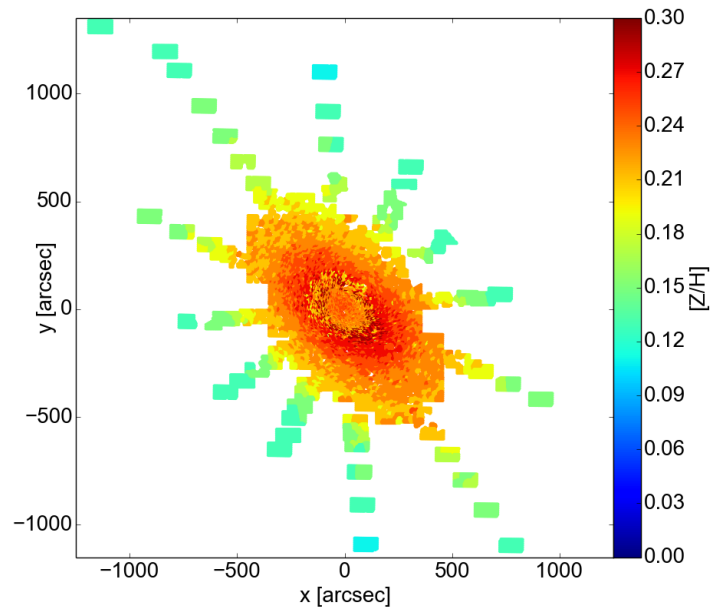


**Figure 6.37:** Metallicity map for the bulge and disk model.

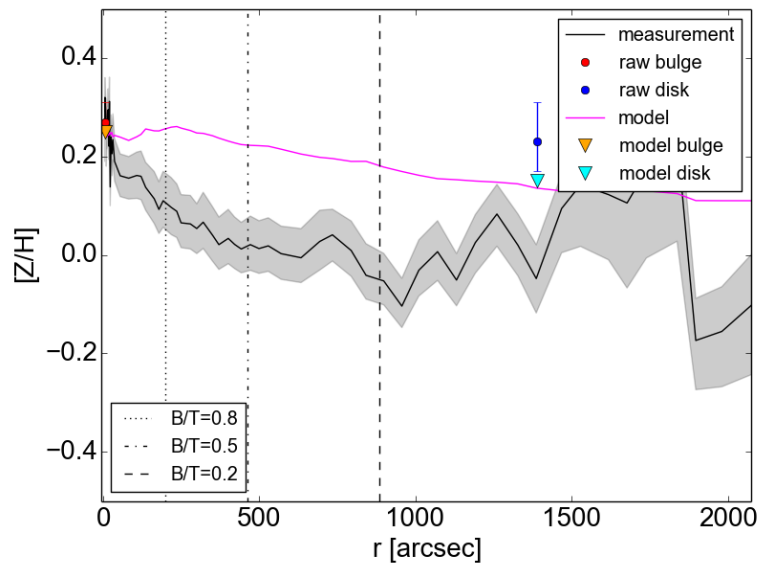


**Figure 6.38:** Comparison of the metallicity profiles of the measurement and the model. The colors are the same as in figure 6.36.

# Chapter 7

## Summary and Outlook

### 7.1 Summary

In this thesis, we have presented results from observations of the Andromeda galaxy M31 with the optical integral field unit spectrograph VIRUS-W.

For several decades, the question has been posed if M31 is a barred galaxy or not (Lindblad, 1956; Stark, 1977; Stark & Binney, 1994; Athanassoula & Beaton, 2006; Beaton et al., 2007). The difficulty in observing the bar of M31 lies in the fact that its inclination is too close to edge-on to clearly detect an elongated structure in the photometry, but not edge-on enough to see the boxy-peanut shaped structure above and below the edge-on disk.

In our dataset, we have looked specifically for signs of the bar in the galaxy. Cuts through the velocity field reveal a “double hump”, which is a sign for bars and usually appears in simulations of barred galaxies, like Bureau & Athanassoula (2005). The offset between the kinematic and the photometric position angle is large enough that M31 is more in the region where barred galaxies lie (Barrera-Ballesteros et al., 2014). The stellar velocity dispersion field shows a drop in the center, with two maxima aligned along the minor axis. While this central drop can be caused by inner disk structures or dust in the center (Falcón-Barroso et al., 2006), it can also be due to the bar, since the stellar orbits making up the bar become more circular in the center (Bureau & Athanassoula, 2005). There are also two plateaus at intermediate radii in the  $\sigma$  profile, a behavior that is also often seen in barred potentials (Bureau & Athanassoula, 2005).

The higher Gauss-Hermite moment  $h3$  is anticorrelated in the disk regions and the very center, which is the expected behavior for a disk component (Bender et al., 1994). In a majority of the bulge area, i.e. the region where bulge light dominates over the disk,  $h3$  is correlated with the velocity  $v$ , which can be achieved by elongated motions which occur along the bar direction Bureau & Athanassoula (2005). Cuts through maps of the stellar kinematics agree very well with cuts through barred models by B16 and Blaña et al. (in prep.).

The gas kinematics, measured using the [OIII] $\lambda$ 5007 line, is more complicated than the stellar kinematics. Many spectra exhibit two separate peaks, resulting

in two kinematically distinct components. One of the two components has faster velocities than the other one. The fast component has disk-like rotation with a very steep gradient in the center. The line of zero velocity is S-shaped, again pointing to a bar. The overall shape of the rotation curve of the first component is qualitatively in agreement with gas in a dynamical model of M31 with a triaxial bulge from [Berman \(2001\)](#). The slower gas component is more perturbed, the regions near the major axis also show ordered rotation, with lower rotation amplitudes. Contrary to [Melchior & Combes \(2011\)](#), we also find rotation of the gas components right into the very center.

The position velocity diagrams of the gas components look similar to what is expected from simulations ([Athanassoula & Beaton, 2006](#)), with a steep arm of high flux in the center and arms with lower slopes. The overall shape of the position-velocity diagram agrees with observations in HI by [Chemin et al. \(2009\)](#), with the steep branch in the position velocity diagram tracing the main gas component. [Chemin et al. \(2009\)](#) measure sometimes up to 5 different components and interpret this in a way that one is the main HI disk, which coincides with the steep slope in the position-velocity diagram. The other components belong to the branches with lower slope in the position-velocity diagrams. According to [Chemin et al. \(2009\)](#), they are low velocities from the outer regions of the HI disk, which have been projected to the center due to warps. However, they can also agree with the lower velocity branches that exist in a barred potential ([Athanassoula & Beaton, 2006](#)).

When looking at the morphology of the gas, we see a spiral pattern, similar to what is seen by [Jacoby et al. \(1985\)](#) in  $H\alpha+[NII]$  and  $[OIII]$ , [Ciardullo et al. \(1988\)](#) in  $H\alpha+[NII]$  and [Boulesteix et al. \(1987\)](#) in  $[NII]$ . This spiral pattern has a lower inclination than the disk, which means it could have been tilted by a non-axisymmetry, like a bar ([Jacoby et al., 1985](#)). Comparing the gas morphology to the expected morphology of the ionized gas in a barred potential, which we take from [Athanassoula & Beaton \(2006\)](#) and adapt to the orientation and the ellipticity of M31, we see that overall, the ionized gas seems to have a rounder appearance than the model, but structures in the center could well correspond to each other. [Block et al. \(2006\)](#) claim that the morphology of M31 in the far infrared is not caused by a bar, but is instead the result of a density wave caused by the collision of M32 with M31. Comparing their gas morphology with our measured one, the ring somewhat corresponds to what we see, but there is no high emission inside the ring, which we observe in  $[OIII]$ . Building on this model, [Melchior & Combes \(2011\)](#) have proposed a scenario of a tilted ring in the center over another rotating disk, to explain line splittings they measure in CO observations. One of their velocity components actually agrees with one of our components, but the other one is off. Their model predicts that the component in the ring has a very narrow line, while the disk leads to a very broad line, which is not what we see, our two components in that region have the same width. We therefore do not think this is a valid scenario and think the bar is a more likely explanation.

From diagnostic diagrams for the ionization of the gas, we find that the gas is mostly ionized by shocks and not at all by starbursts, which agrees with the low star formation rate of M31 (Davidge et al., 2012). This also agrees with the filamentary appearance of the gas morphology, which Jacoby et al. (1985) claim could be either due to shocks or supernovae of type Ia.

We fit stellar populations using Lick absorption indices (Trager et al., 1998), applying the same general method as S10.  $H\beta$  is constant over the whole bulge region, before increasing in the disk. Mg b and several iron indices show an asymmetric behavior in the bulge, being stronger along the major axis and decreasing faster along the minor axis. We compare the measured Lick indices with values from simple stellar population models from Maraston (1998), Maraston (2005) and Thomas et al. (2003). The stellar populations are fairly old, about 11 Gyr for most of the bulge region, their age only drops in the disk. The metallicity shows a gradient, it is much higher than solar in the very center, before gradually declining to be slightly supersolar at the region where the disk starts dominating. It has higher values along the proposed bar major axis (B16) than perpendicular to it, which is also seen in many other barred galaxies. The gradient perpendicular to the bar is comparable with other barred galaxies, while in the direction of the bar, it is higher, but still lower than in other barred galaxies (Seidel et al., 2016). At 0.13 of the bar length taken from B16, the slopes in the metallicity change, with the inner slope being steeper than the outer one, again in agreement with other galaxies (Seidel et al., 2016). The  $\alpha/Fe$  overabundance stays constant at 0.2 for almost the whole galaxy, before dropping only in the very outer regions. Comparing the values in the innermost 260 pc with other galaxies from Thomas & Davies (2006), we see that the bulge of M31 is very similar to them in stellar populations.

Still puzzling is the homogeneous distribution of large age values and the elongated appearance of the metallicities.

We want to test if the appearance of the stellar populations could also be explained without the bar, using just a slowly rotating bulge and a fast rotating disk. For this, we perform a kinematic decomposition, where we fit the measured stellar line-of-sight velocity distributions with two Gaussians, one for the “bulge” and one for the “disk”. The fitting results in two degenerate solutions. In the first solution, there is a slow component with a maximum velocity of 50 km/s, which is taken to be the model bulge, and a fast component with a velocity of 200 km/s, which is then the model disk. In the second solution, both components have similar velocity gradients, being reminiscent of cylindrical rotation of edge-on bars, but this does not agree with what B16 see in their models. We also test the decomposition algorithm on models provided by B16, qualitatively yielding the same results. This is interesting, because in the models we know for a fact that no disk component is present anymore, however, the kinematic decomposition still results in one. We use the first solution of the decomposition to construct a simple model bulge and disk. For this, we take a spectrum from the very center of M31 as a template bulge spectrum and one from the outer regions as the model

disk spectrum, which are fitted with template spectra. The weighted sums of the template stars are taken to be the intrinsic non-broadened model bulge and disk spectrum. These model bulge and disk spectra are then combined according to the  $\frac{B}{T}$  and  $\frac{D}{T}$ -ratios taken from a photometric model image and broadened using  $v_{bulge}$ ,  $\sigma_{bulge}$ ,  $v_{disk}$  and  $\sigma_{disk}$  from the solution of the kinematic decomposition. On this resulting bulge and disk model, the Lick indices and the stellar populations are fitted in the same way as the observed data. The model indices show much larger gradients than the observed ones, resulting also in a fitted age map that does not reproduce the measured age at all. The model age is much younger for most of the bulge region. The fitted metallicity is almost constant, also contrary to the measured values.

In essence, this exercise has shown that the stellar populations measured for M31 cannot be reproduced by a simple model combining an old stellar bulge and a young stellar disk, strengthening the idea of a bar in M31.

To conclude, signs for a bar can be seen in the stellar and the ionized gas kinematics, the ionized gas morphology, as well as the metallicity.

## 7.2 Outlook

The stellar kinematic maps of M31 collected for this thesis will form the basis of a dynamical model with the made-to-measure code **NMAGIC** (de Lorenzi et al., 2007), which will fit the measured kinematic maps. This will result in a model of the stellar mass. The movement of gas particles in this stellar mass potential can then be simulated to see if they result in similar gas morphology and kinematics. The dynamical mass model will be used to estimate how many of the microlensing events measured towards M31 with the PAndromeda (Lee et al., 2012) and We-CAPP (Lee et al., 2015) projects can be expected from self-lensing by the stellar content in the galaxy itself. This then provides us with the number of events we can expect from Massive Dark Halo Objects (MACHOS) (Riffeser et al., 2006).

We will also observe more pointings in M31, especially where we expect the ends of the bar to be, which will allow us to measure its pattern speed.

All these future observations will result in a more complete picture of this fascinating and still puzzling galaxy.

# Appendices



# Appendix A

## Observed objects and lines for wavelength calibration

**Table A.1:** Photometric standard stars

Name	Type	<i>RA</i> J2000.0	<i>DEC</i> J2000.0	Reference for spectra from literature
BD+284211	Op	327.79625	28.86444	<a href="#">Oke (1990)</a>
Feige 66	sdO	189.34833	25.06667	<a href="#">Oke (1990)</a>
Feige 110	DOp	349.99333	-5.16556	<a href="#">Oke (1990)</a>
HD 84937	sdF5	147.23279	13.74614	<a href="#">Le Borgne et al. (2003)</a>

**Table A.2:** Open clusters

Name	<i>RA</i> J2000.0	<i>DEC</i> J2000.0
M37	88.07644	32.55299
M52	350.64167	61.31833

**Table A.3:** Kinematic standard stars

HD(...)	Type	<i>RA</i> J2000.0	<i>DEC</i> J2000.0
5516	G8III-IV	14.25833	23.40111
6203	K0III-IV	15.76057	-4.83660
7010	K0IV	17.90660	60.50629
10380	K3-IIIb	25.35789	5.48761
12929	K2IIIab	31.79336	23.46242
19476	K0III	47.31667	44.84750
20893	K3III	50.68850	20.74210
27348	G8III	65.05000	34.55917
30834	K3III	73.10417	36.69806
35369	G8III	80.94583	-7.81028
37160	G8III-IV	84.18333	9.29306
38309	F0III:n	85.59750	3.98861
39003	K0III	87.81667	39.14778
39118	G8III+...	86.97458	2.01150
39833	G0III	88.12125	-0.51497
42787	M2III	93.24792	6.01625
43039	G8IIIvar	93.84167	29.49861
45415	G9III	96.83500	2.9083
46377	K4III	97.62875	1.311806
46784	M0III	98.20250	5.55383
48433	K1III	100.95000	13.23222
54079	K0III:	106.95583	7.47119
54489	G9III	107.28208	2.25308
58207	G9III+...	111.42917	27.79806
58923	F0III	112.00833	6.94197
61935	K0III	115.30833	-9.55083
62345	G8III	116.10833	24.39806
62437	F0III	115.38000	2.52603
72561	G5III	127.77208	4.92872
76294	G8III-IV	133.84583	5.94528
81192	G7III	141.19167	19.78806
94672	F2III	163.28333	1.00397
104979	G8III	181.30417	8.73222
120136	F7V	206.81667	17.45667
122563	F8IV	210.63333	9.68722
137759	K2III	231.22917	58.96583
169959	A0III	276.72042	6.42347
171802	F5III	279.11583	9.12253
215648	F6III-IV	341.67325	12.1729

**Table A.4:** M31 pointings

Name	Run	<i>RA</i> J2000.0	<i>DEC</i> J2000.0	Name	Run	<i>RA</i> J2000.0	<i>DEC</i> J2000.0
M31_sky	all	11.53792	40.86472	M31_039	Oct11	10.57360	41.21493
M31_001	Oct12	10.28214	41.12755	M31_040	Oct11	10.57361	41.22882
M31_002	Oct11	10.34890	41.15268	M31_041	Oct11	10.57364	41.27048
M31_003	Oct11	10.40076	40.96460	M31_042	Oct11	10.57364	41.25658
M31_004	Oct11	10.40492	41.17239	M31_043	Oct11	10.57365	41.24271
M31_005	Oct11	10.41832	41.28798	M31_044	Oct11	10.57367	41.28435
M31_006	Oct11	10.44288	41.01018	M31_045	Oct11	10.57368	41.29825
M31_007	Feb13	10.44795	41.28241	M31_046	Feb13	10.58292	41.42737
M31_008	Oct11	10.45166	41.18880	M31_047	Oct12	10.58973	41.31922
M31_009	Oct12	10.47257	41.19455	M31_048	Oct11	10.59640	41.41205
M31_010	Oct11	10.47733	41.28408	M31_049	Oct12	10.60721	41.39393
M31_011	Oct11	10.47848	41.37865	M31_050	Aug13	10.60850	41.21078
M31_012	Oct11	10.47872	41.04897	M31_051	Oct11	10.61041	41.17331
M31_013	Oct11	10.49054	41.20247	M31_052	Oct11	10.61042	41.18720
M31_014	Oct12	10.50280	41.28192	M31_053	Oct11	10.61047	41.15935
M31_015	Oct12	10.50799	41.20700	M31_054	Oct11	10.61049	41.20103
M31_016	Oct12	10.50897	41.36180	M31_055	Oct11	10.61050	41.22881
M31_017	Oct11	10.50928	41.08194	M31_056	Oct11	10.61051	41.14541
M31_018	Oct11	10.52325	41.28107	M31_057	Oct11	10.61053	41.25659
M31_019	Oct11	10.53308	41.35001	M31_058	Oct11	10.61059	41.27048
M31_020	Oct11	10.53533	41.11005	M31_059	Oct11	10.61059	41.32602
M31_021	Oct11	10.53665	41.17326	M31_060	Oct11	10.61060	41.29825
M31_022	Oct11	10.53665	41.15937	M31_061	Oct11	10.61060	41.33991
M31_023	Oct11	10.53668	41.18715	M31_062	Oct11	10.61060	41.28436
M31_024	Oct11	10.53671	41.20104	M31_063	Oct11	10.61061	41.31212
M31_025	Oct11	10.53672	41.21493	M31_064	Oct12	10.61090	41.24141
M31_026	Oct11	10.53672	41.22882	M31_065	Oct12	10.61112	41.13033
M31_027	Oct12	10.54264	41.27843	M31_066	Oct11	10.61595	41.38065
M31_028	Feb13	10.54497	41.11908	M31_067	Oct12	10.62485	41.36619
M31_029	Oct12	10.55575	41.33747	M31_068	Aug13	10.64556	41.15523
M31_030	Oct11	10.55748	41.13394	M31_069	Oct11	10.64647	41.14718
M31_031	Oct11	10.57122	41.45238	M31_070	Oct11	10.64731	41.18698
M31_032	Oct11	10.57320	41.32895	M31_071	Oct11	10.64731	41.17310
M31_033	Oct11	10.57352	41.13158	M31_072	Oct11	10.64744	41.21493
M31_034	Oct11	10.57353	41.14548	M31_073	Oct11	10.64745	41.24270
M31_035	Oct11	10.57354	41.15936	M31_074	Oct11	10.64749	41.36766
M31_036	Oct11	10.57356	41.17326	M31_075	Oct11	10.64750	41.33991
M31_037	Oct11	10.57357	41.18714	M31_076	Oct11	10.64750	41.35381
M31_038	Oct11	10.57358	41.20104	M31_077	Oct11	10.64751	41.27039

Name	Run	<i>RA</i> J2000.0	<i>DEC</i> J2000.0	Name	Run	<i>RA</i> J2000.0	<i>DEC</i> J2000.0
M31_078	Oct11	10.64752	41.29825	M31_117	Oct11	10.72137	41.35378
M31_079	Oct11	10.64752	41.31205	M31_118	Oct11	10.72138	41.29821
M31_080	Oct11	10.64754	41.32595	M31_119	Oct11	10.72138	41.21494
M31_081	Oct12	10.64791	41.25539	M31_120	Oct11	10.72138	41.38154
M31_082	Oct12	10.64794	41.19989	M31_121	Oct11	10.72139	41.22876
M31_083	Oct12	10.64805	41.22762	M31_122	Oct11	10.72139	41.20098
M31_084	Oct12	10.64809	41.28322	M31_123	Oct11	10.72139	41.24264
M31_085	Oct11	10.64917	40.96617	M31_124	Oct11	10.72139	41.18708
M31_086	Oct11	10.65502	41.01707	M31_125	Oct11	10.72140	41.17326
M31_087	Oct11	10.65993	41.05947	M31_126	Oct11	10.72151	41.27033
M31_088	Oct11	10.66401	41.09478	M31_127	Oct12	10.72167	41.25548
M31_089	Oct12	10.66638	41.10879	M31_128	Oct12	10.72195	41.33843
M31_090	Oct11	10.66741	41.12417	M31_129	Oct12	10.72196	41.28295
M31_091	Aug13	10.68258	41.28018	M31_130	Oct12	10.72209	41.31064
M31_092	Aug13	10.68266	41.25241	M31_131	Oct12	10.74568	41.17229
M31_093	Feb13	10.68293	41.29478	M31_132	Oct11	10.74983	41.16102
M31_094	Oct11	10.68428	41.18698	M31_133	Oct11	10.75832	41.33989
M31_095	Oct11	10.68433	41.17332	M31_134	Oct11	10.75832	41.39543
M31_096	Oct11	10.68435	41.15942	M31_135	Oct11	10.75833	41.38154
M31_097	Oct11	10.68439	41.20103	M31_136	Oct11	10.75833	41.40932
M31_098	Oct11	10.68440	41.21493	M31_137	Oct11	10.75833	41.35378
M31_099	Oct11	10.68440	41.35375	M31_138	Oct11	10.75834	41.36765
M31_100	Oct11	10.68440	41.24271	M31_139	Oct11	10.75835	41.31211
M31_101	Oct11	10.68441	41.36764	M31_140	Oct11	10.75838	41.21493
M31_102	Oct11	10.68441	41.32597	M31_141	Oct11	10.75840	41.20103
M31_103	Oct11	10.68442	41.33986	M31_142	Oct11	10.75847	41.28427
M31_104	Oct11	10.68455	41.38143	M31_143	Oct11	10.75875	41.27038
M31_105	Oct12	10.68514	41.2276	M31_144	Oct11	10.75876	41.22870
M31_106	Oct12	10.68523	41.31072	M31_145	Oct11	10.75876	41.25648
M31_107	Oct12	10.68529	41.26928	M31_146	Oct11	10.75877	41.24260
M31_108	Oct11	10.70147	41.41671	M31_147	Oct12	10.75889	41.32481
M31_109	Oct12	10.70344	41.42964	M31_148	Oct12	10.75895	41.29692
M31_110	Oct11	10.70493	41.44611	M31_149	Oct12	10.76233	41.14429
M31_111	Oct11	10.70904	41.48145	M31_150	Oct11	10.77206	41.12890
M31_112	Oct11	10.71401	41.52385	M31_151	Oct12	10.78015	41.21899
M31_113	Oct11	10.72000	41.57474	M31_152	Feb13	10.78223	41.10663
M31_114	Oct11	10.72135	41.32599	M31_153	Oct11	10.79527	41.40934
M31_115	Oct11	10.72136	41.39544	M31_154	Oct11	10.79530	41.39543
M31_116	Oct11	10.72136	41.36764	M31_155	Oct11	10.79532	41.38154

Name	Run	<i>RA</i> J2000.0	<i>DEC</i> J2000.0	Name	Run	<i>RA</i> J2000.0	<i>DEC</i> J2000.0
M31_156	Oct11	10.79532	41.33988	M31_195	Oct11	10.97070	41.57630
M31_157	Oct11	10.79533	41.36765	M31_196	Oct12	10.99552	41.60077
M31_158	Oct11	10.79533	41.35378	M31_197	Oct11	11.02114	41.38832
M31_159	Oct11	10.79535	41.32600	M31_198	Oct12	11.10759	41.63241
M31_160	Oct11	10.79537	41.31210				
M31_161	Oct11	10.79543	41.21199				
M31_162	Oct11	10.79543	41.28432				
M31_163	Oct11	10.79544	41.27044				
M31_164	Oct11	10.79545	41.25656				
M31_165	Oct11	10.79547	41.29816				
M31_166	Oct11	10.79578	41.24259				
M31_167	Oct11	10.79696	41.08856				
M31_168	Oct11	10.81188	41.40696				
M31_169	Oct12	10.81422	41.20097				
M31_170	Feb13	10.82074	41.41492				
M31_171	Oct12	10.82727	41.25982				
M31_172	Oct11	10.83229	41.38154				
M31_173	Oct11	10.83236	41.36765				
M31_174	Oct11	10.83237	41.33987				
M31_175	Oct11	10.83237	41.35377				
M31_176	Oct11	10.83244	41.32592				
M31_177	Oct11	10.83245	41.31203				
M31_178	Oct11	10.83425	41.43087				
M31_179	Oct11	10.83536	41.19093				
M31_180	Oct11	10.84556	41.25985				
M31_181	Oct11	10.86055	41.45895				
M31_182	Oct12	10.86103	41.17665				
M31_183	Oct12	10.86237	41.33116				
M31_184	Oct12	10.86767	41.25700				
M31_185	Oct11	10.87867	41.33848				
M31_186	Oct11	10.88972	41.16219				
M31_187	Oct11	10.89143	41.25682				
M31_188	Oct11	10.89149	41.49195				
M31_189	Feb13	10.89542	41.34154				
M31_190	Feb13	10.91748	41.25158				
M31_191	Oct11	10.91774	41.35216				
M31_192	Oct11	10.92788	41.53077				
M31_193	Oct11	10.95041	41.25311				
M31_194	Oct11	10.96513	41.36858				

**Table A.5:** Lines used for wavelength calibration

Wavelength Å	Ionization state
4837.314	Ne I
4863.081	Ne I
4884.917	Ne I
4916.068	Hg I
4957.036	Ne I
5005.159	Ne I
5025.6	Hg II
5031.348	Ne I
5037.751	Ne I
5074.201	Ne I
5080.383	Ne I
5113.672	Ne I
5116.503	Ne I
5122.257	Ne I
5144.938	Ne I
5151.961	Ne I
5188.612	Ne I
5203.896	Ne I
5208.865	Ne I
5222.352	Ne I
5234.027	Ne I
5298.190	Ne VI
5330.778	Ne I
5341.094	Ne I
5343.283	Ne I
5400.562	Ne I
5433.651	Ne I

# Bibliography

- Abd al-Rahman al-Sufi, c. 964, *Ṣuwar al-Kawakib al-Thamaniyah wa-al-Arba'een*. Cited on page 1.
- Adams J.J., Blanc G.A., Hill G.J. et al., 2011, *The HETDEX Pilot Survey. I. Survey Design, Performance, and Catalog of Emission-line Galaxies*, ApJS, 192, 5. Cited on pages 15 and 16.
- Argyle E., 1965, *A Spectrometer Survey of Atomic Hydrogen in the Andromeda Nebula.*, ApJ, 141, 750. Cited on page 3.
- Athanassoula E. & Beaton R.L., 2006, *Unravelling the mystery of the M31 bar*, MNRAS, 370, 1499. Cited on pages xii, 7, 8, 56, 65, 66, 67, 73, 78, 82, 133, and 134.
- Baade W., 1944, *The Resolution of Messier 32, NGC 205, and the Central Region of the Andromeda Nebula.*, ApJ, 100, 137. Cited on page 3.
- Bacon R., Copin Y., Monnet G. et al., 2001, *The SAURON project - I. The panoramic integral-field spectrograph*, MNRAS, 326, 23. Cited on page 84.
- Barazza F.D., Jogee S. & Marinova I., 2008, *Bars in Disk-dominated and Bulge-dominated Galaxies at  $z \sim 0$ : New Insights from  $\sim 3600$  SDSS Galaxies*, ApJ, 675, 1194-1212. Cited on page 6.
- Barden S.C., Sawyer D.G. & Honeycutt R.K., 1998, *Integral field spectroscopy on the WIYN telescope using a fiber array*, in S. D'Odorico, editor, *Optical Astronomical Instrumentation*, volume 3355 of *Proceedings of SPIE*, pages 892–899. Cited on page 11.
- Barmby P., Ashby M.L.N., Bianchi L. et al., 2006, *Dusty Waves on a Starry Sea: The Mid-Infrared View of M31*, ApJL, 650, L45. Cited on pages 6, 8, 9, 34, 35, and 46.
- Barrera-Ballesteros J.K., Falcón-Barroso J., García-Lorenzo B. et al., 2014, *Kinematic alignment of non-interacting CALIFA galaxies. Quantifying the impact of bars on stellar and ionised gas velocity field orientations*, A&A, 568, A70. Cited on pages 57, 59, 71, and 133.

- Beaton R.L., Majewski S.R., Guhathakurta P. et al., 2007, *Unveiling the Boxy Bulge and Bar of the Andromeda Spiral Galaxy*, ApJL, 658, L91. Cited on pages 6, 8, 58, 70, and 133.
- Bender R., Kormendy J., Bower G. et al., 2005, *HST STIS Spectroscopy of the Triple Nucleus of M31: Two Nested Disks in Keplerian Rotation around a Supermassive Black Hole*, ApJ, 631, 280. Cited on pages 3 and 6.
- Bender R., Saglia R.P. & Gerhard O.E., 1994, *Line-of-Sight Velocity Distributions of Elliptical Galaxies*, MNRAS, 269, 785. Cited on pages 22, 58, and 133.
- Berman S., 2001, *Hydrodynamic simulations of the triaxial bulge of M31*, A&A, 371, 476. Cited on pages 7, 66, 73, and 134.
- Bessell M.S., 2005, *Standard Photometric Systems*, ARAA, 43, 293. Cited on pages 36 and 40.
- Binney J., 1985, *Testing for triaxiality with kinematic data*, MNRAS, 212, 767. Cited on page 57.
- Binney J. & Tremaine S., 1987, *Galactic dynamics*. Cited on page 58.
- Binney J. & Tremaine S., 2008, *Galactic Dynamics: Second Edition*, Princeton University Press. Cited on page 58.
- Blaña M., Wegg C., Gerhard O. et al., in prep., *NMAGIC models for M31*, MNRAS. Cited on pages 59, 60, 61, and 133.
- Blaña M., Wegg C., Gerhard O. et al., submitted, *Andromeda chained to the Box - Dynamical Models for M31: Bulge, Bar & Spurs*, abbreviated as B16 in the text. Cited on pages xi, 8, 9, 46, 56, 57, 58, 59, 60, 61, 66, 71, 73, 78, 89, 100, 107, 121, 122, 123, 133, and 135.
- Block D.L., Bournaud F., Combes F. et al., 2006, *An almost head-on collision as the origin of two off-centre rings in the Andromeda galaxy*, Nature, 443, 832. Cited on pages 7, 67, 79, 83, and 134.
- Boissier S. & Prantzos N., 1999, *Chemo-spectrophotometric evolution of spiral galaxies - I. The model and the Milky Way*, MNRAS, 307, 857. Cited on page 6.
- Boulesteix J., Georgelin Y.P., Lecoarer E., Marcelin M. & Monnet G., 1987, *Kinematics of ionized gas in the center of the Andromeda nebula (M31)*, A&A, 178, 91. Cited on pages 3, 7, 78, 79, and 134.
- Bowen I.S., 1927, *The Origin of the Nebulium Spectrum*, Nature, 120, 473. Cited on page 22.
- Braun R., 1991, *The distribution and kinematics of neutral gas in M31*, ApJ, 372, 54. Cited on page 4.

- Braun R., Thilker D.A., Walterbos R.A.M. & Corbelli E., 2009, *A Wide-Field High-Resolution H I Mosaic of Messier 31. I. Opaque Atomic Gas and Star Formation Rate Density*, ApJ, 695, 937. Cited on page 4.
- Brinks E., 1983, *High velocity HI in the inner 5 KPC of M31*, in E. Athanassoula, editor, *Internal Kinematics and Dynamics of Galaxies*, volume 100 of *IAU Symposium*, page 27. Cited on page 4.
- Brinks E. & Burton W.B., 1984, *A high resolution hydrogen line survey of Messier 31. II - The warped flaring hydrogen layer*, A&A, 141, 195. Cited on pages 4 and 8.
- Brinks E. & Shane W.W., 1984, *A high resolution hydrogen line survey of Messier 31. I Observations and data reduction*, A&AS, 55, 179. Cited on pages 4, 7, and 67.
- Bureau M. & Athanassoula E., 2005, *Bar Diagnostics in Edge-On Spiral Galaxies. III. N-Body Simulations of Disks*, ApJ, 626, 159. Cited on pages xii, 56, 57, 58, 59, 67, and 133.
- Burstein D., Faber S.M., Gaskell C.M. & Krumm N., 1984, *Old stellar populations. I - A spectroscopic comparison of galactic globular clusters, M31 globular clusters, and elliptical galaxies*, ApJ, 287, 586. Cited on page 87.
- Burstein D., Faber S.M. & Gonzalez J.J., 1986, *Old stellar populations. III - The metallicities of M5, M71, and M67*, AJ, 91, 1130. Cited on page 87.
- Cappellari M. & Copin Y., 2003, *Adaptive spatial binning of integral-field spectroscopic data using Voronoi tessellations*, MNRAS, 342, 345. Cited on page 17.
- Cappellari M. & Emsellem E., 2004, *Parametric Recovery of Line-of-Sight Velocity Distributions from Absorption-Line Spectra of Galaxies via Penalized Likelihood*, Publications of the Astronomical Society of the Pacific, 116, 138. Cited on page 21.
- Chemin L., Carignan C. & Foster T., 2009, *H I Kinematics and Dynamics of Messier 31*, ApJ, 705, 1395. Cited on pages 4, 8, 65, 66, 67, and 134.
- Chung A. & Bureau M., 2004, *Stellar Kinematics of Boxy Bulges: Large-Scale Bars and Inner Disks*, AJ, 127, 3192. Cited on pages 56, 58, and 59.
- Ciardullo R., Rubin V.C., Ford Jr. W.K., Jacoby G.H. & Ford H.C., 1988, *The morphology of the ionized gas in M31's bulge*, AJ, 95, 438. Cited on pages 3, 7, 78, 79, 82, and 134.
- Combes F., Debbasch F., Friedli D. & Pfenniger D., 1990, *Box and peanut shapes generated by stellar bars*, A&A, 233, 82. Cited on page 8.

- Combes F. & Sanders R.H., 1981, *Formation and properties of persisting stellar bars*, A&A, 96, 164. Cited on page 8.
- Corbelli E., Lorenzoni S., Walterbos R., Braun R. & Thilker D., 2010, *A wide-field HI mosaic of Messier 31. II. The disk warp, rotation, and the dark matter halo*, A&A, 511, A89. Cited on pages 4, 5, 6, and 8.
- Courteau S., Widrow L.M., McDonald M. et al., 2011, *The Luminosity Profile and Structural Parameters of the Andromeda Galaxy*, ApJ, 739, 20. Cited on pages 5 and 13.
- Davidge T.J., McConnachie A.W., Fardal M.A. et al., 2012, *The Recent Stellar Archeology of M31 - The Nearest Red Disk Galaxy*, ApJ, 751, 74. Cited on pages 6 and 135.
- de Grijs R. & Bono G., 2014, *Clustering of Local Group Distances: Publication Bias or Correlated Measurements? II. M31 and Beyond*, AJ, 148, 17. Cited on pages 5 and 6.
- de Lorenzi F., Debattista V.P., Gerhard O. & Sambhus N., 2007, *NMAGIC: a fast parallel implementation of a  $\chi^2$ -made-to-measure algorithm for modelling observational data*, MNRAS, 376, 71. Cited on pages 8, 59, and 136.
- de Vaucouleurs G., 1958, *Photoelectric photometry of the Andromeda nebula in the UBV system*, ApJ, 128, 465. Cited on pages 5 and 6.
- de Vaucouleurs G., de Vaucouleurs A., Corwin Jr. H.G. et al., 1991, *Third Reference Catalogue of Bright Galaxies. Volume I: Explanations and references. Volume II: Data for galaxies between 0<sup>h</sup> and 12<sup>h</sup>. Volume III: Data for galaxies between 12<sup>h</sup> and 24<sup>h</sup>*. Cited on pages 5, 6, and 45.
- Debattista V.P., Carollo C.M., Mayer L. & Moore B., 2005, *The Kinematic Signature of Face-On Peanut-shaped Bulges*, ApJ, 628, 678. Cited on page 59.
- Dehnen W., 2002, *Our Galaxy*, in E. Athanassoula, A. Bosma & R. Mujica, editors, *Disks of Galaxies: Kinematics, Dynamics and Perturbations*, volume 275 of *Astronomical Society of the Pacific Conference Series*, pages 105–116. Cited on page 7.
- del Burgo C., Mediavilla E. & Arribas S., 2000, *High-Ionization Clouds in the Circumnuclear Region of M31*, ApJ, 540, 741. Cited on pages 6 and 64.
- Emerson D.T., 1974, *High resolution observations of neutral hydrogen in M31. I*, MNRAS, 169, 607. Cited on page 4.
- Emsellem E., Fathi K., Wozniak H. et al., 2006, *Gas and stellar dynamics in NGC 1068: probing the galactic gravitational potential*, MNRAS, 365, 367. Cited on page 65.

- Erwin P. & Debattista V.P., 2016, *Caught in the Act: Direct Detection of Galactic Bars in the Buckling Phase*, ApJL, 825, L30. Cited on page 8.
- Eskridge P.B., Frogel J.A., Pogge R.W. et al., 2000, *The Frequency of Barred Spiral Galaxies in the Near-Infrared*, AJ, 119, 536. Cited on page 6.
- Evans I.N., Primini F.A., Glotfelty K.J. et al., 2010, *The Chandra Source Catalog*, ApJS, 189, 37. Cited on page 6.
- Faber S.M., Friel E.D., Burstein D. & Gaskell C.M., 1985, *Old stellar populations. II - an analysis of K-giant spectra*, ApJS, 57, 711. Cited on page 87.
- Fabricius M.H., 2012, *Kinematics across bulge types. a longslit kinematic survey and dedicated instrumentation*, Ph.D. thesis, Ludwig-Maximilians-Universität München, Germany. Cited on page 11.
- Fabricius M.H., Coccato L., Bender R. et al., 2014, *Regrowth of stellar discs in mature galaxies: the two-component nature of NGC 7217 revisited with VIRUS-W*, MNRAS, 441, 2212. Cited on page 14.
- Fabricius M.H., Grupp F., Bender R. et al., 2012a, *VIRUS-W: commissioning and first-year results of a new integral field unit spectrograph dedicated to the study of spiral galaxy bulges*, in *Society of Photo-Optical Instrumentation Engineers (SPIE) Conference Series*, volume 8446 of *Society of Photo-Optical Instrumentation Engineers (SPIE) Conference Series*. Cited on pages 5, 11, and 12.
- Fabricius M.H., Saglia R.P., Fisher D.B. et al., 2012b, *Kinematic Signatures of Bulges Correlate with Bulge Morphologies and Sérsic Index*, ApJ, 754, 67. Cited on page 46.
- Falcón-Barroso J., Bacon R., Bureau M. et al., 2006, *The SAURON project - VII. Integral-field absorption and emission-line kinematics of 24 spiral galaxy bulges*, MNRAS, 369, 529. Cited on pages 57, 58, 63, and 133.
- Fathi K., van de Ven G., Peletier R.F. et al., 2005, *A bar signature and central disc in the gaseous and stellar velocity fields of NGC 5448*, MNRAS, 364, 773. Cited on page 65.
- Fernie J.D., 1970, *The Historical Quest for the Nature of the Spiral Nebulae*, Publications of the Astronomical Society of the Pacific, 82, 1189. Cited on page 2.
- Fisher D., 1997, *Kinematic Profiles of SO Galaxies*, AJ, 113, 950. Cited on page 58.
- Fisher D.B. & Drory N., 2008, *The Structure of Classical Bulges and Pseudobulges: the Link Between Pseudobulges and SÉRSIC Index*, AJ, 136, 773. Cited on page 5.

- Franx M., Illingworth G. & de Zeeuw T., 1991, *The ordered nature of elliptical galaxies - Implications for their intrinsic angular momenta and shapes*, ApJ, 383, 112. Cited on page 57.
- Frei Z. & Gunn J.E., 1994, *Generating colors and K corrections from existing catalog data*, AJ, 108, 1476. Cited on page 39.
- Gamerman D. & Lopes H., 2006, *Markov Chain Monte Carlo: Stochastic Simulation for Bayesian Inference. Second Edition*, Chapman and Hall/CRC. Cited on page 112.
- Ganda K., Falcón-Barroso J., Peletier R.F. et al., 2006, *Late-type galaxies observed with SAURON: two-dimensional stellar and emission-line kinematics of 18 spirals*, MNRAS, 367, 46. Cited on pages 58 and 63.
- García-Barreto J.A. & Rosado M., 2001, *Fabry-Pérot H $\alpha$  Observations of the Barred Spiral NGC 3367*, AJ, 121, 2540. Cited on page 65.
- Gerhard O.E., 1993, *Line-of-sight velocity profiles in spherical galaxies: breaking the degeneracy between anisotropy and mass.*, MNRAS, 265, 213. Cited on page 21.
- Gordon K.D., Bailin J., Engelbracht C.W. et al., 2006, *Spitzer MIPS Infrared Imaging of M31: Further Evidence for a Spiral-Ring Composite Structure*, ApJL, 638, L87. Cited on page 7.
- Gössl C.A. & Riffeser A., 2002, *Image reduction pipeline for the detection of variable sources in highly crowded fields*, A&A, 381, 1095. Cited on page 14.
- Gregersen D., Seth A.C., Williams B.F. et al., 2015, *Panchromatic Hubble Andromeda Treasury. XII. Mapping Stellar Metallicity Distributions in M31*, AJ, 150, 189. Cited on page 100.
- Gurzadyan G.A., 1997, *The Physics and Dynamics of Planetary Nebulae*. Cited on page 23.
- Hafez I., 2010, *Abd al-rahman al-sufi and his book of the fixed stars: a journey of re-discovery*, Ph.D. thesis, James Cook University, Australia. Cited on page 1.
- Hammer F., Puech M., Chemin L., Flores H. & Lehnert M.D., 2007, *The Milky Way, an Exceptionally Quiet Galaxy: Implications for the Formation of Spiral Galaxies*, ApJ, 662, 322. Cited on page 6.
- Hartwig E., 1885, *Ueber den neuen Stern im grossen Andromeda-Nebel*, Astronomische Nachrichten, 112, 355. Cited on page 3.
- Henderson A.P., 1979, *A model for the orientation of M31*, A&A, 75, 311. Cited on pages 5, 45, and 47.

- Hernández-López I., Athanassoula E., Mújica R. & Bosma A., 2009, *M33: The existence of a bar*, in *Revista Mexicana de Astronomía y Astrofísica Conference Series*, volume 37 of *Revista Mexicana de Astronomía y Astrofísica Conference Series*, pages 160–162. Cited on page 7.
- Hill G.J., Gebhardt K., Komatsu E. & MacQueen P.J., 2004, *The Hobby-Eberly Telescope Dark Energy Experiment*, in R.E. Allen, D.V. Nanopoulos & C.N. Pope, editors, *The New Cosmology: Conference on Strings and Cosmology*, volume 743 of *American Institute of Physics Conference Series*, pages 224–233. Cited on page 14.
- Hubble E.P., 1925, *Cepheids in spiral nebulae*, *The Observatory*, 48, 139. Cited on page 3.
- Huggins W. & Miller W.A., 1864, *On the Spectra of Some of the Nebulae. By William Huggins, F.R.A.S. A Supplement to the Paper "On the Spectra of Some of the Fixed Stars William Huggins F.R.A.S., and W. A. Miller, M.D., LL.D., Treas. and V.P.P.S."*, *Royal Society of London Philosophical Transactions Series I*, 154, 437. Cited on page 2.
- Jacoby G.H., Ford H. & Ciardullo R., 1985, *Ionized gas in the center of M31*, *ApJ*, 290, 136. Cited on pages 3, 7, 78, 79, 134, and 135.
- Jarrett T.H., Chester T., Cutri R., Schneider S.E. & Huchra J.P., 2003, *The 2MASS Large Galaxy Atlas*, *AJ*, 125, 525. Cited on pages 33 and 34.
- Kang Y., Bianchi L. & Rey S.C., 2009, *An Ultraviolet Study of Star-Forming Regions in M31*, *ApJ*, 703, 614. Cited on page 6.
- Kapala M.J., Sandstrom K., Groves B. et al., 2015, *The Survey of Lines in M31 (SLIM): Investigating the Origins of [C II] Emission*, *ApJ*, 798, 24. Cited on pages 40 and 43.
- Kelson D.D., Illingworth G.D., van Dokkum P.G. & Franx M., 2000, *The Evolution of Early-Type Galaxies in Distant Clusters. II. Internal Kinematics of 55 Galaxies in the  $z=0.33$  Cluster CL 1358+62*, *ApJ*, 531, 159. Cited on page 21.
- Kelz A., Verheijen M.A.W., Roth M.M. et al., 2006, *PMAS: The Potsdam Multi-Aperture Spectrophotometer. II. The Wide Integral Field Unit PPak*, *Publications of the Astronomical Society of the Pacific*, 118, 129. Cited on page 40.
- Kent S.M., 1989, *A comparison of optical and H I rotation curves in M 31*, *Publications of the Astronomical Society of the Pacific*, 101, 489. Cited on page 4.
- Kormendy J. & Bender R., 1999, *The Double Nucleus and Central Black Hole of M31*, *ApJ*, 522, 772. Cited on pages xi, 13, 33, and 34.
- Kormendy J. & Kennicutt Jr. R.C., 2004, *Secular Evolution and the Formation of Pseudobulges in Disk Galaxies*, *ARAA*, 42, 603. Cited on pages 6 and 7.

- Krajnović D., Cappellari M., de Zeeuw P.T. & Copin Y., 2006, *Kinometry: a generalization of photometry to the higher moments of the line-of-sight velocity distribution*, MNRAS, 366, 787. Cited on page 57.
- Kroupa P., 2001, *On the variation of the initial mass function*, MNRAS, 322, 231. Cited on page 98.
- Kuzio de Naray R., Zagursky M.J. & McGaugh S.S., 2009, *Kinematic and Photometric Evidence for a Bar in NGC 2683*, AJ, 138, 1082. Cited on pages 7, 65, 67, and 74.
- Le Borgne J.F., Bruzual G., Pelló R. et al., 2003, *STELIB: A library of stellar spectra at  $R \sim 2000$* , A&A, 402, 433. Cited on pages 38 and 139.
- Lee C.H., Riffeser A., Koppenhoefer J. et al., 2012, *PAndromeda - First Results from the High-cadence Monitoring of M31 with Pan-STARRS 1*, AJ, 143, 89. Cited on page 136.
- Lee C.H., Riffeser A., Seitz S., Bender R. & Koppenhoefer J., 2015, *Microlensing Events from the 11 Year Observations of the Wendelstein Calar Alto Pixellensing Project*, ApJ, 806, 161. Cited on page 136.
- Lindblad B., 1956, *On a Barred Spiral Structure in the Andromeda Nebula*, Stockholms Observatoriums Annaler, 19. Cited on pages 7, 8, and 133.
- Lynden-Bell D., 1979, *On a mechanism that structures galaxies*, MNRAS, 187, 101. Cited on page 7.
- Maraston C., 1998, *Evolutionary synthesis of stellar populations: a modular tool*, MNRAS, 300, 872. Cited on pages 98 and 135.
- Maraston C., 2005, *Evolutionary population synthesis: models, analysis of the ingredients and application to high-z galaxies*, MNRAS, 362, 799. Cited on pages 98 and 135.
- Marius S., 1614, *Mundus Iovialis*, Johann Lauer, Bürger und Buchhändler zu Nürnberg. Cited on page 1.
- Marius S., 1988, *Mundus Iovialis - Die Welt des Jupiter. Die Entdeckung der Jupitermonde durch den fränkischen Hofmathematiker und Astronomen Simon Marius im Jahr 1609 - lateinisch und deutsch; Herausgegeben und bearbeitet von Joachim Schlör; Naturwissenschaftlich begleitet und mit einem Nachwort versehen von Alois Wilder*, Schrenk-Verlag, Gunzenhausen, 1. Auflage. Cited on page 1.
- Mayall N.U., 1951, *Comparison of Rotational Motions Observed in the Spirals M31 and M33 and in The Galaxy*, Publications of Michigan Observatory, 10, 19. Cited on page 3.

- McElroy D.B., 1983, *Dynamics of the stellar component of the bulge of M31*, ApJ, 270, 485. Cited on page 3.
- Meeks M.L., 1976, *Methods of experimental physics. Vol. 12. Astrophysics. Part-C: Radio observations*. Cited on page 15.
- Melchior A.L. & Combes F., 2011, *Molecular gas in the inner 0.7 kpc-radius ring of M 31*, A&A, 536, A52. Cited on pages xiii, 4, 64, 65, 67, 68, 75, 76, and 134.
- Melchior A.L. & Combes F., 2013, *A cold-gas reservoir to fuel the M 31 nuclear black hole and stellar cluster*, A&A, 549, A27. Cited on page 4.
- Melchior A.L. & Combes F., 2016, *Dense gas tracing the collisional past of Andromeda. An atypical inner region?*, A&A, 585, A44. Cited on pages 4 and 67.
- Melchior A.L., Viallefond F., Guélin M. & Neininger N., 2000, *Detection of CO in the inner part of the bulge of M31*, MNRAS, 312, L29. Cited on page 4.
- Méndez-Abreu J., Corsini E.M., Debattista V.P. et al., 2008, *Confirmation of a Kinematic Diagnostic for Face-On Box/Peanut-shaped Bulges*, ApJL, 679, L73. Cited on page 59.
- Menéndez-Delmestre K., Sheth K., Schinnerer E., Jarrett T.H. & Scoville N.Z., 2007, *A Near-Infrared Study of 2MASS Bars in Local Galaxies: An Anchor for High-Redshift Studies*, ApJ, 657, 790. Cited on page 6.
- Merritt D. & Sellwood J.A., 1994, *Bending instabilities in stellar systems*, ApJ, 425, 551. Cited on page 8.
- Messier C., 1781, *Catalogue des Nébuleuses des amas d'Étoiles (Catalog of Nebulae and Star Clusters)*. Cited on page 2.
- Mould J., 2013, *The Bulge of M31*, Publications of the Astronomical Society of Australia, 30, e027. Cited on page 6.
- Müller F., 2014, *Development Of A Fiber Based Integral Field Unit and Derivation Of The Instrumental Response Function Of An Existing Integral Field Unit*. Cited on page 39.
- Nieten C., Neininger N., Guélin M. et al., 2006, *Molecular gas in the Andromeda galaxy*, A&A, 453, 459. Cited on page 4.
- Nissen P.E., 2013, *Chemical Abundances as Population Tracers*, in T.D. Oswalt & G. Gilmore, editors, *Planets, Stars and Stellar Systems. Volume 5: Galactic Structure and Stellar Populations*, Springer-Verlag, Berlin Heidelberg New York. Cited on page 98.
- Oh K., Sarzi M., Schawinski K. & Yi S.K., 2011, *Improved and Quality-assessed Emission and Absorption Line Measurements in Sloan Digital Sky Survey Galaxies*, ApJS, 195, 13. Cited on page 22.

- Oke J.B., 1990, *Faint spectrophotometric standard stars*, AJ, 99, 1621. Cited on pages 38, 39, and 139.
- Oke J.B. & Gunn J.E., 1983, *Secondary standard stars for absolute spectrophotometry*, ApJ, 266, 713. Cited on page 39.
- Pease F.G., 1918, *The Rotation and Radial Velocity of the Central Part of the Andromeda nebula*, Proceedings of the National Academy of Science, 4, 21. Cited on page 3.
- Pellet A., 1976, *Rotation in the central region of M 31*, A&A, 50, 421. Cited on page 3.
- Peterson C.J. & Huntley J.M., 1980, *Observations of the kinematics of barred spiral galaxies. I - NGC 1300*, ApJ, 242, 913. Cited on page 65.
- Prugniel P., Soubiran C., Koleva M. & Le Borgne D., 2007, *VizieR Online Data Catalog: ELODIE library V3.1*, VizieR Online Data Catalog, 3251, 0. Cited on pages 21 and 125.
- Raha N., Sellwood J.A., James R.A. & Kahn F.D., 1991, *A dynamical instability of bars in disk galaxies*, Nature, 352, 411. Cited on page 8.
- Riffeser A., Fliri J., Seitz S. & Bender R., 2006, *Microlensing toward Crowded Fields: Theory and Applications to M31*, ApJS, 163, 225. Cited on page 136.
- Roberts I., 1888, *Photographs of the nebulae M 31, h 44, and h 51 Andromedae, and M 27 Vulpeculae*, MNRAS, 49, 65. Cited on page 2.
- Roberts M.S. & Whitehurst R.N., 1975, *The rotation curve and geometry of M31 at large galactocentric distances.*, ApJ, 201, 327. Cited on page 4.
- Robitaille T.P. & Whitney B.A., 2010, *The Present-Day Star Formation Rate of the Milky Way Determined from Spitzer-Detected Young Stellar Objects*, ApJL, 710, L11. Cited on page 6.
- Roth M.M., Kelz A., Fechner T. et al., 2005, *PMAS: The Potsdam Multi-Aperture Spectrophotometer. I. Design, Manufacture, and Performance*, Publications of the Astronomical Society of the Pacific, 117, 620. Cited on page 40.
- Rubin V.C. & Ford Jr. W.K., 1970, *Rotation of the Andromeda Nebula from a Spectroscopic Survey of Emission Regions*, ApJ, 159, 379. Cited on pages 3 and 7.
- Rubin V.C. & Ford Jr. W.K., 1971, *Radial Velocities and Line Strengths of Emission Lines across the Nuclear Disk of M31*, ApJ, 170, 25. Cited on pages 3 and 7.

- Saglia R.P., Fabricius M., Bender R. et al., 2010, *The old and heavy bulge of M 31 . I. Kinematics and stellar populations*, A&A, 509, A61, abbreviated as S10 in the text. Cited on pages [xii](#), [xiii](#), [xiv](#), [3](#), [5](#), [6](#), [8](#), [33](#), [34](#), [45](#), [46](#), [47](#), [48](#), [49](#), [51](#), [53](#), [55](#), [57](#), [64](#), [69](#), [77](#), [89](#), [90](#), [92](#), [93](#), [94](#), [95](#), [96](#), [97](#), [98](#), [99](#), [100](#), [104](#), [105](#), [106](#), [125](#), and [135](#).
- Saha K., Martinez-Valpuesta I. & Gerhard O., 2012, *Spin-up of low-mass classical bulges in barred galaxies*, MNRAS, 421, 333. Cited on page [114](#).
- Sarajedini A. & Jablonka P., 2005, *The Metallicity Distribution Function of Field Stars in M31's Bulge*, AJ, 130, 1627. Cited on page [100](#).
- Sarzi M., Falc3n-Barroso J., Davies R.L. et al., 2006, *The SAURON project - V. Integral-field emission-line kinematics of 48 elliptical and lenticular galaxies*, MNRAS, 366, 1151. Cited on pages [21](#), [22](#), and [23](#).
- Sarzi M., Shields J.C., Schawinski K. et al., 2010, *The SAURON project - XVI. On the sources of ionization for the gas in elliptical and lenticular galaxies*, MNRAS, 402, 2187. Cited on pages [84](#) and [85](#).
- Scheiner J., 1899, *On the spectrum of the great nebula in Andromeda.*, ApJ, 9, 149. Cited on page [3](#).
- Seidel M.K., Falc3n-Barroso J., Mart3nez-Valpuesta I. et al., 2016, *The BaLROG project - II. Quantifying the influence of bars on the stellar populations of nearby galaxies*, ArXiv e-prints. Cited on pages [100](#), [108](#), and [135](#).
- Sellwood J.A., 2013, *Dynamics of Disks and Warps*, in T.D. Oswalt & G. Gilmore, editors, *Planets, Stars and Stellar Systems. Volume 5: Galactic Structure and Stellar Populations*, Springer-Verlag, Berlin Heidelberg New York. Cited on page [7](#).
- Sellwood J.A. & Wilkinson A., 1993, *Dynamics of barred galaxies*, Reports on Progress in Physics, 56, 173. Cited on page [7](#).
- Sersic J.L., 1968, *Atlas de galaxias australes*. Cited on page [33](#).
- Skrutskie M.F., Cutri R.M., Stiening R. et al., 2003, *VizieR Online Data Catalog: The 2MASS Extended sources (IPAC/UMass, 2003-2006)*, VizieR Online Data Catalog, 7233. Cited on page [16](#).
- Slipher V.M., 1914, *The Radial Velocity of the Andromeda Nebula*, Popular Astronomy, 22, 19. Cited on page [3](#).
- Stark A.A., 1977, *Triaxial Models of the Bulge of M31*, ApJ, 213, 368. Cited on pages [7](#), [8](#), and [133](#).
- Stark A.A. & Binney J., 1994, *Bar-induced gas velocities in the bulge of M31*, ApJL, 426, L31. Cited on pages [7](#), [8](#), [56](#), [63](#), and [133](#).

- Tabatabaei F.S. & Berkhuijsen E.M., 2010, *Relating dust, gas, and the rate of star formation in M 31*, A&A, 517, A77. Cited on page 6.
- Tamm A., Tempel E., Tenjes P., Tihhonova O. & Tuvikene T., 2012, *Stellar mass map and dark matter distribution in M 31*, A&A, 546, A4. Cited on pages 59 and 71.
- Thomas D. & Davies R.L., 2006, *Rejuvenation of spiral bulges*, MNRAS, 366, 510. Cited on pages 101, 109, and 135.
- Thomas D., Maraston C. & Bender R., 2003, *New clues on the calcium underabundance in early-type galaxies*, MNRAS, 343, 279. Cited on pages 98 and 135.
- Toomre A., 1981, *What amplifies the spirals*, in S.M. Fall & D. Lynden-Bell, editors, *Structure and Evolution of Normal Galaxies*, pages 111–136. Cited on page 7.
- Trager S.C., Worthey G., Faber S.M., Burstein D. & González J.J., 1998, *Old Stellar Populations. VI. Absorption-Line Spectra of Galaxy Nuclei and Globular Clusters*, ApJS, 116, 1. Cited on pages 11, 87, 88, and 135.
- van den Bergh S., 1994, *The enigmatic supernova S Andromedae*, ApJ, 424, 345. Cited on page 3.
- van der Marel R.P. & Franx M., 1993, *A new method for the identification of non-Gaussian line profiles in elliptical galaxies*, ApJ, 407, 525. Cited on pages 21 and 59.
- van Leeuwen F., 2007, *Validation of the new Hipparcos reduction*, A&A, 474, 653. Cited on page 21.
- Veilleux S. & Osterbrock D.E., 1987, *Spectral classification of emission-line galaxies*, ApJS, 63, 295. Cited on page 84.
- Watkins L.L., Evans N.W. & An J.H., 2010, *The masses of the Milky Way and Andromeda galaxies*, MNRAS, 406, 264. Cited on page 6.
- Wenger M., Ochsenbein F., Egret D. et al., 2000, *The SIMBAD astronomical database. The CDS reference database for astronomical objects*, A&AS, 143, 9. Cited on page 21.
- Wilson H.C., 1899, *The Great Nebula in Andromeda*, Popular Astronomy, 7, 507. Cited on page 2.
- Worthey G., Faber S.M., Gonzalez J.J. & Burstein D., 1994, *Old stellar populations. 5: Absorption feature indices for the complete LICK/IDS sample of stars*, ApJS, 94, 687. Cited on pages 21 and 87.
- Yin J., Hou J.L., Prantzos N. et al., 2009, *Milky Way versus Andromeda: a tale of two disks*, A&A, 505, 497. Cited on page 6.

---

## Acknowledgements

First, I would like to express my deepest gratitude to my thesis supervisor Roberto Saglia for giving me the opportunity to work on this exciting project for my PhD, allowing me to go observing multiple times and to attend conferences all over the world. His excellent knowledge about galaxy kinematics and dynamics as well as stellar populations and his endless patience have greatly helped me when writing this thesis. Very special thanks also go to Maximilian Fabricius, who introduced me to the concept of IFU spectroscopy and taught me how to operate the telescope and instrument during observations. I am also thankful to Peter Erwin, whose vast knowledge of galaxies and their properties already helped me in my Master's thesis and during my PhD, and Francesco Montesano, who helped solve many problems surfacing in python programming. A very special thanks also goes to the rest of the OPINAS group, especially for the lively discussions over coffee.

From my fellow PhD students, I first want to thank my friends Philipp Lang and Thomas Siebert for great discussions over lunch, helping me out with IDL and statistics problems and overall support. Then, I am grateful to my officemates Holger Schlagenhauer, Sandesh Kulkarni, Salvador Salazar, Jan Grieb, Fabrizio Finozzi, Martha Lippich and Jiamin Hou, who always kept a nice working atmosphere, but also allowed for breaks and lively discussions about other things than science. From the corridor, I am thankful Matias Blaña for providing me with his models that are also used in this thesis and for great discussions about M31, and to Manuel Behrendt, who, due to his frequent visits, became a somewhat unofficial officemate.

Furthermore, I would like to thank Surangkana Rukdee and Suryashree Aniyan for keeping their patience during the observation runs at the McDonald observatory. Here, I would also like to thank the whole McDonald staff for ensuring smooth runs and, if things didn't go as well, for quickly resolving the issues.

Outside of astronomy, I am thankful for my friends Marc Schneider and Peter Sterflinger, who helped me turn my mind off work and relax.

Lastly, I would like to thank my family, without whose support I would not have been able to see this project through.